Bio-Inspired Engineering of Supramolecular Hydrogels Using Guanosine 5′-Monophosphate as a Primordial Biomolecular Scaffold: From Design Strategies to Emerging Applications

Ph.D. Thesis

By

SURYAKAMAL SARMA



DEPARTMENT OF CHEMISTRY

INDIAN INSTITUTE OF TECHNOLOGY INDORE

JULY 2026

Bio-Inspired Engineering of Supramolecular Hydrogels Using Guanosine 5′-Monophosphate as a Primordial Biomolecular Scaffold: From Design Strategies to Emerging Applications

A THESIS

Submitted in partial fulfillment of the requirements for the award of the degree of

DOCTOR OF PHILOSOPHY

by

SURYAKAMAL SARMA



DEPARTMENT OF CHEMISTRY

INDIAN INSTITUTE OF TECHNOLOGY INDORE

JULY 2026

INDIAN INSTITUTE OF TECHNOLOGY INDORE

I hereby certify that the work which is being presented in the thesis entitled **Bio-Inspired Engineering of Supramolecular Hydrogels Using Guanosine 5′-Monophosphate as a Primordial Biomolecular Scaffold: From Design Strategies to Emerging Applications** in the partial fulfillment of the requirements for the award of the degree of **DOCTOR OF PHILOSOPHY** and submitted in the **DEPARTMENT OF CHEMISTRY, Indian Institute of Technology Indore**, is an authentic record of my own work carried out during the time period from **August, 2021** to **July, 2026** under the supervision of **Prof. Tridib Kumar Sarma**, Associate Professor, Department of Chemistry, Indian Institute of Technology Indore.

The matter presented in this thesis has not been submitted by me for the award of any other degree of this or any other institute.

SURYAKAMAL SARMA

This is to certify that the above statement made by the candidate is correct to the best of my/our knowledge.

PROF. TRIDIB KUMAR SARMA

SURYAKAMAL SARMA has successfully given his/her Ph.D. Oral Examination held on 06/11/2026.

PROF. TRIDIB KUMAR SARMA

ACKNOWLEDGEMENT

Like every meaningful journey, a thesis is never walked alone; it is carried forward on the shoulders of a whole community, woven together by their support and guidance. Without the wisdom, encouragement, and generous assistance of several individuals, this work would not have been possible. To each person who lent their hand, their time, and their belief in this endeavour, I offer my deepest gratitude, for it is through you that this dream became reality.

I am profoundly grateful to my supervisor, Dr. Tridib Kumar Sarma, for his support, guidance and mentorship throughout my doctoral journey. His knowledge, insightful advice, and enthusiasm have been instrumental in shaping this research and in my growth as a researcher. Through his continuous motivation and thoughtful supervision, he encouraged me to explore every aspect of our research with curiosity, rigor, and independence. More importantly, he placed his trust in me during several critical phases of my research and stood firmly by my side whenever I needed guidance and support the most. His confidence in my abilities motivated me to strive for excellence and to overcome obstacles with determination. I will always remain deeply grateful and indebted to him for his faith, mentorship, and encouragement. Above all, I sincerely thank him for giving me the greatest opportunity of my life, to discover my potential, pursue meaningful scientific research, and evolve not only into a better researcher but also into a better individual.

I would like to express my sincere gratitude to my PSPC members, Professor Sanjay Kumar Singh and Dr. Selvakumar Sermadurai, for their constructive suggestions and continuous guidance throughout my doctoral research. I am also thankful to Dr. Umesh A. Kshirsagar, Head of the Department of Chemistry, IIT Indore, Professor Suhas S. Joshi, Director, IIT Indore, and all the faculty members of the Department of Chemistry for their encouragement, valuable insights, and support during the course of my research. I gratefully acknowledge the Department of Science and Technology (DST), Government of

India, for awarding me the INSPIRE Fellowship, which provided the financial support essential for pursuing my doctoral studies. I sincerely thank the Department of Chemistry and the Sophisticated Instrumentation Centre, Indian Institute of Technology Indore, for providing excellent research infrastructure and access to the in-house instrumentation facilities required for this work. I also acknowledge the support extended by the SAIF, IIT Bombay, CRF, IIT Delhi, and IIC, IIT Roorkee for providing access to the HR-TEM, EPR, and XPS characterization facilities, which were indispensable to this research.

I would also like to express my sincere gratitude to Mr. Kinny Pandey, Dr. Ravinder Kumar, Mr. Ghanshyam Bhavsar, Mr. Atul Singh, Mr. Nitin Upadhyay, Mr. Mayur Dhake, and Mr. Pranjal Shrimali for their invaluable technical assistance throughout my research. I am equally thankful to Mr. Manish Kushwaha, Mrs. Vinita Kothari, Mr. Rameshwar Dauhare, Mr. Souvik Debnath, and Mr. Parthiban P. K. for their continuous administrative and official support, which played a vital role in the smooth progress of my doctoral work. I also gratefully acknowledge the assistance and dedicated service of all the technical and non-technical staff of IIT Indore, whose support contributed significantly to the successful completion of this research.

This research would not have been possible without the valuable support and contributions of my collaborators. I sincerely express my gratitude to Professor Hem Chandra Jha, Professor Amit Kumar, and Professor Rajesh Kumar for their guidance and for providing me with the opportunity to carry out the biological and electrochemical aspects of this research. I am also deeply thankful to my collaborators, Dr. Nidhi Varshney, Dr. Love Bansal, and Mr. Ashmad Nayak, for their invaluable assistance with the biological and physics-related studies. Their expertise and collaborative spirit greatly enriched this work. Furthermore, I would like to extend my heartfelt appreciation to Dr. Chanchal Rani, Dr. Deb Kumar Rath, and Ms. Vaishali Saini for their generous assistance throughout the course of my research.

I would like to express my heartfelt gratitude to my seniors, Dr. Amrita Chakraborty, Dr. Vidhi Agarwal, Dr. Debanjan Bagchi, and Dr. Avijit Maity, for warmly welcoming me into the research group and guiding me during the early stages of my doctoral journey. Their support, valuable advice, and encouragement, both scientific and personal, have been instrumental in shaping my research experience. I am equally grateful to my M.Sc. juniors, Ms. Nishita Jain, Mr. Rahul Kumar Sharma, and Ms. Divyanshi Deshwal, with whom I had the privilege of carrying out a significant part of the research presented in this thesis. A special note of gratitude goes to my research colleagues and brothers, Mr. Ravindra Vishwakarma, Mr. Aditya Prasun, and Mr. Tarun Kumar Sahu. Their unwavering companionship, constant encouragement, and unconditional support made my years at IIT Indore truly memorable. They became more than colleagues, they became family, standing by me through every challenge and celebration.

I also sincerely thank my wonderful lab mates and juniors, Mrs. Huma Tabassum, Ms. Priyanka Nath, Ms. Anjali Singh, Ms. Yoshita Chakraborty, Mr. Naveen Kumar, Mr. Suman Chaudhury, and Mr. Rishabh Vishwakarma, for their friendship, continuous support, and for fostering a positive, cheerful, and collaborative atmosphere in the laboratory. Over the years, we have grown together, shared countless experiences, and learned immensely from one another. Finally, I would like to acknowledge my M.Sc. juniors, Mr. Saikat Sinha, Mr. Punit Sharma, Mr. Ankit Gupta, Ms. Ayushi Biyani, Mr. Reetik Chib, Ms. Shaurya Aneja, and Ms. Anamika Devrani, for their encouragement, friendship, and best wishes throughout my doctoral journey. In the never-ending list, I would like to mention a few more names: Mr. Uddipan Sarma, Mr. Angarag Kashyap, Mr. Nabajit Barman, Mr. Kripangkar Choudhury, Mr. Nilotpal Deka, Mr. Dupal Bhagawati and all my friends for their love and support.

Above all, I owe my deepest gratitude to my parents and my family, without whose unconditional love, sacrifices, and faith in me,

this journey would never have been possible. I am profoundly grateful to my mother, Mrs. Bibha Sarma, and my father, Mr. Tirtha Nath Sarma, for their endless love, encouragement, and selfless sacrifices. I would also like to express my heartfelt gratitude to my uncle, Late Upendra Nath Sarma, Dr. Uma Charan Sarma, my aunts, Mrs. Nani Devi and Mrs. Dipali Devi, for their unconditional love, affection, and support throughout my life. I am equally thankful to my brother, Parthakamal, and all my cousins for their endless love, encouragement, and belief in me during every stage of this journey. Last but certainly not least, I wish to express my deepest appreciation to my partner, Ms. Trishna Deka, for being my greatest source of strength throughout this journey. Her unwavering belief in me, boundless patience, selfless support, and constant encouragement, along with her love and companionship, helped me navigate every challenge. Finally, I would like to acknowledge everyone who has, in one way or another, contributed to this journey. Many individuals have supported me, directly or indirectly, and although it is impossible to mention every name, I extend my heartfelt gratitude to all of them.

Suryakamal Sarma

Dedicated to My Family

SYNOPSIS

Introduction

The integration of biomolecules into supramolecular superstructures forms the foundation of natural systems. Biomolecular building blocks such as amino acids, nucleosides/nucleotides, and carbohydrates can spontaneously organize into highly ordered architectures through noncovalent interactions, generating functional materials with precise structural and physicochemical properties *[1-3]*. Among these systems, nucleotide-based assemblies have attracted considerable attention due to their structural versatility and functional significance. One of the most extensively studied motifs is the G-quartet, a planar hydrogen-bonded macrocycle formed through cation-templated assembly of guanosine units, first identified as the structural basis for the aggregation of 5′-guanosine monophosphate (5′-GMP) *[4]*. Through Hoogsteen hydrogen bonding, 5′-GMP self-assembles into supramolecular structures such as G-monomeric aggregates, G-dimers, and highly ordered G-quadruplexes and multiple quartets. These hydrogen-bonded G-quartets further stack via π-π interactions and interlayer hydrogen bonding to generate extended columnar superstructures *[4-6]*. The resulting one-dimensional fibrillar assemblies entangle and cross-link into three-dimensional networks capable of immobilizing solvent molecules, leading to hydrogel formation. Unlike permanently covalently cross-linked polymeric gels, these supramolecular hydrogels are stabilized by dynamic noncovalent interactions, imparting tissue-like softness, high water content, structural adaptability, and reversible stimuli responsiveness toward changes in pH, temperature, and ionic environment *[7]*.

Leveraging the unique self-association behavior of 5′-GMP *[8]*, various biomacromolecules, metal-organic or inorganic clusters, amino acids, synthetic polymers, and small organic molecules can be employed to induce G-quartet formation and generate functional soft materials.

This strategy not only provides a rational approach for designing biogenic materials, but also mimics natural tissue-formation processes while maintaining excellent biocompatibility and biodegradability. This thesis summarizes several bioengineering strategies for developing bio-inspired functional materials using self-assembled 5′-GMP scaffolds as the primary structural framework. Each chapter focuses on a distinct hydrogel design strategy tailored toward specific functionalities, while detailed kinetic, morphological, and spectroscopic investigations provide insight into the self-assembly behavior of 5′-GMP in the presence of different molecular and macromolecular constituents. Additionally, intrinsic and induced properties such as biocatalytic activity, amphiphilic behavior, stimuli responsiveness, dynamic reconfigurability, macromolecular confinement, and ionic conductivity are systematically explored. Finally, the thesis highlights the broad application potential of these self-assembled hydrogels in drug delivery, enzyme-mimetic biocatalysis, and bioelectronics, demonstrating how simple 5′-GMP self-association can be engineered into advanced bio-inspired, bio-derived and biogenic functional hydrogels.

Summary of the Thesis

The thesis comprises of total 7 chapters and the contents of each chapter included in the thesis are discussed in brief as follows:

Chapter 1. **General Introduction and Background**

This chapter provides a brief overview of biomolecular self-assembly and the fundamental principles governing the self-aggregation behavior of nucleotides, with particular emphasis on 5′-GMP-based assemblies. The processes of biomolecular condensation and the transformation of self-assembled architectures into supramolecular hydrogels are discussed. We also provide an overview of guanosine- and GMP-derived supramolecular hydrogels, elucidating their structural organization, formation mechanisms, and physicochemical properties. The chapter further consolidates recent advances in the engineering of self-

assembled supramolecular scaffolds, spanning a broad spectrum of bio-derived and biomedical applications.

Chapter 2. **Chromatin Inspired Bio-condensation between Biomass DNA and Guanosine monophosphate Produces All-nucleic Hydrogel as a Hydrotropic Drug Carrier**

In this chapter, a non-covalent bio-condensation between biomass DNA and guanosine monophosphate (GMP) has been described, mimicking chromatin folding and creating a unique "all-nucleic" DNA-GMP condensates. These condensates initiate the formation of G-quadruplex-based superstructures, assembling into super-helical fibers driven by synergistic hydrogen bonding and stacking, which have been thoroughly investigated through morphological and spectroscopic analysis. This simple, one-step method for the bio-condensation of biomass DNA leads to an "all-nucleic" hydrogel with higher-order self-assembly and excellent mechanical properties. While most of the reported DNA based biomaterials, including hydrogels, require precisely sequenced and molecularly architectured DNA building blocks, we have developed a simple, universal, and facile bio-condensation method that utilizes biomass DNA acquired from any bioresource to fabricate DNA hydrogels. The "all nucleic" biomass DNA hydrogel reported herein has several advantages: (a) all raw materials are nucleic acids (or fragments) derived from bio-resources, (b) the method is green and spontaneous, involving no synthetic steps, thereby can be translated to industrial scale easily, (c) the resultant hydrogel is highly stable, reusable and biocompatible. Furthermore, the hydrogel can encapsulate a variety of drug molecules, both hydrophilic and hydrophobic, with a high loading capacity and shows sustained drug release, demonstrating its competency as a universal drug carrier. We believe this energy-efficient and low-cost method represents a new technique for using biomass DNA as building blocks for the next generation of soft materials.

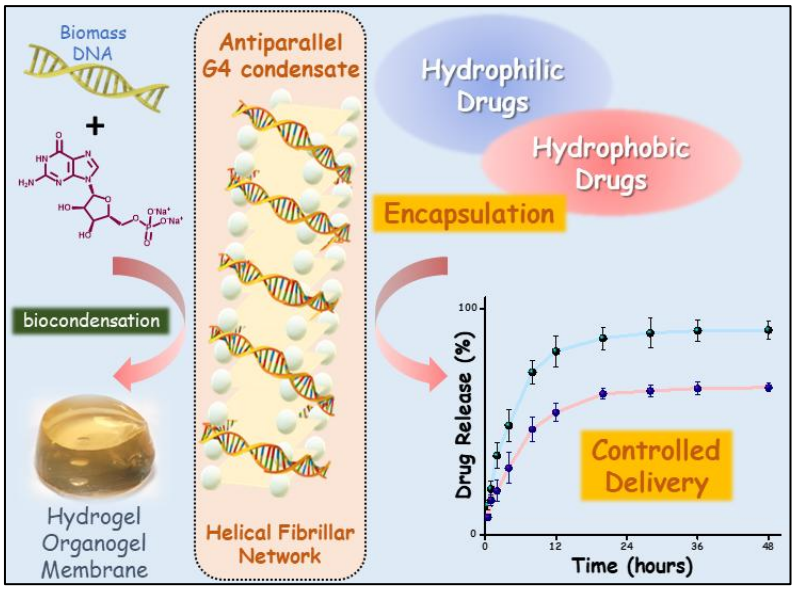


Figure 1. *Schematic illustration of the bio-condensation between biomass DNA and 5′-GMP, leading to all-nucleic hydrogel formation and its application as a hydrotropic drug-delivery carrier.*

Chapter 3. Minimalist Structural Tunability in a Biomass DNA-GMP Hydrogel Enables Programmable Anticancer Drug Release

Precise spatiotemporal control over drug-release kinetics remains a major challenge in anticancer therapy, where maintaining sustained intratumoral drug levels while minimizing systemic toxicity is critically important. In this chapter, we introduce a structure-tunable, biomass-derived DNA-GMP supramolecular hydrogel that enables programmable anticancer drug-release kinetics from a single DNA-GMP nanofibrillar matrix. As discussed in the previous chapter, spontaneous bio-condensation between biomass DNA and 5′-guanosine monophosphate drives the formation of DNA-wrapped, helically stacked G-quadruplex nanofibers, resulting in an intrinsically hydrotropic and amphiphilic hydrogel capable of encapsulating both hydrophilic and hydrophobic drugs. Herein, we demonstrate that minimal physical modulation of the supramolecular architecture, achieved through solvent engineering or biorelevant Ca^{2+} crosslinking, can reprogram the same hydrogel matrix to exhibit distinct drug-release behaviors, including first-order diffusion, Higuchi-type diffusion-controlled release, and zero-order surface erosion-dominated kinetics.

The hydrogels efficiently encapsulate the hydrophilic anticancer drug doxorubicin and the hydrophobic anticancer drug camptothecin, enabling sustained and predictable drug-release profiles under physiological conditions. Structural reorganization within the hydrogel network modulates fibrillar packing, mechanical stiffness, and swelling behavior, thereby directly influencing the underlying drug-transport mechanisms. Biological evaluation of the drug-loaded hydrogels in breast cancer models demonstrates enhanced anticancer efficacy with minimal toxicity toward healthy cells. Notably, camptothecin-loaded hydrogels effectively disrupt three-dimensional tumor spheroids at low drug concentrations (2-5 μM), accompanied by significantly enhanced apoptotic activity. Collectively, these findings establish a universal "all-nucleic" hydrogel platform in which structure-directed microarchitectural control enables tunable and predictable drug delivery, offering a promising strategy for precision anticancer therapeutics.

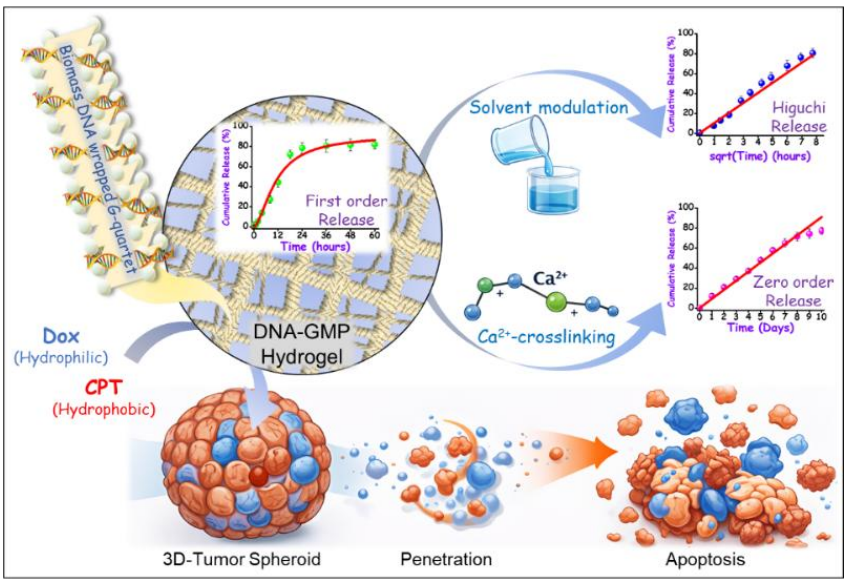


Figure 2. *Schematic representation of Structural Tunability in a Biomass DNA-GMP Hydrogel Enables Programmable Anticancer Drug Release and Therapeutics.*

Chapter 4. **Enzyme-Mimicking "All-Nucleotide" G-Quadruplex Hydrogel as a Dual-Function Microreactor for Biomimetic Cascade Catalysis**

Biomolecular condensation provides an effective strategy for creating confined microenvironments that regulate chemical transformations; however, translating this concept into minimal small-molecule catalytic systems remains largely unexplored. In this chapter, we report an “all-nucleotide” platform that spontaneously condenses into hierarchically organized G-quadruplex (G4)-based supramolecular networks and hydrogels with intrinsic biocatalytic activity. Co-assembly of guanosine 5′-monophosphate (GMP) with adenosine phosphate derivatives demonstrates that phosphate multiplicity and intrinsic acidity cooperatively regulate hierarchical self-assembly. While adenosine monophosphate (AMP) shows limited organization, adenosine di- and triphosphates (ADP and ATP) induce concentration-dependent transitions from liquid-liquid phase-separated droplets to fibrillar networks, with GMP serving as the primary structural scaffold. Mechanistic studies reveal that multivalent phosphate interactions and local pH modulation promote charge screening and proton redistribution, facilitating G-quartet stacking, with ADP exhibiting superior structural organization within an optimal pH window. At higher concentrations, ADP-GMP and ATP-GMP systems form stable self-supporting hydrogels through higher-order assembly. These hydrogels function as efficient metal-free peroxidase mimics with enhanced substrate affinity compared to native horseradish peroxidase. Importantly, the hydrogels also act as confined catalytic microenvironments for enzyme encapsulation, supporting multi-step cascade reactions with improved kinetics and sensitive biomolecular detection. Collectively, this work establishes a minimalistic platform integrating biomolecular condensation with catalysis for artificial microreactors and protocell-inspired materials.

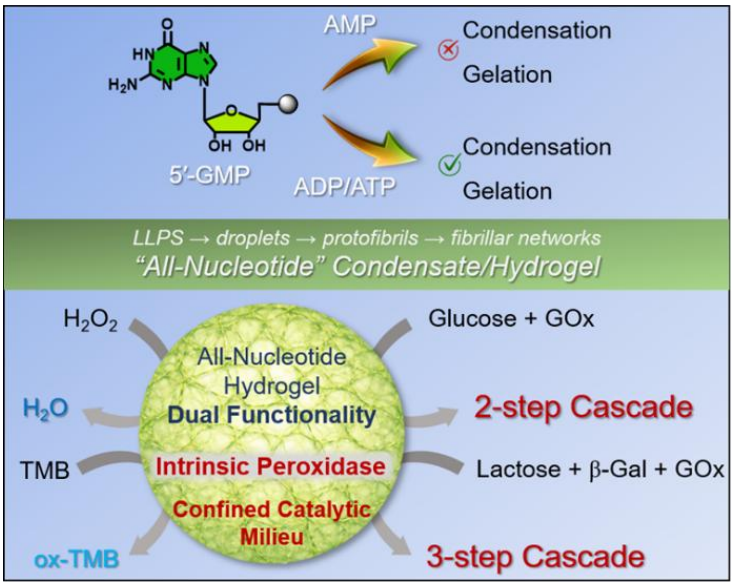


Figure 3. *Schematic representation of the Enzyme-Mimicking "All-Nucleotide" G-Quadruplex Hydrogel as a Dual-Function Microreactor for Biomimetic Cascade Catalysis.*

Chapter 5. Engineering a Nucleotide-Based Artificial Metalloenzyme through Supramolecular Confinement of a Copper-Histidine Cofactor

Natural metalloenzymes achieve remarkable catalytic efficiency through precisely organized metal-ligand active sites embedded within dynamic protein scaffolds. Reproducing such structural and functional complexity in artificial, non-proteinaceous systems remains a major challenge in enzyme mimetics. In this chapter, we present a de novo supramolecular strategy that mimics both the architecture and catalytic function of natural metalloenzymes through simple noncovalent condensation between a Copper-Histidine complex and 5′-guanosine monophosphate (5′-GMP). Leveraging the intrinsic self-assembly behavior of 5′-GMP, a bimetallic Copper-Histidine cofactor is spontaneously confined and stabilized within a hierarchically organized nanofibrous hydrogel, generating an enzyme-like catalytic microenvironment exclusively from pristine biomolecular components. This minimalistic yet robust supramolecular design not only transforms a biogenic metal complex into a functional hydrogel, but also provides a simple strategy for constructing protein-free artificial enzyme systems.

The resulting hydrogel exhibits catechol oxidase-like activity, selectively catalyzing the oxidation of 3,5-di-tert-butylcatechol to 3,5-di-tert-butyl-o-benzoquinone with enzyme-like reaction kinetics and high thermal stability. Importantly, supramolecular confinement within the nucleotide-based hydrogel matrix enhances copper-mediated catalytic activity by facilitating the formation of reactive copper-peroxide intermediates. Collectively, this work demonstrates that nucleotide-directed supramolecular confinement can recreate enzyme-like catalytic pockets, providing a versatile platform for biomolecule-derived artificial biocatalysts.

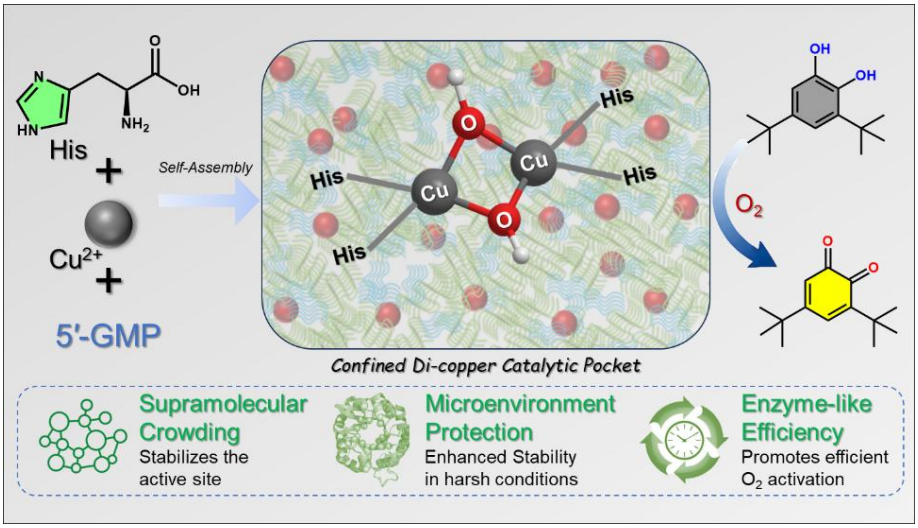


Figure 4. Schematic representation of the design strategy and enzyme-like activity of the Nucleotide-Based Artificial Metalloenzyme.

Chapter 6. Supramolecular Self-Assembly of Conductive Polymer Embedded Enzyme Mimicking GMP-Condensate Hydrogel for Electrochromic Energy Storage Applications

Conductive polymer hydrogels (CPHs) integrate the electrical conductivity of organic polymers with the high-water content, porosity, and tissue-like characteristics of hydrogels, making them highly promising materials for bioelectronic applications. However, conventional polymeric hydrogel matrices often suffer from limitations such as poor biocompatibility, restricted dynamic reconfigurability, limited self-healing capability, and inadequate control over mechanical

properties. In this chapter, we report a 5′-GMP-based supramolecular condensate hydrogel that self-assembles into a hierarchically organized fibrillar network possessing intrinsic metal-free peroxidase-mimetic activity within a micro-confined environment. Exploiting this unique catalytic behavior, the hydrogel matrix enables in situ oxidative polymerization of conductive monomers, including aniline, pyrrole, and PEDOT precursors, resulting in the formation of conductive polymer nanofiber-integrated hybrid hydrogels. The synthesis process is highly energy-efficient, atom-economic, scalable, and environmentally benign, eliminating the need for complex synthetic procedures while allowing the use of a broad range of water-soluble organic acids with diverse functionalities. The resulting conductive hydrogels exhibit excellent mechanical robustness, self-healing behavior, stimuli-responsive sol-gel transitions, and high ionic conductivity arising from the synergistic integration of supramolecular fibrillar networks and conductive polymer architectures. Furthermore, the biomolecular condensate matrix acts as a universal scaffold for conductive polymer growth, demonstrating the versatility of acid-induced biomolecular self-assembled hydrogel systems for fabricating multifunctional conductive materials. The electrochemical performance of the Polyaniline embedded GMP hydrogel was demonstrated through the fabrication of electrochromic energy-storage electrodes and all-solid-state supercapacitors, exhibiting high areal capacitance (343 $mFcm^{-2}$) and energy density (93.36 $Whcm^{-2}$). Collectively, this work establishes biomolecular condensate-assisted conductive hydrogel synthesis as a versatile and scalable platform, highlighting the potential of small biomolecules as both artificial enzyme mimics and programmable supramolecular matrices for next-generation bioelectronic materials.

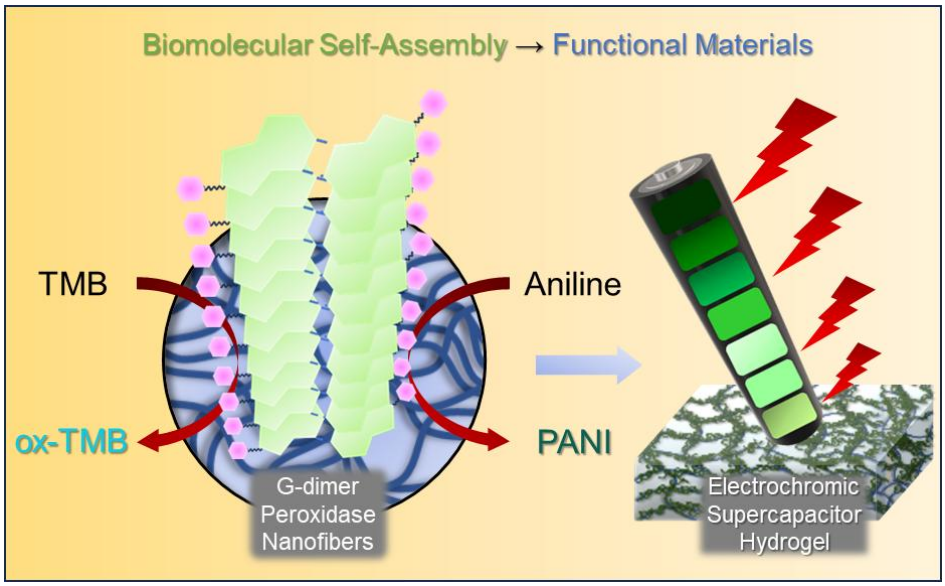


Figure 5. Schematic representation of the Supramolecular Self-Assembly of Polyaniline Embedded Enzyme Mimicking GMP-Condensate Hydrogel for Electrochromic Energy Storage Applications.

Chapter 7. **Conclusion and Future Prospects**

The final chapter summarizes the major findings and significance of the research presented in this thesis while outlining potential future directions. The studies primarily focus on the design strategies, mechanistic understanding, and functional applications of biomolecular self-assembly, with particular emphasis on the unique supramolecular behavior of 5′-GMP. These investigations reveal distinct structure–activity relationships within self-assembled GMP fibrillar networks formed in the presence of diverse molecular crosslinkers, including biomass DNA, nucleotide analogues, catalytically active metal cofactors, and small organic molecules. The resulting hydrogels exhibit diverse structural, mechanical, catalytic, and physicochemical properties that arise from the nature of the biomolecular architecture and precursor components. Such tunable properties have been successfully utilized for the development of programmable drug-delivery systems with controlled release kinetics, artificial enzyme mimetics, multienzyme cascade platforms, and bioelectronic materials. Overall, this work establishes biomolecular self-assembly of 5′-GMP as a

versatile platform for engineering multifunctional supramolecular hydrogels. Future developments in this area are expected to further expand the scope of nucleotide-based nanohybrid hydrogels toward advanced multifunctional materials and next-generation biomolecular technologies.

References

1. Du X., Zhou J., Xu B. (2014), Supramolecular Hydrogels Made of Basic Biological Building Blocks, Chem. Asian J., 9, 1446-1472 (DOI:10.1002/asia.201301693)

2. Gong C., Sun S., Zhang Y. *et al.* (2019), Hierarchical nanomaterials via biomolecular self-assembly and bioinspiration for energy and environmental applications, Nanoscale, 11, 4147-4182 (DOI:10.1039/C9NR00218A)

3. Schmid S.Y., Lachowski K., Chiang H.T. *et al.* (2023), Mechanisms of Biomolecular Self-Assembly Investigated Through In Situ Observations of Structures and Dynamics, Angew. Chem. Int. Ed., 62, e202309725 (DOI:10.1002/anie.202309725)

4. Harraz D.M., Davis J.T. (2018), A self-assembled peroxidase from 5′-GMP and heme, Chem. Commun., 54, 1587-1590 (DOI:10.1039/C7CC09900B)

5. Davis J.T. (2004), G-Quartets 40 Years Later: From 5′-GMP to Molecular Biology and Supramolecular Chemistry, Angew. Chem. Int. Ed., 43, 668-698 (DOI:10.1002/anie.200300589)

6. Davis J.T., Spada G.P. (2007), Supramolecular architectures generated by self-assembly of guanosine derivatives, Chem. Soc. Rev., 36, 296-313. (DOI:10.1039/B600282J)

7. Draper E.R., Adams D.J. (2017), Low-Molecular-Weight Gels: The State of the Art, Chem 3, 390–410 (DOI:10.1016/j.chempr.2017.07.012)

8. Detellier C., Laszlo P. (1980), Role of alkali metal and ammonium cations in the self-assembly of the 5′-guanosine monophosphate dianion, J. Am. Chem. Soc., 102, 1135-1141 (DOI:10.1021/ja00523a033

LIST OF PUBLICATIONS

Thesis Work:

1. **Suryakamal Sarma**, Neha Thakur, Nidhi Varshney, Hem Chandra Jha, Tridib K. Sarma*. Chromatin Inspired Bio-Condensation between Biomass DNA and Guanosine Monophosphate Produces All-Nucleic Hydrogel as a Hydrotropic Drug Carrier, Commun Chem, 2024, *7*, 261. (I.F. 6.5) (DOI: 10.1038/s42004-024-01353-6)
2. **Suryakamal Sarma**, Ashmad Kumar Nayak, Amrita Charabortya, Tarun Kumar Sahua, Yoshita Chakravartya, Amit Kumar*, Tridib K. Sarma*. Minimalist Structural Tunability in a Biomass DNA-GMP Hydrogel Enables Programmable Anticancer Drug Release. *(Manuscript Submitted)*
3. **Suryakamal Sarma,** Divyanshi Deshwal, Tarun Kumar Sahu, Ravindra Vishwakarma, Aditya Prasun, Tridib K Sarma*. Enzyme-Mimicking "All-Nucleotide" G-Quadruplex Hydrogel as a Dual-Function Microreactor for Biomimetic Cascade Catalysis. *Chem. Euro J.* **2026,** 32, e71444. (DOI: 10.1002/chem.71444)
4. **Suryakamal Sarma**, Tridib K Sarma*. Engineering a Nucleotide-Based Artificial Metalloenzyme through Supramolecular Confinement of a Copper-Histidine Cofactor. *(Manuscript Under Preparation)*
5. **Suryakamal Sarma**, Nishita Jain, Love Bansal, Ravindra Vishwakarma, Aditya Prasun, Tarun Kumar Sahu, Rajesh Kumar, Tridib K. Sarma*. Supramolecular Self-Assembly of Polyaniline Embedded Enzyme-Mimicking GMP-Condensate Hydrogel for Electrochromic Energy Storage Applications, ACS Appl. Mater. Interfaces, 2025, 17, 48532-48546. (I.F. 8.2) (DOI: 10.1021/acsami.5c08151.)

Other Publications:

1. Neha Thakur#, **Suryakamal Sarma**#, Vidhi Agarwal, Amrita Chakraborty, Aditya Prasun, Tridib K Sarma*. Acidic Amino Acid Induced 5′-Guanosine Monophosphate Fibrillar Nanozyme: A Highly Efficient Metal-Free Intrinsic Peroxidase Mimic, Nano Lett., 2025, 25, 15407-15415. (I.F. 9.1) (DOI: 10.1021/acs.nanolett.5c04390) *(#Equal Contribution)*
2. Yoshita Chakravarty#, **Suryakamal Sarma**#, Anjali Singh, Tridib K Sarma*. PEDOT: PSS-Induced Supramolecular G-Quartet Hydrogel for Diffusion-Controlled High-Performance Flexible Supercapacitor, ACS Materials Lett., 2026, 8, 1214-1223. (I.F. 8.7) (DOI: 10.1021/acsmaterialslett.6c00044) *(#Equal Contribution)*
3. Amrita Chakraborty#, **Suryakamal Sarma**#, Shakir Ali Siddiqui, Vidhi Agarwal, Aditya Prasun, Ravindra Vishwakarma, Tarun Kumar Sahu, Kshatresh Dutta Dubey*, Tridib K. Sarma*. Supramolecular Nucleotide Hydrogel as an Artificial Carbonic Anhydrase for CO_2 Sequestration. Manuscript under consideration. *(#Equal Contribution)*
4. Sourav Sutradhar#, **Suryakamal Sarma**#, Sonali Palo, Parnashabari Sarkar, Tridib Kumar Sarma, Biswa Nath Ghosh. Copper-induced tert-butoxy-substituted terpyridine hydrogel for enhanced peroxidase-like activity and colourimetric glutathione sensing, New J. Chem., 2025, 49, 16713-16722. (I.F. 2.5) (DOI: 10.1039/D5NJ02354H) *(#Equal Contribution)*
5. **Suryakamal Sarma**, Tarun Kumar Sahu, Rahul Kumar Sharma, Aditya Prasun, Ravindra Vishwakarma, Tridib K. Sarma*. Polyphenol Derived Natural Deep Eutectic Solvents for High Efficiency Cathode Recycling of Li-Ion Batteries, ACS Sustainable Resour. Manage. **2025**, 2, 190-200. (DOI: 10.1021/acssusresmgt.4c00421)
6. **Suryakamal Sarma#**, Shivansh Singh#, Vamshi Krishna Rao, Tridib K. Sarma*, Vinod Kumar *. Exploring the influence of

hydrogen bond donors in deep eutectic solvents on the extraction of metals during the recycling process of lithium-ion batteries, New J. Chem., 2025, 49, 8046-8057. (I.F. 2.5) (DOI: 10.1039/D5NJ01060H) *(#Equal Contribution)*

7. Amrita Chakraborty, Tanushree Ghosh, **Suryakamal Sarma**, Vidhi Agarwal, Rajesh Kumar, Tridib K Sarma*. A multi-stimuli responsive polyoxometalate-guanosine monophosphate hybrid chromogenic smart hydrogel, J. Mater. Chem. C, 2024, 12, 13447-13456. (I.F. 5.2) (DOI: 10.1039/D4TC01973C)
8. Amrita Chakraborty, Annu Rani, Pramesh Sinha, **Suryakamal Sarma**, Vidhi Agarwal, Aditya Prasun, Hem Chandra Jha, Tridib K Sarma*. Guanosine Monophosphate Induced Solubilization of Folic Acid Leading to Hydrogel Formation for Targeted Delivery of Hydrophilic and Hydrophobic Drugs, ACS Appl. Mater. Interfaces, 2025, 17, 11848-11860. (I.F. 8.2) (DOI: 10.1021/acsami.4c21306)
9. Tarun Kumar Sahu, Shaurya Aneja, Ravindra Vishwakarma, Aditya Prasun, **Suryakamal Sarma**, Montu Gogoi, Tridib K. Sarma*. Intermingled Coordination Environments Enable Defect-Engineered Metal-Polyphenol/G-Quadruplex Hydrogel for Enhanced N_2-to-NH_3 Photoconversion, Small, 2026, 22, e14925. (I.F. 12.1) (DOI: 10.1002/smll.202514925)
10. Sourav Sutradhar, Gayathri K Suresh, **Suryakamal Sarma**, Dipankar Das, Parnashabari Sarkar, Shanti Gopal Patra, Biswa Nath Ghosh. Sulphide and iodide anion recognition by a selective copper hydrogel of a chloro substituted terpyridine ligand, Inorg. Chem. Commun., 2024, 170, 113263. (I.F. 5.4) (DOI: 10.1016/j.inoche.2024.113263)
11. Yonas Etafa Tasisa*, Tridib Kumar Sarma, Ramaswamy Krishnaraj, **Suryakamal Sarma**. Band gap engineering of titanium dioxide (TiO_2) nanoparticles prepared via green route and its visible light driven for environmental remediation,

Results in Chemistry, 2024, 11, 101850. (I.F. 4.2) (DOI: j.rechem.2024.101850)

12. Aditya Prasun, Ravindra Vishwakarma, Suryakamal Sarma, Tarun Kumar Sahu, Tridib K Sarma*, Evaporation-Induced Formation of Blue-Emissive Guanine-Based Spherulitic Microstructures, Chem. Commun., 2026, Advance Article. (DOI: 10.1039/D6CC02587K)

List of Patents

1. **Suryakamal Sarma**, Nishita Jain, Tridib K Sarma*, Conductive Polymer embedded Biomolecular Hydrogels (CPBHs) and method thereof. Indian Patent: 569767 *(Granted)*.
2. Amrita Chakraborty, Pramesh Sinha, **Suryakamal Sarma**, Vidhi Agarwal, Aditya Prasun, Hem Chandra Jha*, Tridib K Sarma*, A Supramolecular Hydrogel Composition for the Delivery of an Anti-cancer Drug and method thereof. Indian Patent Application No. 202521102058 *(Filed)*.

TABLE OF CONTENTS

LIST OF FIGURES ..... **XXVIII**

LIST OF TABLES ..... **XXXV**

ACRONYMS ..... **XXXVI**

NOMENCLATURES ..... **XXXVIII**

Chapter 1 ..... **1**

Introduction & General Background **1**

1.1. Biomolecular Self-Assembly 1

1.1.1. Inspiration from Nature 1

1.1.2. Bottom-up Assembly Principle 3

1.1.3. Non-covalent Interactions towards Biomolecular Self-Assembly 4

1.2. Biomolecular Self-Assembly to Supramolecular Hydrogels 6

1.2.1. Supramolecular Hydrogels 6

1.2.2. Biomolecules as Low Molecular Weight Gelators (LMWGs) 8

1.3. Supramolecular Assembly of 5′-GMP and Guanosine Derivatives 15

1.3.1. Early Studies on the Self-Assembly of 5′-Guanosine Monophosphate 15

1.3.2. Hierarchical Self-Assembly of G-Quartets: From Molecular Building Blocks to Supramolecular Architectures 17

1.3.3. The Significant Features of the 5′-GMP G-quartets 21

1.4. Characterization of 5′-GMP based G-Quartet Motifs 24

1.4.1. X-ray diffraction 24

1.4.2. Circular Dichroism Spectroscopy 25

1.4.3. Thioflavin T (ThT) Fluorescence Assay 26

1.4.4. Nuclear Magnetic Resonance (NMR) Spectroscopy 27

1.5. Recent Advances in 5′-GMP-Self-Assembly-Based Hydrogels 28

1.5.1. G-quadruplex in Biomedical Field 29

1.5.2. G-assembly in Biocatalysis 30

1.5.3. GMP-assembly in Bioelectronics 31

1.6. Thesis Objective and Organization of the Thesis 33
1.7. References 35
Chapter 2 55
Chromatin Inspired Bio-condensation Between Biomass DNA and Guanosine Monophosphate Produces All-Nucleic Hydrogel as a Hydrotropic Drug Carrier 55
2.1. Introduction 55
2.2. Results and Discussions 57
2.2.1. Chromatin inspired “all nucleic” G4-condensation 57
2.2.2. DNA/GMP extensive condensation leading to hydrogelation 69
2.2.3. Biocompatibility and Cytotoxicity of the DNA-GMP hydrogel 74
2.2.4. DNA/GMP condensate hydrogel as a dense phase hydrotropic drug carrier 76
2.2.5. The hydrogel enhances the antibacterial activity of the encapsulated drug 81
2.3. Conclusion 83
2.4. Experimental Section 84
2.4.1. Synthesis and characterization of biomass DNA-GMP condensates 84
2.4.2. Synthesis of Biomass DNA hydrogel 84
2.4.3. Mechanical properties studies 85
2.4.4. In-Vitro biocompatibility test 86
2.4.5. Drug loading and encapsulation efficiency 87
2.4.6. Antibacterial activity 88
2.5. References 89
Chapter 3 97
Minimalist Structural Tunability in G-Quadruplex-Driven Biomass DNA Hydrogel Enables Multiple Programmable Drug Release Regimes for Anticancer Therapeutics 97
3.1. Introduction 97
3.2. Results and Discussions 100
3.2.1. Synthetic Strategy of Hydrogels 100
3.2.2. Morphological and Structural Interpretation 104

3.2.3. Mechanical Properties 107
3.2.4. Hydrotropic Drug Encapsulation 109
3.2.5. Modulation in the Drug Release Kinetics 112
3.2.6. Programming the Drug Release Kinetics 116
3.2.7. Cytotoxic Activity of Drug-loaded Hydrogels on Breast Cancer Cells 118
3.2.8. CPT loaded with variable hydrogel combinations disintegrates multicellular spheroids 120
3.2.9. Treating spheroids with CPT loaded in hydrogel induces apoptosis and cellular death 123
3.3. Conclusion 124
3.4. Experimental Section 125
3.4.1. Synthesis of hydrogels 125
3.4.2. Characterization and mechanical property evaluation of the hydrogels 126
3.4.3. Drug encapsulation and sustained release experiments 126
3.4.4. The cellular response to the treatment groups 128
3.4.5. The effect of the treatment groups on MDA-MB-231 spheroids 129
3.4.6. Examining cellular apoptosis induced by the treatment groups in the spheroids using the AO/PI staining method 129
3.4.7. Statistical Analysis 130
3.5. References 130
Chapter 4 139
Enzyme-Mimicking "All-Nucleotide" G-Quadruplex Hydrogel as a Dual-Function Microreactor for Biomimetic Cascade Catalysis. 139
4.1. Introduction 139
4.2. Results and Discussions 142
4.2.1. Design Concept and Biogenic Condensation 142
4.2.2. Morphological Evolution of Nucleotide Condensates 144
4.2.3. Spectroscopic Characterizations and Molecular mechanism of Condensation 147

4.2.4. Hierarchical Fibrillation Driving Hydrogel Formation 154

4.2.5. Intrinsic Peroxidase Mimicking Activity 157

4.2.6. Enabling Biocatalytic Cascade with "All-Nucleotide" Hydrogel 164

4.3. Conclusion 167

4.4. Experimental Section 168

4.4.1. Synthesis of the condensates and hydrogels 168

4.4.2. Characterizations 169

4.4.3. Enzyme Kinetics and Catalytic Assays 170

4.4.4. Enzyme Kinetics and Mechanism 171

4.4.5. Enzymatic Cascade Synthesis and Catalytic Activity 172

4.5. References 173

Chapter 5 182

Engineering a Nucleotide-Based Artificial Metalloenzyme through Supramolecular Confinement of a Copper-Histidine Cofactor ... 182

5.1. Introduction 182

5.2. Result and Discussion 185

5.2.1. Design Strategy, Biomimetic Inspiration and Spontaneous Self-Assembly of the CuHG Hydrogel 185

5.2.2. Structural and Coordination Environment of the Artificial Active Site 188

5.2.3. Hierarchical Organization of the Hydrogel Scaffold . 193

5.2.4. Mechanical Properties of the CuHG hydrogel 196

5.2.5. Catechol Oxidase-Like Catalytic Activity 197

5.2.6. Mechanistic Role of Supramolecular Confinement: Stabilizing the Active Site 199

5.3. Conclusion and Future Scope 201

5.4. Experimental Section 202

5.4.1. Synthesis of CuHG hydrogel 202

5.4.2. Characterizations 203

5.4.3. Enzyme Kinetics 204

5.5. References 205

Chapter 6 212

Supramolecular Self-Assembly of Polyaniline Embedded Enzyme Mimicking GMP-Condensate Hydrogel for Electrochromic Energy Storage Applications 212

6.1. Introduction 212

6.2. Results and Discussions 215

6.2.1. Organic Acid induced Self-Assembly of 5′-GMP 215

6.2.2. Metal-free intrinsic peroxidase activity of the CSA-GMP condensates 222

6.2.3. In-situ polymerization of aniline inside the enzymatic CSA-GMP hydrogel 226

6.2.4. Mechanical properties of the PCGH hydrogel 232

6.2.5. Electrochemical performance of the biomolecular matrix embedded PCGH hydrogel 237

6.3. Conclusion 243

6.4. Experimental Section 244

6.4.1. Preparation of CSA-GMP condensate and matrix hydrogel 244

6.4.2. Characterization of Enzymatic Activity 244

6.4.3. Preparation of Polyaniline Incorporated CSA-GMP Hydrogel (PCGH) 245

6.4.4. Methods 245

6.5. References 247

Chapter 7 257

Conclusion and Future Prospects 257

7.1. Summary 257

7.2. Future Scopes 260

LIST OF FIGURES

Figure No.	Figure	Page No.
Figure 1.1.	Examples of self-assembly and self-organization in nature across multiple length scales.	3
Figure 1.2.	Building functional supramolecular architectures through self-assembly.	4
Figure 1.3.	Hierarchical self-assembly of low-molecular-weight gelators (LMWGs) into supramolecular hydrogels.	7
Figure 1.4.	Small biomolecules and their self-assembled macrostructure in nature.	9
Figure 1.5.	Structural organization of nucleobases, nucleosides, nucleotides, and their supramolecular binding motifs.	13
Figure 1.6.	Schematic representation of the supramolecular architectures formed by nucleobases, including the A-motif, i-motif and G-quadruplex structure.	14
Figure 1.7.	Historical evolution of guanosine 5′-monophosphate (GMP) self-assembly and G-quadruplex research.	16
Figure 1.8.	Representative examples of the self-assembly of GMP and its derivatives.	20
Figure 1.9.	Characteristic structural features of G-quadruplex assemblies by pXRD and CD spectroscopy.	25
Figure 1.10.	Characterization of G-quadruplex structures using fluorescence and NMR spectroscopy.	27
Figure 1.11.	Representative GMP-based hydrogels and composite materials developed for biomedical, biocatalytic, and bioelectronic applications.	32
Figure 2.1.	Chromatin-inspired DNA packaging into a G4-condensate leads to the formation of a helical fibril network.	57

Figure 2.2.	Morphological (FE-SEM, HR-TEM, AFM) and spectroscopic (UV-visible, CD) evaluation of the DNA-GMP condensate.	59
Figure 2.3.	^{1}H-NMR spectra and Zeta Potential of DNA-GMP condensate.	61
Figure 2.4.	Spectroscopic (CD and ThT FL assay) investigations into the concentration-dependent dynamics of the condensation process.	63
Figure 2.5.	Kinetic morphological evolution of DNA-GMP condensate at increasing GMP concentration keeping the DNA concentration constant.	65
Figure 2.6.	Localized Confocal fluorescence images of the evolution of green fluorescence with the increase in GMP concentration.	66
Figure 2.7.	Temperature dependent morphological reconfiguration and dynamic reconfiguration of the DNA-GMP condensate.	68
Figure 2.8.	Transformation of DNA-GMP condensate to DNA-GMP hydrogel at higher concentration.	69
Figure 2.9.	Powder X-Ray diffraction pattern and FTIR spectra of the dried DNA-GMP hydrogel.	70
Figure 2.10.	Mechanical property investigations of the DNA-GMP hydrogel.	73
Figure 2.11.	Determination of cytotoxicity through MTT assay of (**A)** GMP, (**B)** DNA, (**C)** DNA-GMP, in AGS cells.	74
Figure 2.12.	Effect of different biocompatible compounds on the cell death of AGS and A549 cells.	75
Figure 2.13.	Structure of the vitamins and drugs to study the loading and controlled release.	77
Figure 2.14.	Drug diffusion and release behaviour of DNA-GMP hydrogels using model hydrophilic and hydrophobic cargo molecules, demonstrating a common release mechanism independent of drug properties.	78

Figure 2.15.	DNA-GMP hydrogel as a hydrotropic drug carrier, illustrating the site-specific encapsulation of hydrophobic and hydrophilic drugs within the hydrogel fibres, along with UV-vis spectra of drug release and the corresponding polynomial fitting curves.	80
Figure 2.16.	Morphological and mechanical characterization of the DNA-GMP hydrogel before and after drug loading, demonstrating its shelf-life stability and anti-leakage properties.	81
Figure 2.17.	Anti-bacterial activity of gel compound against E. coli.	82
Figure 3.1.	Schematic illustration of DNA packaging into a G-quadruplex (G4) condensate and the synthetic strategy for DG, GDG, and CaDG hydrogels, together with their HR-TEM, FE-SEM, digital images, and spectroscopic characterization.	102
Figure 3.2.	Visual appearance and compositional optimization of DG, GDG, and CaDG hydrogel formulations.	103
Figure 3.3.	Schematic illustration and characterizations of the plausible crosslinking pattern between DNA-GMP nanofibers and Ca^{2+} ions.	106
Figure 3.4.	Rheological and mechanical characterization of DG, GDG, and CaDG hydrogels.	108
Figure 3.5.	Schematic illustration depicting the site-specific encapsulation, efficiency, preservation of mechanical integrity and anti-leakage of drug-loaded nanofibrous hydrogel network.	111
Figure 3.6.	Schematic representation of tunable drug release profiles in DG, GDG, and CaDG hydrogels with drug release kinetics.	114
Figure 3.7.	Controlled release profile of the drug loaded DG-hydrogels in high-glucose DMEM cell culture	116

	medium and systematic day-wise analysis of zero-order drug release from the Dox-loaded CaDG hydrogel.	
Figure 3.8.	Programmable control of drug release kinetics through structure modulation of Dox loaded DG, GDG and CaDG hydrogels.	117
Figure 3.9.	Cytotoxic evaluation of MDA-MB-231 (Triple-Negative breast Cancer cells) in the presence of different treatment groups.	119
Figure 3.10.	Effects of CPT-loaded hydrogel treatment groups on MDA-MB-231 spheroid morphology, radial optical density, and viability.	122
Figure 4.1.	Design concept and morphological outcomes of "all-nucleotide" condensates.	143
Figure 4.2.	Concentration-dependent morphological evolution of nucleotide condensates varying GMP concentration and keeping the adenosine monophosphate derivatives constant at 100 μM.	145
Figure 4.3.	Fluorescence labelling and cargo-enrichment studies of the GMP-concentration-dependent evolution from spherical intermediates to fibrillar assemblies.	
Figure 4.4.	UV-visible absorption spectra and corresponding Job's plots for (a, b) AMP-GMP, (c, d) ADP-GMP, and (e, f) ATP-GMP systems.	147
Figure 4.5.	Spectroscopic characterization of G-quadruplex formation and molecular interactions in nucleotide condensates. CD spectra, FTIR absorbances and resonance Raman spectra of AMG, ADG, and ATG systems.	148
Figure 4.6.	Zeta potential values of the pristine nucleotides and corresponding condensates, illustrating changes in surface charge upon condensation.	150

Figure 4.7.	Evaluation of π-π stacking and hierarchical assembly using Thioflavin T (ThT) fluorescence.	152
Figure 4.8.	Proposed mechanistic illustration of GMP-driven G-quadruplex formation and π-π stacking, facilitated by multivalent phosphate interactions, leading to hierarchical fibrillar assembly and hydrogel formation.	154
Figure 4.9.	Hydrogel formation and rheological characterization of nucleotide condensates.	155
Figure 4.10.	Self-recovery, pH stability of ADG and ATG hydrogels evaluated by time-dependent oscillatory rheology.	156
Figure 4.11.	Intrinsic peroxidase-mimicking activity, kinetic analysis and controlled kinetic assays of the 'all-nucleotide' hydrogels.	160
Figure 4.12.	Hydroxyl radical (•OH)-mediated reaction pathway underlying the peroxidase-like activity of ADG and ATG condensates.	161
Figure 4.13.	Control experiments demonstrating the critical role of G-quadruplex assembly in the intrinsic peroxidase-like activity of ADG hydrogels.	162
Figure 4.14.	Schematic illustration of enhanced substrate affinity and catalytic efficiency within ADG/ATG fibrillar hydrogel networks.	163
Figure 4.15.	Multi-enzyme cascade catalysis within the ADG hydrogel microreactor, illustrating two-step and three-step enzymatic cascade reactions and their kinetic analysis.	165
Figure 4.16.	Control experiment highlighting the role of the confined microenvironment in the ADG hydrogel.	166
Figure 5.1.	Structural comparison between the di-copper active site of native catechol oxidase (left) and the biomimetic CuHG hydrogel (right).	186

Figure 5.2.	Schematic illustration of the spontaneous formation of the CuHG hydrogel through CuH complexation and nucleotide-directed self-assembly.	187
Figure 5.3.	UV-visible characterization and linear correlation of the CuH complex and CuHG hydrogel.	189
Figure 5.4.	XPS analysis of the CuH complex and its structural integrity within the CuHG hydrogel.	191
Figure 5.5.	(a) TGA graphs and (b) Cyclic Voltammogram of CuH complex and CuHG hydrogel respectively.	192
Figure 5.6.	Hierarchical organization of the CuHG hydrogel scaffold.	194
Figure 5.7.	Structural characterization of the G-quadruplex framework in the CuHG hydrogel.	195
Figure 5.8.	Rheological characterization of the CuHG hydrogel.	197
Figure 5.9.	Catechol oxidase-like catalytic activity of the CuHG hydrogel.	198
Figure 5.10.	Mechanistic role of supramolecular confinement in stabilizing the catalytically active di-copper intermediate.	201
Figure 6.1.	Schematic illustration of the enzymatic GMP molecular hydrogel, which undergoes in situ polymerization of aniline to form a polyaniline-embedded CSA-GMP nanofibrous hydrogel (PCGH) scaffold.	214
Figure 6.2.	Schematic of CSA and GMP condensation and formation of G-dimers and corresponding microscopic and UV-visible characterization.	215
Figure 6.3.	Spectroscopic, 1H-NMR and 2D-DOSY NMR analysis of CSA-GMP condensate.	217
Figure 6.4.	Kinetic morphological evolution of CSA-GMP condensation: Confocal fluorescence images of the	219

	progression of green fluorescence along with the fibrillation with the increase in GMP concentration.	
Figure 6.5.	Schematic illustration and characterization depicting the concentration-driven transformation of CSA-GMP fibrillar condensates into a transparent hydrogel matrix.	221
Figure 6.6.	Intrinsic peroxidase enzyme-like activity nano-fibrous CSA-GMP condensate.	225
Figure 6.7.	Reaction mechanism determination of the peroxidase activity of CSA-GMP condensate.	226
Figure 6.8.	Schematic illustration of the fabrication of the PCGH hydrogel and its microscopic and spectroscopic characterization.	228
Figure 6.9	Comparison between conventional and matrix assisted polymerization	229
Figure 6.10.	Digital photographs showing the bio-degradation of the PCGH.	222
Figure 6.11.	Mechanical performance of the CSA-GMP and PCGH hydrogels.	234
Figure 6.12.	Temperature dependent rheological analysis and thermo-reversibility of CSA-GMP and PCGH hydrogels.	236
Figure 6.13.	Schematic illustration of the compressibility test of PCGH at different external strain ranges and ex-situ FESEM images.	237
Figure 6.14.	PCGH as electrochromic supercapacitor electrode.	240
Figure 6.15.	PCGH as “all-solid state” energy storage device.	242
Figure 7.1.	Schematic overview of the thesis highlighting the versatile functional landscape of 5′-GMP-based supramolecular self-assembly.	259

LIST OF TABLES

Table No.	Table	Page No.
Table 2.1	Encapsulation Efficiencies of the Drug Molecules	76
Table 3.1	Encapsulation efficiency calculation for Dox	127
Table 3.2	Encapsulation efficiency calculation for CPT	127
Table 4.1	Comparison of the kinetic constants of ADG hydrogel with recently reported metal-free peroxidase-mimicking systems and benchmark catalysts.	159
Table 6.1	Comparison of electrochemical performances of PANI-based flexible supercapacitors.	242

ACRONYMS

DNA	Deoxyribonucleic Acid
RNA	Ribonucleic Acid
5′-GMP	5′-Guanosine Monophosphate
G4	G-quadruplex
LMWG	Low-Molecular-Weight Gelator
NMR	Nuclear Magnetic Resonance
SAXS	Small-Angle X-ray Scattering
AFM	Atomic Force Microscopy
FE-SEM	Field-Emission Scanning Electron Microscopy
HR-TEM	High-Resolution Transmission Electron Microscopy
FTIR	Fourier Transform Infrared Spectroscopy
CD	Circular Dichroism
NOE	Nuclear Overhauser Effect
DOSY	Diffusion-Ordered Spectroscopy
FL	Fluorescence Spectroscopy
PXRD	Powder X-ray Diffraction
PEDOT:PSS	Poly(3,4-ethylenedioxythiophene):Poly(styrenesulfonate)
Fmoc	Fluorenylmethyloxycarbonyl
LipoG	Lipophilic guanosine derivatives
U	Uracil

A	Adenine
G	Guanine
C	Cytosine
UV-Vis	Ultraviolet-Visible Spectroscopy
PBS	Phosphate-Buffered Saline
ThT	Thioflavin T
MTT	3-(4,5-Dimethylthiazol-2-yl)-2,5-diphenyltetrazolium Bromide
IC50	Half-Maximal Inhibitory Concentration
ICDD	International Centre for Diffraction Data
LLPS	Liquid-Liquid Phase Separation
AMP	Adenosine Monophosphate
ADP	Adenosine Diphosphate
ATP	Adenosine Triphosphate
LOD	Limit of Detection
MOFs	Metal Organic Frameworks
ESI-MS	Electrospray Ionization Mass Spectrometry
EXAFS	Extended X-ray Absorption Fine Structure
PCGH	polyaniline-embedded CSA-GMP nanofibrous hydrogel
ITO	Indium Tin Oxide
PEO	Poly(ethylene oxide)

NOMENCLATURES

λ	Wavelength
π	Pi
nm	Nanometer
Å	Ångström
ε	Extinction coefficient
M	Molar concentration
mM	Millimolar
mV	Millivolt
Hz	Hertz
µL	Microliter
a.u.	Arbitrary unit
eV	Electron volt
θ	Theta
s	Second
min	Minute
µM	Micromolar
mS	Micro siemens
σ	Sigma
cm	Centimeter
°C	Degree Celsius
K	Kelvin
mg	Milligram
ppm	Parts per million
Pa	Pascal
mm	Millimeter
$Rad.s^{-1}$	Radian per second

Chapter 1

1. Introduction & General Background

The integration of biomolecules into supramolecular nanostructures forms the basis of the natural world. Nature exemplifies self-assembly through simple molecular building blocks that spontaneously organize into highly ordered architectures via cooperative non-covalent interactions; from DNA's double helix and protein folding to cellular membranes and complex biological structures. Inspired by these processes, biomolecular self-assembly has emerged as a powerful bottom-up strategy for engineering adaptive, multifunctional materials. Among these, supramolecular hydrogels derived from low-molecular-weight biomolecules have garnered significant interest owing to their biocompatibility, dynamic reversibility, and ability to mimic biological organization.*[1-4]*

This chapter introduces the fundamental concepts of biomolecular self-assembly and the role of non-covalent interactions in forming hierarchical supramolecular architectures. It surveys hydrogels built from amino acids, peptides, nucleic acids, and carbohydrates, with emphasis on nucleobases, nucleosides, and nucleotides as low molecular weight gelators, particularly guanosine derivatives. The structural features, physicochemical properties, and characterization of 5′-GMP-based G-quartets and G-quadruplexes are discussed, alongside recent advances in their biomedical, biocatalytic, and bioelectronic applications, establishing the foundation for subsequent chapters.

1.1. Biomolecular Self-Assembly

1.1.1. Inspiration from Nature

Nature offers abundant examples of self-assembly, wherein simple building blocks spontaneously organize into ordered structures through local interactions without external guidance. Over billions of

years of evolution, natural systems have developed hierarchical architectures spanning length scales from nanometers to kilometers, giving rise to complex structures with extraordinary structural and functional sophistication.*[2]*

At the molecular level, self-assembly reinforces the organization of fundamental machinery of life. DNA molecules form stable double helices through complementary base pairing and π-π stacking interactions (**Figure 1.1a**), while phospholipids spontaneously assemble into bilayer membranes that define cellular boundaries (**Figure 1.1b**). Similarly, proteins attain their functional conformations through folding driven by hydrogen bonding, hydrophobic interactions, and electrostatic forces.*[5,6]*

Self-assembly and self-organization are also evident at larger length scales. The spiral arrangement of sunflower seeds (**Figure 1.1c**) follows phyllotactic principles for efficient packing, whereas the hierarchical venation pattern of leaves (**Figure 1.1d**) facilitates mechanical support and nutrient transport. Pinecones (**Figure 1.1e**) and mollusk shells (**Figure 1.1f**) exhibit intricate geometries formed through controlled biological growth.*[2]*

Beyond living systems, self-organized structures are found in geological environments. Coral reefs (**Figure 1.1g**) arise from the collective growth of countless organisms, while ripple patterns in desert sand dunes (**Figure 1.1h**) emerge through the interplay of wind, sand, and gravity.*[7]* These examples highlight a universal principle of nature: complex architectures can emerge from relatively simple components through spontaneous organization. Understanding the underlying mechanisms that govern these natural self-assembly processes has not only provided valuable insights into the formation of hierarchical structures in nature but has also inspired the design and development of artificial self-assembled systems. In these systems, molecular or nanoscale building blocks are programmed to organize into predetermined architectures, offering a powerful strategy for creating

adaptive, hierarchical, and multifunctional materials with diverse technological applications.

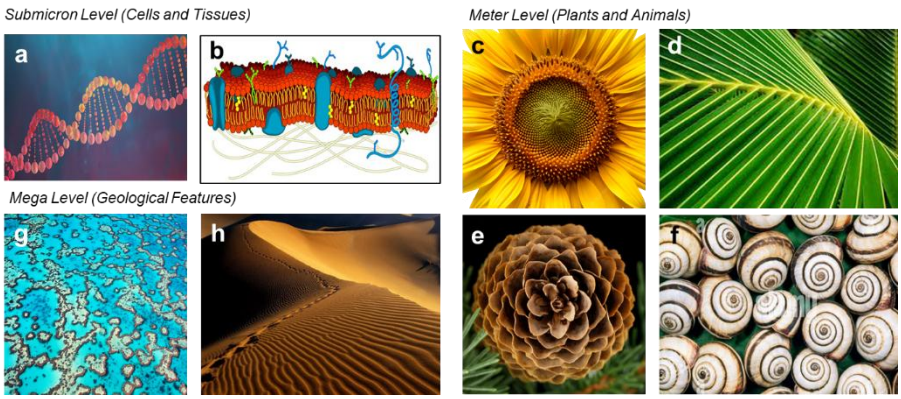


Figure 1.1. *Examples of self-assembly and self-organization in nature across multiple length scales.* ***(a)*** *DNA double helix,* ***(b)*** *phospholipid bilayer membrane,* ***(c)*** *spiral phyllotactic arrangement in a sunflower,* ***(d)*** *hierarchical venation pattern in a plant leaf,* ***(e)*** *layered architecture of a pinecone,* ***(f)*** *spiral growth pattern in snail shells,* ***(g)*** *mega-scale organization of coral reef structures and* ***(h)*** *ripple patterns formed in desert sand dunes through wind-driven self-organization. [2,7,8]*

1.1.2. Bottom-up Assembly Principle

Bottom-up assembly is a fundamental strategy in which complex structures are constructed from simple molecular or nanoscale building blocks through spontaneous organization. Unlike top-down approaches that involve removal or patterning of bulk materials, bottom-up assembly exploits the intrinsic ability of individual components to interact and organize into ordered architectures. The assembly process is governed by thermodynamic and kinetic factors, where molecules minimize free energy through non-covalent interactions, including hydrogen bonding, electrostatic interactions, π-π stacking, hydrophobic interactions, and van der Waals forces. These weak interactions collectively direct the formation of discrete supramolecular motifs, which further evolve into hierarchical structures across multiple length scales.*[9,10]*

Nature extensively employs the bottom-up approach to construct functional biological architectures. Biomolecules such as nucleic acids, proteins, lipids, and carbohydrates spontaneously organize into highly

ordered structures essential for life. For example, nucleotides assemble into the double-helical DNA structure, amino acids fold into functional proteins, and phospholipids organize into bilayer membranes defining cellular boundaries. Although individually weak, cooperative non-covalent interactions govern the structure and function of biological macromolecules. Inspired by nature, bottom-up self-assembly has emerged as a powerful strategy for engineering adaptive and multifunctional materials by programming diverse biomolecular building blocks into predetermined nanostructures for wide range of applications.*[10-12]*

1.1.3. Non-covalent Interactions towards Biomolecular Self-Assembly

Biomolecular self-assembly is governed by a delicate interplay of various non-covalent interactions that collectively direct molecular recognition, structural organization, and the formation of hierarchical architectures.(**Figure 1.2**) Although individually weak, these interactions act cooperatively to regulate the conformation, stability, and functionality of biomolecular assemblies.*[13]*

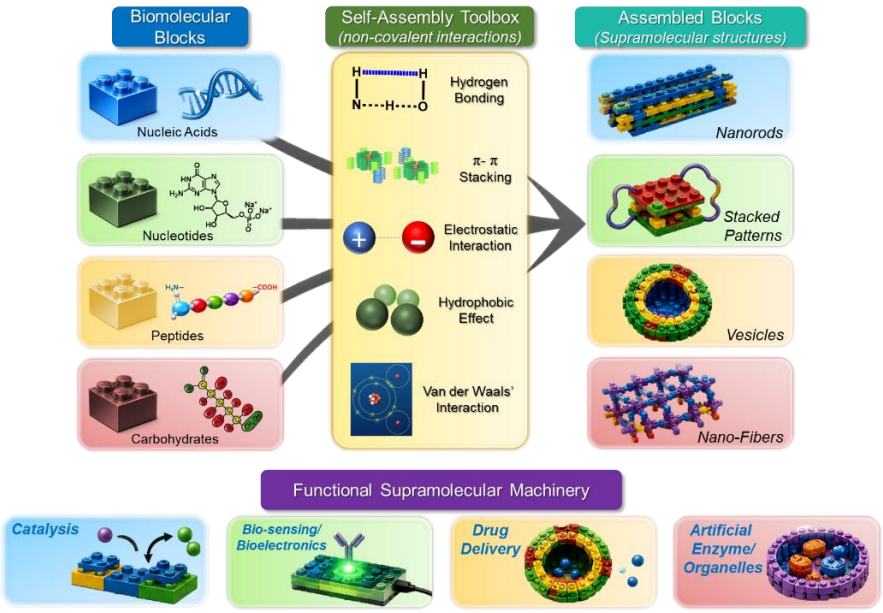


Figure 1.2. *Building functional supramolecular architectures through self-assembly. Simple biomolecular building blocks, assembled by nature, create complex supramolecular systems for a wide range of functions and applications.*

Hydrogen Bonds: In biomolecular self-assembly, hydrogen bonds promote directional growth of biomolecules with long-range order to form one-dimensional (1D) nanostructures. Additionally, hydrogen bonds between biomolecule hydrogen atoms and electronegative atoms on material surfaces enhance biomolecule-material interactions, enabling functional hybrid nanomaterials.*[14-16]* For example, Li et al. demonstrated diphenylalanine micro-rod formation through stable intermolecular hydrogen bonds with the solvent system, exhibiting optical waveguiding properties.*[17]* Similarly, Xue et al. investigated DNA binding with GO using surface plasmon resonance (SPR), finding that hydrogen bonds play a key role in single-stranded DNA (ssDNA) interactions with GO, enabling fabrication of a novel biosensor for highly sensitive and selective ssDNA target determination.*[18]*

Electrostatic Interaction: Electrostatic interactions govern the attraction and repulsion between charged functional groups, thereby facilitating molecular recognition and stabilizing supramolecular architectures in aqueous environments. These interactions are particularly important in the formation of biomolecular condensates and physically crosslinked materials.*[19-21]* For example, complex coacervation between positively charged peptides and negatively charged nucleic acids has been utilized to construct biomolecular condensates for intracellular delivery and protocell models. Likewise, electrostatic interactions between anionic polysaccharides and cationic proteins have enabled the fabrication of injectable hydrogels with enhanced mechanical strength and controlled drug release.*[22-24]*

π-π Stacking Interaction: π-π stacking between aromatic residues of peptides and nucleic acids drives self-assembly of diverse biomolecular building blocks, promoting molecular recognition and stabilizing higher-order architectures. Aromatic motifs linked with biomolecules enable highly ordered superstructures and functional hybrids.*[25,26]* Wakabayashi et al. demonstrated that aromatic peptide amphiphiles undergo cooperative π-π interactions forming fibrous nanostructures

capable of enzymatic functionalization.*[27]* Redondo-Gómez et al. reported complementary host-guest peptide amphiphiles self-assembling into dynamic hydrogels through synergistic aromatic interactions.*[28]* Similarly, guanine-rich DNA sequences organize into helical G-quadruplex fibres stabilized by interplanar π-stacking between adjacent G-quartets, yielding highly ordered supramolecular architectures.*[29]*

Hydrophobic Interactions: Hydrophobic interactions arise from the tendency of nonpolar moieties to minimize water exposure, playing a crucial role in self-assembly of peptides, proteins, lipids, and nucleic acids. Hydrophobic residues drive protein folding and aggregation, while in nucleic acids, nonpolar groups facilitate stacking and phase segregation into ordered assemblies, stabilizing mesoscale architectures and imparting stimuli-responsive properties.*[30-32]* A representative example is an artificial nucleic acid analogue containing 3,5-bis(trifluoromethyl)benzene as a hydrophobic base surrogate, where two complementary strands spontaneously form a duplex solely through hydrophobic interactions, eliminating the need for conventional Watson-Crick hydrogen bonding.*[33]*

1.2. Biomolecular Self-Assembly to Supramolecular Hydrogels

1.2.1. Supramolecular Hydrogels

Supramolecular hydrogels are three-dimensional, water-rich networks formed through spontaneous self-assembly of small molecules or biomacromolecules via reversible non-covalent interactions, without permanent covalent crosslinks.*[34]* In aqueous environments, hydrogelators undergo hierarchical self-assembly into nanostructures that entangle into three-dimensional networks capable of immobilizing large amounts of water. Consequently, supramolecular hydrogels exhibit viscoelastic properties including solid-like behaviour and resistance to flow without applied shear force. Unlike polymeric hydrogels relying on covalently crosslinked chains, supramolecular hydrogels contain self-

assembled nanofiber networks constituting the solid matrix for water encapsulation. Despite containing more than 97% water, they possess rheological properties comparable to polymeric hydrogels with excellent stimuli-responsiveness.*[35]*

Supramolecular hydrogel formation is driven by non-covalent interactions including hydrogen bonding, π-π stacking, electrostatic interactions, and hydrophobic effects. These interactions govern molecular recognition and nanostructure formation while endowing hydrogels with dynamic and reversible characteristics. Consequently, supramolecular hydrogels rapidly respond to variations in pH, temperature, ionic strength, and ligand-receptor interactions, making them highly attractive for stimuli-responsive applications.(**Figure 1.3**) Additionally, most hydrogelators possess amphiphilic characteristics similar to naturally occurring self-assembled biological systems, further emphasizing their biomimetic nature.*[36-40]*

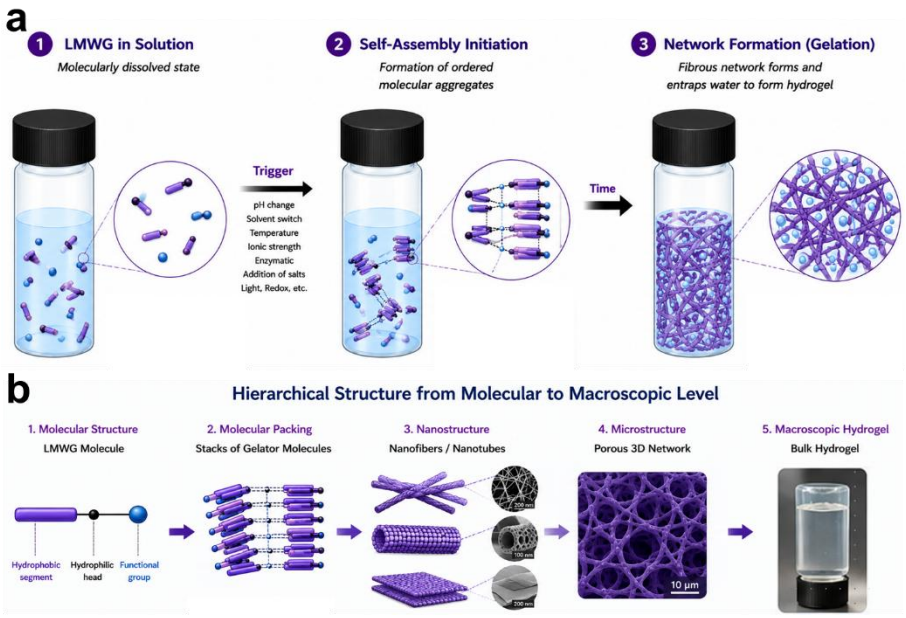


Figure 1.3. *Hierarchical self-assembly of low-molecular-weight gelators (LMWGs) into supramolecular hydrogels. (a) Schematic illustration of the gelation process, where dissolved LMWG molecules undergo stimulus-triggered self-assembly through non-covalent interactions. (b) Hierarchical organization of supramolecular hydrogels across multiple length scales, progressing from the molecular structure of the gelator to molecular packing, nanostructures (nanofibers, nanotubes, or nanosheets), porous microstructures, and ultimately the macroscopic hydrogel.[41]*

Compared with polymeric hydrogels, supramolecular hydrogels offer unique advantages from their low-molecular-weight building blocks. Their reversible non-covalent assembly makes them inherently biodegradable and biocompatible. Hydrogelators generally have molecular weights below 2000 Da, enabling efficient renal clearance compared with polymeric materials typically exceeding 30,000 Da. Moreover, hydrogelators can be synthesized as chemically pure compounds through established organic procedures, minimizing impurities and avoiding cytotoxicity associated with chemical crosslinking. Unlike polymeric networks with variable functional group distribution, hydrogelator self-assembly produces highly ordered structures with regular molecular arrangements and well-defined architectures.*[42-44]*

Initially, most low-molecular-weight hydrogelators were synthetic organic molecules such as urea derivatives*[45,46]* serine-based amphiphiles*[47]* and aroyl-L-cystine derivatives*[48]*. However, pristine biomolecules and biomacromolecules as hydrogelators have attracted increasing attention due to their intrinsic biological functions and biomedical suitability.*[49,50]* Successful implementation in three-dimensional cell culture*[51]*, biomolecular screening*[52]*, wound healing*[53]*, and drug delivery*[52-54]* has further stimulated exploration of fundamental biological building blocks as hydrogelators. Since nature relies extensively on self-assembly of nucleic acids, proteins, and polysaccharides for diverse biological functions, small molecules derived from these building blocks provide an ideal platform for biomimicry. Therefore, supramolecular hydrogels based on biological building blocks hold great promise for developing adaptive soft materials with designed biological functions.*[35]*

1.2.2. Biomolecules as Low Molecular Weight Gelators (LMWGs)

Naturally occurring bio-macromolecular building blocks have emerged as attractive hydrogelators owing to their abundance, biocompatibility, structural diversity, and inherent self-assembling

capabilities. In living systems, amino acids, nucleotides, and monosaccharides spontaneously organize into proteins, nucleic acids, and polysaccharides performing essential biological functions. (**Figure 1.4**) Their intrinsic propensity to self-assemble through non-covalent interactions enables hierarchical nanostructures with unique properties including molecular recognition, sequence programmability, tuneable conformations, biodegradability, and bioactivity. These systems are classified into amino acid- and protein-based, nucleotide- and nucleic acid-based, saccharide-derived, and hybrid hydrogels.*[55-61]*

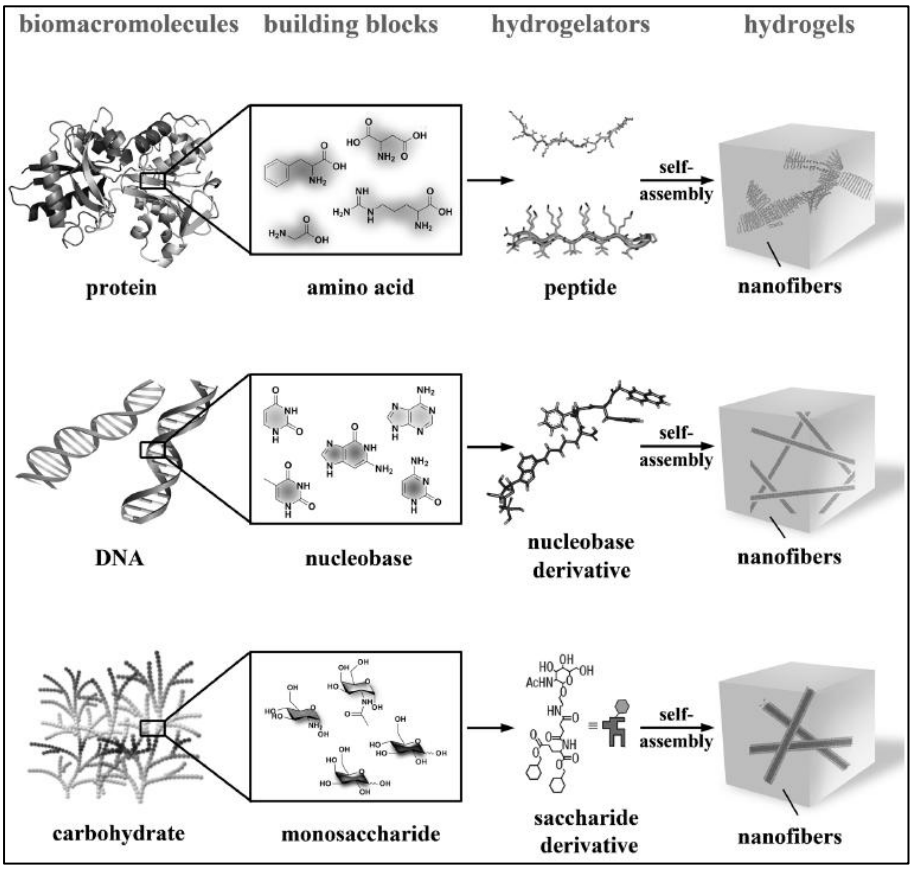


Figure 1.4. *Small biomolecules and their self-assembled macrostructure in nature.[35] (Copyright 2014 Wiley)*

1.2.2.1. Amino Acids and Proteins as LMWGs

Amino acids and short peptides constitute one of the most extensively studied classes of LMWGs owing to their structural simplicity, synthetic versatility, biocompatibility, and intrinsic propensity for supramolecular self-assembly. Their assembly is driven

by a combination of hydrogen bonding, hydrophobic interactions, electrostatic interactions, and π–π stacking, enabling the formation of ordered secondary structures such as α-helices and β-sheets that hierarchically evolve into one-dimensional fibrillar networks and three-dimensional hydrogel matrices. The incorporation of aromatic residues or aromatic protecting groups (e.g., Fmoc and naphthalene derivatives) significantly enhances the gelation propensity by increasing the extent of π-conjugation and promoting directional π–π stacking interactions, thereby lowering the critical gelation concentration and stabilizing the supramolecular architecture. Representative systems, including L-phenylalanine, diphenylalanine (FF), and Fmoc-protected peptides, exemplify how aromatic side chains reinforce fibril formation, improve mechanical rigidity, and facilitate the formation of robust supramolecular hydrogels. The inherent conformational flexibility of short peptides further enables hierarchical organization into functional soft materials with tunable physicochemical and biological properties. *[62-64]*

Woolfson et al. reported α-helical peptide pairs self-assembling into fibrillar hydrogels containing more than 99% water, exhibiting excellent mechanical strength and supporting PC12 cell differentiation, demonstrating extracellular matrix mimicry.*[65]* Schneider and Pochan developed β-hairpin peptides MAX1 and MAX8, undergoing environmentally triggered folding and self-assembly into rigid nanofibrous hydrogels supporting fibroblast proliferation, stem cell encapsulation, and tissue regeneration, while MAX1 exhibited broad-spectrum antibacterial activity against Gram-positive and Gram-negative bacteria.*[66]* Furthermore, Fmoc-protected peptides such as Fmoc-Tyr and Fmoc-diphenylalanine form highly ordered fibrillar networks enabling enzyme-instructed self-assembly for cell culture and drug delivery applications.*[67,68]*

1.2.2.2. Nucleotides and Nucleic Acids as building blocks

Nucleobases and nucleotide derivatives are attractive building blocks owing to their molecular recognition through complementary hydrogen bonding and aromatic π-stacking, resembling structural organization of DNA and RNA, enabling ordered supramolecular architectures with high specificity and responsiveness. Among nucleobases, guanosine derivatives are particularly important, forming G-quartets and higher-order assemblies stabilized by Hoogsteen hydrogen bonding and π-π interactions, further evolving into nanofibers and hydrogels with excellent structural stability.*[69-72]* Xu et al. demonstrated nucleobase-containing hydrogelators by conjugating nucleobases with peptide motifs, yielding supramolecular hydrogels with improved biological functions.*[73]* Additionally, adenine- and thymine-containing hydrogelators exploit complementary base pairing to direct molecular organization and form stimuli-responsive hydrogels.*[74]* Owing to their nucleic acid-mimicking molecular recognition, these materials have attracted considerable attention for gene delivery, biosensing, and biomimetic nanotechnology applications.*[75]*

1.2.2.3. Supramolecular Hydrogels Made of Saccharides

Saccharides are abundant biological molecules possessing excellent water solubility, biodegradability, and biocompatibility. Multiple hydroxyl groups provide numerous hydrogen-bonding sites, facilitating self-assembly and stable hydrogel network formation. Additionally, carbohydrate-based materials exhibit low toxicity and resemble extracellular matrix components, making them highly attractive for biomedical applications.*[76-79]*

Lin et al. reported glucosamine-derived hydrogelators self-assembling into nanofibrous hydrogels with enhanced biocompatibility and mechanical stability.*[80]* Vancomycin-based hydrogelators containing carbohydrate moieties form supramolecular networks through ligand-receptor interactions, exhibiting antibacterial

properties.*[49,50]* Glycosylated hydrogelators have been developed to improve water solubility and bioactivity, producing hydrogels suitable for cell culture, tissue engineering, and controlled drug delivery. Saccharide incorporation not only enhances biological compatibility but also introduces additional molecular recognition motifs beneficial for biomedical applications.*[81,82]*

1.2.2.4. Hybrids of Basic Biological Building Blocks

Although individual biomolecular classes possess unique advantages, combining different biological building blocks within a single hydrogelator produces synergistic effects and multifunctional properties. Hybrid systems integrate structural diversity of amino acids, molecular recognition of nucleobases, and hydrophilicity of carbohydrates, mimicking natural bio-macromolecular complexity.

Nucleobase-amino acid conjugates combine peptide self-assembly with base-pairing interactions forming nanofibrous hydrogels with enhanced mechanical properties and biological functions.*[83-87]* Glycopeptide hydrogelators consisting of peptide and carbohydrate segments exhibit improved water solubility, biocompatibility, and cell affinity, suitable for tissue engineering and drug delivery.*[88-90]* More sophisticated systems incorporating all three biomolecular building blocks (amino acids, nucleobases, and monosaccharides) generate hierarchical structures closely resembling biological matrices, responding to external stimuli and providing promising platforms for regenerative medicine, controlled release, molecular imaging, and biomimetic materials design.*[91,92]* The synergistic integration of diverse biological building blocks thus enables the construction of advanced supramolecular materials with emergent properties transcending those of individual components.

1.2.2.5. Nucleobases, Nucleosides, Nucleotides analogues as LMWGs

Nucleobases, nucleosides, and nucleotides are compelling low-molecular-weight gelators (LMWGs) because they carry the same

noncovalent interaction toolkit: hydrogen bonding, π-π stacking, and electrostatic forces, governing DNA and RNA architecture, opening a rational route to supramolecular gels with programmable structure.

Nucleobases are nitrogen-containing heterocycles divided into purines (adenine, guanine) and pyrimidines (cytosine, thymine, uracil). (**Figure 1.5 a, b**) Pyrimidines present a single edge bearing hydrogen-bond donors and acceptors, whereas the bicyclic purine scaffold exposes multiple faces enabling richer, more directional interactions. Covalent linkage of a nucleobase to ribose via an N-glycosidic bond yields a nucleoside, gaining an additional structural element promoting supramolecular organisation. (**Figure 1.5 c**) Further phosphorylation yields a nucleotide, whose anionic phosphate group introduces electrostatic interactions and, under acidic conditions, serves simultaneously as a hydrogen-bond donor, expanding assembly cross-linking potential.

The canonical Watson-Crick base pairing governs nucleobase recognition, where adenine pairs with uracil or thymine through two hydrogen bonds and guanine pairs with cytosine through three hydrogen bonds. Additionally, Hoogsteen and reverse Watson-Crick geometries provide alternative pairing modes, broadening the structural repertoire available to gel designers.*[70,93,94]* (**Figure 1.5 d**)

Extended aromatic surfaces and multiple hydrogen-bonding edges make purines particularly prone to higher-order assembly through cooperative π-π stacking and directional intermolecular recognition. These interactions drive base triple formation, such as U•A•U and G•G•C, which polymerize into one-dimensional ribbons and elongated supramolecular architectures.*[97,98]* pH introduces additional structural control by unlocking alternative pairing modes: under acidic conditions, adenine-rich sequences adopt parallel A-motif duplexes stabilized by protonated $A•A^+$ pairs, while cytosine-rich sequences organize into intercalated i-motif tetraplexes through hemiprotonated $C•C^+$ pairs. (**Figure 1.6 a, b**) Both motifs assemble and disassemble

reversibly with pH changes, making them inherently stimuli-responsive platforms for dynamic, switchable nucleic acid nanomaterials.*[99]*

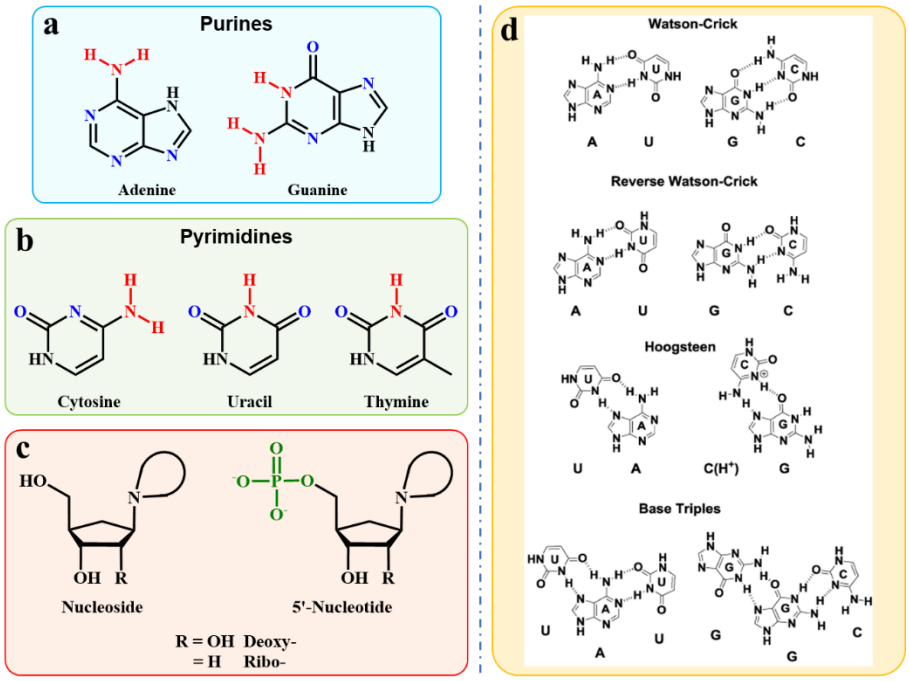


Figure 1.5. (a, b) *Hydrogen-bond donor (red) and acceptor (blue) sites of the purine and pyrimidine nucleobases, respectively. Together with their intrinsic π-π stacking capability, these features facilitate diverse self-assembly pathways and molecular recognition processes.* ***(c)*** *Covalent attachment of a nucleobase to a D-ribose sugar through a glycosidic bond yields a nucleoside, while subsequent phosphorylation of the ribose generates a nucleotide. The negatively charged phosphate group (green) further enables electrostatic interactions.* ***(d)*** *Representative nucleobase binding motifs illustrating the non-covalent interactions that govern supramolecular assembly.[70,95,96]*

Among all nucleobase assemblies, guanine uniquely forms the G-quartet, a planar, cation-templated macrocycle in which four guanine units are cyclically arranged and mutually stabilized by eight Hoogsteen hydrogen bonds. Monovalent or divalent cations occupying the central cavity coordinate the carbonyl oxygens of all four guanines, providing electrostatic stabilization essential for quartet integrity. (**Figure 1.6 c**) First identified through the self-aggregation of 5′-guanosine monophosphate, G-quartets are recognized across diverse systems ranging from native nucleosides and oligonucleotides to synthetic

derivatives, with relevance spanning structural biology, medicinal chemistry, and supramolecular materials design.[*93,94,100,101]*

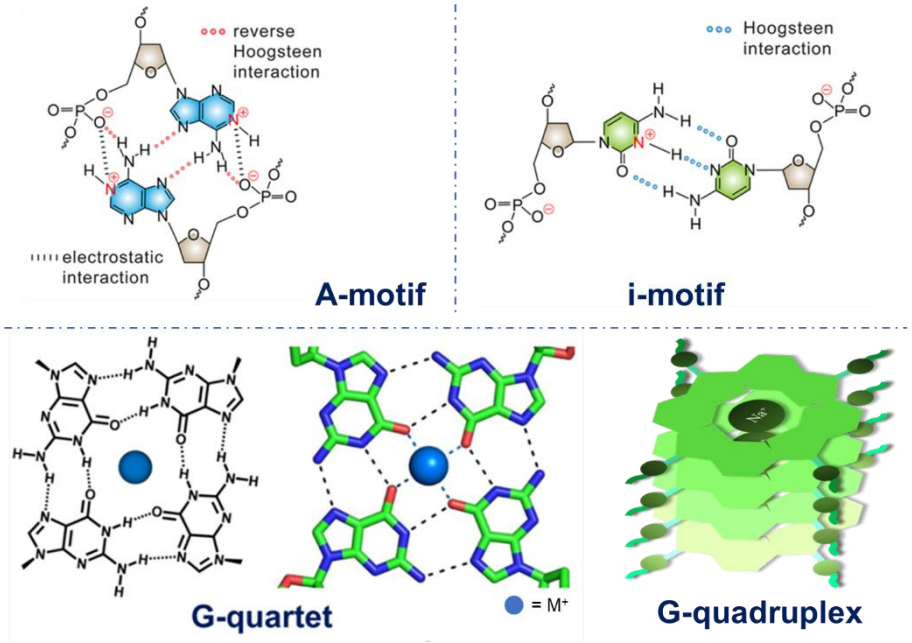


Figure 1.6. *Schematic representation of the supramolecular architectures formed by nucleobases, including the A-motif stabilized by adenine-adenine (A:A) base pairing and electrostatic interactions, the i-motif composed of hemiprotonated cytosine-cytosine ($C:C^+$) base pairs, and the G-quadruplex structure formed through Hoogsteen hydrogen-bonded G-quartets that further stack via π-π interactions to generate higher-order G-quadruplex assemblies.[94,99]*

1.3. Supramolecular Assembly of 5′-GMP and Guanosine Derivatives

1.3.1. Early Studies on the Self-Assembly of 5′-Guanosine Monophosphate

Guanosine derivatives are among the most intriguing self-assembling nucleotides, forming highly ordered supramolecular architectures through complementary hydrogen bonding and π-π stacking. Early studies by Gellert and co-workers established the structural basis of guanosine self-association, revealing that both 3′-GMP and 5′-GMP assemble into planar G-quartets composed of four guanine bases linked through eight hydrogen bonds, stacking approximately 3.25 Å apart to form helical columns.*[102]* Concurrently,

Fresco and Massoulie demonstrated that polyguanylic acid forms multistranded helices in solution, further confirming the role of stacked G-quartets in stabilizing guanine-rich assemblies.*[103]* (**Figure 1.7**)

Subsequent investigations revealed that the self-assembly of 5′-GMP is strongly influenced by pH and alkali metal ions. Under basic conditions, smaller aggregates suitable for NMR characterization are formed. Na^+ and K^+ ions selectively stabilize G-quartets by coordinating with the four carbonyl oxygen atoms at the tetrad center, leading to the proposal of discrete G8•M^+ octamers as fundamental building blocks for extended stacked columns.*[104-108]* Later crystallographic studies confirmed that K^+ ions are sandwiched between adjacent G-quartets, providing additional stability. These findings represented early demonstrations of ion-directed structural organization in nucleotides, laying the foundation for dynamic combinatorial chemistry.*[109-111]*

A significant outcome of these studies was the remarkable kinetic stability of 5′-GMP assemblies. Unlike most hydrogen-bonded systems existing in rapid equilibrium with monomeric components, the ^1H NMR spectra of 5′-GMP·Na^+ displayed distinct resonances corresponding to both monomeric and assembled species, indicating slow exchange and unusual kinetic stability in aqueous media. Detailed multinuclear NMR studies by Laszlo, Detellier and co-workers provided further insights into assembly dynamics.*[112,113]* ^{23}Na NMR measurements revealed that Na^+ ions exchange within the [5′-GMP]$_8$·Na^+ octamer several orders of magnitude faster than conventional ligand exchange, occurring without complete disruption of the octameric framework.*[114]* Thermodynamic analyses of the [5′-GMP]$_8$·K^+ octamer ($\Delta H = -17\pm2$ kcal mol^{-1}; $\Delta S = -51\pm6$ cal mol^{-1}K^{-1}) confirmed that assembly is predominantly enthalpy-driven, governed by synergistic cation coordination and hydrogen bonding rather than hydrophobic interactions.*[113]*

Beyond discrete assemblies, guanosine systems exhibit hierarchical self-organization. G-quadruplex columns undergo lateral

association at higher concentrations, producing hexagonal liquid crystalline phases and entangled fibrillar networks, establishing an important link between molecular self-assembly and long-range supramolecular organization.*[94,115]* These foundational studies collectively laid the conceptual groundwork for contemporary supramolecular chemistry, inspiring rational design of biogenic materials replicating the structural logic and functional sophistication of biological counterparts.

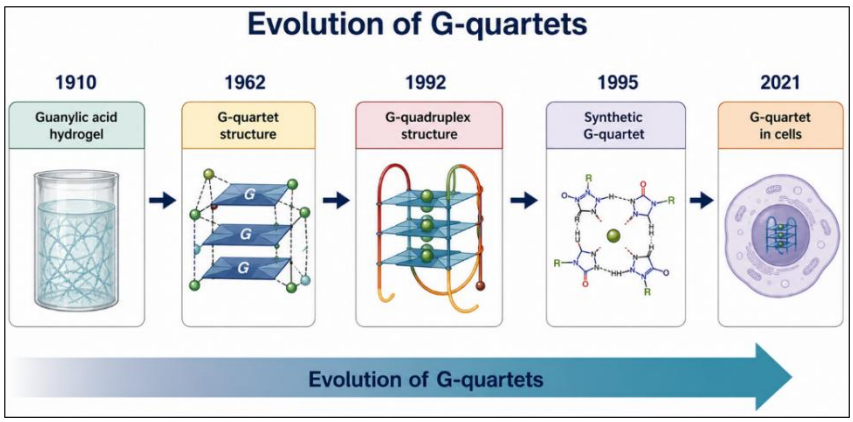


Figure 1.7. *Historical evolution of guanosine 5'-monophosphate (GMP) self-assembly and G-quadruplex research. The timeline highlights key milestones, beginning with the discovery of the intrinsic gelation of guanylic acid (1910)[116], followed by the demonstration of G-quartet formation and their helical stacking by Gellert and co-workers (1962)[102], structural elucidation of G-quadruplex architectures through molecular studies (1992)[117], and the demonstration of the existence of G-quartet-based suprastructures referred to as G-quadruplexes in human cells (2012)[118], laying the foundation for understanding GMP supramolecular assembly and functional nucleic acid materials.*

1.3.2. Hierarchical Self-Assembly of G-Quartets: From Molecular Building Blocks to Supramolecular Architectures

Beyond their biological significance in DNA and RNA, G-quadruplex structures are prevalent throughout the human genome, transcriptome, and ncRNAome, bridging molecular structure with biological function. The fascination of G-quartets as supramolecular building blocks, however, originates from their remarkable ability to form both lipophilic and water-soluble assemblies from pristine 5′-GMP and diverse guanosine and guanine derivatives.*[119,120]*

- ***Lipophilic guanosine derivatives their higher-order supramolecular assemblies***

Lipophilic guanosine derivatives (LipoGs) have provided a versatile platform for understanding G-quartet formation and their transformation into higher-order supramolecular architectures in organic media. Seminal studies by Davis and Gottarelli independently demonstrated that suitably protected guanosine and isoguanosine derivatives self-assemble in the presence of K^+ ions to form discrete G-quartets stacking into octameric assemblies, where a potassium ion is sandwiched between two quartet planes, highlighting remarkable ion selectivity favoring K^+ over smaller alkali metal ions.*[117,121]*

Structural modifications of LipoGs offer precise control over assembly topology and stability. Introduction of a C8-acetylphenyl substituent expands the hydrogen-bonding network from eight to twelve hydrogen bonds and increases π-surface area, generating highly stable columnar hexadecameric structures consisting of four stacked G-quartets. Remarkably, replacing K^+ with Sr^{2+} induces reversible topological transformation to octameric assembly, demonstrating that supramolecular organization can be controlled solely through electrostatic effects.*[122,123]* Incorporation of a photo-responsive styryl group at C8 position of guanine ring enables reversible light-controlled switching between assembled and disassembled states through trans-to-cis isomerization at 365 nm and restoration at 254 nm.*[124]* Furthermore, 8-bromo-2′,3′-O-isopropylidene-5′-tert-butyldimethylsilyl-guanosine revealed that solvent polarity, cation identity, and ion-pair separation energy collectively govern assembly stoichiometry, yielding octameric, dodecameric, or hexadecameric structures.*[125]* Thus, all these studies reflects that the LipoG assemblies exhibit remarkable topological diversity and stimuli-responsiveness programmable through structural modification and external stimuli, providing a powerful foundation for designing functional supramolecular systems.*[100]*

- ***Lipophilic versus water-soluble G-quartets: Advantages and Advancements of hydrophilic G-quartets***

Although lipophilic guanosine derivatives have been invaluable for elucidating G-quartet formation in organic media, water-soluble guanine systems have significantly expanded G-quartet chemistry toward biologically relevant environments. Hydrophilic G-quartets offer compatibility with aqueous media, accessibility to biological systems, and ability to form diverse supramolecular architectures under near-physiological conditions.*[102,105,126]*

5′-Guanosine monophosphate (5′-GMP), the simplest water-soluble guanine derivative, was among the earliest systems investigated for G-quartet formation. In the presence of Na^+, GMP molecules assemble into discrete G-quartets further stacking into micrometer-long rod-like structures. Whereas K^+ induces twisted helical fibers composed of continuous hydrogen-bonded guanine strands with approximately fifteen guanosine units per turn, elucidated through SEM and multidimensional NMR studies.*[127,128]* (**Figure 1.8 a**)

Beyond monomeric systems, the naturally occurring cyclic dimer c-di-GMP, an important bacterial second messenger, adopts higher-order quadruplex structures only in the presence of aromatic intercalators such as proflavine or thiazole orange.(**Figure 1.8 b**) These molecules intercalate between G-quartet layers, stabilizing a cage-like octameric assembly and demonstrating how small molecules can direct supramolecular organization.*[129,130]*

Further advances were achieved through water-soluble template-assembled synthetic G-quartets, in which four 2′-deoxyguanosine-3′-monophosphate units are covalently attached to a cavitand scaffold. (**Figure 1.8 c**) Unlike lipophilic systems, these hydrophilic synthetic G-quartets fold intramolecularly into stable quartets even without metal ions, serving as biomimetic platforms for probing interactions with G-quadruplex ligands.*[131]*

The transition from lipophilic to water-soluble G-quartets has preserved rich structural diversity while enabling biologically compatible systems, opening new opportunities in supramolecular chemistry, molecular recognition, and chemical biology. Thus, 5′-GMP as a monomeric building block for aqueous-phase functional soft materials provides a compelling platform for developing biogenic systems while simultaneously establishing a rational framework for engineering artificial nature-mimicking supramolecular architectures.

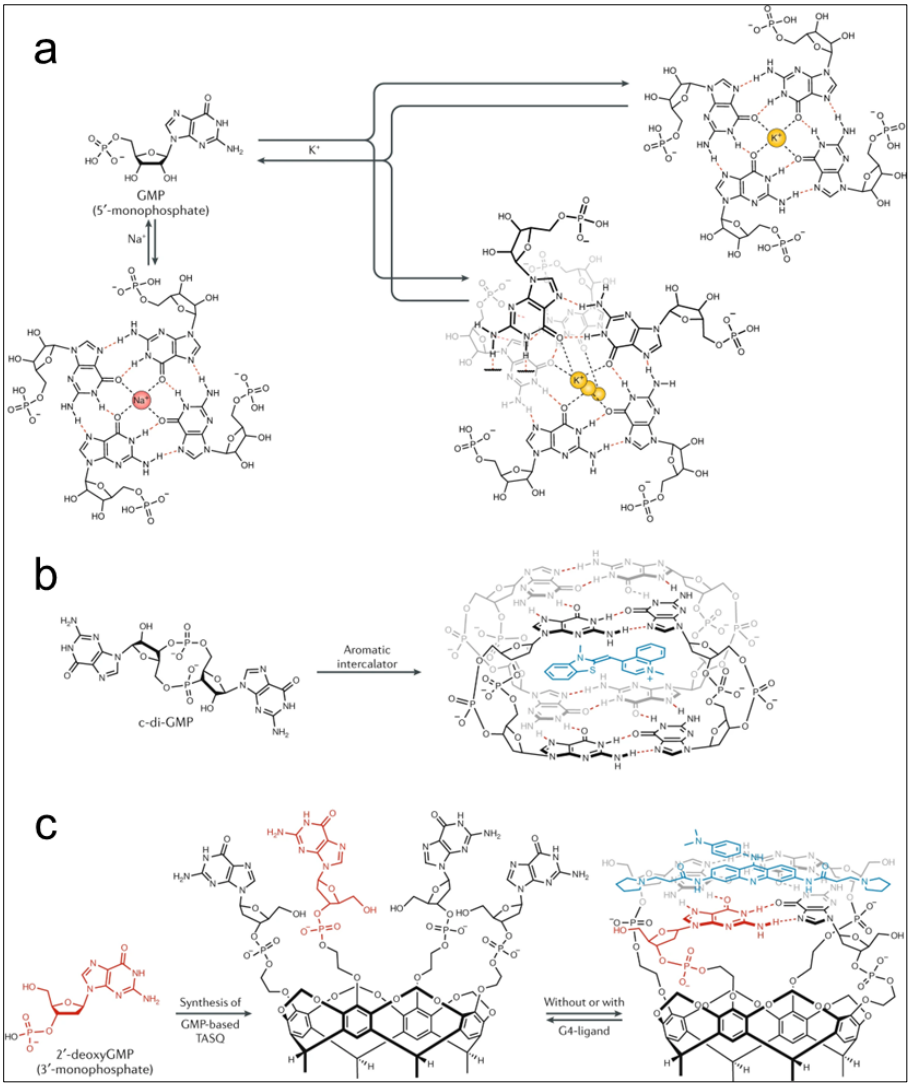


Figure 1.8. (a) *Monomeric guanosine monophosphate (GMP) can self-assemble in discrete G-quartets in the presence of Na^+ and K^+, but the latter can also trigger the formation of micrometer-long, helical rod-like structures comprising continuous, open-ended G-quartet.[126]* ***(b)*** *The dimeric GMP c-di-GMP can form G-quadruplexes comprising four c-di-GMP molecules upon interaction with aromatic*

inducers that intercalate between two layers of G-quartets.[129] ***(c)*** *Tetrameric GMP can be assembled intramolecularly to provide water-soluble template-assembled synthetic G-quartets (TASQ) that fold into intramolecular SQ without cations and serve as a platform for investigating the G-quartet interactions of G4-ligands.[131] (Reproduced with permission from [100], 2019, Springer Nature)*

1.3.3. The Significant Features of the 5′-GMP G-quartets

1.3.3.1. The Cationic Channel Stabilizing the G-quartets

A G-quartet comprises four guanine bases arranged in a planar structure through eight Hoogsteen hydrogen bonds, stabilized by monovalent cations such as Na^+, K^+, Tl^+, and NH_4^+. The inward-facing O6 carbonyl groups of guanines create a highly electronegative cavity that would otherwise experience strong electrostatic repulsion destabilizing stacked quartets. Cations occupying the space between successive G-quartets establish favorable cation-dipole interactions with eight carbonyl oxygen atoms, neutralizing charge repulsion, reinforcing quartet stacking, and preserving the cooperative hydrogen-bonding network. Computational studies reveal that stabilization arises from a delicate balance of electrostatic, polarization, charge-transfer, and dispersion interactions, with K^+ displaying highest affinity owing to its optimal ionic radius and desolvation energy within the channel. Experimental studies on 5′-GMP assemblies further demonstrated selective K^+ binding within the inner cavity, while Na^+ preferentially screens the negatively charged phosphate groups surrounding the assembly.*[113,126,128,132]*

Beyond structural stabilization, cation-filled channels impart ion-conducting properties to G-quartet stacks, where alkali ions migrate along the central axis through successive binding sites facilitated by polarization effects. The cation-filled channel is regarded as one of nature's earliest examples of a self-organized ionic conduit, inspiring models for primitive protocells and compartmentalized chemical systems. Owing to spontaneous assembly of guanine-rich nucleotides under plausible prebiotic conditions, G-quartets have been proposed as primitive polynucleotide frameworks participating in early information

storage and catalytic processes. Consequently, G-quartet-based supramolecular architectures are emerging as versatile platforms for ionic conductors, nanowires, biosensors, neuromorphic devices, and next-generation bioelectronic applications.*[113,133]*

1.3.3.2. Hydration water drives the self-assembly of 5′-guanosine monophosphate: The Thermodynamics of the Self-Assembly

Unlike many aromatic biomolecules whose assembly is predominantly driven by hydrophobic π–π stacking, 5′-GMP self-organization arises from a delicate interplay of Hoogsteen hydrogen bonding, cation coordination, π-stacking, and solvation effects. Early studies by Detellier et al. proposed that 5′-GMP self-association is primarily enthalpy-driven, as ordered G-quartet formation is accompanied by significant configurational entropy loss. However, a comprehensive understanding of thermodynamic contributions, particularly the role of hydration water, remained elusive until recently.*[113]*

Tao et al. addressed this through temperature-dependent terahertz spectroscopy and NMR studies, demonstrating that hydration water actively regulates GMP self-assembly thermodynamics.*[134]* THz calorimetry correlated hydration contributions to enthalpy and entropy with changes in effective molar absorptivity, while the overall free energy of G-quartet formation is described by:

$$\Delta \boldsymbol{G(G4)} = \Delta \boldsymbol{H_{G4}(GMP)} + \Delta \boldsymbol{H_{G4}(hydr.)} - \boldsymbol{T}\Delta \boldsymbol{S_{G4}(GMP)} - \boldsymbol{T}\Delta \boldsymbol{S_{G4}(hydr.)}$$

G-quartet formation is accompanied by release of bound water molecules from hydrophilic guanosine sites into bulk water. Although this release incurs an unfavorable hydration enthalpy penalty (ΔH_{G4} (hydr.) > 0) due to disruption of strong water-solute hydrogen bonds, it provides a favorable entropy gain ($-T\Delta S_{G4}$ (hydr.) < 0) from increased freedom of released water molecules. These opposing contributions explain the observed parabolic temperature dependence of G-quartet populations. Around room temperature, entropic gain from water release

compensates the hydration enthalpy cost, promoting assembly. At lower temperatures, stronger water-solute hydrogen bonding makes water release enthalpically unfavorable, whereas at higher temperatures, diminishing distinction between bound and bulk water reduces the entropic driving force. Thus, hydration water emerges as an active thermodynamic regulator governing stability and temperature-responsive behavior of GMP supramolecular assemblies.

1.3.3.3. The Amphiphilic Nature of the G-quartet

The G-quartet possesses intrinsic amphiphilic character arising from anisotropic distribution of polar and nonpolar functionalities within the assembly. Four guanine bases connected through Hoogsteen hydrogen bonds generate a planar macrocycle where inwardly oriented carbonyl oxygen atoms create a highly polar central cavity selectively coordinating monovalent cations, while peripheral sugar-phosphate backbones and exocyclic amino groups provide hydrophilic interfaces. In contrast, the extended π-surface of stacked guanine bases and exposed C8-H regions confer hydrophobic character, resulting in distinct segregation of hydrophilic and hydrophobic domains.*[135]*

This amphiphilic nature governs hierarchical organization of G-quartets into higher-order supramolecular architectures, enabling simultaneous interaction with aqueous environments and hydrophobic interfaces. Molecular dynamics studies revealed that lipophilic cavities selectively accommodate hydrophobic ligands, while structured water molecules occupying the grooves stabilize assemblies through extended hydration networks. Such coexistence of hydrophilic ionic channels and hydrophobic surfaces enables G-quartets to facilitate ion transport, molecular recognition, and membrane interactions. Consequently, the amphiphilic nature of G-quartets underlies their broad utility in supramolecular chemistry, biomolecular self-assembly, and functional materials for nanotechnology and bioelectronic applications.*[136-139]*

1.4. Characterization of 5′-GMP based G-Quartet Motifs

Over the past two decades, investigations of lipophilic and hydrophilic G-quartets have provided fundamental insights into the structural, dynamic, and thermodynamic principles governing G-quartet assembly, transforming this field into a platform for state-of-the-art characterization methods. Since the pioneering crystallographic studies of Gellert et al., a wide range of complementary experimental and computational techniques have been employed to elucidate G-quartet structure and behavior.*[102]* X-ray diffraction, and SAXS*[140]*, together with AFM[*141]* and SEM*[126]*, have investigated morphology and higher-order organization. Solution-state spectroscopic techniques including FTIR*[142]*, Raman*[143*], IRMPD*[144,145]*, CD, and VCD*[146,147]* have provided valuable information on hydrogen-bonding interactions and supramolecular chirality. ^{1}H, ^{23}Na, and DOSY NMR spectroscopy have enabled detailed characterization of cation-templated assemblies under near-physiological conditions, while MM and MD simulations have offered atomic-level insights into G-quartet formation and ion channeling.*[113,128]* Collectively, these approaches have established a comprehensive understanding of G-quartet structure and dynamics, facilitating development of functional materials for soft matter, nanotechnology, and chemical biology.

1.4.1. X-ray diffraction

Powder X-ray diffraction (PXRD) provides compelling structural evidence for G-quartet formation and their hierarchical organization into fibrillar architectures through π-π stacking. A characteristic reflection at $2\theta \approx 4.5°$ corresponds to a lattice spacing of 2.2 nm, consistent with the diameter of a single G-quartet plane, while a second reflection at $2\theta \approx 27°$ corresponds to a lattice spacing of 0.33 nm, characteristic of the interplanar distance between adjacently stacked G-quartet layers stabilized through π-π interactions.*[139,148,149]* (**Figure 1.9 a**)

1.4.2. Circular Dichroism Spectroscopy

Circular dichroism (CD) spectroscopy is among the most powerful techniques for characterizing G-quartet and G-quadruplex structures in solution, where observed ellipticity originates from exciton coupling between stacked guanine bases. Classical empirical rules associate specific CD signatures with distinct quadruplex topologies. Parallel G-quadruplexes exhibit a strong positive band at 260-265 nm with a negative band near 240-245 nm, while antiparallel structures display a positive maximum at 290-295 nm and a negative band around 260 nm. Hybrid (3+1) quadruplexes show two positive maxima at approximately 265 and 290 nm with a negative minimum at 245 nm.*[150]* (**Figure 1.9 b, c**)

Del Villar-Guerra et al. established a quantitative framework by constructing a reference library of 23 G-quadruplexes of known high-resolution structure. Through principal component analysis and singular value decomposition, they demonstrated that CD spectra enable quantitative estimation of anti-anti, syn-anti, and anti-syn guanine base step fractions, as well as contributions from lateral and diagonal loops. Importantly, CD signatures correlate more strongly with guanine stacking geometry than with strand orientation, transforming CD spectroscopy from a qualitative tool into a powerful method for extracting secondary structural information from G-quartet assemblies in solution. In GMP assemblies, cation-dependent polymorphism further influences spectral signatures, with K^+ favoring parallel arrangements and Rb^+ promoting antiparallel stacking.*[147,150,151]*

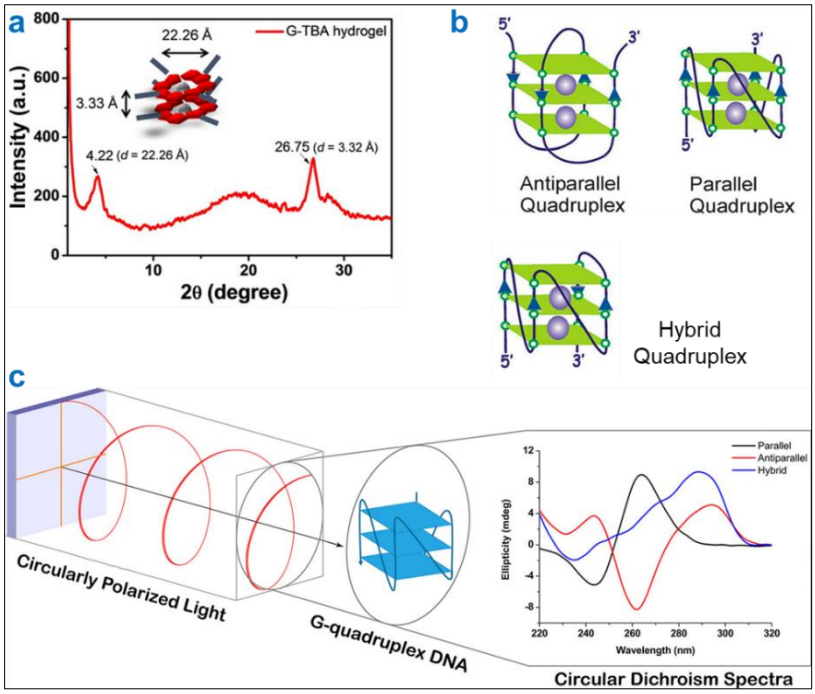


Figure 1.9. *Characteristic structural features of G-quadruplex assemblies.* ***(a)*** *Powder X-ray diffraction (PXRD) pattern showing the signature reflections corresponding to stacked G-quartet assemblies.[152]* ***(b)*** *Schematic representation of the three major G-quadruplex topologies: parallel, antiparallel, and hybrid conformations.* ***(c)*** *Representative circular dichroism (CD) spectra corresponding to the distinct G-quadruplex conformations, highlighting their characteristic chiroptical signatures. (Reproduced with permission from [151], 2017, American Chemical Society)*

1.4.3. Thioflavin T (ThT) Fluorescence Assay

Thioflavin T (ThT) interacts with G-quartet assemblies through π-π stacking and groove interactions. In aqueous solution, free ThT exists as a molecular rotor with unrestricted rotation between its benzothiazole and dimethylaminobenzene rings, promoting non-radiative relaxation and resulting in weak fluorescence. Upon encountering a G-quadruplex, ThT associates with stacked G-quartet surfaces or occupies grooves and external binding sites, where the confined environment restricts intramolecular rotation, suppresses non-radiative decay, and dramatically enhances fluorescence emission, producing a characteristic turn-on signal. (**Figure 1.10 a**)

Fluorescence enhancement depends strongly on G-quartet topology and accessibility. Parallel and hybrid G-quadruplexes provide favorable

binding sites exhibiting 20-100-fold enhancements, whereas duplex DNA and single-stranded nucleic acids induce only weak responses. The thrombin-binding aptamer, containing only two G-quartet layers, produces little enhancement, suggesting minimum groove depth or extended π-surface is required for efficient ThT sequestration. Multiple cooperative binding events have been reported for human telomeric G-quadruplexes. Consequently, fluorescence intensity enhancement (FL/FL_0) serves as a convenient label-free probe for monitoring G-quartet assembly and topology.*[153-155]* (**Figure 1.10 b, c**)

1.4.4. Nuclear Magnetic Resonance (NMR) Spectroscopy

Solution-state NMR spectroscopy has provided unparalleled insight into the structure and dynamics of G-quartet assemblies. ^{1}H NMR serves as a sensitive probe for identifying self-associated species through characteristic H8 and imino proton resonances. For Na_2(5′-GMP), four distinct peaks in the H8 region between 7.1 and 8.6 ppm are assigned to monomeric, dimeric, and tetrameric species. The outer peaks at 8.5 ppm (H_α) and 7.2 ppm (H_δ) with equal intensities are attributed to tetrameric 5′-GMP with C2′-endo and C3′-endo sugar pucker conformations respectively, while the H_γ peak at 7.9 ppm indicates monomeric and the H_β peak at 8.2 ppm corresponds to dimeric 5′-GMP. (**Figure 1.10 d**) Integration of H8 signals enable quantification of population distribution across self-assembled species.*[128,142]* Additionally, imino proton signals and H8-N2H/N1H NOE cross-peaks confirmed Hoogsteen hydrogen-bonded G-quartet formation. Diffusion-ordered spectroscopy (DOSY) distinguished these species according to translational diffusion coefficients, enabling selective identification of slowly diffusing G-quartet aggregates from faster monomeric and dimeric species. (**Figure 1.10 e**) A combined DOSY-NOESY approach eliminated spectral overlap and provided inter quartet NOE correlations establishing head-to-tail stacking arrangements and right-handed helical organization of Na_2(5′-GMP).*[128]* Additional NOESY cross-peaks and J-coupling analysis revealed stacked G-quartets consisting of alternating C2′-endo

and C3′-endo guanosine residues, providing atomic-level description of the quadruple helical structure.

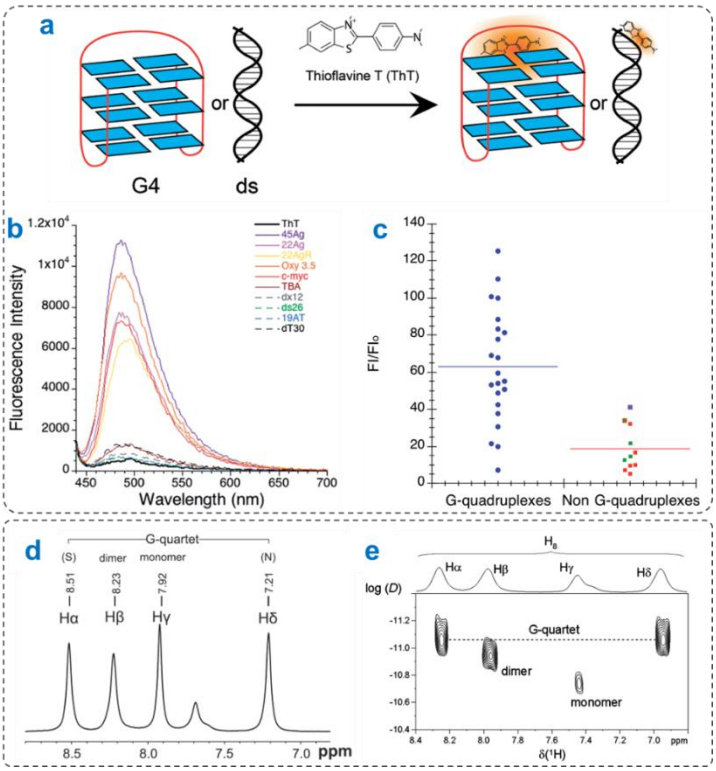


Figure 1.10. *Characterization of G-quadruplex structures using fluorescence and NMR spectroscopy.* ***(a)*** *Schematic illustration of the thioflavin T (ThT) fluorescence assay, demonstrating the selective binding of ThT to G-quadruplexes (G4), which results in a significant fluorescence enhancement, whereas single- and double-stranded nucleic acids produce only weak fluorescence.* ***(b)*** *Fluorescence emission spectra of ThT in the absence (black) and presence of various oligonucleotides, highlighting its selective response toward G-quadruplex structures.* ***(c)*** *Dot plot comparing the fluorescence enhancement of ThT for different nucleic acid conformations.[154]* ***(d)*** *^{1}H NMR spectrum of the H8 proton region[142] and* ***(e)*** *Two-dimensional ^{1}H diffusion-ordered spectroscopy (DOSY) NMR spectrum of 1.0 M Na_2(5′-GMP) in D_2O at 278 K, illustrating the monomeric, dimeric, and G-quartet assemblies.[128] ((Reproduced with permission from [128], 2014, Oxford University Press)*

1.5. Recent Advances in 5′-GMP-Self-Assembly-Based Hydrogels

Among guanine-derived building blocks, 5′-guanosine monophosphate (5′-GMP), a primordial biomolecule, possesses immense potential for constructing functional soft materials. Its unique

propensity to undergo sophisticated supramolecular self-assembly into G-quadruplex fibrillar networks provides a versatile biocompatible and biomimetic platform. Furthermore, the ability of these assemblies to interact with biomacromolecules, organic, and inorganic moieties enables integration of complementary functionalities into hybrid soft materials, opening new avenues spanning biomedicine, catalysis, and bioelectronics.

1.5.1. G-quadruplex in Biomedical Field

The intrinsic biocompatibility, high water content, dynamic nature, and stimuli-responsive behavior of GMP-based supramolecular hydrogels have positioned them as promising platforms for drug delivery and tissue engineering. Thakur et al. demonstrated that Fe^{3+}/Ca^{2+} dual-crosslinked GMP-derived G-quadruplex hydrogels exhibited excellent biocompatibility and pH-responsive sustained zero-order doxorubicin release, highlighting their potential as chemotherapeutic delivery systems (**Figure 1.11 a**).*[156]* Yoneda et al. reported binary guanosine/GMP hydrogels encapsulating small molecules and proteins including methylene blue and cytochrome c, with tunable pH-responsive release kinetics governed by fibrillar network mesh size, alongside self-healing behavior and high cell viability (**Figure 1.11 b**).*[157]* Godoy-Gallardo et al. developed a printable guanosine/GMP bioink for soft tissue reconstruction, where mesenchymal stem cells remained viable within three-dimensional scaffolds, demonstrating potential in regenerative medicine and bioprinting (**Figure 1.11 c**).*[158]* Sarma et al. introduced a chromatin-inspired all-nucleic hydrogel through bio-condensation of biomass DNA and GMP, exhibiting excellent mechanical properties and sustained release of both hydrophilic and hydrophobic therapeutics (**Figure 1.11 d**).*[135]* Additionally, Chakraborty et al. fabricated polyoxometalate-GMP hybrid hydrogels possessing haloperoxidase-like activity with potent antibacterial and antifouling properties against Gram-positive and Gram-negative bacteria, indicating promise for wound healing applications.*[159]* Collectively, these studies underscore the remarkable

versatility of GMP-based supramolecular hydrogels integrating controlled drug release, tissue engineering, antimicrobial activity, and regenerative functions within a single adaptable platform.

1.5.2. G-assembly in Biocatalysis

The hierarchical self-assembly of GMP into G-quadruplex architectures has emerged as a versatile platform for enzymatic biocatalysis and artificial enzyme development. Chakraborty et al. demonstrated that Keggin-type polyoxometalate incorporation into GMP fibrillar hydrogels generated mechanically robust matrices with efficient haloperoxidase-like activity, promoting catalytic oxidative halogenation and antibacterial performance (**Figure 1.11 e**).*[159]* Xu et al. reported a hybrid catalyst through co-assembly of GMP, Fmoc-lysine, and Cu^{2+} ions, generating ordered copper-cluster active sites resembling natural catechol oxidases, exhibiting remarkable oxidase-mimetic activity and exceptional thermal stability (**Figure 1.11 f**).*[160]* Recently, Thakur et al. demonstrated that 5′-GMP condensation with aspartic acid produced fibrillar G-quadruplex nanostructures with intrinsic metal-free peroxidase-like activity, where nanoconfined architecture enhanced substrate affinity and hydroxyl radical generation, providing catalytic efficiencies comparable to horseradish peroxidase (**Figure 1.11 g**).*[161]* Coupling this nanozyme with glucose oxidase enabled cascade biocatalysis for sensitive glucose and glutathione detection. Hu et al. encapsulated Fe-porphyrin metal-organic frameworks together with glucose oxidase within a 5′-GMP hydrogel matrix, facilitating efficient cascade reactions for smartphone-assisted colorimetric glucose detection (**Figure 1.11 h**).*[162]* Collectively, these studies demonstrate that GMP-based supramolecular assemblies provide dynamic nanoconfined environments capable of organizing catalytic centers, promoting substrate accessibility, and mimicking natural enzyme microenvironments, establishing them as promising platforms for next-generation artificial enzymes and biomimetic biocatalytic systems.

1.5.3. GMP-assembly in Bioelectronics

The ability of GMP to self-assemble into hierarchically organized G-quartet fibrillar architectures has attracted considerable interest for bioelectronic and energy storage applications. Thakur et al. demonstrated that phytic acid-induced GMP G-quadruplex hydrogels possess high ionic conductivity, self-healing, and thermo-reversible behavior, enabling their use as gel electrolytes in flexible electrochromic devices, where highly ordered G-quartet channels facilitated efficient ion transport while the biocompatible supramolecular network provided mechanical robustness (**Figure 1.11 i**).*[148]* Sarma et al. exploited the intrinsic peroxidase-like activity of camphorsulfonic acid-induced GMP condensates to achieve in situ oxidative polymerization of aniline, generating polyaniline-embedded conductive hydrogels with enhanced mechanical strength, self-healing characteristics, and high ionic conductivity, subsequently employed to fabricate electrochromic energy-storing electrodes and all-solid-state supercapacitors exhibiting high areal capacitance and energy density.*[163]* Chakravarty et al. reported a supramolecular conductive hydrogel through PEDOT:PSS-induced 5′-GMP fibrillar G-quadruplex self-assembly, where PEDOT:PSS acted simultaneously as electronic conductor and structure-directing agent, generating continuous Na^+ ion diffusion channels and promoting diffusion-controlled pseudocapacitive charge storage. The synergistic coupling of electronic conduction through PEDOT chains and ionic transport through GMP channels yielded flexible all-solid-state supercapacitors with exceptional specific capacitance, energy density, cycling stability, and mechanical flexibility (**Figure 1.11 j**).*[164]* These investigations collectively establish GMP-based supramolecular hydrogels as versatile biocompatible matrices that seamlessly integrate ionic and electronic transport, charting a compelling trajectory toward next-generation bioelectronic devices, flexible supercapacitors, electrochromic systems, and wearable energy storage technologies.

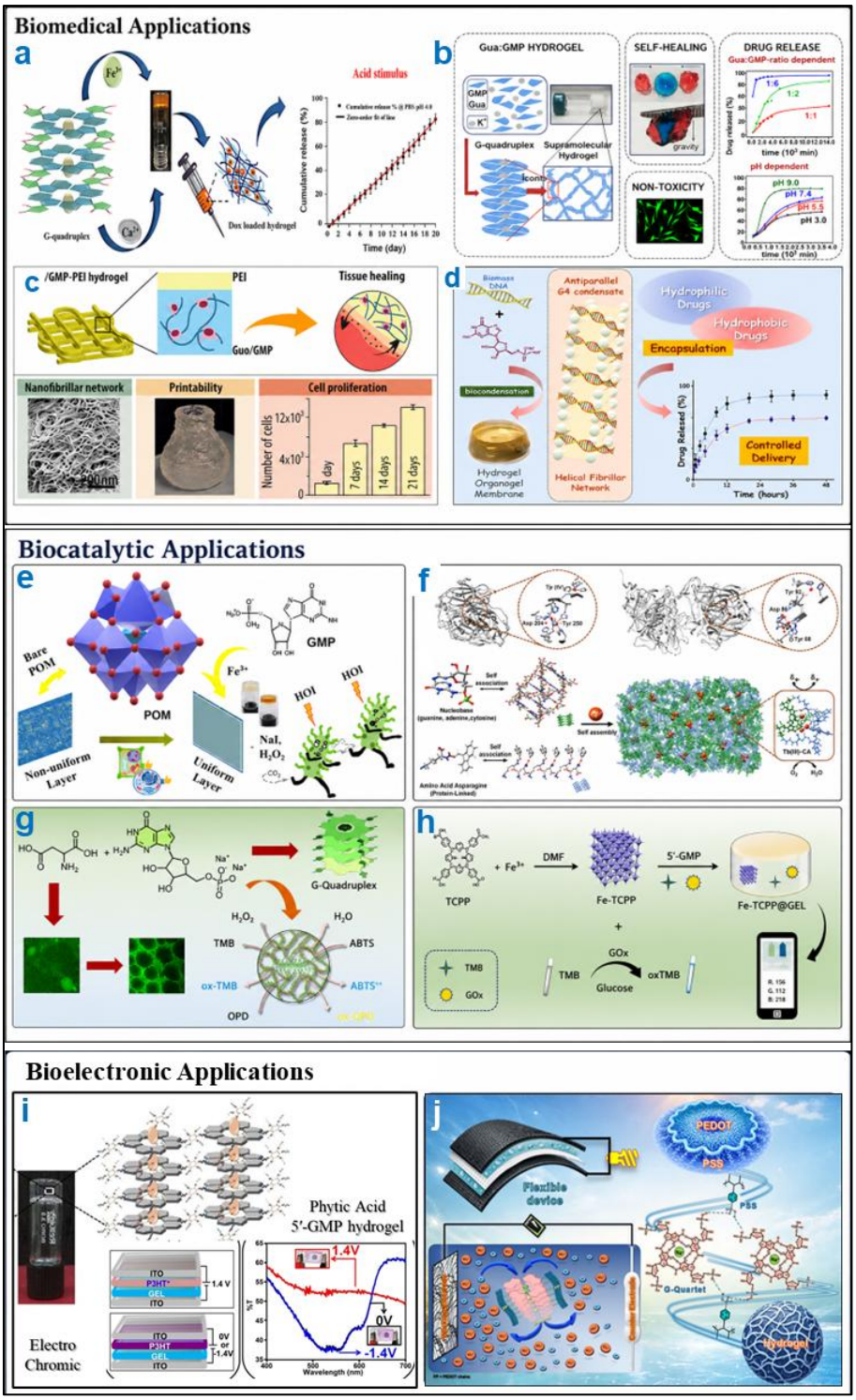


Figure 1.11. *Representative GMP-based hydrogels and composite materials developed for biomedical, biocatalytic, and bioelectronic applications. Biomedical applications:* ***(a)*** *Bimetal-crosslinked 5'-GMP supramolecular hydrogel exhibiting pH-responsive zero-order drug release[156];* ***(b)*** *guanosine-GMP hydrogel with excellent cytocompatibility and high cell viability[157];* ***(c)*** *printable guanosine/GMP bioink for soft tissue engineering and reconstruction[158];* ***(d)*** *DNA-GMP bio-condensate-derived hydrogel functioning as a hydrotropic carrier for the encapsulation and*

controlled delivery of both hydrophilic and hydrophobic drugs[135]. Biocatalytic applications: ***(e)*** *polyoxometalate-GMP hydrogel with haloperoxidase-like catalytic activity[159];* ***(f)*** *co-assembled GMP/Fmoc-lysine/Cu^{2+} hydrogel featuring ordered copper-cluster active sites that mimic natural catechol oxidase;* ***(g)*** *acidic amino acid-induced GMP G-quadruplex nanofibrous hydrogel exhibiting intrinsic peroxidase-like activity;* ***(h)*** *Fe-porphyrin metal-organic frameworks and glucose oxidase encapsulated within a 5′-GMP hydrogel matrix for efficient cascade catalysis and smartphone-assisted colorimetric glucose sensing. Bioelectronic applications:* ***(i)*** *phytic acid-induced GMP G-quadruplex hydrogel for flexible electrochromic devices; and* ***(j)*** *PEDOT:PSS-integrated 5′-GMP fibrillar G-quadruplex hydrogel exhibiting diffusion-controlled pseudocapacitive charge storage for energy-storage applications.*

1.6. Thesis Objective and Organization of the Thesis

The central theme of this thesis is to investigate the supramolecular self-assembly of 5′-GMP and its translation into functional soft materials. As a biogenic molecule of fundamental interest, we explore the physicochemical properties and emergent functions of hydrogels derived from the self-associative building block 5′-GMP. Beginning with a thorough understanding of the self-assembly mechanism and structure-activity relationships, we progressively investigate diverse biogenic applications of the developed functional hydrogels. While each working chapter examines the dynamic self-assembled fibrillar network of 5′-GMP, we also systematically study the hierarchical self-assembly behavior of the resulting nanofibrillar network hydrogels through controlled kinetic morphological, and spectroscopic analyses performed at lower concentrations. Thus, while the primary objective of the thesis is the development of functional hydrogels with applications spanning drug delivery, biocatalysis, and bioelectronics, the underlying structure-activity relationships and self-assembly mechanisms are also rigorously examined in every chapter. Collectively, this thesis work establishes 5′-GMP as a primordial functional building block for the rational design and development of bio-derived functional materials.

The following sections provide a brief description of the contents and organization of the thesis:

Chapter 2 describes the bio-inspired condensation of biomass DNA and guanosine monophosphate (5′-GMP) to construct an "all-nucleic" supramolecular hydrogel. Detailed spectroscopic and morphological studies are presented to elucidate the hierarchical self-assembly process leading to G-quadruplex-based fibrillar networks. Furthermore, the hydrotropic and amphiphilic nature of the hydrogel and its ability to encapsulate and sustain the release of both hydrophilic and hydrophobic drugs are investigated.

Chapter 3 focuses on the development of a structurally tunable DNA-GMP hydrogel platform for programmable anticancer drug delivery. Various supramolecular engineering approaches are employed to modulate the microarchitecture and mechanical properties of the hydrogel, thereby enabling distinct drug-release mechanisms. In addition, the therapeutic efficacy of the drug-loaded hydrogels is evaluated using two-dimensional cell cultures and three-dimensional tumor spheroid models.

Chapter 4 presents the design of enzyme-mimicking "all-nucleotide" G-quadruplex hydrogels formed through biomolecular condensation between GMP and adenosine phosphate derivatives. The influence of phosphate multiplicity and local microenvironment on phase behavior and hierarchical self-assembly is systematically examined. Moreover, the resulting hydrogels are explored as intrinsic peroxidase mimics and confined catalytic microreactors for biomimetic cascade reactions and biosensing applications.

Chapter 5 describes the construction of a nucleotide-based artificial metalloenzyme by supramolecular confinement of a copper-histidine cofactor within a GMP hydrogel network. The chapter discusses how the confined microenvironment stabilizes catalytically active intermediates and recreates enzyme-like active pockets. Detailed mechanistic and electrochemical investigations are carried out to understand the enhanced catechol oxidase-like activity and catalytic efficiency of the resulting biomimetic system.

Chapter 6 discusses the fabrication of conductive polymer-embedded GMP condensate hydrogels through in situ oxidative polymerization mediated by the intrinsic nanozyme activity of the hydrogel matrix. The synergistic integration of supramolecular fibrillar networks with conductive polymer architectures is shown to impart excellent mechanical, self-healing, and ionic conductive properties. Finally, the electrochemical performance of the resulting hybrid hydrogels is demonstrated through their application in electrochromic energy-storage devices and all-solid-state supercapacitors.

Chapter 7 summarizes the major findings and significance of the research presented in this thesis, emphasizing the diverse design strategies and functional applications of GMP-based supramolecular hydrogels. The structure-property relationships governing self-assembly and functionality are highlighted, together with the roles of various molecular crosslinkers and cofactors. Finally, potential future directions are discussed, outlining opportunities for the development of advanced biomolecular materials for biomedical, catalytic, and bioelectronic applications.

1.7. References

1. Chen, X., Yin, et al. (2010), Buckling patterns of thin films on curved compliant substrates with applications to morphogenesis and three-dimensional micro-fabrication, Soft Matter, 6, 5667-5680 (DOI: 10.1039/C0SM00401D.)

2. Chen, X., and Yin, J. (2013), Mechanical Self-Assembly in Nature. In Mechanical Self-Assembly: Science and Applications, Springer, pp. 1-8. (DOI: 10.1007/978-1-4614-4562-3_1.)

3. Chen, X. (2013), Mechanical Self-Assembly: Science and Applications, (978-1-4614-4561-6)

4. Whitesides, G.M., Mathias, et al. (1991), Molecular Self-Assembly and Nanochemistry: a Chemical Strategy for the Synthesis of

Nanostructures, Science 254, 1312-1319 (DOI: 10.1126/science.1962191.)

5. Li, H., LaBean, T.H., et al. (2011), Nucleic acid-based nanoengineering: novel structures for biomedical applications, Interface Focus, 1, 702-724 (DOI: 10.1098/rsfs.2011.0040.)

6. Kim, N.H., Choi, H., et al. (2022), Supramolecular assembly of protein building blocks: from folding to function, Nano Convergence, 9, 4 (DOI: 10.1186/s40580-021-00294-3.)

7. Parteli, E.J.R., Durán, et al. (2009), Dune formation under bimodal winds, Proc. Natl. Acad. Sci. U. S. A., 106, 22085-22089 (DOI: 10.1073/pnas.0808646106.)

8. Mendes, A.C., Baran, et al. (2013), Self-assembly in nature: using the principles of nature to create complex nanobiomaterials, WIREs Nanomedicine and Nanobiotechnology, 5, 582-612 (DOI: 10.1002/wnan.1238.)

9. Lash, M.H., Fedorchak, et al. (2015), Scaling up self-assembly: bottom-up approaches to macroscopic particle organization, Soft Matter, 11, 5597-5609 (DOI: 10.1039/C5SM00764J.)

10. Song, N., Tian, et al. (2024), Self-Assembly in Living Cells: Bottom-Up Syntheses in Natural Factory, ACS Appl. Mater. Interfaces, 16, 45821-45829 (DOI: 10.1021/acsami.4c10653.)

11. Chagri, S., Ng, et al. (2022), Designing bioresponsive nanomaterials for intracellular self-assembly, Nat Rev Chem, 6, 320-338 (DOI: 10.1038/s41570-022-00373-x.)

12. Zhang, J., Wang, et al. (2022), Microfabrication of peptide self-assemblies: inspired by nature towards applications, Chem. Soc. Rev. 51, 6936-6947 (DOI: 10.1039/D2CS00122E.)

13. Wang, L., Gong, et al. (2019), Controlling the Self-Assembly of Biomolecules into Functional Nanomaterials through Internal

Interactions and External Stimulations: A Review. Nanomaterials 9, 285 (DOI: 10.3390/nano9020285.)

14. Bartocci, S., Berrocal, et al. (2018), Peptide-Driven Charge-Transfer Organogels Built from Synergetic Hydrogen Bonding and Pyrene–Naphthalenediimide Donor-Acceptor Interactions, Chem. Euro. J., 24, 2920-2928 (DOI: 10.1002/chem.201704487.)

15. Wu, Y.-L., Bobbitt, et al. (2018), Tunable Crystallinity and Charge Transfer in Two-Dimensional G-Quadruplex Organic Frameworks, Angew. Chem. Int. Ed., 57, 3985-3989 (DOI: 10.1002/anie.201800230.)

16. Bilbao, N., Destoop, et al. (2016), Two-Dimensional Nanoporous Networks Formed by Liquid-to-Solid Transfer of Hydrogen-Bonded Macrocycles Built from DNA Bases, Angew. Chem. Int. Ed., 55, 659-663 (DOI: 10.1002/anie.201509233.)

17. Li, Q., Jia, et al. (2015), Controlled Rod Nanostructured Assembly of Diphenylalanine and Their Optical Waveguide Properties, ACS Nano, 9, 2689-2695 (DOI: 10.1021/acsnano.5b00623.)

18. Xue, T., Cui, et al. (2014), Surface plasmon resonance technique for directly probing the interaction of DNA and graphene oxide and ultra-sensitive biosensing, Biosensors and Bioelectronics, 58, 374-379 (DOI: 10.1016/j.bios.2014.03.002.)

19. Kundu, B., Eltohamy, et al. (2016), Biomimetic Designing of Functional Silk Nanotopography Using Self-assembly, ACS Appl. Mater. Interfaces, 8, 28458-28467 (DOI: 10.1021/acsami.6b07872.)

20. Miao, L., Fan, et al. (2016), The construction of functional protein nanotubes by small molecule-induced self-assembly of cricoid proteins, Chem. Commun., 52, 4092-4095 (DOI: 10.1039/C6CC00632A.)

21. Sun, F., Chen, et al. (2017), High-Resolution Insights into the Stepwise Self-Assembly of Nanofiber from Bioactive Peptides, J. Phys. Chem. B, 121, 7421-7430 (DOI: 10.1021/acs.jpcb.7b03626.)

22. Palchoudhury, S., Zhou, et al. (2017), Self-assembly of P22 protein cages with polyamidoamine dendrimer and inorganic nanoparticles, J. Mater. Res., 32, 465-472 (DOI: 10.1557/jmr.2016.439.)

23. Sun, H., Zhang, et al. (2016), Micelle-Induced Self-Assembling Protein Nanowires: Versatile Supramolecular Scaffolds for Designing the Light-Harvesting System, ACS Nano, 10, 421-428 (DOI: 10.1021/acsnano.5b05213.)

24. Zhao, L., Zou, et al. (2017), Enzyme-Triggered Defined Protein Nanoarrays: Efficient Light-Harvesting Systems to Mimic Chloroplasts, ACS Nano, 11, 938-945 (DOI: 10.1021/acsnano.6b07527.)

25. Law, A.S.-Y., Yeung, et al. (2017), Arginine-Rich Peptide-Induced Supramolecular Self-Assembly of Water-Soluble Anionic Alkynylplatinum(II) Complexes: A Continuous and Label-Free Luminescence Assay for Trypsin and Inhibitor Screening, ACS Appl. Mater. Interfaces, 9, 41143-41150 (DOI: 10.1021/acsami.7b12319.)

26. Wang, M., Lin, et al. (2018), DNA-hosted copper nanoclusters/graphene oxide based fluorescent biosensor for protein kinase activity detection, Analytica Chimica Acta, 1012, 66-73 (DOI: 10.1016/j.aca.2018.01.029.)

27. Wakabayashi, R., Syahid Fathullah, et al. (2025), Self-Assembling Aromatic Peptide Amphiphile Fibers for Multivalent Display of Enzymatically Linked Antigenic Proteins, ACS Appl. Mater. Interfaces, 17, 44240-44248 (DOI: 10.1021/acsami.5c10222.)

28. Redondo-Gómez, C., Abdouni, et al. (2019), Self-Assembling Hydrogels Based on a Complementary Host-Guest Peptide Amphiphile Pair, Biomacromolecules, 20, 2276-2285 (DOI: 10.1021/acs.biomac.9b00224.)

29. Spiegel, J., Adhikari, et al. (2020), The Structure and Function of DNA G-Quadruplexes, Trends in Chemistry, 2, 123-136 (DOI: 10.1016/j.trechm.2019.07.002.)

30. Liu, L.-H., Li, et al. (2014), Self-Assembly of Hybridized Peptide Nucleic Acid Amphiphiles, ACS Macro Lett., 3, 467-471 (DOI: 10.1021/mz5001916.)

31. McGuinness, K., Nanda, V. (2017), Collagen mimetic peptide discs promote assembly of a broad range of natural protein fibers through hydrophobic interactions, Org. Biomol. Chem., 15, 5893-5898 (DOI: 10.1039/C7OB01073G.)

32. Tanaka, M., Abiko, et al. (2015), Two-dimensional self-assembly of amphiphilic peptides; adsorption-induced secondary structural transition on hydrophilic substrate, J. Coll. Inter. Science, 442, 82-88 (DOI: 10.1016/j.jcis.2014.11.021.)

33. Wang, R., Wang, et al. (2014), Trifluoromethylated nucleic acid analogues capable of self-assembly through hydrophobic interactions, Chem. Sci., 5, 4076-4081 (DOI: 10.1039/C4SC01162G.)

34. Mehta, P., Sharma, et al. (2023), Hydrogels: An overview of its classifications, properties, and applications, J. Mech. Behavior Biomed. Mater., 147, 106145 (DOI:10.1016/j.jmbbm.2023.106145.)

35. Du, X., Zhou, et al. (2014), Supramolecular Hydrogels Made of Basic Biological Building Blocks, Chem. Asian J., 9, 1446-1472 (DOI:10.1002/asia.201301693.)

36. Boekhoven, J., Stupp, S.I. (2014), 25th Anniversary Article: Supramolecular Materials for Regenerative Medicine, Adv. Mater., 26, 1642-1659 (DOI: 10.1002/adma.201304606.)

37. Estroff, L.A., Hamilton, et al. (2004), Water Gelation by Small Organic Molecules, Chem. Rev., 104, 1201-1218 (DOI: 10.1021/cr0302049.)

38. Webber, M.J., Appel, et al. (2016), Supramolecular biomaterials, Nat. Mater., 15, 13-26 (DOI: 10.1038/nmat4474.)

39. Wei, G., Su, et al. (2017), Self-assembling peptide and protein amyloids: from structure to tailored function in nanotechnology, Chem. Soc. Rev., 46, 4661-4708 (DOI: 10.1039/C6CS00542J.)

40. Du, X., Zhou, et al. (2015), Supramolecular Hydrogelators and Hydrogels: From Soft Matter to Molecular Biomaterials, Chem. Rev., 115, 13165-13307 (DOI: 10.1021/acs.chemrev.5b00299.)

41. Chivers, P.R.A., Smith, et al. (2019), Shaping and structuring supramolecular gels, Nat Rev Mater, 4, 463-478 (DOI: 10.1038/s41578-019-0111-6.)

42. Weiss, R.G (2014), The Past, Present, and Future of Molecular Gels. What Is the Status of the Field, and Where Is It Going? J. Am. Chem. Soc., 136, 7519-7530 (DOI: 10.1021/ja503363v)

43. Draper, E.R., Adams, D.J (2017), Low-Molecular-Weight Gels: The State of the Art. Chem, 3, 390-410 (DOI: 10.1016/j.chempr.2017.07.012)

44. J. Skilling et al. (2014), , Insights into low molecular mass organic gelators: a focus on drug delivery and tissue engineering applications. Soft Matter 10, 237–256 (DOI: 10.1039/C3SM52244J)

45. Hanabusa, K., Yamada et al. (1996), Prominent Gelation and Chiral Aggregation of Alkylamides Derived from trans-1,2-Diaminocyclohexane, Angew. Chem. Int. Ed., 35, 1949-1951 (DOI: 10.1002/anie.199619491)

46. Estroff, L.A., Hamilton, A.D (2000), Effective Gelation of Water Using a Series of Bis-urea Dicarboxylic Acids, Angew. Chem. Int. Ed., 39, 3447-3450 (DOI: 10.1002/1521-3773(20001002)39:19%3C3447::AID-ANIE3447%3E3.0.CO;2-X)

47. Boettcher et al. (2001), Comparative Cryo-Electron Microscopy of Noncovalent N-Dodecanoyl- (d- and l-) serine Assemblies in Vitreous Toluene and Water. Langmuir 17, 873-877 (DOI: 10.1021/la001054p)

48. Menger, F.M., Caran, K.L (2000), Anatomy of a Gel. Amino Acid Derivatives That Rigidify Water at Submillimolar Concentrations. J. Am. Chem. Soc. 122, 11679-11691 (DOI: 10.1021/ja0016811)

49. Xing et al. (2002), Hydrophobic Interaction and Hydrogen Bonding Cooperatively Confer a Vancomycin Hydrogel: A Potential Candidate for Biomaterials. J. Am. Chem. Soc. 124, 14846-14847 (DOI: 10.1021/ja028539f)

50. Zhang et al. (2004), Molecular Recognition Remolds the Self-Assembly of Hydrogelators and Increases the Elasticity of the Hydrogel by 106-Fold. J. Am. Chem. Soc. 126, 15028-15029 (DOI: 10.1021/ja044401g)

51. Branco, M.C., Schneider, J.P (2009), Self-assembling materials for therapeutic delivery. Acta Biomaterialia 5, 817-831 (DOI: 10.1016/j.actbio.2008.09.018)

52. Yang et al. (2008), Enzymatic Hydrogelation of Small Molecules. Acc. Chem. Res. 41, 315-326 (DOI: 10.1021/ar7001914)

53. Ulijn et al. (2007), Bioresponsive hydrogels. Mater. Today, 10, 40-48 (DOI: 10.1016/S1369-7021(07)70049-4)

54. Nowak, A., Breedveld, V., Pakstis, L. et al. (2002), Rapidly recovering hydrogel scaffolds from self-assembling diblock copolypeptide amphiphiles, Nature, 417, 424-428 (DOI: 10.1038/417424a)

55. McManus et al. (2016), The physics of protein self-assembly. Current Opinion in Colloid & Interface Science 22, 73-79 (DOI: 10.1016/j.cocis.2016.02.011)

56. Qi et al. (2018), Self-Assembled Peptide-Based Nanomaterials for Biomedical Imaging and Therapy, Adv. Mater., 30, 1703444 (DOI: 10.1002/adma.201703444)

57. Marchesan et al. (2015), The Phe-Phe Motif for Peptide Self-Assembly in Nanomedicine, Molecules 20, 19775-19788 (DOI: 10.3390/molecules201119658)

58. Wang, Z.-G., Ding, B (2014), Engineering DNA Self-Assemblies as Templates for Functional Nanostructures, Acc. Chem. Res., 47, 1654-1662 (DOI: 10.1021/ar400305g)

59. Shaham-Niv et al. (2015), Extension of the generic amyloid hypothesis to nonproteinaceous metabolite assemblies, Science Adv., 1, e1500137 (DOI: 10.1126/sciadv.1500137)

60. Shaham-Niv et al. (2018), Intrinsic Fluorescence of Metabolite Amyloids Allows Label-Free Monitoring of Their Formation and Dynamics in Live Cells, Angew. Chem. Int. Ed., 57, 12444-12447 (DOI: 10.1002/anie.201806565)

61. Shaham-Niv et al. (2018), Metabolite amyloid-like fibrils interact with model membranes. Chem. Commun. 54, 4561-4564 (DOI: 10.1039/C8CC01423J)

62. Abramovich, L. A., Gazit, E. (2014), The physical properties of supramolecular peptide assemblies: from building block association to technological applications, Chem. Soc. Rev., 43, 6881-6893 (DOI: 10.1039/c4cs00164h)

63. Binaymotlagh et al. (2022), Peptide-Based Hydrogels: New Materials for Biosensing and Biomedical Applications, Materials, 15, 5871 (DOI: 10.3390/ma15175871)

64. Shimizu, T (2003), Bottom-Up Synthesis and Morphological Control of High-Axial-Ratio Nanostructures through Molecular Self-Assembly, Polym J., 35, 1-22 (DOI: 10.1295/polymj.35.1)

65. Banwell et al. (2009), Rational design and application of responsive α-helical peptide hydrogels, Nat. Mater., 8, 596-600 (DOI: 10.1038/nmat2479)

66. Branco, M.C., Schneider, J.P (2009), Self-assembling materials for therapeutic delivery, Acta Biomaterialia, 5, 817-831 (DOI: 10.1016/j.actbio.2008.09.018)

67. Zhang et al. (2003), Supramolecular Hydrogels Respond to Ligand-Receptor Interaction, J. Am. Chem. Soc., 125, 13680-13681 (DOI: 10.1021/ja036817k)

68. Jayawarna et al. (2007), Three-dimensional cell culture of chondrocytes on modified di-phenylalanine scaffolds, Biochem Soc Trans., 35, 535-537 (DOI: 10.1042/BST0350535)

69. Pu et al. (2018), Nucleobases, nucleosides, and nucleotides: versatile biomolecules for generating functional nanomaterials, Chem. Soc. Rev., 47, 1285-1306 (DOI: 10.1039/c7cs00673j)

70. Peters, G.M.,, Davis, J.T (2016), Supramolecular gels made from nucleobase, nucleoside and nucleotide analogs, Chem. Soc. Rev., 45, 3188-3206 (DOI: 10.1039/c6cs00183a)

71. Godoy-Gallardo et al. (2023), Nucleoside-Based Supramolecular Hydrogels: From Synthesis and Structural Properties to Biomedical and Tissue Engineering Applications, ACS Biomater. Sci. Eng., 9, 40-61 (DOI: 10.1021/acsbiomaterials.2c01051)

72. Sreenivasachary, N.,, Lehn, J. M. (2005), Gelation-driven component selection in the generation of constitutional dynamic hydrogels based on guanine-quartet formation, Proc. Natl. Acad. Sci. U. S. A., 102, 5938-5943 (DOI: 10.1073/pnas.0501663102)

73. Li et al. (2012), Supramolecular hydrogels formed by the conjugates of nucleobases, Arg-Gly-Asp (RGD) peptides, and glucosamine, Soft Matter, 8, 7402-7407 (DOI: 10.1039/c2sm25725d)

74. Liu et al. (2017), Bioinspired Adhesive Hydrogel Driven by Adenine and Thymine, ACS Appl. Mater. Interfaces, 9, 17645-17652 (DOI: 10.1021/acsami.7b04832)

75. Li et al. (2020), Supramolecular nucleobase-functionalized polymers: synthesis and potential biological applications, J. Mater. Chem. B, 8, 1576-1588 (DOI: 10.1039/c9tb02393c)

76. Lee, K.Y., Mooney, D.J (2012), Alginate: Properties and biomedical applications, Progress in Polymer Science, 37, 106-126 (DOI: 10.1016/j.progpolymsci.2011.06.003)

77. Goyal et al. (2010), Synthesis and characterization of d-glucosamine-derived low molecular weight gelators, Tetrahedron, 66, 5962-5971 (DOI: 10.1016/j.tet.2010.05.071)

78. Wang et al. (2006), Synthesis and characterization of monosaccharide lipids as novel hydrogelators, Carbohydrate Research, 341, 705-716 (DOI: 10.1016/j.carres.2006.01.023)

79. Wang et al. (2009), Synthesis and Characterization of Monosaccharide-Derived Carbamates as Low-Molecular-Weight Gelators, Langmuir, 25, 8696-8705 (DOI: 10.1021/la804337g)

80. Talloj et al. (2018), Glucosamine-Based Supramolecular Nanotubes for Human Mesenchymal Cell Therapy, ACS Appl. Mater. Interfaces, 10, 15079-15087 (DOI: 10.1021/acsami.8b03226)

81. Freudenberg et al. (2016), Glycosaminoglycan-Based Biohybrid Hydrogels: A Sweet and Smart Choice for Multifunctional Biomaterials, Adv. Mater., 28, 8861-8891 (DOI: 10.1002/adma.201601908)

82. Zhang et al. (2025), Recent advances in glycopeptide hydrogels: design, biological functions, and biomedical applications. Front. Bioeng. Biotechnol. 13 (DOI: 10.3389/fbioe.2025.1577192)

83. Yang et al. (2012), Supramolecular hydrogel of kanamycin selectively sequesters 16S rRNA, Chem. Commun., 48, 9257-9259 (DOI: 10.1039/c2cc34935c)

84. Gao et al. (2012), Using supramolecular hydrogels to discover the interactions between proteins and molecular nanofibers of small

molecules, Chem. Commun., 48, 8404-8406 (DOI: 10.1039/c2cc33631f)

85. Roviello et al. (2011), Evidences for supramolecular organization of nucleopeptides: synthesis, spectroscopic and biological studies of a novel dithymine l-serine tetrapeptide, Mol Biosyst, 7, 1073-1080 (DOI: 10.1039/C0MB00214C)

86. Azzam, M.E., Algranati, I.D (1973), Mechanism of Puromycin Action: Fate of Ribosomes after Release of Nascent Protein Chains from Polysomes, Proc. Natl. Acad. Sci. U. S. A., 70, 3866-3869 (DOI: 10.1073/pnas.70.12.3866)

87. Haaima et al. (1996), Peptidnucleinsäuren (PNAs) aus chiralen Aminosäuren und Thymin-Monomeren: Hybridisierungs- und Löslichkeitseigenschaften von D-Lysin-PNA, Angew. Chem., 108, 2068-2070 (DOI: 10.1002/ange.19961081712)

88. Zhao et al. (2011), β-Galactosidase-instructed formation of molecular nanofibers and a hydrogel, Nanoscale, 3, 2859-2861 (DOI: 10.1039/c1nr10333d)

89. Yang et al. (2007), d-Glucosamine-based supramolecular hydrogels to improve wound healing, Chem. Commun., 43, 843-845 (DOI: 10.1039/b616563j)

90. Wang et al. (2011), A saccharide-based supramolecular hydrogel for cell culture. Carbohydrate Research, 346, 1013-1017 (DOI: 10.1016/j.carres.2011.03.031)

91. Kuang et al. (2013), Interactions between cellular proteins and morphologically different nanoscale aggregates of small molecules, RSC Adv., 3, 7704-7707 (DOI: 10.1039/c3ra41523f)

92. Whitesides, G.M., Wong, A.P (2006), , The Intersection of Biology and Materials Science, MRS Bulletin, 31, 19-27 (DOI: 10.1557/mrs2006.2)

93. Davis, J.T., Spada, G.P (2007), Supramolecular architectures generated by self-assembly of guanosine derivatives, Chem. Soc. Rev., 36, 296-313 (DOI: 10.1039/b600282j)

94. Davis, J.T (2004), G-Quartets 40 Years Later: From 5′-GMP to Molecular Biology and Supramolecular Chemistry, Angew. Chem. Int. Ed., 43, 668-698 (DOI: 10.1002/anie.200300589)

95. Neidle. S. and Balasubramanian, S. (2007), Quadruplex Nucleic Acids, RSC Cambridge (978-0-85404-374-3)

96. Fritzsche, W. and Spindler, L. Guanine Quartets, Structure and Applications, RSC Cambridge (978-1-84973-460-8)

97. Xu, X., Chen, S. J. (2020), Topological constraints of RNA pseudoknotted and loop-kissing motifs: applications to three-dimensional structure prediction, Nucleic Acids Res, 48, 6503-6512 (DOI: 10.1093/nar/gkaa463)

98. Leontis et al. (2002), The non-Watson-Crick base pairs and their associated isostericity matrices, Nucleic Acids Res, 30, 3497-3531 (DOI: 10.1093/nar/gkf481)

99. Hu et al. (2022), Acid-Resistant and Physiological pH-Responsive DNA Hydrogel Composed of A-Motif and i-Motif toward Oral Insulin Delivery, J. Am. Chem. Soc., 144, 5461-5470 (DOI: 10.1021/jacs.1c13426)

100. Stefan, L., Monchaud, D (2019), Applications of guanine quartets in nanotechnology and chemical biology, Nat Rev Chem, 3, 650-668 (DOI: 10.1038/s41570-019-0132-0)

101. Varshney et al. (2020), The regulation and functions of DNA and RNA G-quadruplexes, Nat Rev Mol Cell Biol, 21, 459-474 (DOI: 10.1038/s41580-020-0236-x)

102. Gellert et al. (1962), Helix formation by guanylic acid. Proc. Natl. Acad. Sci. U. S. A., 48, 2013-2018 (DOI: 10.1073/pnas.48.12.2013)

103. Fresco, J.R., Massoulie, Jean (1963), Polynucleotides. V. Helix-Coil Transition of Polyriboguanylic Acid, J. Am. Chem. Soc., 85, 1352-1353 (DOI: 10.1021/ja00892a031)

104. Pinnavaia et al. (1975), Self-assembled 5′-guanosine monophosphate, nuclear magnetic resonance evidence for a regular, ordered structure and slow chemical exchange, J. Am. Chem. Soc., 97, 7198-7200 (DOI: 10.1021/ja00857a059)

105. Pinnavaia et al. (1978), Alkali metal ion specificity in the solution ordering of a nucleotide, 5′-guanosine monophosphate, J. Am. Chem. Soc., 100, 3625-3627 (DOI: 10.1021/ja00479a070)

106. Sessler, J.L., Sathiosatham, et al. (2000), A G-Quartet Formed in the Absence of a Templating Metal Cation: A New 8-(N,N-dimethylaniline) guanosine Derivative, Angew. Chem. Int. Ed., 39, 1300-1303 (DOI: 10.1002/(SICI)1521-3773(20000403)39:7%3C1300::AID ANIE1300%3E3.0.CO;2-I)

107. Bouhoutsos-Brown et al. (1982), Structure-directing properties of sodium(+) ion in the solution ordering of guanosine 5'-monophosphate. Stoichiometry of aggregation, binding to ethidium, and modes of sodium(+) ion complexation, J. Am. Chem. Soc., 104, 6576-6584 (DOI: 10.1021/ja00388a017)

108. Eimer, W., Dorfmueller, T (1992), Self-aggregation of guanosine 5'-monophosphate, studied by dynamic light scattering techniques, J. Phys. Chem., 96, 6790-6800 (DOI: 10.1021/j100195a048)

109. Horvath, M.P.,, Schultz, S.C (2001), DNA G-quartets in a 1.86 Å resolution structure of an Oxytricha nova telomeric protein-DNA complex1, J. Molecular Biol., 310, 367-377 (DOI: 10.1006/jmbi.2001.4766)

110. Haider et al. (2002), Crystal Structure of the Potassium Form of an Oxytricha nova G-quadruplex, J. Molecular Biol. 320, 189-200 (DOI: 10.1016/S0022-2836(02)00428-X)

111. Forman et al. (2000), Toward Artificial Ion Channels: A Lipophilic G-Quadruplex, J. Am. Chem. Soc., 122, 4060-4067 (DOI: 10.1021/ja9925148)

112. Borzo et al. (1980), Proton, sodium-23, and phosphorus-31 NMR studies of the self-assembly of the 5'-guanosine monophosphate dianion in neutral aqueous solution in the presence of sodium cations, J. Am. Chem. Soc., 102, 1124-1134 (DOI: 10.1021/ja00523a032)

113. Detellier, C., Laszlo, P (1980), Role of alkali metal and ammonium cations in the self-assembly of the 5'-guanosine monophosphate dianion, J. Am. Chem. Soc., 102, 1135-1141 (DOI: 10.1021/ja00523a033)

114. Delville et al. (1979), Determination of the correlation time for a slowly reorienting spin-3/2 nucleus: Binding of Na+ with the 5′-GMP supramolecular assembly, J Magnetic Reson., 34, 301-315 (DOI: 10.1016/0022-2364(79)90006-4)

115. Harraz, D.M., Davis, J.T (2018), A self-assembled peroxidase from 5′-GMP and heme, Chem. Commun., 54, 1587-1590 (DOI: 10.1039/c7cc09900b)

116. Levene, P.A (1919), CRYSTALLINE GUANYLIC ACID. J. Biol. Chem., 40, 171-174 (DOI: 10.1016/S0021-9258(18)87275-1)

117. Davis et al. (1995), Self-Assembled Ionophores from Isoguanosine, J. Org. Chem., 60, 4167-4176 (DOI: 10.1021/jo00118a038)

118. Rodriguez et al. (2012), Small-molecule-induced DNA damage identifies alternative DNA structures in human genes, Nat Chem Biol, 8, 301-310 (DOI: 10.1038/nchembio.780)

119. Rhodes, D., Lipps, H.J (2015), G-quadruplexes and their regulatory roles in biology, Nucleic Acids Res, 43, 8627-8637 (DOI: 10.1093/nar/gkv862)

120. Cammas, A., Millevoi, S (2017), RNA G-quadruplexes: emerging mechanisms in disease, Nucleic Acids Res, 45, 1584-1595 (DOI: 10.1093/nar/gkw1280)

121. Gottarelli et al. (1995), Self-assembly in organic solvents of a deoxyguanosine derivative induced by alkali metal picrates, J. Chem. Soc. Chem. Commun., 31, 2555-2557 (DOI: 10.1039/C39950002555)

122. Gubala et al. (2004), Expanding the Hoogsteen Edge of 2‘-Deoxyguanosine: Consequences for G-Quadruplex Formation, Org. Lett, 6, 4735,4738 (DOI: 10.1021/ol048013v)

123. Otero et al. (2005), Guanine Quartet Networks Stabilized by Cooperative Hydrogen Bonds, Angew. Chem. Int. Ed., 44, 2270-2275 (DOI: 10.1002/anie.200461586)

124. Lena et al. (2010), Triggering of Guanosine Self-Assembly by Light. Angew. Chem. Int. Ed., 49, 3657-3660 (DOI: 10.1002/anie.201000805)

125. González-Rodríguez et al. (2009), G-quadruplex self-assembly regulated by Coulombic interactions, Nat. Chem, 1, 151-155 (DOI: 10.1038/nchem.177)

126. Hightower et al. (2009), Supramolecular Structure and Polymorphism of Alkali Metal Salts of Guanosine 5′-Monophosphate: SEM and NMR Study, J. Phys. Chem. B, 113, 12214-12219 (DOI: 10.1021/jp904383y)

127. Wu et al. (2017), On the Helical Structure of Guanosine 5′-Monophosphate Formed at pH 5: Is It Left- or Right-Handed?, J. Nucleic Acids, 2017, 6798759 (DOI: 10.1155/2017/6798759)

128. Wu, G., Kwan, I.C.M (2009), Helical Structure of Disodium 5′-Guanosine Monophosphate Self-Assembly in Neutral Solution, J. Am. Chem. Soc., 131, 3180-3182 (DOI: 10.1021/ja809258y)

129. Nakayama et al. (2011), Thiazole Orange-Induced c-di-GMP Quadruplex Formation Facilitates a Simple Fluorescent Detection of

This Ubiquitous Biofilm Regulating Molecule, J. Am. Chem. Soc., 133, 4856-4864 (DOI: 10.1021/ja1091062)

130. Nakayama et al. (2011), c-di-GMP can form remarkably stable G-quadruplexes at physiological conditions in the presence of some planar intercalators, Chem. Commun, 47, 4766-4768 (DOI: 10.1039/c0cc05432a)

131. Bare et al. (2013), Synthesis of a Single G-Quartet Platform in Water, J. Am. Chem. Soc., 135, 11985-11989 (DOI: 10.1021/ja405100z)

132. Wong et al. (2005), Disodium Guanosine 5′-Monophosphate Self-Associates into Nanoscale Cylinders at pH 8: A Combined Diffusion NMR Spectroscopy and Dynamic Light Scattering Study, J. Am. Chem. Soc, 127, 6990-6998 (DOI: 10.1021/ja042794d)

133. Miles, H.T., Frazier, J. (1978), Poly(I) helix formation. Dependence on size-specific complexing to alkali metal ions, J. Am. Chem. Soc., 100, 8037-8038 (10.1021/ja00493a058)

134. Tao et al. (2024), Hydration water drives the self-assembly of guanosine monophosphate, Biophys. J., 123, 931-939 (DOI: 10.1016/j.bpj.2024.03.005)

135. Sarma et al. (2024), Chromatin inspired bio-condensation between biomass DNA and guanosine monophosphate produces all-nucleic hydrogel as a hydrotropic drug carrier, Commun Chem, 7, 261 (DOI: 10.1038/s42004-024-01353-6)

136. Li et al. (2011), Identification of nonplanar small molecule for G-quadruplex grooves: Molecular docking and molecular dynamic study, Bioorganic & Medicinal Chemistry Letters, 21, 6969–6972 (DOI: 10.1016/j.bmcl.2011.09.125)

137. Li et al. (2021), Water spines and networks in G-quadruplex structures, Nucleic Acids Res, 49, 519-528 (DOI: 10.1093/nar/gkaa1177)

138. Gresh et al. (2017), Channeling through Two Stacked Guanine Quartets of One and Two Alkali Cations in the Li+, Na+, K+, and Rb+ Series. Assessment of the Accuracy of the SIBFA Anisotropic Polarizable Molecular Mechanics Potential, J. Phys. Chem. B, 121, 3997-4014 (DOI: 10.1021/acs.jpcb.7b01836)

139. Sutyak et al. (2016), Controlling molecularity and stability of hydrogen bonded G-quadruplexes by modulating the structure's periphery, Chem. Commun, 52, 11112-11115 (DOI: 10.1039/c6cc06271g)

140. Gonnelli et al. (2013), Small-Angle X-ray Scattering Study of Self-Assembling Lipophilic Guanines in Organic Solvents: G-Quadruplex Formation and Cation Effects in Cyclohexane, J. Phys. Chem. B, 117, 1095-1103 (DOI: 10.1021/jp3121929)

141. Kunstelj et al. (2007), Self-organization of guanosine 5′-monophosphate on mica, Colloids and Surfaces B: Biointerfaces 59, 120-127 (DOI: 10.1016/j.colsurfb.2007.04.022)

142. Gao et al. (2017), Temperature and pressure limits of guanosine monophosphate self-assemblies, Sci Rep 7, 9864 (DOI: 10.1038/s41598-017-10689-0)

143. Mudroňová et al. (2016), Effect of ribose versus 2′-deoxyribose residue in guanosine 5′-monophosphates on formation of G-quartets stabilized by potassium and sodium cations, Vibrational Spectroscopy, 82, 60-65 (DOI: 10.1016/j.vibspec.2015.12.002)

144. Azargun et al. (2017), The intrinsic stabilities and structures of alkali metal cationized guanine quadruplexes, Phys. Chem. Chem. Phys., 19, 1281-1287 (DOI: 10.1039/c6cp07301h)

145. Azargun, M., Fridgen, T.D (2015), Guanine tetrads: an IRMPD spectroscopy, energy resolved SORI-CID, and computational study of M(9-ethylguanine)4+ (M = Li, Na, K, Rb, Cs) in the gas phase, Phys. Chem. Chem. Phys, 17, 25778-25785 (DOI: 10.1039/c5cp00580a)

146. Panda, M., Walmsley, J.A (2011), Circular Dichroism Study of Supramolecular Assemblies of Guanosine 5′-Monophosphate, J. Phys. Chem. B, 115, 6377-6383 (DOI: 10.1021/jp201630g)

147. del Villar-Guerra et al. (2018), G-Quadruplex Secondary Structure Obtained from Circular Dichroism Spectroscopy, Angew. Chem. Int. Ed., 57, 7171-7175 (DOI: 10.1002/anie.201709184)

148. Thakur et al. (2021), Ion Conductive Phytic Acid-G Quadruplex Hydrogel as Electrolyte for Flexible Electrochromic Device, ChemNanoMat, 7, 613-619 (DOI: 10.1002/cnma.202100072)

149. Plank et al. (2017), Supramolecular hydrogels for environmental remediation: G4-quartet gels that selectively absorb anionic dyes from water, Chem. Commun. 53, 6235–6238 (DOI: 10.1039/c7cc03118a)

150. Carvalho et al. (2017), Circular Dichroism of G-Quadruplex: a Laboratory Experiment for the Study of Topology and Ligand Binding, J. Chem. Educ, 94, 1547-1551 (DOI: 10.1021/acs.jchemed.7b00160)

151. Gattuso et al. (2016), Circular Dichroism of DNA G-Quadruplexes: Combining Modeling and Spectroscopy To Unravel Complex Structures, J. Phys. Chem. B, 120, 3113-3121 (DOI: 10.1021/acs.jpcb.6b00634)

152. Ghosh et al. (2021), Pt Nanoparticles Supported on a Dynamic Boronate Ester-Based G-quadruplex Hydrogel as a Nanoreactor, Chem. Asian J., 16, 215-223 (DOI: 10.1002/asia.202001284)

153. Mohanty et al. (2013), Thioflavin T as an Efficient Inducer and Selective Fluorescent Sensor for the Human Telomeric G-Quadruplex DNA, J. Am. Chem. Soc, 135, 367-376 (DOI: 10.1021/ja309588h)

154. Renaud de la Faverie et al. (2014), Thioflavin T as a fluorescence light-up probe for G4 formation, Nucleic Acids Res, 42, e65 (DOI: 10.1093/nar/gku111)

155. Bhasikuttan, A.C., Mohanty, J (2015), Targeting G-quadruplex structures with extrinsic fluorogenic dyes: promising fluorescence sensors, Chem. Commun, 51, 7581-7597 (DOI: 10.1039/c4cc10030a)

156. Thakur et al. (2019), Biocompatible Fe3+ and Ca2+ Dual Cross-Linked G-Quadruplex Hydrogels as Effective Drug Delivery System for pH-Responsive Sustained Zero-Order Release of Doxorubicin, ACS Appl. Bio Mater, 2, 3300-3311 (DOI: 10.1021/acsabm.9b00334)

157. Yoneda et al. (2021), Self-assembled guanosine-hydrogels for drug-delivery application: Structural and mechanical characterization, methylene blue loading and controlled release, Materials Science and Engineering: C, 121, 111834 (DOI: 10.1016/j.msec.2020.111834)

158. Godoy-Gallardo et al. (2023), Advanced Binary Guanosine and Guanosine 5′-Monophosphate Cell-Laden Hydrogels for Soft Tissue Reconstruction by 3D Bioprinting, ACS Appl. Mater. Interfaces 15, 29729–29742 (DOI: 10.1021/acsami.2c23277)

159. Chakraborty et al. (2024), Polyoxometalate-Guanosine Monophosphate Hydrogels with Haloperoxidase-like Activity for Antibacterial Performance, Biomacromolecules, 25, 104-118 (DOI: 10.1021/acs.biomac.3c00845)

160. Xu et al. (2023), A supramolecular metalloenzyme possessing robust oxidase-mimetic catalytic function, Nat Commun, 14, 4040 (DOI: 10.1038/s41467-023-39779-6)

161. Thakur et al. (2025), Acidic Amino Acid Induced 5′-Guanosine Monophosphate Fibrillar Nanozyme: A Highly Efficient Metal-Free Intrinsic Peroxidase Mimic, Nano Lett., 25, 15407-15415 (DOI: 10.1021/acs.nanolett.5c04390)

162. Hu et al. (2023), The construction of Fe-porphyrin nanozymes with peroxidase-like activity for colorimetric detection of glucose, Analytical Biochemistry, 675, 115224 (DOI: 10.1016/j.ab.2023.115224)

163. Sarma et al. (2025), Supramolecular Self-Assembly of Polyaniline Embedded Enzyme-Mimicking GMP-Condensate Hydrogel for Electrochromic Energy Storage Applications, ACS Appl. Mater. Interfaces, 17, 48532-48546 (DOI: 10.1021/acsami.5c08151)

164. Chakravarty et al. (2026), PEDOT:PSS-Induced Supramolecular G-Quartet Hydrogel for Diffusion-Controlled High-Performance Flexible Supercapacitor, ACS Materials Lett., 8, 1214-1223 (DOI: 10.1021/acsmaterialslett.6c00044)

Chapter 2

2. Chromatin Inspired Bio-condensation Between Biomass DNA and Guanosine Monophosphate Produces All-Nucleic Hydrogel as a Hydrotropic Drug Carrier

2.1. Introduction

Within cells, subcellular controlled microenvironments or compartments have evolved to facilitate and regulate specific biocatalytic processes, with some characterized by membrane-bound structures composed of lipid bilayers, while others exist in a membrane-less form resulting from the phase separation of proteins and nucleic acids.*[1,2]* Liquid-liquid phase transition of biological macromolecules result in the formation of the non-membrane-bound compartments such as the nucleoli, centrosomes, stress granules etc. *[3-5]* For example, in eukaryotic cells, genomic DNA packaged into chromatin, primarily guided by the core histone and linker histone proteins, forming an octamer of histones, which eventually forms left-handed hierarchical superhelix.*[6,7]* These chromatin structures essentially control all nuclear processes involving DNA, including transcription, DNA replication and DNA repair.*[8,9]* These natural compartments have inspired the creation of synthetic microenvironments or bio condensates for purposes like accelerating enzymatic reactions, aiding small molecule synthesis, and delivering drugs or therapeutic biomolecules.*[10,11]* Liquid phase condensation of DNA resulting in the formation of biomolecular condensates such as concentrated droplets, gels or reversible aggregates via associative interactions have inspired material scientists for fabrication of various functional materials.*[12,13]* DNA is a versatile and abundant biomass (estimated at 50 billion metric tons)*[14,15]* and can be used to form a variety of

novel biohybrid materials such as DNA gels*[16,17]*, DNA dendrimers*[18]*, DNA nanoflowers*[19]*, three-dimensional crystals*[20,21]*, DNA origami*[22]*, constitutional dynamic networks*[23]* etc.

Most of the biological phase separations of DNA involve polyelectrolytes with nonuniform charge distribution and multivalent reciprocity associated via electrostatic interactions. However, the bio-condensation of DNA via non-electrostatic association that involves the formation of such as G-quadruplexes (G4), has been less exploited. G-4s play an important role in several cellular pathways that include DNA replication, gene expression and telomere maintenance.*[24]* Herein, we describe a non-covalent bio-condensation between DNA and guanosine monophosphate (GMP) that mimics chromatin folding, resulting in unique "all-nucleic" DNA-GMP condensates. This synergy leads to the formation of G-4 based superstructures, which ultimately assemble into super-helical fibres. The unique hierarchical self-assembly of randomly coiled DNA into an ordered fibrillar network, the evolution of helicity in these fibres, and the extent of condensation through synergistic hydrogen bonding and stacking have been thoroughly investigated. Additionally, the dynamic reconfigurability of these condensates through mass transition and thermodynamic aspects has also been investigated. Interestingly, this bio-condensation at higher concentration, can be extended to a supramolecular “all nucleic” hydrogel with excellent mechanical properties. The transformation of randomly coiled biomass DNA to an ordered helical G-quadruplex superstructures through non-covalent interactions induce reconfiguration and switch-ability to the hydrogel, that result in diverse applications such as stimuli responsiveness, self-healing, sustained drug release etc. Utilizing biomass DNA as a building polymeric block for smart DNA-based materials is gaining attention due to the complexity and cost associated with cascade self-assembly of carefully sequenced and patterned oligonucleotides and DNA scaffolds.*[25-28]*

The “all nucleic” biomass DNA hydrogel reported herein has several advantages: (a) all raw materials are nucleic acids (or fragments) derived from bio-resources, (b) the method is green and spontaneous, involving no synthetic steps, thereby can be translated to industrial scale easily, (c) the resultant hydrogel is highly stable, reusable and biocompatible. Furthermore, the hydrogel can encapsulate a variety of drug molecules, both hydrophilic and hydrophobic, with a high loading capacity and shows sustained drug release. To the best of our knowledge, this is the first report of a biomass DNA hydrogel formed through physical crosslinking involving a nucleotide.

2.2. Results and Discussions

2.2.1. Chromatin inspired “all nucleic” G4-condensation

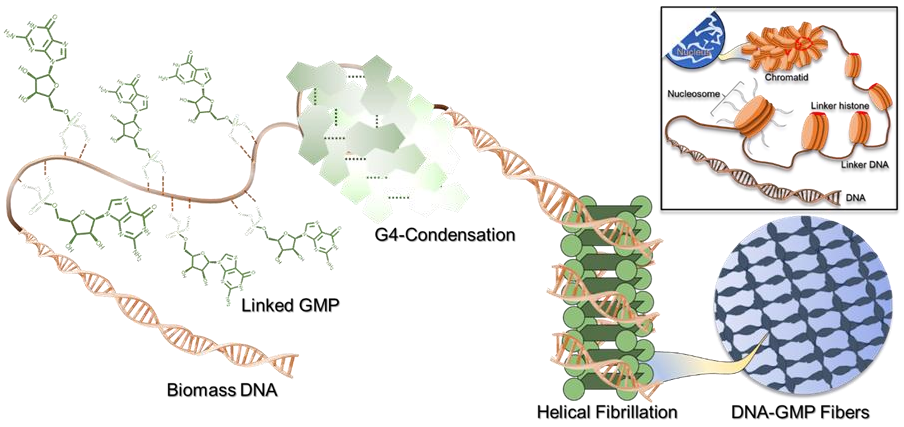


Figure 2.1. *Chromatin-inspired DNA packaging into a G4-condensate leads to the formation of a helical fibril network. From left to right: the chemical structure of the guanosine monophosphate nucleotide is followed by a schematic diagram of G4-condensation and the formation of a DNA-wrapped π-π stacked helical superstructure.*

In cells, arrays of nucleosomes organize the DNA within chromatin. Each nucleosome core comprises of an octamer assembled from two copies each of histone proteins, around which 145-147 base pairs of DNAs are wrapped. The nucleosome's histone octamer core constitutes a left-handed protein superhelix composed of four histone dimers arranged spirally.*[6,8]* Similar to the histones, four guanine bases can associate through Hoogsteen hydrogen bonding to form a guanine tetrad, having square planner structure. Two or more guanine tetrads

stack on top of each other to form G-quadruplexes, stabilized by a cation such as K^+, Na^+, NH_4^+ *etc. [29-31]* Inspired from the DNA packaging of chromatin guided by linker and core histones, it could be expected that bio-condensation of DNA can occur through wrapping around the G4 assembly. Interestingly, we observed that DNA and GMP have synergistic effect towards the formation of the bio-condensate, where DNA facilitates the G4 formation, which in turn induce condensation of DNA leading to a helical self-assembly similar to DNA packaging around the histone proteins in chromatin **(Figure 2.1)**.

A simple mixing of salmon milt biomass DNA (40 μg/mL) and 150 μM GMP-Na_2 at 37 ℃ under physiological pH of 7.4 and further incubation for 12 hours led to the formation of a bio-condensate. Salmon milt biomass DNA was used for the studies due to their commercial availability and low cost. Scanning electron microscope (SEM) images showed highly entangled fibrillar network with an average diameter of 240 ± 15 nm of each fibre **(Figure 2.2 a)**. The nanofibers bundled together to form larger fibres, as confirmed by the high-resolution SEM images shown in **Figure 2.2 b**. High resolution TEM images showed the helical superstructure formation of the DNA-GMP condensates (**Figure 2.2 c**). Transmission electron microscopy (TEM) studies further confirmed the formation of highly intertwined fibrillar morphology with an average diameter of 23 ± 8 nm as calculate through mean width calculation (**Figure 2.2 d**). Further, Atomic force microscopy studies validated the formation of fibrillar nanostructures with an average height of 12 nm (**Figure 2.2 e, f**).

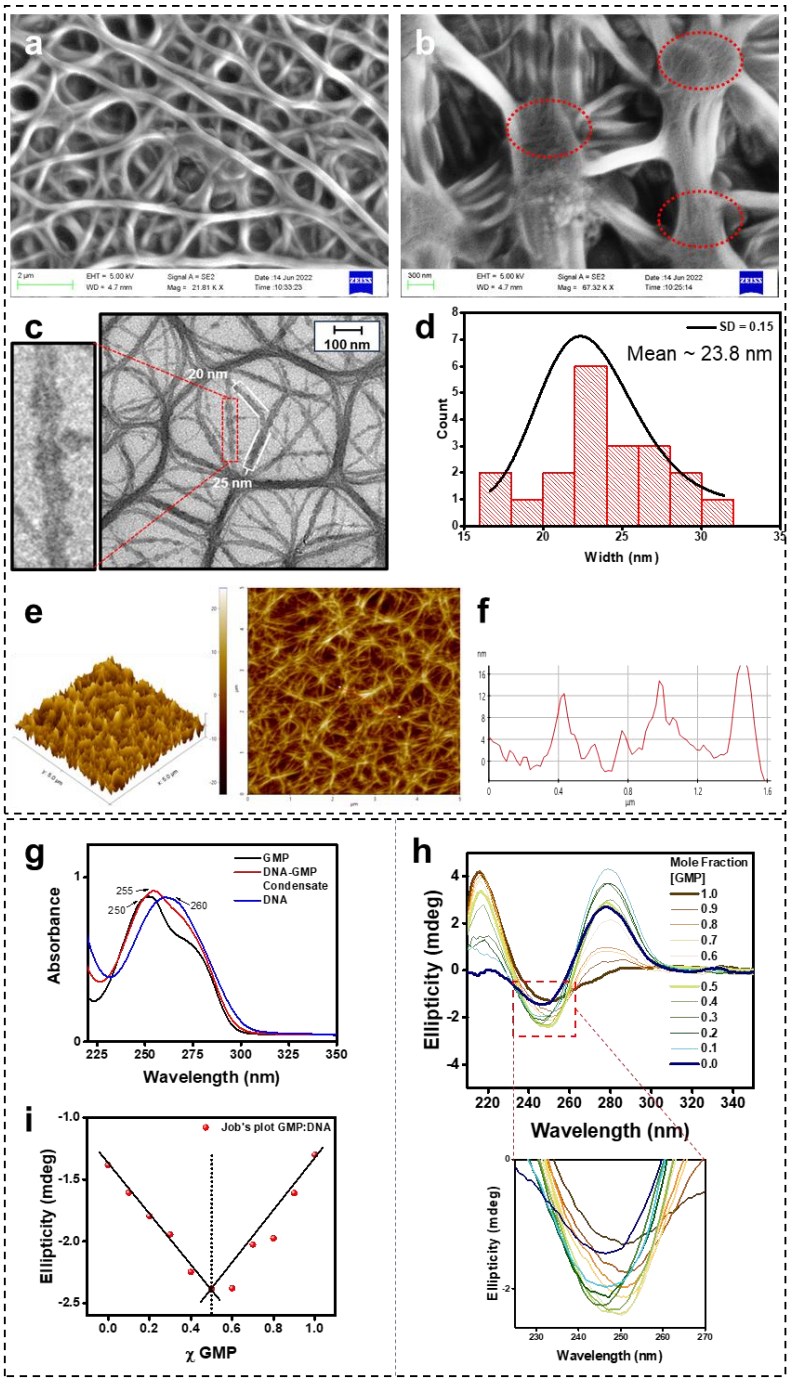


Figure 2.2. *Morphological and spectroscopic evaluation of the DNA-GMP condensate.* ***(a)*** *FE-SEM images of the DNA-GMP condensate [40 µg/mL DNA and 150 µM GMP] showing dense fibril network and* ***(b)*** *high resolution image with the red circled area showing the bundled fibers.* ***(c)*** *HRTEM image of the fibres showing the helicity (inset) of the fibres and* ***(d)*** *plot showing the average diameter and the range of diameters of each fiber of the hydrogel network.* ***(e)*** *3-dimensional atomic force microscopic (AFM) image of the DNA-GMP condensate [40 µg/mL DNA and 150 µM GMP]* ***(f)*** *the height scale showing the height distribution bundles of the fibers.* ***(g)*** *UV-visible spectra of GMP, DNA-GMP condensate [40 µg/mL DNA and 150 µM GMP],*

showing the bathochromic shift. ***(h)*** *Circular dichroism study of DNA-GMP interaction at various mole-fraction of GMP [40 µg/mL DNA and 150 µM GMP] and extended figure between the range 230-270 nm showing the negative ellipticity at 250 nm.* ***(i)*** *Job's plot was constructed from the CD signal at 250 nm for DNA-GMP interaction.*

Various spectroscopic studies were carried out to understand the supramolecular interactions leading to the bio-condensation. The absorption spectrum of GMP, having λ_{max} at 251 nm exhibit a bathochromic shift upon addition of biomass DNA, indicating the formation of a noncovalent assembly (**Figure 2.2 g**).*[32]* Circular dichroism spectroscopy reveals the formation of G4-condensation with a negative cotton band at 250 nm following an antiparallel G-quartet pattern **(Figure 2.2 h)**.*[33,34]* The negative cotton band at 250 nm showed an incremental enhancement until a stoichiometry of 1:1 molar ratio of DNA and GMP, inferring the optimum formation of G-quadruplexes under these conditions (**Figure 2.2 g**). Job's plot analysis based on the CD signal at 250 nm revealed a maximum response at an apparent 1:1 composition of DNA and GMP (**Figure 2.2 i**). However, because the biomass DNA is heterogeneous, with a distribution of molecular weights and chain lengths, the observed ratio should not be interpreted as an exact binding stoichiometry. It instead represents an apparent optimum composition, corresponding to the maximum G4-related chiroptical response under the experimental conditions.

The ^{1}H-NMR spectrum of the DNA-GMP condensate shows a broad peak in the 10-12 ppm range, characteristic of G4 formation associated with the imino protons of guanine in a G-tetrad **(Figure 2.3 a)**.*[35,36]* Due to the presence of the DNA macromolecule, the imino proton signals of the GMP guanine moieties overlap in this region, resulting in a relatively broad and flat peak in the full NMR spectrum. While this broad peak does not confirm the exact G4 conformation, it does indicate the formation of a G4 network through the self-assembly of GMP molecules. Zeta potential measurements were also carried out to evaluate the changes in the surface charge of DNA, GMP, and the DNA-GMP condensate. The zeta potential of DNA and GMP changed

from -46.36 mV and -28.39 mV, respectively to -21.18 mV upon condensate formation **(Figure 2.3 b)**. The acidic nature of DNA promotes the self-assembly of GMP into G4 strands, suggesting that biomass DNA condensation is facilitated in an acidic environment, where DNA macromolecules and self-assembled GMP molecules are likely to interact through hydrogen bonding between their phosphate groups. Additionally, Na^+ ions occupy the G4 cavities, forming a positively charged ion channel after the condensation of DNA and GMP. This positive ion channel, along with the stabilization of phosphate groups through non-covalent interactions, contributes to the reduction of the overall negative surface charge of the DNA-GMP condensate.

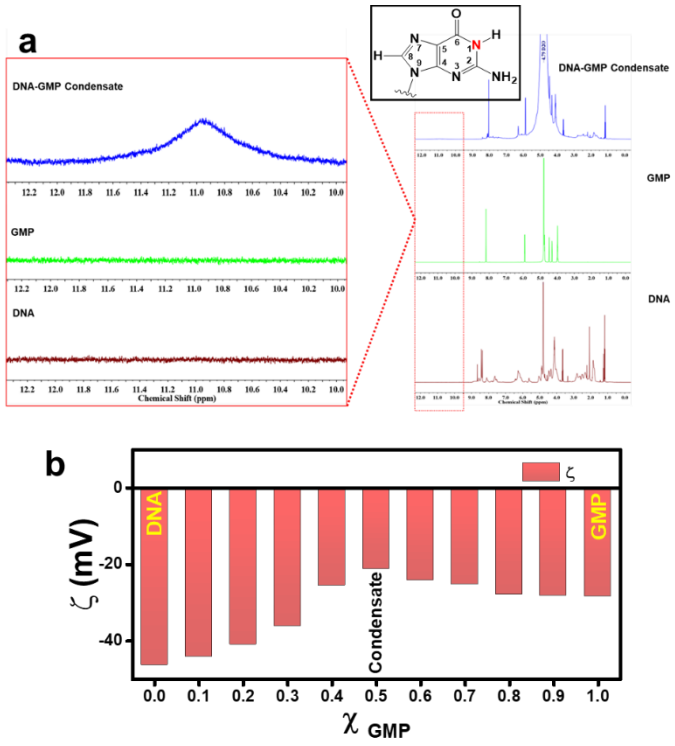


Figure 2.3. (a) *^{1}H-NMR spectra of DNA-GMP condensate [40 µg/mL DNA and 150 µM GMP], GMP and DNA, highlighting the 10-12 ppm region for the imino proton of guanine base. Chemical structure shows the imino proton linked to the N1-(red marked) site of guanine base.* ***(b)*** *Zeta potential of DNA-GMP condensate at various stoichiometry of DNA and GMP [40 µg/mL DNA and 150 µM GMP].*

For a deeper understanding of the condensation process, a thorough mechanistic analysis was conducted. First, circular dichroism (CD) spectroscopy was conducted to confirm the extent of formation of

G4 assembly upon addition of variable amount of GMP at fixed DNA concentration as shown in **Figure 2.4 a**. The ellipticity showed a sigmoidal decrease from $\theta_{250\ nm}$ = -0.2 to $\theta_{250\ nm}$ = -0.8, suggesting an increase in G4 formation with an increase in GMP concentration **(Figure 2.4 b)**. The possibility of DNA wrapped π-π stacked G4 moieties leading to nano-fibrillation in the condensate were confirmed by a Thioflavin T (ThT) assay. The fluorogenic dye ThT is widely used for the detection of G4 motifs through fluorescence light-up in the visible region.*[37]* The noncovalent interactions between ThT and G4 channel stabilize the dye in a rigid, planar structure via end stacking, groove binding, or intercalation, thus greatly reducing its usual nonradiative torsional relaxation. This results in fluorescence enhancement by several folds.*[38,39]* Concomitant to the G4 formation, the fluorescence emission spectra of ThT-assay showed a remarkable linear increase in the intensity (FL/FL_0) from 22-fold (due to intrinsic affinity of ThT towards biomass DNA) to 30-fold at a GMP concentration of 150 μM (λ_{em}^{max} = 491 nm) **(Figure 2.4 c, d)**. This suggests that G4 formation and stacked fibrillation can be regulated with the amount of GMP.

The formation of G4-associated supramolecular assemblies in the DNA-GMP system is supported by several complementary spectroscopic and structural observations. The negative CD band at ~250 nm indicates the development of ordered guanine assemblies, and the broad ^{1}H-NMR signal in the 10-12 ppm region is consistent with imino protons involved in Hoogsteen hydrogen bonding. PXRD shows a characteristic interplanar spacing of ~0.32 nm, consistent with π-π stacked guanine-rich structures, and the enhancement of ThT fluorescence indicates the presence of G4-associated binding environments. Together, these results suggest a pathway to fibrillar condensation in which DNA promotes the formation of G4 motifs, which then stack through π-π interactions into supramolecular nano-strands. Further investigations using complementary structural techniques would provide more definitive topological confirmation.

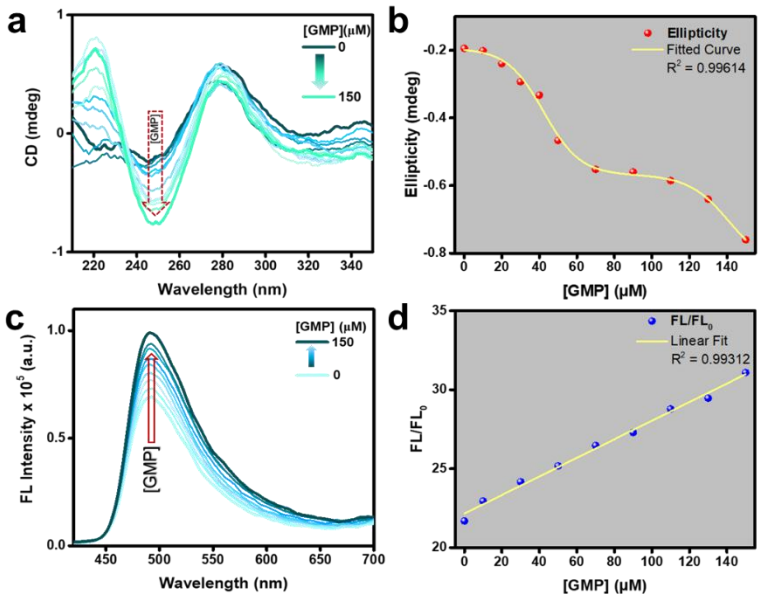


Figure 2.4. *Spectroscopic investigations into the concentration-dependent dynamics of the condensation process.* ***(a)*** *CD spectra at various GMP concentration (0-150 μM) and constant DNA amount (40 μg/mL) with incremental negative cotton band at 250 nm,* ***(b)*** *sigmoidal decrease in the ellipticity at 250 nm,* ***(c)*** *FL spectra of ThT assay (ThT concentration 10 μM) at various GMP concentration from 0-150 μM and constant DNA concentration (40 μg/mL) and* ***(d)*** *Linear incremental fitting of FL/FL$_0$ ratio for ThT assay.*

To gain more insight into the self-assembly process and the underlying interactions during the bio-condensation of DNA and GMP, concentration dependent aggregation kinetic studies were carried out using various microscopic techniques. Since GMP played a key role in the G4 assembly and stacked fibrillation, we monitored the morphological evolution at various GMP concentrations, while keeping the DNA concentration (40 μg/mL) fixed. The random DNA biopolymers started to organize into small self-assembled nanoaggregates, even when 10 μM of GMP was added, suggesting that DNA starts to organize around the G4 formed even at such a low concentration of GMP **(Figure 2.5 a, b)**. At an increased GMP concentration of 30 μM, with more G4 core formation, DNA is adsorbed onto the surface and self-assembled into a spherical hollow superstructure with a corona-like formation **(Figure 2.5 c)**. Upon further enhancing the GMP concentration to 50 μM, the stacked fibrillation

process starts with the appearance of anisotropic nano-blocks along with unwrapped DNAs as shown in **Figure 2.5 d**. At an increased GMP concentration of 70 μM, non-covalent interactions between G4-tetrads and DNA wrapping around the G4 strands led to the formation of elongated rod-like structures with prominent helical chirality **(Figure 2.5 e)**. The concentration dependent anisotropic growth was further evident at a GMP concentration of 90 μM, as the nano-fibrillation took precedence **(Figure 2.5 f)**, which further crosslinked to form a dense entangled fibril network at GMP concentrations of 120 and 150 μM **(Figure 2.5 g, h)**. Thus, it can be inferred that at higher concentrations (>100 μM) of GMP, all the randomly aggregated DNA coils uniformly wrap around the G4-moieties and form π-π stacked helical DNA-GMP fibrillar condensates. Atomic force microscopy (AFM) studies of the condensates at variable concentration of GMP (at a fixed concentration of DNA) further confirmed the growth pattern from small anisotropic building blocks to the highly entangled fibrillar network with increasing concentration of GMP from 50 to 150 μM **(Figure 2.5 i-l)**. The height profile of the nanoaggregates at lower GMP concentration (50 and 70 μM) showed much higher average height (approx. 50 nm) as compared to the height of the nanofibrils formed (approx. 12 nm) at higher concentration (120 and 150 μM). This difference may be associated with variations in the degree of structural organization and compaction during DNA-GMP co-assembly. It further suggests that incomplete organization of DNA and GMP at lower GMP concentrations may result in the formation of aggregated structures, whereas at the optimum concentration, a homogeneous fibrillar morphology is obtained. Although this interpretation is consistent with the observed morphological evolution, further comparison with DNA-only aggregates would provide the precise structural contribution of DNA.

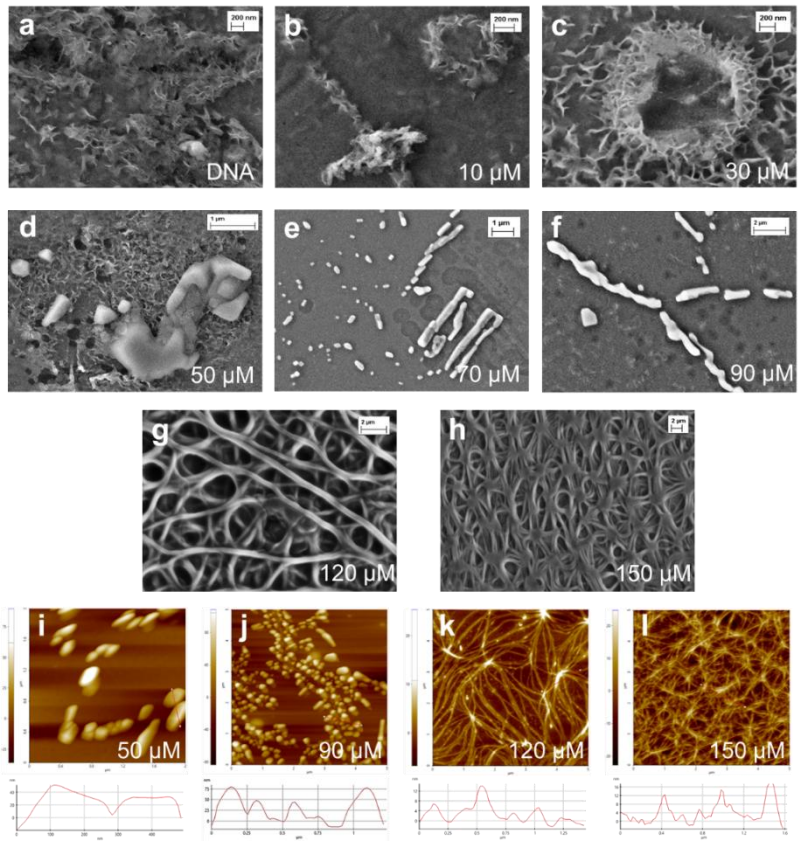


Figure 2.5. (a-h) *FESEM images showing the morphological evolution of the DNA-GMP condensates at increasing GMP concentration keeping the DNA concentration constant [40 μg/mL].* ***(i-l)*** *AFM images showing the morphological evolution of the DNA-GMP condensates at increasing GMP concentration (Scale bar included in the image) at fixed DNA concentration [40 μg/mL DNA] along with their height profile.*

To further understand the involvement of π-π stacking during the anisotropic morphology evolution of the DNA-GMP condensations, confocal laser microscopy studies were carried out using Thioflavin-T labelling at variable GMP concentrations, while keeping DNA concentration fixed (40 μg/mL). Thioflavin-T binds to G4 fibril channels, resulting in the fluorescence enhancement in the green region.*[37,38]* **Figure 2.6 a-d** shows the confocal fluorescence microscopy images of the ThT-labelled DNA/GMP condensates. At a very low GMP concentration of 10 μM, only blue fluorescence was observed owing to the intrinsic fluorescence of DNA. This suggests the presence of large amount of random DNA at the initial stage of G4 formation **(Figure 2.6 a)**. When the GMP concentration was increased to 50 μM, the formation of nanoaggregates could be observed in the

bright field image, however these aggregates also showed blue fluorescence **(Figure 2.6 b)**. As the GMP concentration increased to 90 µM, the nano-fibrillation process started, as indicated by the appearance of green fluorescence alongside the intrinsic DNA emission in the ThT assay **(Figure 2.6 c)**. At a high GMP concentration (150 µM), the condensate appeared as a homogeneous fibrillar network with predominantly green fluorescence (**Figure 2.6 d**). This suggests that most of the DNA molecules participate in condensation, giving strong ThT emission from the π-π stacked G4 assemblies. At low GMP concentrations, the abundance of randomly coiled DNA meant that the weak blue intrinsic emission of DNA dominated. As the GMP concentration increased, green emission from ThT bound to G4 stacks began to appear alongside the blue DNA fluorescence, and it became the dominant signal at higher concentrations. This progressive shift indicates a growing population of ThT-binding sites within the assembled DNA-GMP structures. Together, these controlled fluorescence microscopy studies suggest that GMP concentration strongly influences the π-π stacking pattern, with an optimal concentration yielding a homogeneous fibrillar network.

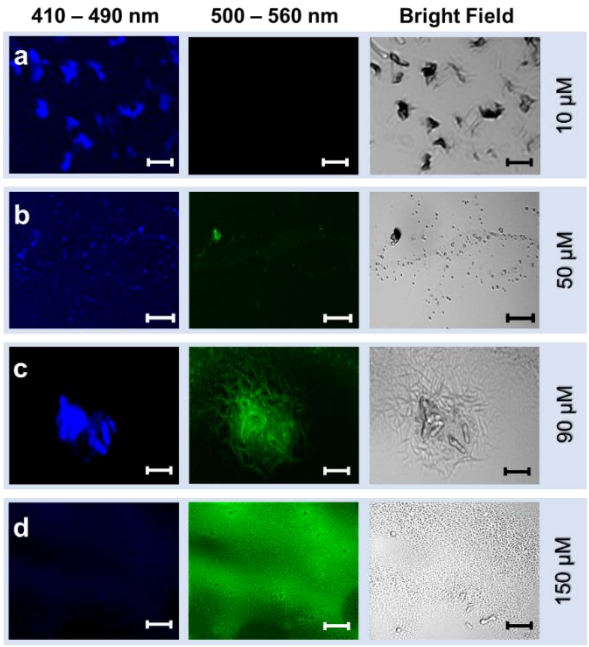


Figure 2.6. (a-d) *Confocal fluorescence images of the evolution of green fluorescence with the increase in GMP concentration (scale bar ~ 5 µm for a-c and 10 µm for d).*

In order to further ascertain the dynamic reconfiguration of the bio-condensate, temperature dependent studies were performed. The variable-temperature CD spectra of the DNA-GMP condensate (40 μg/mL DNA and 150 μM GMP) showed only a marginal change in the intensity of the negative Cotton band at 250 nm, maintaining similar ellipticity across the temperature range of 10 °C to 50 °C **(Figure 2.7 c)**. On the other hand, the emission of ThT bound condensate was significantly quenched when temperature was increased from 10 °C to 50 °C **(Figure 2.7 d)**. At higher temperature, the ThT molecules which were bound in the rigid and more planar G4 grooves were released, thereby activating the nonradiative torsional relaxation channel.*[38]* The results showed the possibility of modulation in dynamics of π-π interactions within the condensate at variable temperature. This was verified from the FESEM micrographic studies **(Figure 2.7 a)**, which showed that the highly fibrillar and entangled condensate network at 30 °C, was converted into small nanoaggregates at 40 °C. At 50 °C, one exclusively finds aggregated microspheres decorated with the smaller aggregates with the protrusion of thin petal-like structures from the surface, which were formed at the expense of the nanofibrils. Further fractal self-assembly of these microstructures led to complex flower-like superstructures at 60 °C. This morphological evolution might be attributed to the dynamic liquid condensation phases of DNAs, which forms noncanonical linear aggregates through physical aggregation. As the temperature increases, the weakening of end-to-end adhesion in DNA-wrapped G4-condensation leads to the formation of smaller linear aggregates on the surface of the homogeneous fibrillar network.*[40]* The progression in the self-assembly of these linear aggregates along a uniaxial columnar pathway, eventually creates petal-like structures on the surface, which gradually evolve into a flower-like spherical morphology in the matrices.*[41,42]* Notably, the temperature dependent morphological rearrangements were dynamic and reversible in nature as the DNA-GMP bio-condensates spontaneously reassemble and

recovered to their highly fibrillary morphology upon cooling down to 30 °C **(Figure 2.7 b)**.

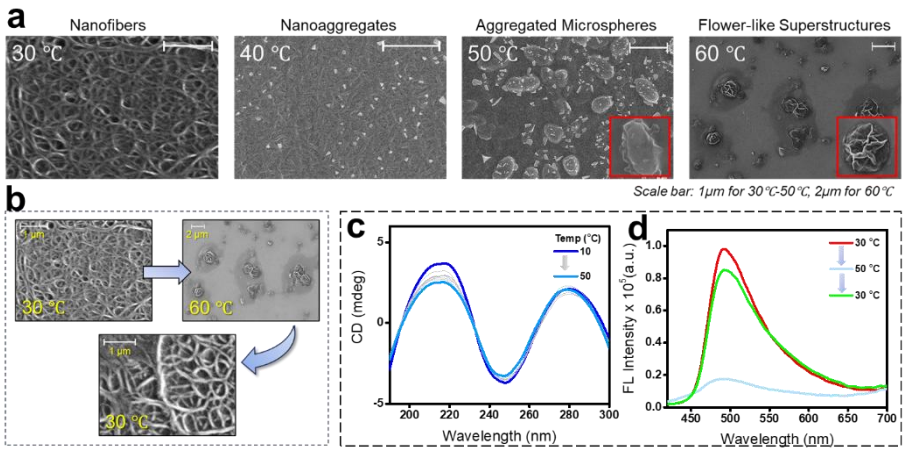


Figure 2.7. (a) *Temperature dependent morphological reconfiguration of the DNA-GMP condensate [40 μg/mL DNA and 150 μM GMP] from 30 °C to 60 °C. (Scale bar: 1μm for 30°C-50°C, 2μm for 60°C).* ***(b)*** *Dynamic reconfiguration of the DNA-GMP condensate [40 μg/mL DNA and 150 μM GMP]. FESEM images demonstrate the transformation from a fibrillar to a nanoflower-like structure, followed by a reversion to the original fibrillar morphology in the same solution of condensate.* ***(c)*** *Temperature dependent CD spectra and* ***(d)*** *ThT assay illustrating the reversible fluorescence intensity of the same solution of condensate during a temperature transition from 30 to 60 to 30 °C.*

Based on the concentration-dependent morphological evolution, spectroscopic observations, and helical features observed through electron microscopy, we propose a cooperative assembly mechanism in which GMP-derived G-quartet structures provide a supramolecular framework for the organization of biomass DNA. The observed helical fibrillar morphology suggests the possible association of DNA with the stacked guanine-rich assemblies. However, the precise molecular arrangement of DNA around individual G4 structures has not been directly resolved. Therefore, the proposed mechanism represents a plausible model of hierarchical DNA–GMP co-assembly. The term chromatin-inspired organization is used to describe the conceptual similarity in DNA condensation and higher-order structural organization, rather than suggesting molecular equivalence with histone-mediated chromatin assembly.

2.2.2. DNA/GMP extensive condensation leading to hydrogelation

As the bio-condensation of DNA and GMP lead to fibrillar nanostructures in dilute condition, we further studied their self-assembly process at higher concentration of both the constituents. When the condensation was carried out at a concentration of 40 mg/mL of salmon milt DNA and 150 mM of GMP, a highly stable light-yellow hydrogel was formed spontaneously **(Figure 2.8 a)**. Controlled experiments suggest that the gelation can take place in a wide range of concentration with minimum of 30 mg/mL of DNA and 75 mM of GMP respectively **(Figure 2.8 b)**. The hydrogel can be molded into various shapes using different templates **(Figure 2.8 c)**. Thin membranes of the hydrogel also can be obtained by slicing or thin coating followed by drying even at room temperature **(Figure 2.8 d)**.

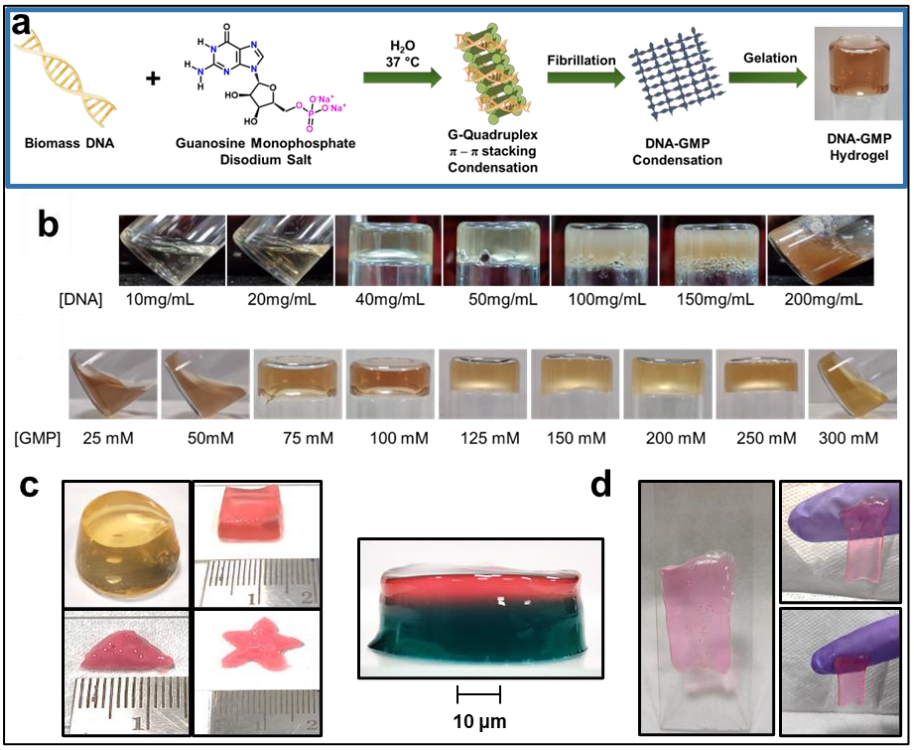


Figure 2.8. (a) *Transformation of DNA-GMP condensate to DNA-GMP hydrogel at higher concentration.* ***(b)*** *Digital Images showing the minimum and maximum range of concentration needed for the formation of stable DNA-GMP hydrogel as the concentration of DNA increases from 10mg mL^{-1} to 200 mg mL^{-1} concerning constant GMP (100 mM) and concentration of GMP increases from 25 mM to 300 mM at a stable DNA concentration of 40 mg/mL.* ***(c)*** *Digital photographs of DNA-GMP*

hydrogel (dye loaded) with diverse shapes and ***(d)*** *thin membrane formation of the dye-loaded hydrogel. (scale bar 10 µm).*

The powder X-ray diffraction pattern of the lyophilized DNA-GMP hydrogel showed a diffraction peak at 2θ of 2.4° (d = 3.85 nm) and 2θ of 27.8° (d = 0.32 nm) corresponding to the diameter of a single G-tetrad and interplanar separation of G-tetrads through π- π stacking respectively **(Figure 2.9 a)**.*[43]* In the FT-IR spectra, the bands at 1218 cm^{-1} and 1067 cm^{-1} in GMP, corresponding to the P=O and P−O stretching bands of the phosphate groups, were significantly reduced in intensity in the DNA-GMP hydrogel suggesting the involvement of phosphate groups in extensive hydrogen bonding. Furthermore, the bands at 1687 cm^{-1} (C=O stretching) and 1600 cm^{-1} (N-H bending) in GMP were shifted to 1700 cm^{-1} and 1606 cm^{-1} respectively, suggesting the involvement of these functional groups of GMP in G-quadruplex formation **(Figure 2.9 b, c)**.*[44,45]* These studies confirmed that at higher concentration also similar mechanism follows, where, randomly coiled biomass DNA form ordered helical strands by wrapping around the π-π stacked G4 nano-strands, which entangle densely to form a porous network of hydrogel with absorbed water.*[46]*

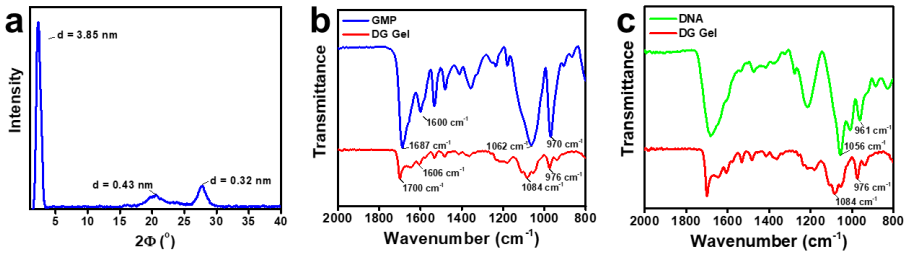


Figure 2.9. (a) *Powder X-Ray diffraction pattern of the dried DNA-GMP hydrogel.* ***(b)*** *FTIR spectra focusing on the 2000-600 cm^{-1} region to evaluate the shift of C=O peak from 1687 cm^{-1} to 1700 cm^{-1}, N-H bending peak from 1600 cm^{-1} to 1606 cm^{-1}, P=O peak of the phosphate group from 1062 cm^{-1} to 1084 cm^{-1} and P-O peak from 970 cm^{-1} to 976 cm^{-1} concerning GMP to the H-bonded self-assembled DNA-GMP gel.* ***(c)*** *the comparison of biomass DNA and DNA-GMP hydrogel at the region 2000-600 cm^{-1} region shows that the shift of P=O peak of phosphate groups from 1056 cm^{-1} to 1084 cm^{-1} and P-O peak of the same phosphate group from 961 cm^{-1} to 976 cm^{-1} was observed with respect to DNA the self-assembled DNA-GMP hydrogel was observed.*

The mechanical and viscoelastic properties of the prepared DNA-GMP hydrogel were evaluated via oscillatory rheological measurements. In the dynamic strain and frequency sweep studies, the storage modulus (G′) of the hydrogel was found to be several orders higher than the loss modulus (G″), indicating dominance of the elastic behaviour over its viscous nature **(Figure 2.10 a, b)**. Dynamic strain sweep measurements demonstrate the effect of GMP concentration (low, medium and high) on the mechanical properties of the DNA-GMP hydrogel. The storage modulus (G′) increases up to a GMP concentration of 150 mM, but decreases with further increases in concentration **(Figure 2.10 d)**. Therefore, the optimal GMP concentration for the DNA-GMP hydrogel, providing the best mechanical properties, is 150 mM. The physical integrity of the hydrogel was further assessed through a thixotropic loop test. At a low strain of 1%, the hydrogel shows elastic nature (G′ > G″), whereas, the viscous nature dominates upon increasing the strain to 500% (G″ > G′). The hydrogel was reverted back immediately to its original elastic state when the strain was reduced to 1% and this behaviour can be observed over several cycles **(Figure 2.10 c)**. This shows excellent injectability capabilities of the hydrogel. In addition, the self-healing properties of the DNA-GMP hydrogels were studied by adjoining the surfaces of two dye-doped pieces, as well as cut-and-rejoin experiment where a robust and healed hydrogel was obtained within 5 minutes, without any external energy input **(Figure 2.10 e, f, g)**. The stiffness and toughness of the healed hydrogel suggest that due to the involvement of non-specific supramolecular interactions such as H- bonding and π-π stacking, a quick recovery and fluidity of the hydrogel could be achieved.

The DNA-GMP hydrogel was converted into a sol upon heating at 50 °C, which could be reverted back to a gel upon cooling to 25 °C. This thermo-reversible behaviour could be observed over several cycles without any appreciable changes in their mechanical robustness **(Figure 2.10 g, h)**. The gel-to-sol transition, driven by temperature, can be linked to the dynamic reconfigurability of the DNA-GMP condensate,

suggesting that dynamic morphological changes significantly impact the self-assembly process. Further, a pH-responsive reversible sol-gel transition was observed in the DNA-GMP hydrogel. When the pH was increased to 12, the hydrogel was converted into a sol, which could be reverted back upon bringing the pH back to 5.5. This pH tuneable gel-sol transition could also be repeated over several cycles **(Figure 2.10 g, i)**. In a highly basic medium, the hydrogen-bonded G-quadruplex network is disrupted leading to a sol, which can be reformed under suitable acidic environment. As the fibril network was knitted through only weak interactions, the gel to sol transition can be easily altered by external stimuli like temperature and pH.

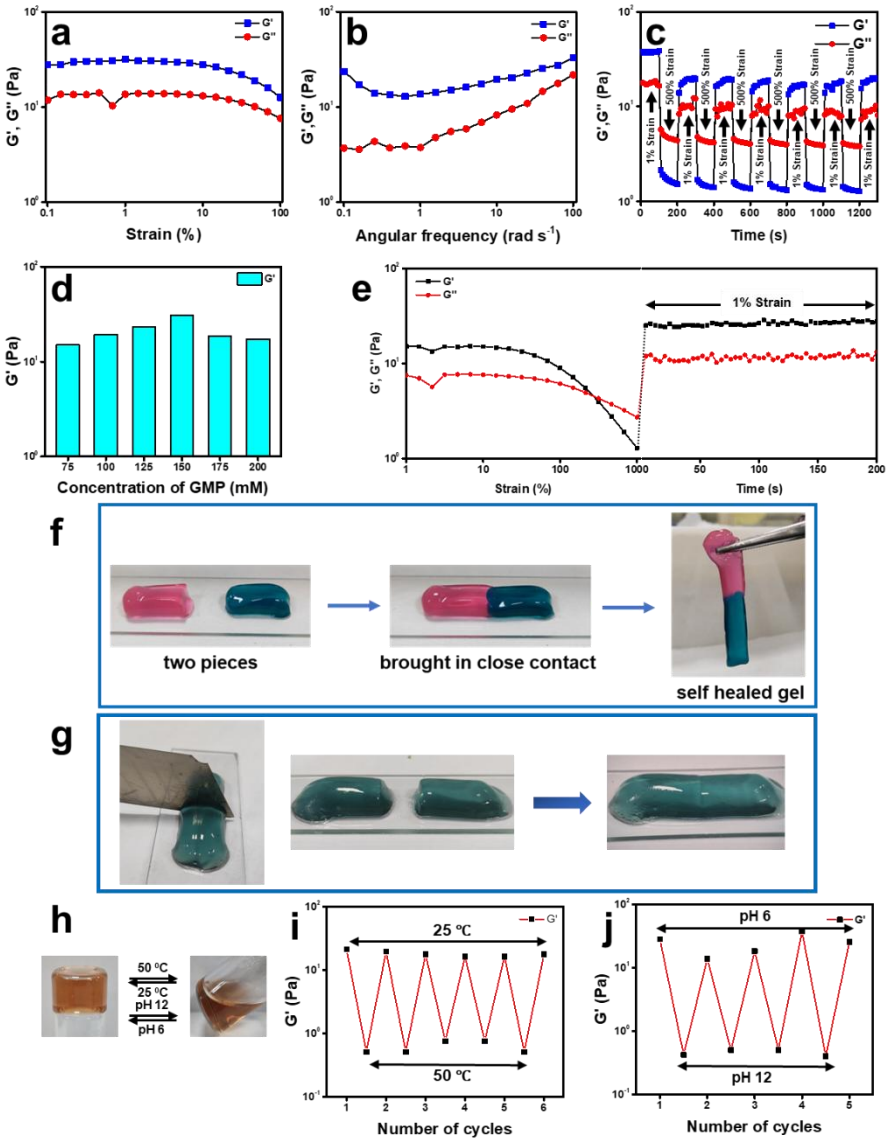


Figure 2.10. *Mechanical property investigations of the DNA-GMP hydrogel.* ***(a)*** *Dynamic strain-sweep rheological experiment of DNA-GMP hydrogel.* ***(b)*** *Angular frequency sweep experiment for the hydrogel at constant strain of 1%.* ***(c)*** *Thixotropic loop measurement for DNA-GMP hydrogel at a constant angular frequency of 10 rad s-1 with changing the strain from 1% to 500%.* ***(d)*** *Dynamic strain sweep measurements showing storage modulus (G) of DNA-GMP hydrogel at different concentration of GMP at a constant strain of 1%.* ***(e)*** *Strain sweep measurement (left) followed by immediate recovery from 1000% strain to 1% strain (right) of the DNA-GMP hydrogel at 25 °C.* ***(f, g)*** *Self-healing ability of the DNA-GMP hydrogel upon close contact via adhesion and cut-and-rejoin experiment,* ***(i)*** *Stimuli responsiveness of the DNA-GMP hydrogel upon temperature and pH,* ***(j)*** *Cyclic thermo-reversible rheological study of the hydrogel and* ***(k)*** *Cyclic pH-reversible rheological study of DNA-GMP hydrogel.*

2.2.3. Biocompatibility and Cytotoxicity of the DNA-GMP hydrogel

As the constituents of the hydrogel are all nucleic acids, it is expected that the hydrogel will show high biocompatibility. This was reflected in the IC_{50} values of GMP, DNA and DNA-GMP hydrogel which was 760 μM, 1814 μM, and 1496 μM respectively using AGS cells. Further, cell death studies assessed by IC_{10} values showed that the DNA-GMP gel imparted no toxicity on both AGS and A549 cells. DNA-GMP showed a significantly lesser apoptotic cells in both A549 ($p < 0.05$) and AGS ($p < 0.001$) cells in comparison to untreated cells, showing its biocompatible nature **(Figure 2.11 and 2.12)**.*[47]*

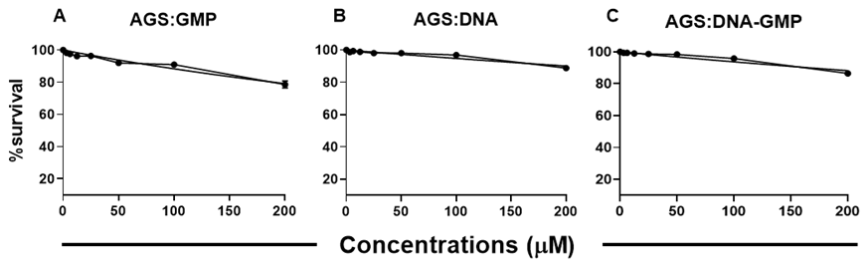


Figure 2.11. *Determination of cytotoxicity through MTT assay of (**A**) GMP, (**B**) DNA, (**C**) DNA-GMP, in AGS cells. Cell cytotoxicity was determined through MTT assay for 24 hr time point. 10,000 cells were seeded in 96 well plate. After 24 hours, cells were treated with different concentration of the compounds to check the cell viability.*

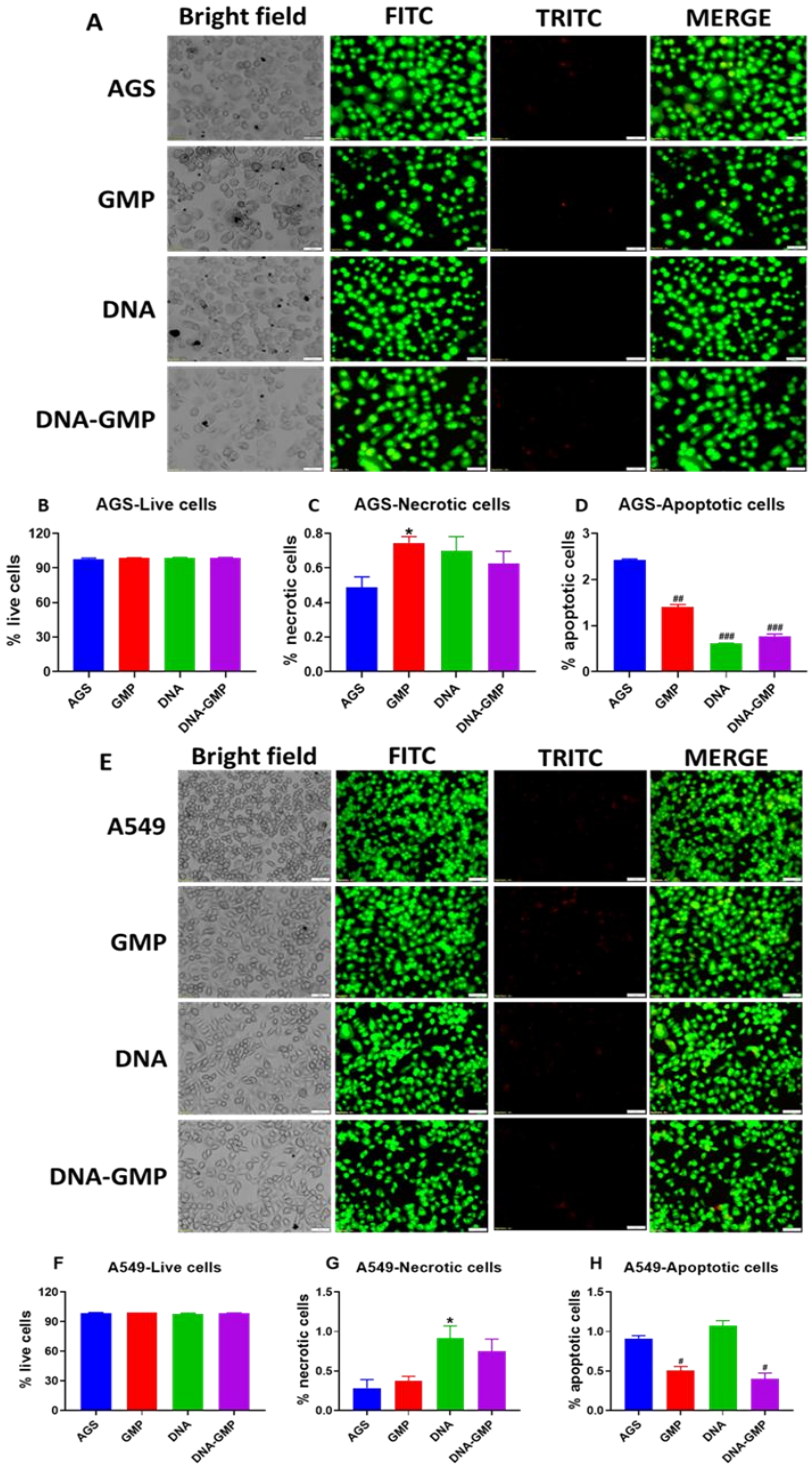


Figure 2.12. *Effect of different biocompatible compounds on the cell death of AGS and A549 cells.* ***A*** *&* ***E*** *A representative image showing live, necrotic and apoptotic cells with green, red, yellow color respectively as detected by acridine orange (AO)/ethidium bromide (EB) staining by fluorescence microscope. The bar graph represents the quantification of* ***B*** *Live,* ***C*** *Necrotic,* ***D*** *Apoptotic cells in AGS cells after 24 hours treatment,* ***F*** *Live,* ***G*** *Necrotic,* ***H*** *Apoptotic cells in A549 cells after 24 hours treatment. The experiment was performed for three biological replicates, and the*

*results are shown as the mean ± SD for two independent experiments. Data were statistically analysed using an unpaired t-test. p values were estimated using GraphPad Prism version 8, and p values of 0.05, 0.01, and 0.001 were considered statistically significant and represented by */#, **/##, and ***/###, denoting upregulation/downregulation respectively.*

2.2.4. DNA/GMP condensate hydrogel as a dense phase hydrotropic drug carrier

Supramolecular hydrogels derived from biomolecules hold potential as a drug carrier. Especially a noncanonical nucleic acid conformation such as G-quadruplex is found to be overrepresented in cancer containing genes and has been used as a valuable tool in cancer therapeutics.*[48-51]* Although both DNA and GMP are highly water soluble, the G-quadruplex can act as a hydrotropic system by trapping water insoluble molecules in the small cavities formed by vertically stacked guanine tetrads **(Figure 2.15 a)**.*[52-54]* Also, the dynamic reconfigurability and the excellent stimuli responsiveness of the hydrogel (**Figure 2.10**) provides alteration towards from fibrillar morphology to petal condensed microspheres which facilitates the ease for encapsulation and sustained release of drug molecules at physiological conditions. Therefore, we focused on using the DNA-GMP hydrogel as a drug carrying agent for both water-soluble and sparingly water-soluble drugs **(Figure 2.13)**.

We have studied two vitamins: (a) Vitamin B_2, riboflavin*[55]* and (b) Vitamin B_{12}, cyanocobalamin*[56]* as model water soluble drugs to be entrapped in the DNA-GMP hydrogel. Addition of vitamins, DNA and GMP in an aqueous medium, under physiological conditions resulted in the vitamin encapsulated hydrogels and after repeated washing, it was found that the hydrogel could encapsulate 86% and 78% of vitamin B_2 and B_{12} **(Table 2.1)**.

In order to establish the DNA-GMP hydrogel as a carrier for hydrophobic drugs, the loading of alkaloid drug molecule Piperine (with antimicrobial, antidepressant, anti-inflammatory, and anti-angiogenic and potential anti-cancer properties)*[57]*, fluoroquinolone-based drug

Ciprofloxacin (used for the treatment of bone and joint infections, intra-abdominal infections)*[58,59]* and Enoxacin (antibacterial agent used in the treatment of urinary tract infections and gonorrhea)*[60,61]* were studied. Mixing of the drug molecules, DNA and GMP in an aqueous medium and heating at 37 °C led to the drug loaded hydrogels. Although all these drug molecules were only sparingly soluble in water, however, they could be easily mixed in an aqueous medium containing DNA and GMP. After several washing cycles of the drug loaded hydrogel using PBS buffer, the encapsulation efficiency was estimated by UV-visible spectroscopy using calibration curves and was found to be 95%, 92% and 77% for Piperine, Ciproflaxacin and Enoxacin respectively **(Table 2.1)**. This in situ drug loading process in the hydrogel was highly efficient for different drug molecules and unbound drug molecules could be removed easily to avoid any side effects.

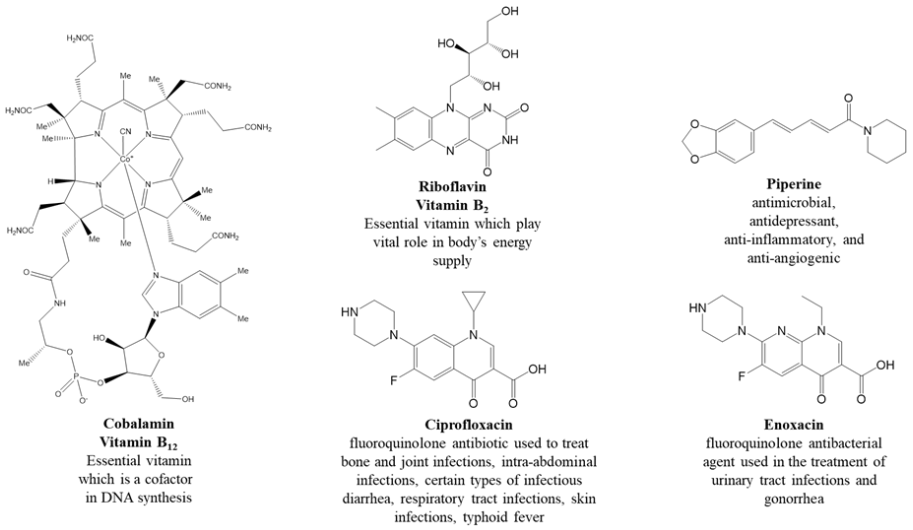


Figure 2.13. *Structure of the vitamins and drugs to study the loading and controlled release.*

Table 2.1. *Encapsulation Efficiencies of the Drug Molecules*					
Drug	**λ_{max} (nm)**	**Linear Eq.**	**Initial Concentration (C_1) (mg mL^{-1})**	**Unloaded Drug Concentration (C_1) (mg mL^{-1})**	**Encapsulation Efficiency $\frac{C_1 - C_2}{C_1} \times 100$ (%)**
Vitamin B_2	445	y = 1.87x + 0.08	0.0935	0.0133	85.69
Vitamin B_{12}	359	y = 0.77x + 0.05	0.2213	0.0489	77.89
Piperine	340	y = 0.99x + 0.04	0.099	0.0047	95.25
Ciprofloxacin	320	y = 0.96x + 0.01	0.7030	0.0591	91.6
Enoxacin	339	y = 0.51x + 0.04	0.783	0.1815	76.8

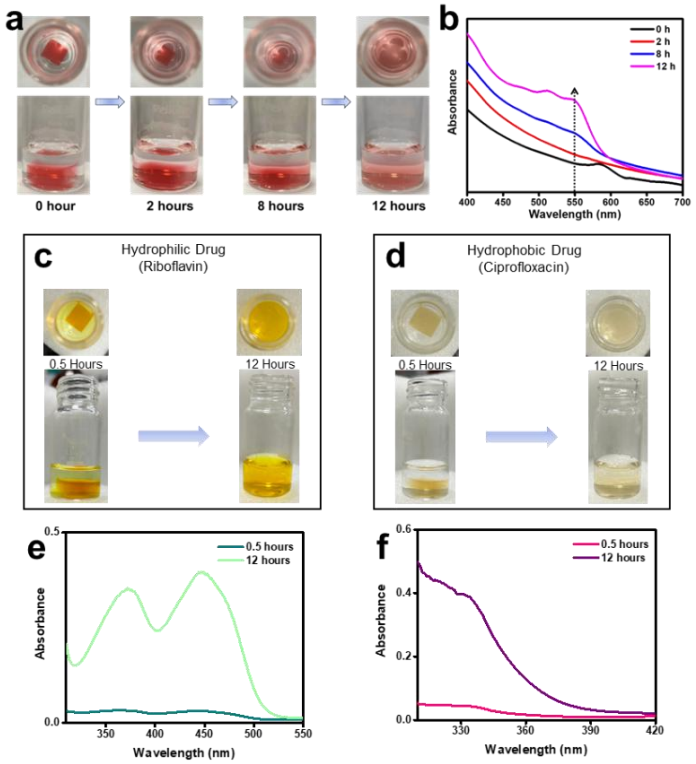


Figure 2.14. (a) *Digital photographs showing the diffusion behaviour of the drug (vitamin B_{12}) loaded hydrogel and releasing of drugs to buffer medium (PBS pH 7.4) at various time intervals and* ***(b)*** *corresponding UV curve of the supernatant buffer solution showing the increment of absorbance value of the corresponding peak at 550 nm for vitamin B_{12}. Diffusion mechanism and drug release behaviour for* ***(c)*** *and* ***(e)*** *hydrophilic drug (Riboflavin),* ***(d)*** *and* ***(f)*** *hydrophobic drug (Ciprofloxacin) showing that similar drug release mechanism by the DNA-GMP hydrogel for all the drugs.*

In a typical drug release experiment, all the drug loaded hydrogels (1mL) were separately covered with PBS buffer solution (3 mL, pH 7.4) and incubated at 37 °C. To determine the release at a regular time interval, an aliquot of 400 µL was collected and replaced with fresh buffer. A time-dependent drug release experiment was conducted to elucidate the drug delivery mechanism **(Figure 2.14 a, b)**. The results indicated a first-order, diffusion-based release, where the swelling of the fibrillar network enables the entrapped drug to diffuse into the buffer medium. Both hydrophilic and hydrophobic drugs exhibited similar sustained release profiles, suggesting that the hydrogel follows a consistent release mechanism for all drug types **(Figure 2.14 c, d, e, f)**.

Drug release profiles were monitored by UV-visible spectrophotometry at the absorption maxima of the respective drugs with the help of calibration curves **(Figure 2.15 b, c, e, f, h, i, k, l, n and o)**. The DNA-GMP hydrogel showed a sustained release of 81% and 91% of vitamin B_2 after 12 and 48 hours respectively **(Figure 2.15 d)**. On the other hand, a more sustained release of 73% after 12 hours and 87% after 48 hours were observed in case of much bulkier vitamin B_{12} **(Figure 2.15 g)**. In case of the hydrophobic therapeutic drug piperine, a sustained delivery was achieved with a release rate of 78.9% at 12 hours and 83.7% after 48 hours with DNA-GMP hydrogel **(Figure 2.15 j)**. Ciprofloxacin shows a sustained release profile of 64.3% at 12 hours and 74.2% after 48 hours, respectively **(Figure 2.15 m)**. Again, for the antibacterial drug enoxacin, a sustained release of 54% and 65% were obtained at 12 hours and 48 hours respectively **(Figure 2.15 p)**.

Drug-loaded hydrogel stability and the effect of drug molecules on bio-condensation were evaluated. SEM showed no significant morphological changes after drug loading (**Figure 2.16 a**), and mechanical properties remained comparable to the DNA-GMP hydrogel (**Figure 2.16 b**). Shelf-life and anti-leakage tests showed effective drug encapsulation for up to 28 days, with minimal leakage during weekly washes (**Figure 2.16 c, d**). Collectively, the hydrogel serves as an

efficient carrier for both water-soluble and sparingly soluble drugs via a diffusion mechanism, providing new impetus for sustained drug delivery.

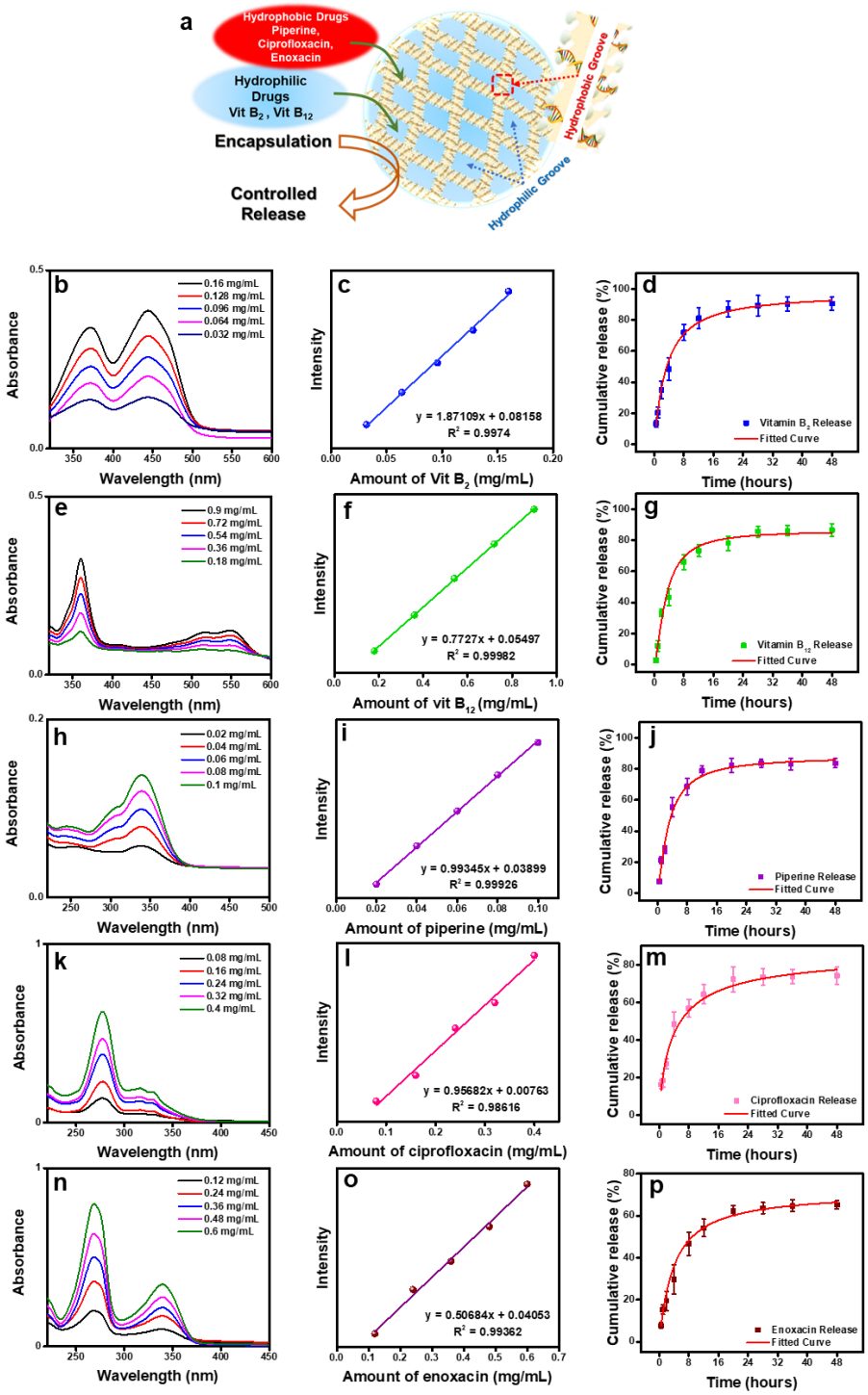


Figure 2.15. *DNA-GMP hydrogel as a hydrotropic drug carrier.* ***(a)*** *Diagram illustrating the site-specific encapsulation of hydrophobic and hydrophilic drugs within the DNA-GMP hydrogel fibres. UV-vis spectra of* ***(b)*** *vitamin* B_2, ***(e)*** *vitamin* B_{12}, ***(h)*** *piperine,* ***(k)*** *ciprofloxacin and* ***(n)*** *enoxacin in simulated body fluid (pH 7.4,*

phosphate buffer saline solution) at different concentrations. Calibration curves of ***(c)*** *vitamin* B_2, ***(f)*** *vitamin* B_{12}, ***(i)*** *piperine,* ***(l)*** *ciprofloxacin and* ***(o)*** *enoxacin. Release profiles of* ***(d)*** *vitamin* B_2, ***(g)*** *vitamin* B_{12}, ***(j)*** *piperine,* ***(m)*** *ciprofloxacin and* ***(p)*** *enoxacin, from drug loaded DNA-GMP hydrogel and corresponding polynomial fitting curves.*

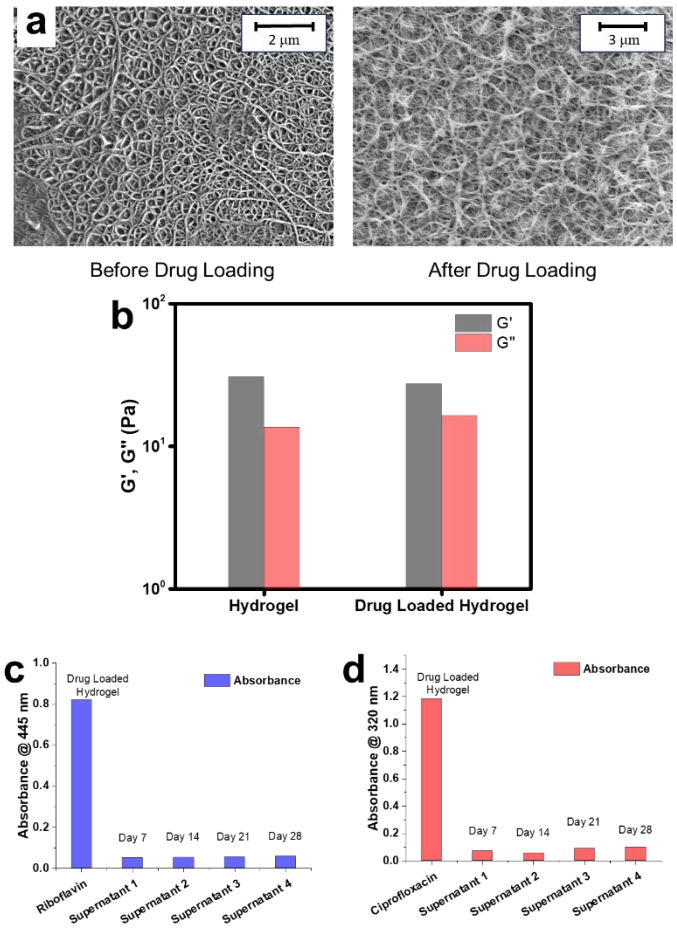


Figure 2.16. (a) *Morphological analysis of the hydrogel before and after drug loading showing that the bio-condensation does not get affected by the drug entrapment and* ***(b)*** *mechanical properties of the hydrogel and drug load loaded showing similar storage and loss modulus value. Shelf-life and anti-leakage activity of the hydrogel was shown by the UV-visible absorbance value of the drugs, showing* ***(c)*** *hydrophilic drug riboflavin and* ***(d)*** *hydrophobic drug ciprofloxacin for a time period of 28 days.*

2.2.5. The hydrogel enhances the antibacterial activity of the encapsulated drug

To demonstrate the drug-carrier capacity of the DNA-GMP hydrogel in real-time biological system, we conducted a systematic antibacterial assay using ciprofloxacin as a model drug. The antibacterial efficacy of ciprofloxacin (Cipro) and ciprofloxacin-loaded

DNA-GMP hydrogel (Cipro-gel) was tested against *E. coli* using a disc diffusion assay. Clear inhibition zones around the disks indicated that both formulations effectively inhibited bacterial growth. For pristine ciprofloxacin, the zone of inhibition increased with higher concentrations, with 0.5 µg showing a larger zone than the positive control, ampicillin. Similarly, for Cipro-gel, increasing the drug concentration enhanced the inhibition zone, with 0.5 µg showing greater inhibition than both the positive control ampicillin and ciprofloxacin alone **(Figure 2.17)**. These results suggest that encapsulating the drug in the DNA condensate hydrogel enhances its antibacterial efficacy, demonstrating that the DNA-GMP hydrogel serves as an excellent drug carrier with improved biological activity.

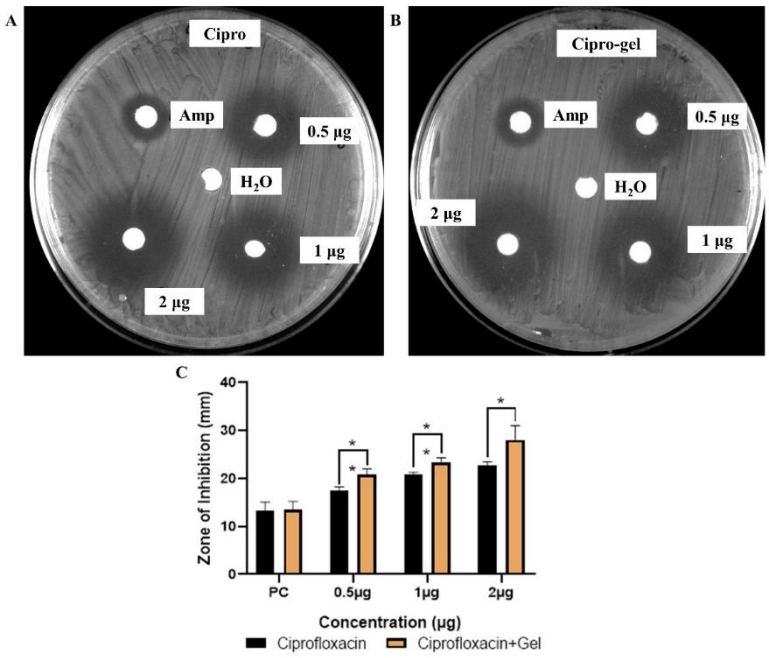


Figure 2.17. *Anti-bacterial activity of gel compound against E. coli.* ***A.*** *Representative clear zone of inhibition of Ciprofloxacin against E. coli,* ***B.*** *Representative clear zone of inhibition of Ciprofloxacin-gel against E. coli and* ***C****. Bar graph showing the antibacterial activity of the Cipro and Cipro-gel compound against E. coli. Cipro-gel possesses the significantly more anti-bacterial activity than positive control Ampicillin and other compound ciprofloxacin. The experiment was performed for three biological replicates, and the results are shown as the mean ± SD for two independent experiments. Data were statistically analysed using an unpaired t-test. p values were estimated using GraphPad Prism version 8, and p values of 0.05, 0.01, and 0.001 were*

*considered statistically significant and represented by */#, **/##, and ***/###, denoting upregulation/downregulation respectively.*

2.3. Conclusion

In conclusion, taking a cue from DNA condensation in chromatin, we have demonstrated a facile pathway for biomass DNA condensation through a simple mixing of DNA with a nucleotide guanosine monophosphate. The bio-condensate was formed through a synergistic effect, where the acidic nature of DNA induced the formation of G4 supramolecular structures. The randomly coiled DNA macromolecules wrapped around the stacked G-4 strands resulting in a helical fibrillar network. The spectroscopy and microscopy studies showed the concentration dependent self-assembled process leading to highly entangled network. At higher concentration of the nucleic acid constituents, a mechanically robust, stimuli-responsive and self-healable hydrogel could be obtained. The process can be extended to form an membranes, and composite hydrogels. Given the abundance of biomass DNA, this versatile, programmable, and biocompatible "all-nucleic" DNA-GMP hydrogel could serve as a sustainable alternative to petroleum-based polymers in the production of soft materials. The DNA-GMP hydrogel can function as a universal hydrotropic drug carrier, promoting a steady release of both hydrophobic and hydrophilic drugs. The bio-condensate and hydrogel formation using biomass DNA in the presence of GMP through non-covalent interactions paves away a simple methodology for soft material fabrication with application potential for advanced applications such as DNA switches and DNA-based machines. Using a similar protocol, the bio-condensation process can be extended to RNA, which we are currently pursuing.

2.4. Experimental Section

2.4.1. Synthesis and characterization of biomass DNA-GMP condensates

Mixing salmon milt DNA (40 μg/mL) with 150 μM of disodium guanosine monophosphate ($GMPNa_2$) in water yields a homogeneous, transparent solution. After incubating this solution at 37 °C for 12 hours, the formation of condensate is observed visually by using a simple red laser, which demonstrates a visible Tyndall effect. For further controlled experiments, condensates were prepared using the same protocol but with varying concentrations of GMP. These different GMP concentration condensates were then subjected to circular dichroism (CD) spectroscopy and field emission scanning electron microscopy (FE-SEM) imaging. For variable temperature studies, the condensate formed with 40 μg/mL DNA and 150 μM GMP was used. For steady-state fluorescence (FL) measurements, DNA-GMP condensates were prepared with varying concentrations of GMP, and all samples were incubated with 10 μM Thioflavin T (ThT) dye. The ThT-labelled condensates were excited at 425 nm for steady-state FL measurements. For confocal imaging, the same ThT-labelled condensates, prepared with different GMP concentrations, were drop-cast onto glass cover slips, and confocal microscopy was performed using a laser with an excitation wavelength of 405 nm. The zeta potential of the condensates was measured at various stoichiometric ratios, maintaining constant concentrations of DNA and GMP during condensation.

2.4.2. Synthesis of Biomass DNA hydrogel

For the synthesis of the DNA-GMP hydrogel, 40 mg of salmon test DNA was precisely dissolved in 1 mL of Mili-Q water, with gentle stirring and maintaining a constant heat of 37 ℃ resulting in a homogeneous solution. Following 5 minutes of stirring, 61.2 mg (150 mM) of Guanosine Monophosphate Disodium Salt was added to the solution. The solution promptly transformed into a transparent, light brown colour. Within 2-3 minutes of cooling to room temperature, a

transparent DNA-GMP hydrogel was obtained. The confirmation of hydrogel formation was obtained through the simple inverse tube method.

2.4.3. Mechanical properties studies

The rheological investigations of synthesized hydrogels were performed using a parallel plate geometry of diameter 25 mm. The dynamic strain sweep measurements were taken at a constant angular frequency (ω) of 10 $rads^{-1}$ and frequency sweep experiments of hydrogel was measured at a constant strain (γ) value of 1% at 25 °C. The thixotropic step-strain measurements with respect to time intervals were carried out at variable strain values of 0.1% and 500% at a constant 10 $rads^{-1}$ of ω.

Two different dye loaded gels each of 2 mL synthesized inside rectangular molds. After aging, both dye-loaded hydrogels were taken close to each other joined using mild mechanical press and after 5 minutes the self-healed hydrogel could be lifted in air. The storage modulus (G′) values of the original and self-healed gel were calculated at 1% constant strain. The dynamic sweep test followed by time dependent storage and loss modulus calculation at a constant strain at 1% was also evaluated to confirm the self-healing ability.

To obtain the thermo-reversibility property of the hydrogel, the gel was heated homogeneously at 50 ℃ to form a solution and evaluated the mechanical strength. Same gel was cooled down to room temperature to reversible formation of gel and evaluated the mechanical properties. To study the effect of the pH-reversibility, 5 µL of 4M NaOH solution was added that increases the pH of the medium to 12. The hydrogel was completely dissociated to sol state within 5 minutes. The sol was converted into a gel upon addition of 5 µL of 4M H_2SO_4 (pH 5.5) and this reversible sol-gel transition could be obtained for 4 cycles.

2.4.4. In-Vitro biocompatibility test

- **Mammalian Cell Culture**

A549 (human lung adenocarcinoma) and AGS (human gastric adenocarcinoma) cells were cultured in Dulbecco's minimal essential medium (DMEM) supplemented with 10% fetal bovine serum (FBS) and 1% antibiotic and antimycotic solution. Cells were cultured at 37 °C in a humidified incubator at 5% CO_2. Compounds for treatment were prepared in DMEM supplemented with 10% FBS.

- **Cell Viability Assay**

For the MTT assay, about 10,000 cells per well were seeded in 96-well plates and incubated for 24 h. Further, cells were treated with different concentrations of GMP, DNA, and DNA-GMP for 24 h. Subsequently, media was extracted from the wells, and 50 µL per well of MTT dye (0.5 mg/mL in PBS) was added and incubated for 3 h at 37 °C. Next, 100 µL of DMSO was added to each well, and absorbance at 570 nm was recorded using a microplate reader.

- **EB-AO staining**

The assessment of the apoptotic, necrotic, and live cells after exposure to compounds was done by EB/AO dual staining. The cells were stained with acridine orange and ethidium bromide mixture (100 µg/ml each) for 20 min at 37 ˚C followed by PBS washing by PBS. The analysis of the cell stage (apoptotic/ necrotic) was done manually by observing the color characteristics.

- **Statistical analysis**

All the experimental results were recorded from a set of triplicates. Data were statistically tested using an unpaired t-test. p values were estimated using GraphPad Prism version 8, and p values of 0.05, 0.01, and 0.001 were considered statistically significant and represented by */#, **/##, and ***/###, respectively.

2.4.5. Drug loading and encapsulation efficiency

A 1 mg mL^{-1} aqueous solution comprising Riboflavin (vitamin B_2), Cobalamin (vitamin B_{12}), piperine, ciprofloxacin, and enoxacin was prepared through continuous stirring. To this solution containing the drug molecules, biomass DNA was added, followed by the gradual addition of GMP-Na_2 at the same concentration (40 mg mL^{-1} for DNA and 150 mM for GMP), while maintaining a constant temperature of 37 ℃. After a cooling and aging period of 10 minutes, self-standing stable drug loaded hydrogels were successfully formed. These hydrogels were subsequently employed for investigating the encapsulation and sustained drug release behavior of the hydrogel. 1 mg mL^{-1} of drug-dissolved solution was used for the preparation of the hydrogel. To remove the unbound drug molecules, the hydrogel was washed with 3 mL of pH 7.4 PBS solution. The absorbance of washed supernatant was measured using a UV-vis spectrophotometer. The amount of vitamin or drug molecules encapsulated inside the hydrogel matrix was estimated by subtracting the vitamin or drug present in the supernatant buffer from the amount taken initially, and the loading percentage was calculated using the following equation:

$$\text{Encapsulation efficiency (\%)} = \frac{\text{Amount of Vit/Drug present after washing}}{\text{Initial amount of Vit/Drug}} \times 100$$

To study the sustained release profile of vitamin and piperine-loaded hydrogels, 1 mL of vitamin and piperine-loaded hydrogels were taken in three separate glass vials, and 3 mL of phosphate buffer saline solution (10 mM PBS, pH 7.4) was added. All three vials were incubated at 37 ℃. At different time intervals, a small aliquot of 400 µL was removed and collected separately from each vial and fresh PBS solution of same amount of 400 µL was added to each vial. The absorbance of collected samples was measured at the wavelength of 445 nm, 550 nm, 340 nm, 320 nm and 339 nm for vitamin B_2, vitamin B_{12}, piperine, ciprofloxacin and enoxacin, respectively, using a UV-vis spectrophotometer. To ascertain the accuracy, the experiments were performed three times and the average value with an error bar was

plotted to the sustained drug release profile. The calculation for the cumulative release of the drug is shown below,

$$\text{The cumulative release of drug} = \frac{M_t}{M_\infty} \times 100$$

Where M_t and M_∞ are the amount of drug released at time t and the initial quantity of drug encapsulated inside the hydrogel, respectively. From the calibration curve of each vitamin and drug, we got a linear relation between the concentration (amount) and absorbance value. Therefore, for the simplicity of calculation, we have taken the absorbance value directly to calculate the cumulative release of the drug.

To evaluate the shelf-life and anti-leakage properties of the drug-loaded hydrogel, samples were stored at 4°C. At fixed intervals over a 28-day period, the hydrogels were washed with PBS buffer, and drug leakage was monitored by measuring the UV-visible absorbance of the supernatant.

2.4.6. Antibacterial activity

- **Bacterial strain**

A gram-negative bacterial strain was used to check for antibacterial activity of the compounds. *Escherichia coli* (DH5α) was used in this study. *E. coli* was cultured in Luria Broth agar (Becton, Dickinson and Company, New Jersey, USA) and incubated at 37 °C for 12 h. Pure colonies were picked up and cultured in Luria broth media (Becton, Dickinson and Company, New Jersey, USA) overnight in a rotary shake of 220 rpm at 37 °C.

- **Disc Diffusion Method**

The antimicrobial activity of gel compounds against the gram-negative bacterial strain was monitored with the disk diffusion method.*[66,67]* The E. coli strain was spread on the LB agar plate. The Ciprofloxacin compound and Ciprofloxacin loaded DNA-GMP hydrogel compound was dissolved in H_2O. The different compound concentration was used 0.5, 1, and 2 µg, 10 µl of each solution was impregnated into sterile,

blank discs of 6 mm in diameter. H_2O was used as negative control. Ampicillin (Himedia, India) (100 μg/μl) were used as positive control in E. coli. The plate was incubated at 37 ^oC for 24 h in their respective conditions and the zone of inhibition was measured. Antimicrobial activity was determined by measuring the zone of inhibition diameter (mm) around the discs. The assay was performed twice.

2.5. References

1. Netzer, A., Katzir et al. (2023), Emergent properties of melanin-inspired peptide/RNA condensates, Proc. Natl. Acad. Sci. U. S. A., 120, e2310569120 (DOI: 10.1073/pnas.2310569120.)
2. Lampel, A. (2020), Biology-Inspired Supramolecular Peptide Systems, Chem, 6, 1222–1236 (DOI: 10.1016/j.chempr.2020.03.005.)
3. Boisvert, F.-M., van Koningsbruggen et al. (2007), The multifunctional nucleolus, Nat Rev Mol Cell Biol, 8, 574–585 (DOI: 10.1038/nrm2184.)
4. Brangwynne, C.P. (2013), Phase transitions and size scaling of membrane-less organelles, J. Cell Biol., 203, 875–881 (DOI: 10.1083/jcb.201308087.)
5. Brangwynne, C.P., Eckmann et al. (2009), Germline P Granules Are Liquid Droplets That Localize by Controlled Dissolution/Condensation, Science, 324, 1729–1732 (DOI: 10.1126/science.1172046.)
6. Fyodorov, D.V., Zhou et al. (2018), Emerging roles of linker histones in regulating chromatin structure and function, Nat Rev Mol Cell Biol, 19, 192–206 (DOI: 10.1038/nrm.2017.94.)
7. Zhou, K., Gaullier et al. (2019), Nucleosome structure and dynamics are coming of age, Nat Struct Mol Biol, 26, 3–13 (DOI: 10.1038/s41594-018-0166-x.)

8. Kornberg, R.D. (1974), Chromatin Structure: A Repeating Unit of Histones and DNA, Science, 184, 868–871 (DOI: 10.1126/science.184.4139.868.)
9. Kornberg, R.D., Thomas et al. (1974), Chromatin Structure: Oligomers of the Histones, Science, 184, 865–868 (DOI: 10.1126/science.184.4139.865.)
10. Longstreet, A.R., McQuade et al. (2013), Organic Reaction Systems: Using Microcapsules and Microreactors to Perform Chemical Synthesis, Acc. Chem. Res., 46, 327–338 (DOI: 10.1021/ar300144x.)
11. Krinsky, N., Kaduri et al. (2018), Synthetic Cells Synthesize Therapeutic Proteins inside Tumors, Adv. Healthc. Mater., 7, 1701163 (DOI: 10.1002/adhm.201701163.)
12. Veis, A. (2011), A review of the early development of the thermodynamics of the complex coacervation phase separation, Adv. Colloid Interface Sci., 167, 2–11 (DOI: 10.1016/j.cis.2011.01.007.)
13. King, J.T., Shakya et al. (2021), Phase separation of DNA: From past to present, Biophys. J., 120, 1139–1149 (DOI: 10.1016/j.bpj.2021.01.033.)
14. Landenmark, H.K.E., Forgan et al. (2015), An Estimate of the Total DNA in the Biosphere, PLOS Biol., 13, e1002168 (DOI: 10.1371/journal.pbio.1002168.)
15. Bar-On, Y.M., Phillips et al. (2018), The biomass distribution on Earth, Proc. Natl. Acad. Sci. U. S. A., 115, 6506–6511 (DOI: 10.1073/pnas.1711842115.)
16. Lee, J.B., Peng et al. (2012), A mechanical metamaterial made from a DNA hydrogel, Nat. Nanotech., 7, 816–820 (DOI: 10.1038/nnano.2012.211.)
17. Um, S.H., Lee et al. (2006), Enzyme-catalysed assembly of DNA hydrogel, Nat. Mater., 5, 797–801 (DOI: 10.1038/nmat1741.)
18. Meng, H.-M., Zhang et al. (2014), DNA Dendrimer: An Efficient Nanocarrier of Functional Nucleic Acids for Intracellular

Molecular Sensing, ACS Nano, 8, 6171–6181 (DOI: 10.1021/nn5015962.)

19. Lv, J., Dong et al. (2020), Programmable DNA Nanoflowers for Biosensing, Bioimaging, and Therapeutics, Chem. Euro. J, 26, 14512–14524 (DOI: 10.1002/chem.202002242.)
20. Park, S.Y., Lytton-Jean et al. (2008), DNA-programmable nanoparticle crystallization, Nature, 451, 553–556 (DOI: 10.1038/nature06508.)
21. Li, Z., Liu et al. (2019), Making Engineered 3D DNA Crystals Robust, J. Am. Chem. Soc., 141, 15850–15855 (DOI: 10.1021/jacs.9b06613.)
22. Hong, F., Zhang et al. (2017), DNA Origami: Scaffolds for Creating Higher Order Structures, Chem. Rev., 117, 12584–12640 (DOI: 10.1021/acs.chemrev.6b00825.)
23. Yue, L., Wang et al. (2020), Nucleic Acid Based Constitutional Dynamic Networks: From Basic Principles to Applications, J. Am. Chem. Soc., 142, 21577–21594 (DOI: 10.1021/jacs.0c09891.)
24. Rhodes, D., Lipps et al. (2015), G-quadruplexes and their regulatory roles in biology, Nucleic Acids Res., 43, 8627–8637 (DOI: 10.1093/nar/gkv862.)
25. Wang, D., Cui et al. (2020), Transformation of Biomass DNA into Biodegradable Materials from Gels to Plastics for Reducing Petrochemical Consumption, J. Am. Chem. Soc., 142, 10114–10124 (DOI: 10.1021/jacs.0c02438.)
26. Han, J., Guo et al. (2021), Sustainable Bioplastic Made from Biomass DNA and Ionomers, J. Am. Chem. Soc., 143, 19486–19497 (DOI: 10.1021/jacs.1c08888.)
27. Nayak, S., Kumar et al. (2022), Biomass derived self-assembled DNA-dot hydrogels for enhanced bacterial annihilation, Nanoscale, 14, 16097–16109 (DOI: 10.1039/D2NR03810B.)
28. Shin, M., Ryu et al. (2015), DNA/Tannic Acid Hybrid Gel Exhibiting Biodegradability, Extensibility, Tissue Adhesiveness,

and Hemostatic Ability, Adv. Funct. Mater., 25, 1270–1278 (DOI: 10.1002/adfm.201403992.)

29. Dong, J., O'Hagan et al. (2022), Switchable and dynamic G-quadruplexes and their applications, Chem. Soc. Rev., 51, 7631–7661 (DOI: 10.1039/D2CS00317A.)
30. Davis, J.T. (2004), G-Quartets 40 Years Later: From 5′-GMP to Molecular Biology and Supramolecular Chemistry, Angew. Chem. Int. Ed., 43, 668–698 (DOI: 10.1002/anie.200300589.)
31. Chakraborty, A., Ravi et al. (2021), Harnessing the physicochemical properties of DNA as a multifunctional biomaterial for biomedical and other applications, Chem. Soc. Rev., 50, 7779–7819 (DOI: 10.1039/D0CS01387K.)
32. Chantot, J.F., Sarocchi et al. (1971), Physico-chemical properties of nucleosides: 4, — Gel formation by guanosine and its analogues. Biochimie, 53, 347–354 (DOI: 10.1016/S0300-9084(71)80101-3.)
33. del Villar-Guerra, R., Trent et al. (2018), G-Quadruplex Secondary Structure Obtained from Circular Dichroism Spectroscopy, Angew. Chem. Int. Ed., 57, 7171–7175 (DOI: 10.1002/anie.201709184.)
34. Chen, J., Gao et al. (2021), Kinetic control of chirality and circularly polarized luminescence in G-quartet materials, J. Mater. Chem. B, 9, 7140–7144 (DOI: 10.1039/D1TB00683E.)
35. Adrian, M., Heddi et al. (2012), NMR spectroscopy of G-quadruplexes, Methods, 57, 11–24 (DOI: 10.1016/j.ymeth.2012.05.003.)
36. Gao, M., Harish et al. (2017), Temperature and pressure limits of guanosine monophosphate self-assemblies, Sci Rep, 7, 9864 (DOI: 10.1038/s41598-017-10689-0.)
37. Renaud de la Faverie, A., Guédin et al. (2014), Thioflavin T as a fluorescence light-up probe for G4 formation, Nucleic Acids Res., 42, e65 (DOI: 10.1093/nar/gku111.)

38. Mohanty, J., Barooah et al. (2013), Thioflavin T as an Efficient Inducer and Selective Fluorescent Sensor for the Human Telomeric G-Quadruplex DNA, J. Am. Chem. Soc., 135, 367–376 (DOI: 10.1021/ja309588h.)
39. Bhasikuttan, A.C., Mohanty et al. (2015), Targeting G-quadruplex structures with extrinsic fluorogenic dyes: promising fluorescence sensors, Chem. Commun., 51, 7581–7597 (DOI: 10.1039/C4CC10030A.)
40. Zanchetta, G., Nakata et al. (2008), Phase separation and liquid crystallization of complementary sequences in mixtures of nanoDNA oligomers, Proc. Natl. Acad. Sci. U. S. A., 105, 1111–1117 (DOI: 10.1073/pnas.0711319105.)
41. Nakata, M., Zanchetta et al. (2007), End-to-End Stacking and Liquid Crystal Condensation of 6– to 20–Base Pair DNA Duplexes, Science, 318, 1276–1279 (DOI: 10.1126/science.1143826.)
42. Zhu, G., Hu et al. (2013), Noncanonical Self-Assembly of Multifunctional DNA Nanoflowers for Biomedical Applications, J. Am. Chem. Soc., 135, 16438–16445 (DOI: 10.1021/ja406115e.)
43. Thakur, N., Chaudhary et al. (2021), Ion Conductive Phytic Acid-G Quadruplex Hydrogel as Electrolyte for Flexible Electrochromic Device, ChemNanoMat, 7, 613–619 (DOI: 10.1002/cnma.202100072.)
44. Zuber, G., Prestrelski et al. (1992), Application of Fourier transform infrared spectroscopy to studies of aqueous protein solutions, Anal. Biochem., 207, 150–156 (DOI: 10.1016/0003-2697(92)90516-A.)
45. Gabelica, V., Rosu et al. (2008), Infrared Signature of DNA G-Quadruplexes in the Gas Phase, J. Am. Chem. Soc., 130, 1810–1811 (DOI: 10.1021/ja077321w.)
46. Zhang, H., Grinstaff et al. (2014), Recent Advances in Glycerol Polymers: Chemistry and Biomedical Applications, Macromol.

Rapid Commun., 35, 1906–1924 (DOI: 10.1002/marc.201400389.)

47. Jakhmola, S., Jha et al. (2021), Glial cell response to Epstein-Barr Virus infection: A plausible contribution to virus-associated inflammatory reactions in the brain, Virology, 559, 182–195 (DOI: 10.1016/j.virol.2021.04.005.)
48. Carvalho, J., Mergny et al. (2020), G-quadruplex, Friend or Foe: The Role of the G-quartet in Anticancer Strategies, Trends Mol. Med., 26, 848–861 (DOI: 10.1016/j.molmed.2020.05.002.)
49. Kosiol, N., Juranek et al. (2021), G-quadruplexes: a promising target for cancer therapy, Mol. Cancer., 20, 40 (DOI: 10.1186/s12943-021-01328-4.)
50. Bates, P.J., Reyes-Reyes et al. (2017), G-quadruplex oligonucleotide AS1411 as a cancer-targeting agent: Uses and mechanisms, Biochimica et Biophysica Acta (BBA) - General Subjects, 1861, 1414–1428 (DOI: 10.1016/j.bbagen.2016.12.015.)
51. Li, K., Yatsunyk et al. (2021), Water spines and networks in G-quadruplex structures, Nucleic Acids Res., 49, 519–528 (DOI: 10.1093/nar/gkaa1177.)
52. Li, J., Jin et al. (2011), Identification of nonplanar small molecule for G-quadruplex grooves: Molecular docking and molecular dynamic study, Bioorg. Med. Chem. Lett., 21, 6969–6972 (DOI: 10.1016/j.bmcl.2011.09.125.)
53. Xiao, F., Chen et al. (2020), Hydrophobic Interaction: A Promising Driving Force for the Biomedical Applications of Nucleic Acids, Adv. Science, 7, 2001048 (DOI: 10.1002/advs.202001048.)
54. Spiegel, J., Adhikari et al. (2020), The Structure and Function of DNA G-Quadruplexes, Trends Chem., 2, 123–136 (DOI: 10.1016/j.trechm.2019.07.002.)

55. Masschelin, P.M., Saha et al. (2023), Vitamin B2 enables regulation of fasting glucose availability, eLife, 12, e84077 (DOI: 10.7554/eLife.84077.)
56. Green, R., Allen et al. (2017), Vitamin B12 deficiency, Nat Rev Dis Primers, 3, 1–20 (DOI: 10.1038/nrdp.2017.40.)
57. Tiwari, A., Mahadik et al. (2020), Piperine: A comprehensive review of methods of isolation, purification, and biological properties, Med. Drug Discov., 7, 100027 (DOI: 10.1016/j.medidd.2020.100027.)
58. Mason, D.J., Power et al. (1995), Antibacterial action of ciprofloxacin, Antimicrobial Agents and Chemotherapy, 39, 2752–2758 (DOI: 10.1128/aac.39.12.2752.)
59. Vance-Bryan, K., Guay et al. (1990), Clinical Pharmacokinetics of Ciprofloxacin, Clin Pharmacokinet, 19, 434–461 (DOI: 10.2165/00003088-199019060-00003.)
60. Henwood, J.M., Monk et al. (1988), Enoxacin, Drugs, 36, 32-66 (DOI: 10.2165/00003495-198836010-00004.)
61. Melo, S., Villanueva et al. (2011), Small molecule enoxacin is a cancer-specific growth inhibitor that acts by enhancing TAR RNA-binding protein 2-mediated microRNA processing, Proc. Natl. Acad. Sci. U. S. A., 108, 4394–4399 (DOI: 10.1073/pnas.1014720108.)
62. Taladriz-Blanco, P., Buurma et al. (2011), Reversible assembly of metal nanoparticles induced by penicillamine, Dynamic formation of SERS hot spots. J. Mater. Chem., 21, 16880–16887 (DOI: 10.1039/C1JM12175H.)
63. Piao, J., Zhou et al. (2018), Colorimetric human papillomavirus DNA assay based on the retardation of avidin-induced aggregation of gold nanoparticles, Microchim Acta, 185, 537 (DOI: 10.1007/s00604-018-3065-2.)
64. Franke, M., Leubner et al. (2017), Immobilization of pH-sensitive CdTe Quantum Dots in a Poly(acrylate) Hydrogel for

Microfluidic Applications, Nanoscale Res Lett, 12, 314 (DOI: 10.1186/s11671-017-2069-x.)

65. Zhou, Y., Damasceno et al. (2018), Unusual multiscale mechanics of biomimetic nanoparticle hydrogels, Nat Commun, 9, 181 (DOI: 10.1038/s41467-017-02579-w.)
66. Ngamsurach, P., Praipipat et al. (2022), Antibacterial activities against Staphylococcus aureus and Escherichia coli of extracted Piper betle leaf materials by disc diffusion assay and batch experiments, RSC Adv., 12, 26435–26454 (DOI: 10.1039/D2RA04611C.)
67. Razmavar, S., Abdulla et al. (2014), Antibacterial Activity of Leaf Extracts of Baeckea frutescens against Methicillin-Resistant Staphylococcus aureus, BioMed Res. Int., 2014, 521287 (DOI: 10.1155/2014/521287.)

Chapter 3

3. Minimalist Structural Tunability in G-Quadruplex-Driven Biomass DNA Hydrogel Enables Multiple Programmable Drug Release Regimes for Anticancer Therapeutics

3.1. Introduction

Controlled drug delivery is a cornerstone of modern therapeutic design, aimed at achieving precise spatial and temporal regulation of drug release while maintaining effective concentrations at target sites and minimizing systemic exposure.*[1-4]* This control is vital in chemotherapy, where potent cytotoxic drugs have narrow therapeutic windows and often cause severe off-target toxicity.*[5,6]* Uncontrolled burst release can damage healthy tissues, while insufficient or fluctuating release compromise efficacy.*[7-9]* Therefore, delivery systems capable of predictable and sustained release are essential for improving both safety and therapeutic outcomes.*[10]* Classical drug release models, such as, first-order, Higuchi, and zero-order kinetics, establish fundamental frameworks for understanding controlled release.*[11,12]* First-order kinetics generate concentration-dependent release with an initial burst followed by rapid depletion, limiting suitability for prolonged therapy. The Higuchi model, based on diffusion from porous matrices, offers improved predictability but associated with constant diffusivity, uniform drug distribution, and minimal swelling, restricting its validity for long-term therapeutics. Zero-order release, on the other hand, provides constant, concentration-independent release and stable drug levels, minimizing side effects.*[13,14]* However,

achieving true zero-order kinetics requires sophisticated architectures or engineered diffusion barriers, posing materials design challenges.*[15]*

Numerous synthetic and bio-derived carriers have been developed to control drug release kinetics. Despite their structural diversity, most of the synthetic carriers rely on a single dominant release mechanism, limiting tunability and predictability.*[16-19]* Their uniform microstructure makes it tedious to control the diffusion or swelling-based release under physiological conditions. Consequently, rational designing of delivery systems with controllable and predictable kinetics remains a major challenge. A desirable goal is to develop a universal platform with tunable molecular architecture, where the release kinetics can be systematically modulated via minimalistic microstructural alterations.*[20,21]* This will facilitate a single matrix to be transformed into multiple states, each associated with distinct diffusion or swelling mechanism, offers a promising route toward programmable drug delivery. While synthetic polymeric materials have been extensively explored, issues related to long-term biocompatibility, degradation products, and cytotoxicity persist.*[22,23]* In contrast, bio-derived carriers such as reversible aggregates, hydrogels and liposomes etc. address these limitations through intrinsic biodegradability and physiological compatibility.*[17,24]* Among them, supramolecular nanofibrillar hydrogels have drawn particular attention as drug delivery platforms due to their dynamic and reconfigurable networks, tunable mechanics, and stimuli-responsive diffusion behavior. Their structural similarity to biological tissues and controllable assembly makes them adaptable to complex biomedical environments.*[25-27]* DNA, a naturally abundant and programmable biomolecule, serves as an especially attractive building block for hierarchical systems. Beyond its genetic role, DNA functions as a structural polymer capable of organizing into diverse supramolecular architectures, including hydrogels, hierarchical networks, and crystalline assemblies, while retaining intrinsic biocompatibility and scalability.*[28-30]* Spontaneous condensation of biomass-derived DNA with 5′-guanosine

monophosphate (5′-GMP) induces G-quadruplex formation, leading to helically stacked nanofibrillar assemblies that further resulted into an "all-nucleic" hydrogel, as demonstrated in our previous chapter.*[31]* Although this hydrogel exhibits excellent hydrotropic character, its drug release kinetics predominantly follow a first-order profile with limited tunability.*[31,32]*

In this chapter, a tunable DNA-GMP hydrogel platform is introduced in which controlled microstructural modulation directs mechanical strength, degradation, and drug release kinetics. Two distinct hydrogel variants are engineered through simple structural interventions: (i) substituting water with a glycerol-water co-solvent enhances fibrillar alignment and network density, improving mechanical robustness and retarding drug diffusion; and (ii) incorporating divalent Ca^{2+} ions crosslink the nanofibers, introducing partial crystallinity and markedly increasing stiffness. Together, these modifications enable predictable tuning of release behavior spanning first-order diffusion, Higuchi-type slow release, and zero-order kinetics, all within a single biocompatible, nucleic acid-derived scaffold. The resulting hydrogels further exhibit broad pH stability, stimuli-responsiveness, injectability, and amphiphilic character, rendering them well-suited for anticancer drug delivery.

Further, the versatility of these platforms is demonstrated through encapsulation and sustained release of both hydrophilic and hydrophobic anticancer drugs. Doxorubicin, a water-soluble topoisomerase II inhibitor, serves as the hydrophilic model,*[33,34]* while camptothecin (CPT), a potent but poorly water-soluble topoisomerase I inhibitor, served as a challenging hydrophobic model drug. While several CPT analogues have reached clinical use, improving delivery of the parent hydrophobic CPT molecule remains highly desirable.*[35-37]* The DNA-GMP hydrogels act as effective hydrotropic carriers, enabling efficient CPT encapsulation, enhanced stability, and prolonged release. Beyond physicochemical performance, in vitro and

ex vivo studies confirm sustained drug activity with reduced off-target toxicity, underscoring biocompatibility and physiological relevance. Overall, these findings establish tunable nucleic acid-based hydrogels as a versatile, sustainable platform for precisely regulated anticancer drug delivery.

3.2. Results and Discussions

3.2.1. Synthetic Strategy of Hydrogels

The hydrogel systems were designed using a minimal, structure-driven supramolecular strategy based on biomolecular condensation between biomass-derived DNA and 5′-guanosine monophosphate (5′-GMP). The self-assembly of 5′-GMP proceeds through Hoogsteen hydrogen bonding, leading to the formation of G-quadruplex (G4) stacks.*[38,39]* As demonstrated in our previous work, biomass DNA promotes this condensation by providing a mildly acidic environment and by wrapping around the columnar G4 assemblies, yielding helically organized DNA-GMP nanofibers. Progressive association of these fibrils generates a three-dimensional, non-covalently crosslinked "all-nucleic" hydrogel (DG) (**Figure 3.1A**).*[31]* While the pristine DG hydrogel exhibits excellent stability and dynamic reconfigurability, its swelling and diffusion behavior leads to predominantly first-order drug release. To introduce predictable tunability without altering the molecular composition, two simple physical modulation strategies were employed to reprogram the higher-order fibrillar organization (**Figure 3.1Bi**). **(a)** Solvent modulation was introduced by replacing pure aqueous media with a glycerol-water mixture. Glycerol was selected as a solvent-modulating component for its hydrogen-bonding ability, its capacity to maintain GMP solubility, and its compatibility with aqueous biomolecular systems. Although glycerol is widely used in pharmaceutical and biomedical formulations, its biological effects depend on concentration and exposure conditions. The glycerol/water mixture was therefore chosen to maintain hydrogel integrity and enhance mechanical properties, not on the assumption that it is

biocompatible at this concentration. The cytocompatibility of the resulting GDG formulation was subsequently evaluated in cellular studies. [*40,41,61,62]* Its incorporation enhances intermolecular hydrogen bonding and solvent-polymer interactions, promoting fibrillar bundling and denser microstructural organization, thereby yielding a mechanically robust GDG hydrogel while preserving the underlying DNA-GMP fibrillar framework. **(b)** Divalent Ca^{2+} ions were employed as biologically relevant crosslinkers to further modulate the supramolecular architecture. Calcium ions were selected for their strong affinity toward phosphate groups, physiological relevance, and ability to induce ionic crosslinking without perturbing G4 chirality or π-π stacking.*[42,43]* Their incorporation into the DG precursor promotes inter-fibrillar crosslinking via phosphate coordination, resulting in nanofiber bundling, partial crystallinity, and the formation of a mechanically rigid, heterogeneous CaDG hydrogel.

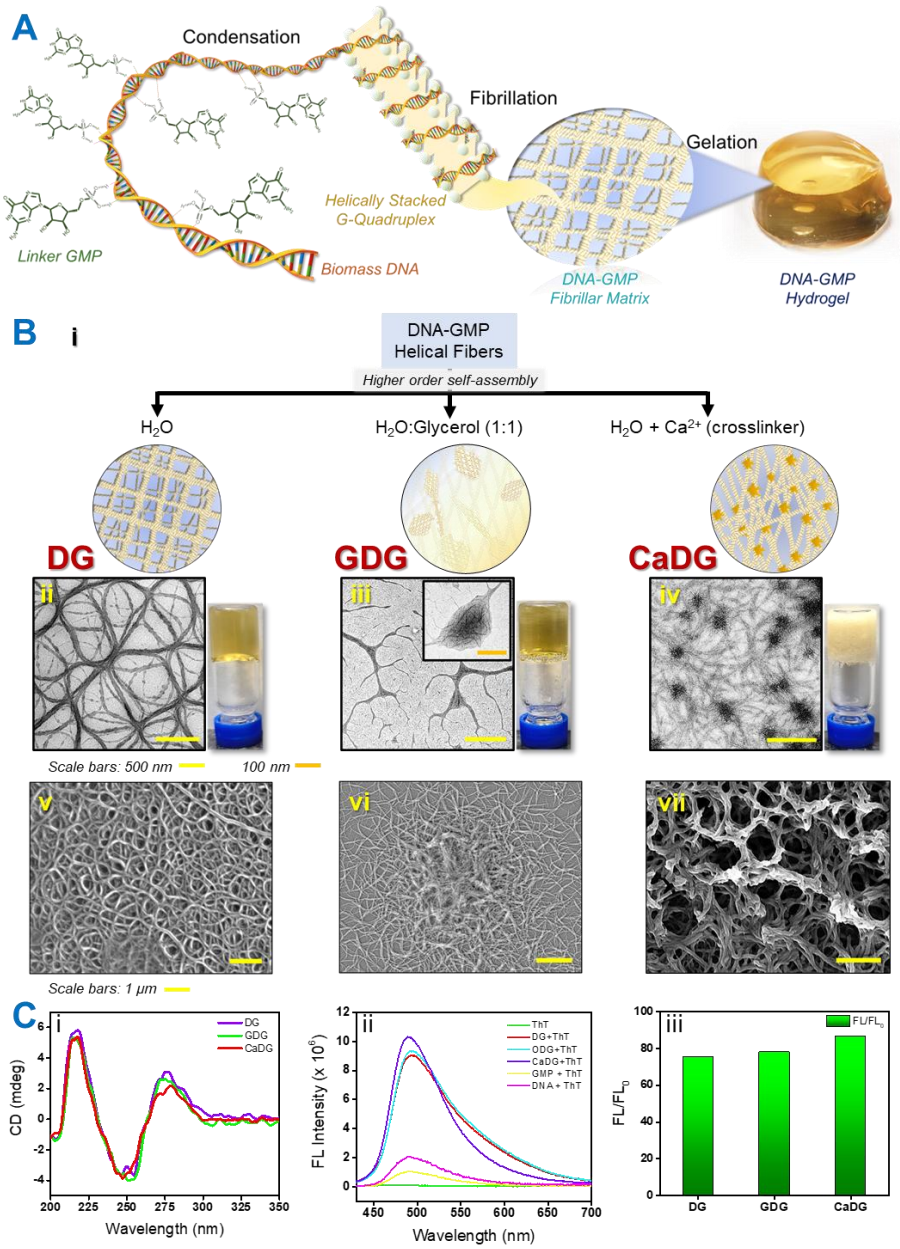


Figure 3.1. A. *Schematic of the DNA packaging into a G4-condensate leads to the formation of a helical fibril network followed by DG hydrogel.[31]* ***B. (i)*** *Synthetic strategy of the DG, GDG and CaDG hydrogels using a similar DNA-GMP fibrillar matrix. HR-TEM micrograph and digital image of hydrogel* ***(ii)*** *DG (100 times diluted),* ***(iii)*** *GDG (50 times diluted),* ***(iv)*** *CaDG (50 times diluted). FE-SEM images of 100 times diluted hydrogels,* ***(v)*** *DG,* ***(vi)*** *GDG,* ***(v)*** *CaDG.* ***C.*** *Spectroscopic characterization of the hydrogels,* ***(i)*** *circular dichroism spectrum (1000 times diluted) showing the formation of anti-parallel G4 assembly in a similar extent for the hydrogels,* ***(ii)*** *FL spectra of ThT assay (ThT concentration ~ 5 μM) of hydrogels (1000 times diluted) and* ***(iii)*** *comparative FL/FL_0 ratio of hydrogels showing the stacking of G4-assembly.*

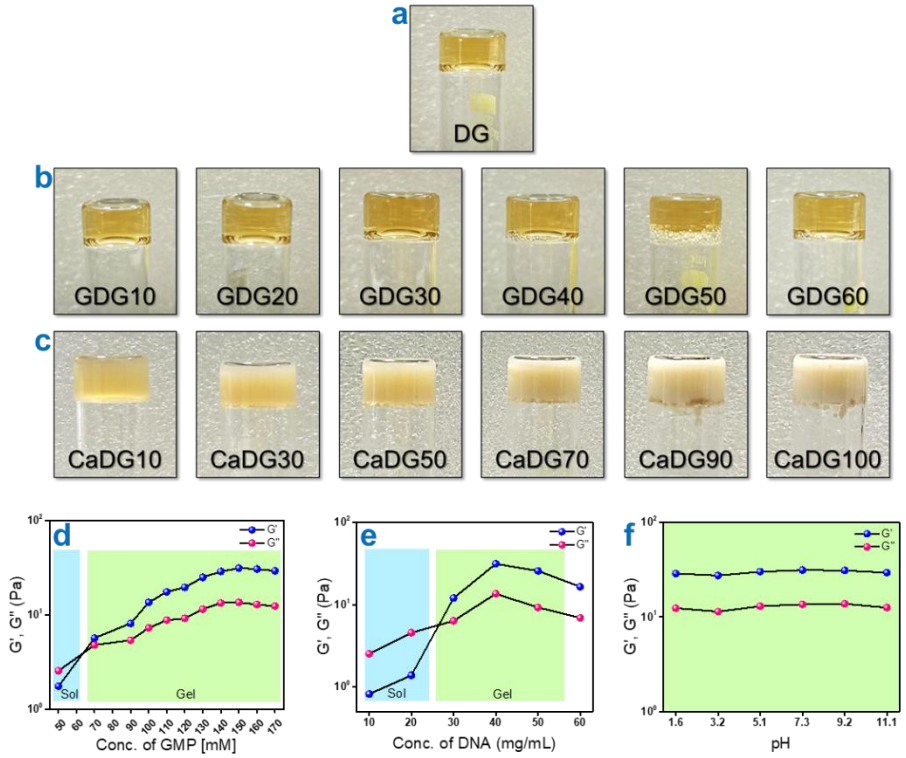


Figure 3.2. *Visual appearance of hydrogel formulations with varying compositions.* ***(a)*** *DG hydrogel.* ***(b)*** *GDG hydrogels illustrating progressive opacity with incremental glycerol content from 10% to 60% (GDG10-GDG60).* ***(c)*** *CaDG hydrogels demonstrating increasing opacity with rising Ca^{2+} concentration from 10 mM to 100 mM (CaDG10-CaDG100). Optimization of gelation conditions for DNA-GMP hydrogel formation.* ***(d)*** *Gelation behavior with varying GMP concentrations.* ***(e)*** *Gelation profiles across different DNA concentrations.* ***(f)*** *pH-dependent gelation efficiency.*

Briefly, simple mixing of biomass DNA (40 $mg.mL^{-1}$, extracted from salmon testes) and 5-GMP (150 mM) in aqueous medium under physiological conditions yielded a homogeneous, transparent, light-yellow DG hydrogel (**Figure 3.2a**). The optimized minimum gelation concentrations were 30 $mg.mL^{-1}$ for DNA and 70 mM for 5′-GMP (**Figure 3.2d, 3.2e**). The hydrogel exhibited excellent stability over a broad pH range (1.6-11) (**Figure 3.2f**), indicating high adaptability. To investigate hydrogel formation in an aqueous-organic environment, a water/glycerol solvent system was employed while maintaining the optimized DNA and GMP concentrations, resulting in a homogeneous GDG hydrogel with enhanced mechanical stability (**Figure 3.2b, Figure 3.4b**). In contrast, control solvent systems such as DMSO/water,

acetonitrile/water, and ethanol/water produced precipitates due to poor GMP solubility, justifying the selection of glycerol for its compatibility with GMP. The GDG hydrogels remained stable across 10-60% (v/v) glycerol-water mixtures (**Figure 3.2b**). In a complementary approach, Ca^{2+} ions were introduced as fibrillar crosslinkers by adding 50 mM anhydrous $CaCl_2$ to the DG precursor solution, followed by stirring and aging, yielding an opaque CaDG hydrogel with markedly enhanced mechanical strength. The hydrogel remained stable over Ca^{2+} concentrations ranging from 10 to 100 mM, with increasing opacity observed at higher ion loadings (**Figure 3.2c**).

3.2.2. Morphological and Structural Interpretation

The effects of solvent modulation and Ca^{2+}-mediated crosslinking on the supramolecular architecture of the DNA-GMP hydrogels were evaluated using complementary microscopic and spectroscopic techniques. High-resolution TEM (HRTEM) and Field-emission SEM (FESEM) images of the pristine DG hydrogel revealed a homogeneous, entangled network of helically organized DNA-GMP nanofibers formed around columnar G-quadruplex stacks, consistent with a diffusion-dominated and swelling-controlled network (**Figure 3.1 B(ii), (v) and inset**). Upon solvent modulation with a glycerol-water mixture, the GDG hydrogel (50% v/v) exhibited pronounced fibrillar reorganization. HRTEM and FESEM images showed enhanced nanofiber bundling and the formation of micro-pocket-like domains, leading to increased network density and reduced pore accessibility (**Figure 3.1 B(iii), (vi) and inset**). This structural compaction rationalizes the suppressed swelling and slower, diffusion-controlled fibrillar assembly. In contrast, Ca^{2+} incorporation produced a rigid, highly crosslinked CaDG hydrogel (50 mM Ca^{2+}) featuring compact, bundled nanofibers and localized crystalline domains arising from ion-mediated inter-fibrillar coordination (**Figure 3.1 B(iv), (vii) and inset**). The resulting reduction in network porosity and increased stiffness restrict bulk swelling and favor surface-dominated erosion, providing a structural basis slow-release behavior.

Spectroscopic analyses were further conducted to probe the chemical arrangement and chirality of DNA-GMP condensates.*[44]* Circular dichroism spectroscopy of the diluted DG, GDG, and CaDG hydrogel samples revealed a negative Cotton band around 250 nm, accompanied by a positive signal in the longer-wavelength region. This spectral signature is consistent with the formation of antiparallel G-quadruplex-like topology, as reported in previous studies. The retention of this characteristic feature across the three formulations suggests that glycerol-mediated solvent modulation and Ca^{2+} crosslinking does not substantially alter the underlying G4-associated chiroptical characteristics (**Figure 3.1 Ci**).*[31,45]* The Thioflavin T (ThT) assay, used to assess π-π stacking among G-quartet macrocycles, showed pronounced fluorescence enhancement in all hydrogels, confirming strong ThT and G4 interactions.*[46]* Quantitatively, DG and GDG hydrogels showed comparable fluorescence enhancement ($FL/FL_0 \approx$ 80), whereas CaDG exhibited a higher FL/FL_0 ratio (~91), reflecting increased stacking due to Ca^{2+}-induced higher-order assembly and nanofiber bundling (**Figure 3.1 Cii, iii**).*[31]* Altogether, microscopic and spectroscopic analyses reveal that solvent variation primarily alters the fibrillar organization without affecting the intrinsic DNA-GMP condensation mechanism, while Ca^{2+} crosslinking reinforces both morphological rigidity and nanoparticle stacking within the hydrogel network.*[47,48]*

Owing to Ca^{2+} crosslinking with the DNA-GMP fibrillar matrix, the DG hydrogel changed from a homogeneous transparent gel to a heterogeneous opaque one (**Figure 3.3 a**). To evaluate the chemical transformations induced by this crosslinking, systematic morphological and spectroscopic analyses were performed. The ThT-labelled confocal image of the diluted (x1000) CaDG hydrogel (**Figure 3.3 b**) revealed two aggregated fibrillar streams, where thick fibers align along the edges of the nano-fibrillar network. The corresponding green fluorescence confirmed extensive crosslinking and bundling of DNA-GMP nanofibers inside the streams. Thus, Ca^{2+}-ion crosslinking lead the edge

thickening and nanofiber bundling, thus, enhancing the rigidity of the crosslinked morphology. The presence of Ca^{2+} within the fibrillar matrix was also verified by EDX mapping (**Figure 3.3 c**). FTIR and pXRD analysis further elucidated the interaction of Ca^{2+} with the DNA-GMP framework. In the FTIR spectra, relative to DG, the phosphate vibration peaks shifted while those of the sugar groups remained unchanged; the C=O band intensity decreased without a shift (**Figure 3.3 d**). These results indicated that Ca^{2+} primarily interacts with phosphate functionalities, leaving the G4-chirality, π-π stacking, and sugar groups unaffected. XRD patterns of both DG and CaDG hydrogels retained reflections at d = 2.2 nm (G4-structure) and d = 0.32 nm (π-π stacking).*[49]* Additionally, three distinct crystalline peaks appeared in CaDG in between θ = 30º to 60º, corresponding to calcite and hydroxyapatite (**Figure 3.3 e**). Collectively, these results confirmed that Ca^{2+} ions crosslink the DNA-GMP nanofibers through phosphate groups, inducing fiber bundling and forming a more rigid, heterogeneous CaDG hydrogel network (**Figure 3.3 f**).

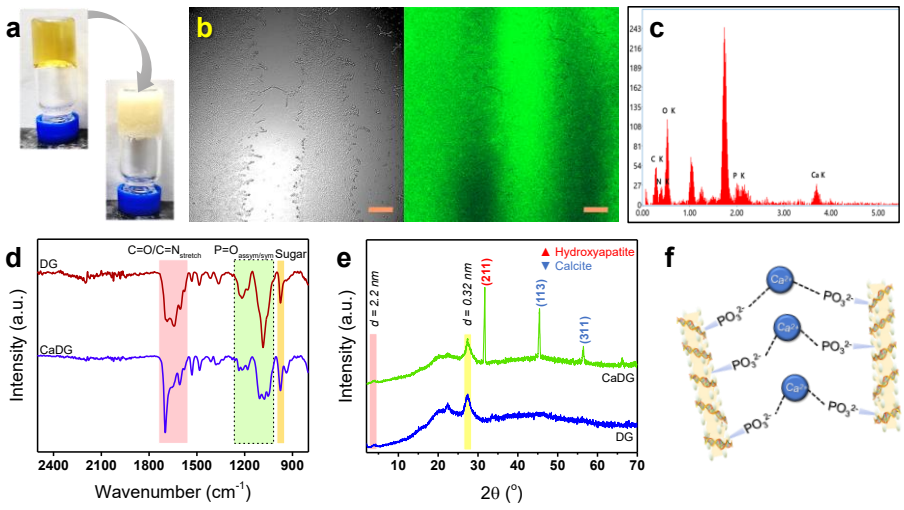


Figure 3.3. (a) *Digital images showing the change in the physical texture of the DG hydrogel upon Ca^{2+} crosslinking to form the CaDG hydrogel;* ***(b)*** *confocal laser microscopic images of ThT-labelled ([ThT] ~ 5 μM) CaDG hydrogel recorded in bright-field and green emission channels, scale bar ~ 10 μm;* ***(c)*** *EDX spectrum confirming the elemental composition of the CaDG hydrogel matrix;* ***(d)*** *FTIR spectra of DG and CaDG hydrogels highlighting the changes in functional groups upon crosslinking;* ***(e)*** *pXRD patterns of dried DG and CaDG hydrogels with reference peaks*

of calcite (ICDD 01-072-1937) and hydroxyapatite (ICDD 09-0432)[50-51] and ***(f)*** *schematic illustration of the plausible crosslinking pattern between DNA-GMP nanofibers and* Ca^{2+} *ions.*

3.2.3. Mechanical Properties

The mechanical properties of the hydrogels were investigated through oscillatory rheology. The influence of solvent modulation and divalent metal crosslinking on mechanical behavior was analyzed using amplitude and frequency sweep experiments. In all hydrogels, the storage modulus (G′) consistently exceeded the loss modulus (G″) across the strain range, confirming their viscoelastic nature. The linear viscoelastic region (LVE), however, varied with strain. The strain threshold of the GDG hydrogel (50% v/v glycerol/water) decreased from 216% for DG to 68.2% upon solvent alteration. Further crosslinking with Ca^{2+} (80 mM) reduced it to 4.64% (**Figure 3.4 a**). Despite the reduced LVE threshold, both solvent modulation and metal crosslinking markedly enhanced the hydrogel strength. The G′ and G″ values of GDG were about tenfold higher than those of DG, while in CaDG, both moduli increased nearly 1000-fold, indicating significant structural reorganization (**Figure 3.4 b**). Glycerol acted as a reinforcing agent by promoting clusterization of DNA-GMP nanofibers into dense micro-pockets, strengthening inter-fibrillar associations. Ca^{2+} further enhanced stacking, bundling, and rigidity of the nanofiber network, producing a compact structure with strengths comparable to polymeric fibers or thermoplastic elastomers.*[52]* Such high strength achieved through noncovalent biomolecular condensation is remarkable. Frequency sweep analyses (0.1-100 $rad.s^{-1}$) confirmed excellent viscoelastic stability, with G′ consistently exceeding G″ (**Figure 3.4 c**). Thixotropic tests demonstrated reversible gel-sol-gel transitions, validating the hydrogels' injectability and printability. DG, GDG, and CaDG recovered their gel states after cyclic strain shifts of 1%-500%-1% (**Figure 3.4 d**), 1%-300%-1% (**Figure 3.4 e**), and 1%-100%-1% (**Figure 3.4 f**), respectively. These behaviors affirmed their suitability as drug delivery systems with tunable mechanical and viscoelastic

properties. **Figure 3.4 g** illustrates the injectability, printability, and fibrous microstructures of the hydrogels.

To optimize glycerol content for GDG hydrogel synthesis, samples prepared with varying glycerol/water ratios (up to 60% v/v) were tested for mechanical stability, considering DNA and GMP solubility limits. The 50% v/v glycerol/water mixture yielded the highest and most stable moduli and was therefore selected for further studies (**Figure 3.4 h**). Similarly, varying Ca^{2+} concentrations (10-100 mM) were examined, revealing 80 mM as the optimum level, providing maximal strength and viscoelastic integrity for subsequent applications (**Figure 3.4 i**).

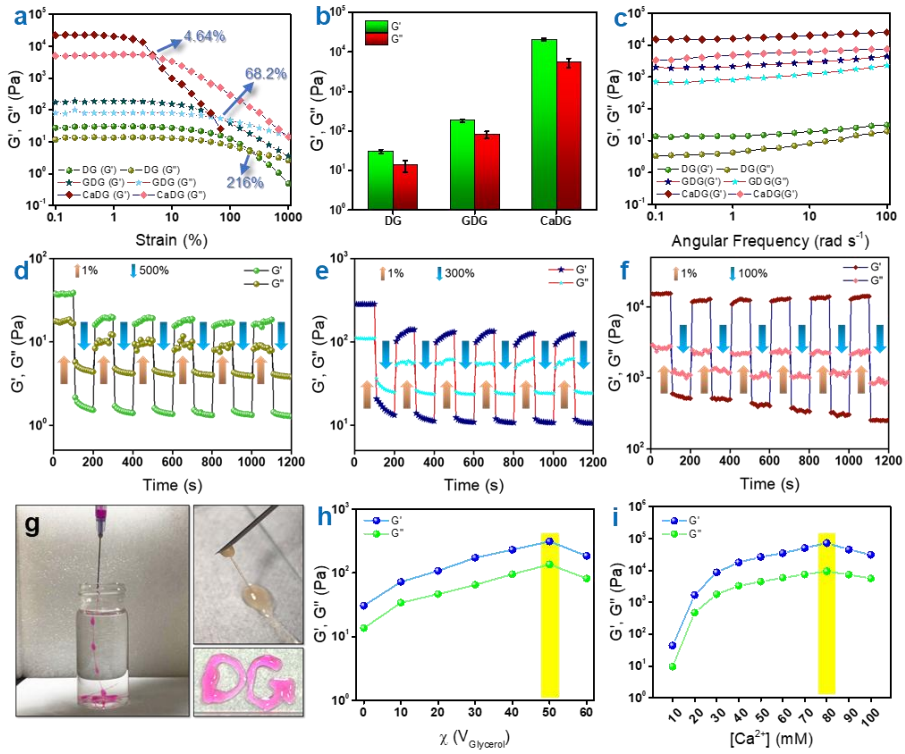


Figure 3.4. *Rheological and mechanical characterization of DG, GDG, and CaDG hydrogels.* ***(a)*** *Amplitude-sweep measurements at a constant angular frequency of 10 rad.s^{-1},* ***(b)*** *Comparative storage (G') and loss (G'') modulus values at 1% strain and 10 rad.s^{-1},* ***(c)*** *Frequency sweep measurements at 1% strain for DG, GDG, and CaDG hydrogels.* ***(d-f)*** *Thixotropic loop tests (low-high-low strain cycles) demonstrating injectability and printability of* ***(d)*** *DG,* ***(e)*** *GDG, and* ***(f)*** *CaDG hydrogels.* ***(g)*** *Digital images illustrating fibrillar stability, injectability, and shape retention using dye-doped DG hydrogel, highlighting practical applicability.* ***(h)*** *Glycerol/water (v/v) ratio-*

dependent rheology of GDG hydrogels, with maximum G′ and G″ observed at 50% glycerol. ***(i)*** *Ca^{2+} concentration-dependent rheology of CaDG hydrogels, showing peak G′ and G″ at 80 mM Ca^{2+}.*

3.2.4. Hydrotropic Drug Encapsulation

In our previous study, the DG hydrogel was demonstrated to be an effective hydrotropic carrier capable of encapsulating and sustaining the release of both hydrophilic and hydrophobic drugs with comparable efficiency.*[31]* The excellent drug encapsulation arose from hydrotropic G4 cavities rather than passive pore trapping (**Figure 3.5 a**). The hydrotropic nature was further supported by the ThT assay, in which ThT molecules intercalate into the hydrophobic cavities of the stacked G-quartet noncovalent macrocyclic framework. These distinctive structural and functional features of the DG hydrogel were also retained in GDG and CaDG hydrogels, as their molecular packing and fundamental assembly characteristics remain unaffected by solvent modulation or crosslinking.*[53,54]*

Leveraging this unique hydrotropic behavior, two anticancer drugs, hydrophilic doxorubicin (Dox) and camptothecin (CPT), were selected for sustained drug-encapsulation studies (**Figure 3.5 b**). Dox, a well-studied topoisomerase II inhibitor administered intravenously, is widely used in the treatment of breast, bladder, lung, stomach, ovarian, and thyroid cancers.*[55]* In contrast, CPT, a plant-derived alkaloid and a potent topoisomerase I inhibitor, remains less explored owing to its extremely poor water solubility, which limits its effective administration in physiological environments.*[36]* Given their contrasting solubility profiles, the hydrotropic DG-based hydrogels are well-positioned to encapsulate both hydrophilic (Dox) and highly hydrophobic (CPT) drug molecules, enabling controlled and sustained release behavior.

Simple mixing of the drugs with the solid biomass DNA and GMP, followed by gentle stirring at 37 °C and subsequent cooling for 5 minutes, resulted in the formation of drug-encapsulated hydrogels. A similar encapsulation approach was employed for the GDG and CaDG

hydrogel systems. This spontaneous encapsulation behavior, effective for both hydrophilic and hydrophobic drug molecules, was particularly remarkable and highly efficient. The encapsulation efficiencies of the hydrogels were evaluated by repeatedly washing the samples with PBS solution and measuring the absorbance of the supernatant. Detailed procedures and calculations for determining encapsulation efficiencies were provided in the **Table 3.1**.*[31]* (section 3.4) All three hydrogel systems exhibited excellent encapsulation efficiency for both Dox and CPT, highlighting their unique hydrotrope-like characteristics (**Figure 3.5 b**). The high drug loading efficiency ensured minimal presence of unbound drug molecules, thereby reducing potential side effects. The maximum drug loading capacity per milliliter of hydrogel was quantified, and the results are summarized in **Figure 3.5 c**. The drug-loaded hydrogels were aged under physiological conditions for 12 hours before being utilized as soft interfaces for sustained drug release experiments.

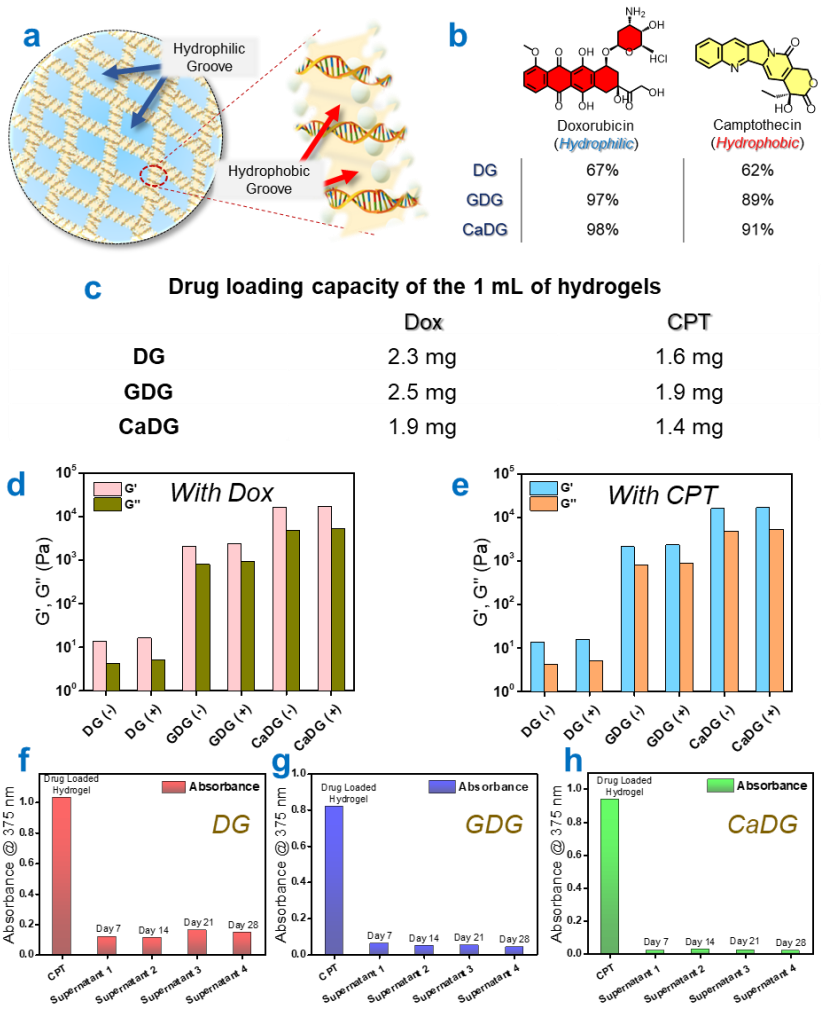


Figure 3.5. ***(a)*** *Schematic illustration depicting the site-specific encapsulation of hydrophobic and hydrophilic drugs within the nanofibrous hydrogel network.* ***(b)*** *Chemical structures of the encapsulated drugs, doxorubicin (Dox) and camptothecin (CPT), along with their respective encapsulation efficiencies.* ***(c)*** *Drug loading capacity of the 1 mL of hydrogels. Rheological characterization demonstrating preserved mechanical integrity of hydrogels upon drug loading. Storage (G') and loss (G'') moduli for hydrogels* ***(d)*** *loaded with Dox and* ***(e)*** *loaded with CPT. Shelf-life and anti-leakage performance of the hydrogels assessed via UV-vis absorbance of CPT over 28 days,* ***(f)*** *DG,* ***(g)*** *GDG, and* ***(h)*** *CaDG hydrogels, respectively, demonstrating sustained drug retention.*

The rheological analysis (**Figure 3.5 d and 3.5 e**) confirmed that the drug-loaded hydrogels exhibited mechanical properties comparable to their unloaded counterparts. Furthermore, shelf-life and leakage tests demonstrated that the hydrogels effectively retained the encapsulated drugs for up to 28 days, with only minimal drug release observed during the periodic weekly wash cycles (**Figure 3.5 f-h**).

3.2.5. Modulation in the Drug Release Kinetics

In this drug release study, each drug-loaded hydrogel (1 mL) was immersed in phosphate-buffered saline (PBS, 3 mL, pH 4) and incubated at 37 °C. Acidic buffer was employed in all release experiments to demonstrate that anticancer drug release is favored under acidic conditions, mimicking the mildly acidic extracellular environment typically found around cancer cells.*[31,56]* At predetermined time intervals, 400 µL aliquots were withdrawn and immediately replaced with fresh buffer to maintain sink conditions. Drug release was quantified by UV-visible spectrophotometry at the respective absorption maxima i.e. 480 nm for Dox and 375 nm for CPT.

Notably, upon solvent exchange and introduction of metal crosslinking, the DG hydrogel exhibited not only modified physical and mechanical properties but also tunable sustained drug release behavior (**Figure 3.6 a**). The DG hydrogel displayed comparable encapsulation efficiencies for both Dox and CPT, which can be attributed to its amphiphilic character. Under sustained release conditions, the DG hydrogel showed cumulative releases of approximately 82% for Dox and 78.5% for CPT after 60 hours, indicative of efficient yet controlled delivery. Kinetic analysis revealed that the release of both drugs from the DG hydrogel was best described by a first-order model, suggesting that the release rate is governed by the remaining drug content within the matrix (**Figure 3.6 d, e**). The release profile for the DG hydrogel followed a first-order kinetic equation of the form*[11,12]* (Eq 1),

$$\log C = \log C_0 - \frac{K_1 t}{2.303} \qquad \text{(Eq. 1)}$$

where C is the amount (or % remaining) at time t, C_0 is the initial amount, and K_1 is the first-order rate constant. For the DG hydrogel, the K_1 values were determined to be 11.36 and 9.2 for Dox and CPT, respectively, as obtained from fitting the release data with a Hill-type model.

In the presence of 50% glycerol-water as the solvent, the GDG hydrogel exhibited not only higher encapsulation efficiency but also a distinctly modified drug release profile. Under identical release conditions, the drug-loaded GDG hydrogels were immersed in PBS, where they displayed comparable long-term swelling behavior to the DG hydrogels. However, the release of both drugs from the GDG hydrogel was markedly slower, and the initial burst release observed at approximately 12-20 hours for the DG system was effectively suppressed in the GDG formulation. This behavior suggested a stronger diffusional barrier and more restricted molecular mobility within the micro-pocket-like fibrillar network. The superior mechanical strength of the GDG hydrogel relative to the DG hydrogel was also consistent with its slower swelling behavior in the drug-loaded state. Consequently, the release data for the GDG hydrogel were best described by the Higuchi model (**Figure 3.6 b, c**), showing cumulative releases of approximately 80% for Dox and 73% for CPT after 60 hours.

The Higuchi model describes diffusion-controlled release from a matrix, where release is proportional to the square root of time (Eq 2), and the profiles were fitted using the following equation.*[11,12]*

$$Q_t = k_H t^{1/2} \qquad \text{(Eq 2)}$$

Where Q_t is the cumulative amount of drug released per unit area at time t and k_H is the Higuchi dissolution constant. For the GDG hydrogel, the k_H values were determined to be 10.05 and 10.14 for Dox and CPT, respectively, as obtained from fitting the release data with a linear fitting model.

For both the DG and GDG hydrogel systems, drug release was primarily governed by swelling, followed by gradual matrix dissolution in PBS, which in turn liberates the encapsulated drug molecules over time. In contrast, the CaDG hydrogel did not display this swelling-controlled dissolution behavior. Owing to its much higher stiffness and more opaque, robust network compared with DG and GDG, the CaDG hydrogel underwent extremely slow dissolution in PBS and instead

eroded progressively from the outer surface. This observation indicateed that drug release from CaDG is dominated by surface erosion rather than bulk swelling, creating the possibility of achieving an approximately zero-order release profile. To examine this, sustained release experiments were performed using the same overall protocol, but with sampling carried out at day-wise intervals instead of hourly to capture the slower release process more accurately.

The sustained release profile for the CaDG hydrogel was found to have zero order kinetics, delivering a constant drug release within a similar time interval showing a maximum of 77% and 71% for Dox and CPT, respectively after 10 days (**Figure 3.6 f, g**). The drug release kinetics was fitted using the following zero-order kinetic equation (Eq 3)*[11,12]*,

$$Q_t = Q_0 + k_0 t \qquad \text{(Eq 3)}$$

where Q_t is the amount (or % cumulative) drug released at time t, Q_0 is the initial amount, and k_0 is the zero-order rate constant. For the CaDG hydrogel, the k_0 values were determined to be 0.39 and 0.29 for Dox and CPT, respectively, as obtained from fitting the release data with a linear fitting model.

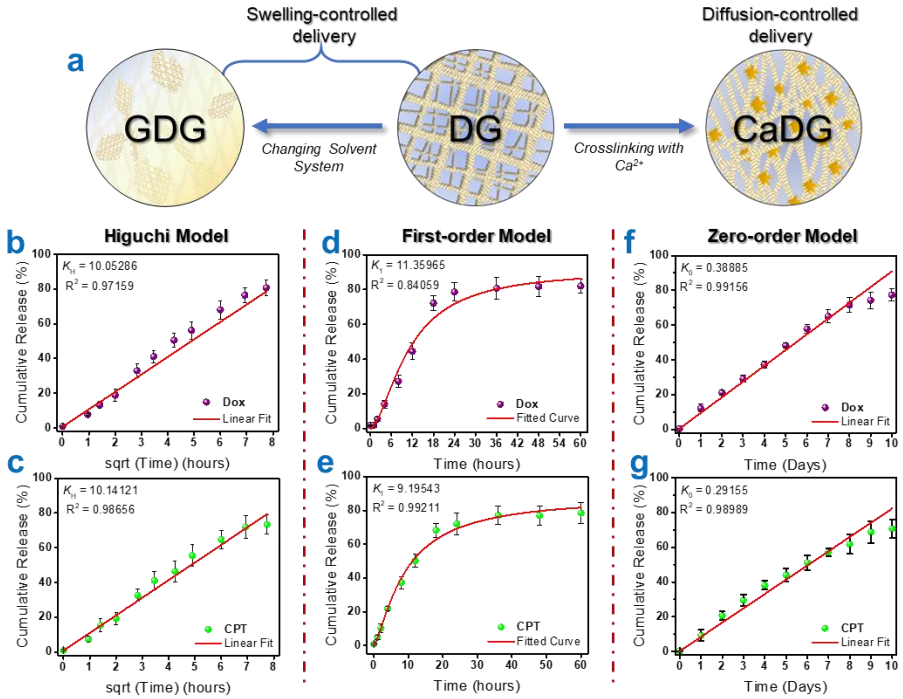


Figure 3.6. (a) *Schematic representation of tunable drug release profiles in DG, GDG, and CaDG hydrogels. Drug release kinetics of* ***(b-c)*** *GDG,* ***(d-e)*** *DG, and* ***(f-g)*** *CaDG hydrogels following Higuchi, first-order, and zero-order models, respectively, for Dox and CPT.*

To evaluate the influence of pH and physiological conditions on drug release behavior, Dox and CPT-loaded DG hydrogels were subjected to sustained release studies in high-glucose DMEM cell culture medium. The release profile of the pristine DG hydrogel remained largely unchanged under these conditions, indicating that the hydrogel maintains structural integrity and release profile in physiologically relevant environments, thereby confirming its compatibility for biological applications (**Figure 3.7 a, b**). To further elucidate the release kinetics and validate the zero-order mechanism of the CaDG hydrogel, a systematic day-wise analysis was performed (**Figure 3.7. c, d**). The presence of Ca^{2+} ions crosslinking the negatively charged DNA-GMP nanofibers imparted structural rigidity and compactness to the network, favoring gradual surface erosion over swelling. In acidic environments, the enhanced drug release is likely triggered by superficial matrix peeling, leading to controlled, stimuli-responsive dissolution of the hydrogel surface over time.

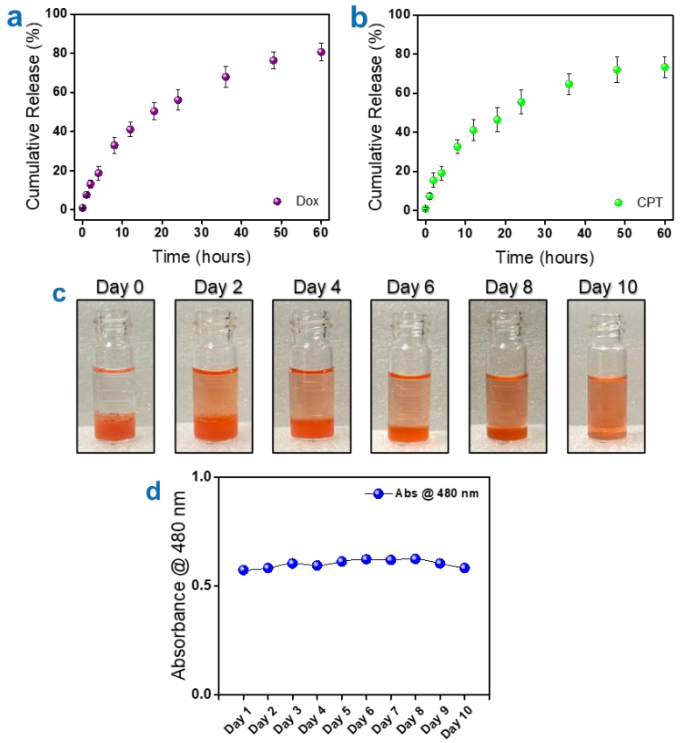


Figure 3.7. *Controlled release profile of the* ***(a)*** *Dox and* ***(b)*** *CPT loaded DG-hydrogels in high-glucose DMEM cell culture medium. Systematic day-wise analysis of zero-order drug release from the Dox-loaded CaDG hydrogel.* ***(c)*** *Digital photographs showing progressive erosion of the hydrogel over successive days.* ***(d)*** *UV-vis absorbance profiles at 480 nm, corresponding to Dox, demonstrating a consistent day-wise release pattern indicative of zero-order kinetics.*

3.2.6. Programming the Drug Release Kinetics

A central feature of the DNA-GMP hydrogel platform is its ability to achieve programmable drug release through controlled microarchitectural modulation. By varying the glycerol content in GDG hydrogels and the Ca^{2+} concentration in CaDG hydrogels, the release mechanism can be systematically reconfigured without altering the underlying molecular composition (**Figure 3.8 a**). Increasing glycerol content promotes fibrillar bundling and microdomain formation, resulting in a denser network with reduced swelling and minimized burst release. This structural reorganization resulted in a more controlled and sustained drug release profile, effectively suppressing the burst release observed in the pristine DG hydrogel, particularly during the 12-36 h release window (**Figure 3.8 b**). Consequently, the release behavior

progressively transitioned from first-order kinetics toward a more regulated Higuchi-type diffusion-controlled profile, as evidenced by the increasing Higuchi fitting coefficient (R^2) with increasing glycerol content in the GDG hydrogel system (**Figure 3.8 c**). Similarly, increasing Ca^{2+} concentration enhances inter-fibrillar crosslinking and network rigidity, shifting the dominant transport mechanism from bulk swelling to surface erosion. This structural evolution induces the emergence of zero-order release behavior at relatively low Ca^{2+} concentrations and progressively extends the release duration, ultimately providing sustained drug release for up to 10 days (**Figure 3.8 d**). Collectively, these results demonstrate that simple physical modulation of a common DNA-GMP nanofibrillar matrix enables predictable programming of drug transport pathways, allowing access to first-order, Higuchi-type, and zero-order release regimes within a single supramolecular hydrogel platform.

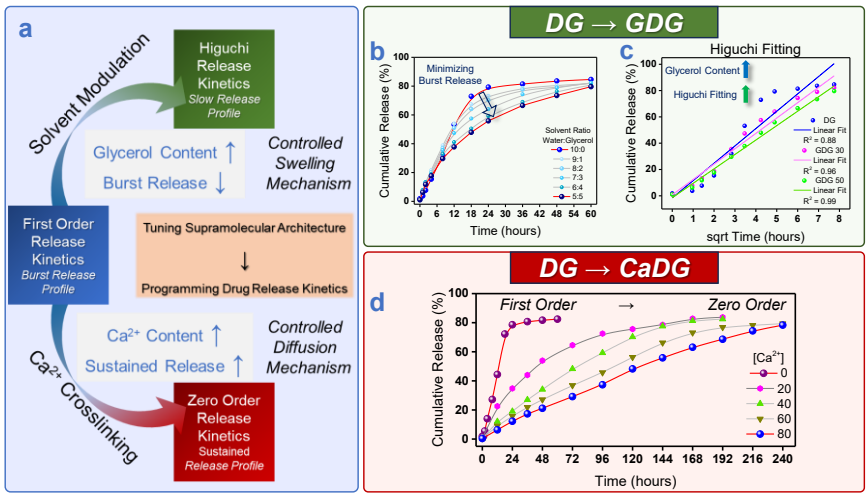


Figure 3.8. *Programmable control of drug release kinetics through structure modulation of Dox loaded DG, GDG and CaDG hydrogels.* ***(a)*** *Schematic illustration showing how solvent modulation and Ca^{2+}-mediated crosslinking reconfigure the supramolecular architecture of a common DNA-GMP matrix, enabling transitions between first-order, Higuchi-type, and zero-order release regimes.* ***(b,c)*** *Increasing glycerol content suppresses burst release and progressively improves Higuchi-type diffusion-controlled release through enhanced fibrillar organization and reduced swelling.* ***(d)*** *Increasing Ca^{2+} concentration promotes inter-fibrillar crosslinking and network rigidity, transforming swelling-driven transport into surface erosion-controlled release and enabling sustained zero-order kinetics for up to 10 days.*

3.2.7. Cytotoxic Activity of Drug-loaded Hydrogels on Breast Cancer Cells

As hydrotropic drug carriers, the hydrogels efficiently encapsulated both Dox and CPT with comparable loading efficiencies and enabled sustained release with tunable kinetics. While Dox is a clinically established, water-soluble anticancer agent, CPT is a highly potent yet poorly soluble drug whose therapeutic application is limited by instability and systemic toxicity, despite its promise against aggressive cancers such as triple-negative breast cancer.[35,36,57] The ability of the hydrogels to solubilize and controllably deliver CPT highlighted their potential to enhance the efficacy of hydrophobic chemotherapeutics while mitigating off-target effects. Consequently, comprehensive cellular studies were performed using breast cancer models to evaluate the therapeutic efficacy and selective cytotoxicity of the hydrogel carriers, demonstrating pronounced anticancer activity with minimal toxicity toward healthy cells and establishing their suitability as efficient and biocompatible delivery vehicles, particularly for hydrophobic chemotherapeutics.

The developed hydrogel system enabled efficient intracellular delivery of the water-insoluble anticancer drug CPT, thereby improving its bioavailability and therapeutic efficacy. This enhanced delivery promoted pronounced growth inhibition and induces apoptotic cell death in cancer cells. To evaluate the effect of CPT-loaded hydrogels on the viability of MDA-MB-231 cells, three treatment groups: DG+CPT, GDG+CPT and CaDG+CPT, along with their corresponding unloaded controls (DG, GDG and CaDG), were incubated with cultured cells. The morphological alterations in treated cells were subsequently examined under a bright-field microscope.

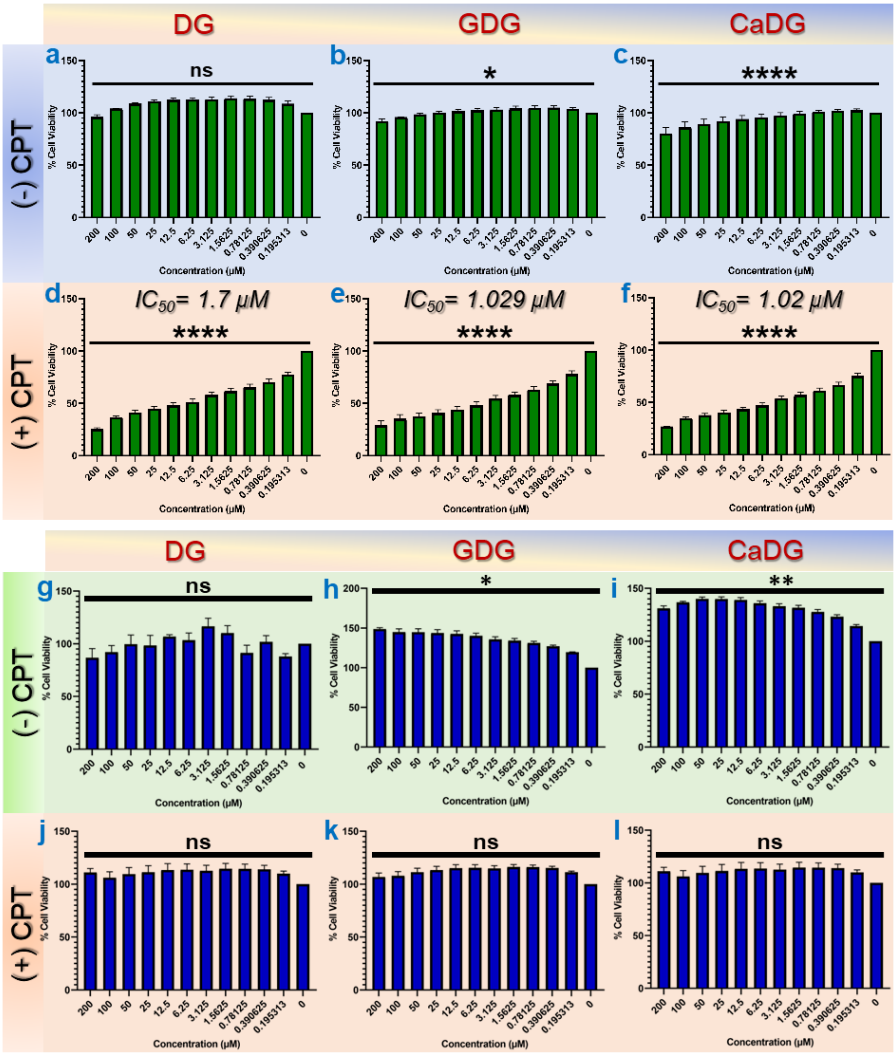


Figure 3.9. *Cytotoxic evaluation of MDA-MB-231 (Triple-Negative breast Cancer cells) in the presence of different treatment groups.* ***(a)*** *DG,* ***(b)*** *GDG,* ***(c)*** *CaDG alone and drug-loaded hydrogels,* ***(d)*** *DG+CPT,* ***(e)*** *GDG+CPT, and* ***(f)*** *CaDG+CPT. Cytotoxic evaluation of HEK-293 cells in the presence of different treatment groups.* ***(g)*** *DG,* ***(h)*** *GDG,* ***(i)*** *CaDG, (d) DG + CPT, (e) GDG + Glycerol + CPT, (f) CaDG + CPT. The data represents mean percentage cell viability ± standard error (S.E) (n=3). Statistical analysis was performed using two-way ANOVA. Significance was determined by comparing 200 µM and 0 µM conditions (CPT equivalent concentration) in each treatment group. (ns, non-significant, *p<0.05, ****p<0.0001)*

The control treatment group containing the unloaded hydrogel DG showed no significant change in cell viability compared to control (**Figure 3.9 a**), whereas GDG, and CaDG did show significant change which remained in the cytocompatibile range indicating that the corresponding treatments are not cytotoxic (**Figure 3.9 b, c**). The results

obtained in the unloaded hydrogel formulations reveals that the hydrogel matrices do not adversely affect the MDA-MB-231 cell survival under the observed conditions. In contrast, groups treated with CPT-loaded hydrogels showed distinct morphological alterations, and their cell viability was quantitatively evaluated using the MTT assay (**Figure 3.9 d, e and f**). The effective inhibitory concentration (IC_{50}), defined as the concentration required to reduce cell viability by 50%, was found to be relatively low, indicating a strong cytotoxic effect. Among the various formulations, the CaDG+CPT system demonstrated the lowest IC_{50} value (1.02 μM) than that of DG+CPT (1.7 μM) and GDG+CPT (1.029 μM). This enhanced efficacy can be attributed to its denser network structure, which likely restricts the rapid diffusion of CPT, assisting a slower and more sustained drug release that maintains prolonged cytotoxic activity.

All six treatment formulations (DG, GDG, CaDG, DG+CPT, GDG+CPT and CaDG+CPT) were evaluated for their cytocompatibility using non-tumorous HEK-293 cells to assess potential cytotoxic effects. Among these, the unloaded treatment group (DG) exhibited no significant reduction in cell viability, indicating excellent biocompatibility (**Figure 3.9 g**). Whereas, GDG, and CaDG showed significant change in the cell viability but remained in the cytocompatible range (**Figure 3.9 h, i**). Those loaded with CPT (DG, GDG, and CaDG) treatment groups did not produce any marked decrease in cell viability, suggesting CPT-loaded formulations exhibit preferential cytotoxicity towards MDA-MB-231 (Triple Negative Breast Cancer) while maintaining compatibility with non-cancerous cells. (**Figure 3.9 j, k and l**).

3.2.8. CPT loaded with variable hydrogel combinations disintegrates multicellular spheroids

Multicellular spheroids offer significant advantages for evaluating drug efficacy and drug delivery performance due to their ability to closely mimic the native tumor microenvironment. To

investigate the effect of CPT encapsulated within various hydrogel formulations, MDA-MB-231 spheroids were treated with these formulations for 48 hours, and the therapeutic outcomes of all combinations were subsequently assessed. MDA-MB-231 spheroids were treated in triplicate with hydrogel-encapsulated CPT at concentrations of 2 μM and 5 μM, respectively. Following 48 hours of treatment, the spheroids were visualized under a brightfield microscope to assess morphological alterations induced by the formulations. Untreated spheroids displayed a characteristic architecture comprising a dense central core, indicative of hypoxia-driven compaction and reduced proliferation, surrounded by a lighter peripheral region representing actively proliferating cells with access to nutrients from the culture medium (**Figure 3.10 a**). In contrast, spheroids treated with 2 μM and 5 μM CPT-loaded DG hydrogels exhibited a pronounced loss of the dense core, disrupted and irregular surfaces, and diminished compaction (**Figure 3.10 b, c, d**). The integrity of these spheroids was further analyzed through radial optical intensity profiling. Control spheroids presented a typical U-shaped intensity curve corresponding to the compact core and well-defined periphery, whereas treated spheroids displayed a flattened profile, signifying the loss of structural integrity resulting from cell death, apoptosis, or vacuolation (**Figure 3.10 e**). Quantitative analysis of morphological changes using the circularity index revealed a marked reduction in circularity for treated spheroids, confirming the drug-induced disruption of structural compactness and the emergence of irregular, fragmented boundaries consistent with spheroid disintegration (**Figure 3.10 l**).

Similarly, the spheroids were also treated with two other formulations, GDG+CPT and CaDG+CPT, at the same CPT concentrations of 2 μM and 5 μM respectively. Both treatment groups exhibited comparable morphological disintegration of the spheroids when observed under brightfield microscopy. The treated spheroids showed an increase in radial optical intensity, reflected as a flattened curve, consistent with the loss of the dense core structure (**Figure 3.10**

f, g). Furthermore, the emergence of irregular, fragmented, and uneven spheroid boundaries was corroborated by a decrease in the circularity index, indicating a loss of structural compactness upon treatment (**Figure 3.10 l**).

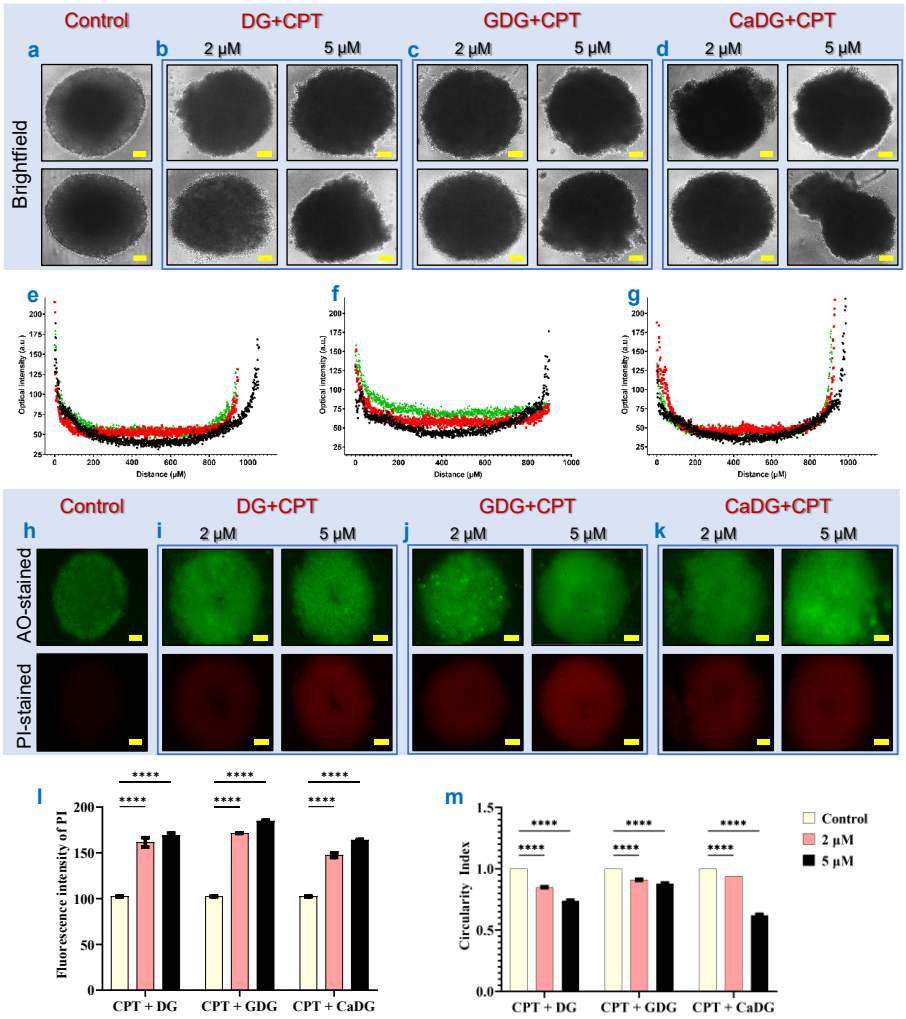


Figure 3.10. *Effects of CPT-loaded hydrogel treatment groups on MDA-MB-231 spheroid morphology, radial optical density, and viability after 48 hours of treatment.* ***(a)*** *Bright-field images of untreated control MDA-MB-231 spheroids.* ***(b-d)*** *Bright-field images of MDA-MB-231 spheroids treated with DG + CPT.* ***(b)****, GDG + CPT* ***(c)****, and CaDG + CPT* ***(d)*** *at 2 µM and 5 µM CPT.* ***(e-g)*** *Radial optical density profiles extracted from bright-field images showing spatial distribution of optical intensity across spheroid diameter(black-control, red-2 µM CPT treatment, green-2 µM CPT treatment)* ***(e)*** *DG + CPT,* ***(f)*** *GDG + CPT, and* ***(g)*** *CaDG + CPT. AO/PI dual-stained images of* ***(h)*** *control spheroids showing viable (acridine orange, green) and non-viable (propidium iodide, red) cell populations.* ***(i-k)*** *AO/PI-stained spheroids following treatment with* ***(i)*** *DG + CPT,* ***(j)*** *GDG + CPT, and* ***(k)*** *CaDG + CPT at 2 µM and 5 µM CPT.* ***(l)*** *Quantification of spheroid circularity index under each treatment*

condition indicating treatment-dependent loss of sphericity. ***(m)*** *Quantitative analysis of PI fluorescence intensity for each treatment condition. Data are shown as mean ± S.E; (n=3). Statistical analysis was performed using two-way ANOVA. Significance is indicated as ****p<0.0001. The brightfield and fluorescence images were obtained in identical magnification and imaging condition. The scale bar (100 μm) is representative of all the corresponding images in the figure.*

3.2.9. Treating spheroids with CPT loaded in hydrogel induces apoptosis and cellular death

To evaluate CPT-induced apoptosis and cell death, MDA-MB-231 spheroids were treated with different formulations for 48 hours. Following treatment, the spheroids were incubated with acridine orange and propidium iodide (AO/PI) staining solution for 30 minutes and subsequently visualized under a fluorescence microscope to assess apoptotic responses. AO selectively stains live cells with intact membranes, emitting green fluorescence, whereas PI penetrates cells with compromised membranes and labels them red, indicating late apoptosis or necrosis. All treatment groups demonstrated a notable increase in red fluorescence intensity post-treatment, indicating enhanced membrane disruption and cell death, while the overall green fluorescence remained largely unaffected. This can be attributed to AO binding nucleic acids, where early apoptosis induced by CPT does not immediately alter total DNA content (**Figure 3.10 h-k**).[58] Quantitative fluorescence analysis revealed a significant, concentration-dependent increase in red emission for spheroids treated with 2 μM and 5 μM CPT formulations compared to untreated controls (**Figure 3.10 m**). Among the treatment groups, spheroids treated with CaDG+CPT exhibited a relatively lower increase in red fluorescence compared to GDG+CPT treated spheroids. This attenuation is likely due to the presence of calcium ions, which are known to modulate apoptotic signaling, promote cell survival pathways, and regulate cellular processes such as autophagy.[59,60]

3.3. Conclusion

This study reports a sustainable, biomass-derived DNA-GMP hydrogel platform that enabled precise and predictable control over anticancer drug release kinetics within a single supramolecular matrix. Unlike conventional systems that require multiple carrier compositions to achieve distinct release profiles, this platform exploited physical modulation of a single nanofibrillar DNA-GMP architecture to continuously tune drug release behavior. Simple alteration of the solvent environment or introduction of biorelevant Ca^{2+} crosslinking reprogramed the same molecular framework to access first-order, Higuchi-type diffusion-controlled, and zero-order erosion-dominated release regimes. At the molecular level, spontaneous condensation between biomass DNA and 5′-guanosine monophosphate induced the formation of helically stacked G-quadruplex nanofibers, generating a hydrotropic and intrinsically amphiphilic network. This hierarchical organization created coexisting hydrophobic cavities and inter-fibrillar aqueous channels, enabling efficient encapsulation of both hydrophilic and highly hydrophobic anticancer drugs. Importantly, solvent-induced fibrillar bundling and Ca^{2+}-mediated crosslinking modulated nanofiber packing density, mechanical stiffness, and swelling behavior without perturbing the underlying G-quadruplex assembly, thereby allowing structure-driven regulation of drug transport mechanisms. The translational relevance of this platform is demonstrated through sustained and tunable delivery of Dox and CPT, a clinically challenging and poorly soluble anticancer agent. The hydrogels exhibited injectability, mechanical adaptability, and pH-responsive release behavior, supporting their suitability for localized and precision chemotherapy. Extensive cellular evaluations using breast cancer models were conducted to assess the therapeutic efficacy and selective cytotoxicity of the hydrogel carriers. CPT-loaded hydrogels effectively reduced breast cancer cell viability in monolayer cultures and disintegrate three-dimensional breast cancer spheroids at low drug concentrations (2-5 μM), as evidenced by spheroid fragmentation and

enhanced apoptotic activity. Integrating two-dimensional cytotoxicity and three-dimensional tumor spheroid outcomes, this work established a universal nucleic acid-based hydrogel platform in which structure-driven microarchitectural control enabled programmable drug release kinetics, offering a versatile and translationally relevant strategy for next-generation anticancer drug delivery.

3.4. Experimental Section

3.4.1. Synthesis of hydrogels

For the preparation of the DG hydrogel, 40 mg of salmon sperm DNA was accurately dissolved in 1 mL of Milli-Q water under gentle stirring at a constant temperature of 40 °C to obtain a uniform solution. After 5 minutes of stirring, 61.2 mg (corresponding to 150 mM) of guanosine monophosphate disodium salt was introduced into the solution. The mixture immediately turned into a transparent light-brown solution, which upon cooling to room temperature for 2-3 minutes, yielded a clear DNA-GMP hydrogel. Additionally, various DNA and GMP concentrations were tested to study their influence on the mechanical properties of hydrogel. The successful formation of the hydrogel was verified by the simple inverted tube method.

For the synthesis of the GDG hydrogel, a similar procedure was followed, with the only modification being the use of a glycerol:water solvent system at varying volume ratios. The resulting hydrogels were designated as GDG10 to GDG60, corresponding to glycerol contents ranging from 10% to 60% (v/v), respectively. Similarly, Ca^{2+}-doped CaDG hydrogels were synthesized using the same concentrations of DNA and GMP, with the addition of calcium chloride in concentrations ranging from 10 mM to 100 mM. The resulting hydrogels were designated as CaDG10 to CaDG100, corresponding to the respective Ca^{2+} concentrations. Upon Ca^{2+} incorporation, the initially transparent hydrogels became opaque, indicating ion-mediated crosslinking within the network.

3.4.2. Characterization and mechanical property evaluation of the hydrogels

Microscopic analyses were performed after diluting each hydrogel to the desired concentration, followed by the preparation of thin films via uniform drop-casting onto either glass substrates or carbon film-supported copper grids. For spectroscopic and zeta potential measurements, the hydrogels were similarly diluted with Milli-Q water to the appropriate concentrations. FT-IR spectra were recorded directly from the hydrogel samples using an ATR accessory, with water baseline correction applied to minimize solvent interference. Powder X-ray diffraction (pXRD) analyses were conducted on the corresponding freeze-dried xerogel samples of each hydrogel system.

Dynamic strain sweep experiments were conducted at a fixed angular frequency (ω= 10 rad.s^{-1}), while frequency sweep measurements were performed at a constant strain (γ = 1%) and temperature of 25 °C. Concentration-dependent rheological studies were also carried out by comparing the corresponding storage and loss moduli obtained from strain sweep measurements at a fixed strain. Thixotropic step-strain tests were performed over defined time intervals by alternating low and high strain values at a constant angular frequency of 10 rad s^{-1}, showing the structural integrity and injectability of the hydrogels.

3.4.3. Drug encapsulation and sustained release experiments

Both doxorubicin (Dox) and camptothecin (CPT) were introduced into the hydrogel precursor solution at a concentration of 1 mg mL^{-1} prior to gelation. Both hydrophilic (Dox) and hydrophobic (CPT) drugs were efficiently encapsulated within the forming hydrogel matrix, indicating a spontaneous and uniform entrapment mechanism across all hydrogel formulations. Following a cooling and aging period of approximately 10 minutes, self-standing and mechanically stable drug-loaded hydrogels were obtained. These systems were subsequently utilized to investigate the encapsulation efficiency and sustained release behavior of the embedded drugs. To investigate the encapsulation

efficiency, the hydrogels were carefully washed with 3 mL of phosphate-buffered saline (PBS, pH 7.4) to eliminate any unbound or loosely adsorbed drug molecules. The absorbance of the collected washings (supernatant) was recorded using a UV-visible spectrophotometer. The effective amount of drug encapsulated within the hydrogel matrix was determined by subtracting the quantity of unbound drug (measured in the supernatant) from the initial amount added. The percentage of drug loading was then calculated using the following relation:

$$\text{Encapsulation Efficiency} = \frac{Amount\ of\ drug\ present\ after\ washing}{Initial\ amount\ of\ drug\ loaded} \times 100$$

Table 3.1. *Encapsulation efficiency calculation for Dox*

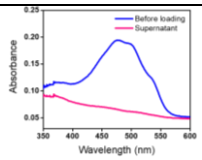
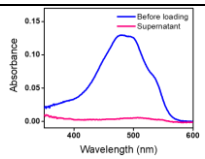
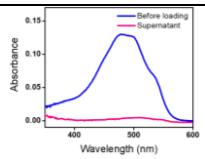
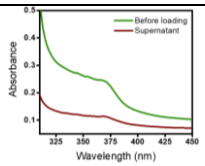
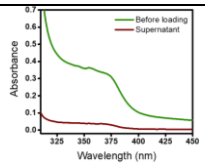
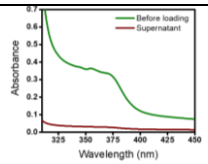
Hydrogel	**DG**	**GDG**	**CaDG**
UV curve			
Linear Eq.*	$y = 4.71123x + 0.08571$	$y = 4.71123x + 0.08571$	$y = 4.71123x + 0.08571$
Abs# $\mathbf{C_1}$ (Initial)	0.19417	0.12827	0.12827
Abs# $\mathbf{C_2}$ (Supernatant)	0.06608	0.00366	0.00233
EE Eq.	$\frac{C_1 - C_2}{C_1} \times 100$	$\frac{C_1 - C_2}{C_1} \times 100$	$\frac{C_1 - C_2}{C_1} \times 100$
EE (%)	**65.97**	**97.14**	**98.18**

Table 3.2. *Encapsulation efficiency calculation for CPT*

Hydrogel	**DG**	**GDG**	**CaDG**
UV curve			
Linear Eq.*	$y = 24.3422x + 0.01014$	$y = 24.3422x + 0.01014$	$y = 24.3422x + 0.01014$
Abs## $\mathbf{C_1}$ (Initial)	0.24657	0.33892	0.34121
Abs## $\mathbf{C_2}$ (Supernatant)	0.11342	0.03658	0.02908
EE Eq.	$\frac{C_1 - C_2}{C_1} \times 100$	$\frac{C_1 - C_2}{C_1} \times 100$	$\frac{C_1 - C_2}{C_1} \times 100$
EE (%)	**54**	**89.2**	**91.47**

* From Calibration Curve # @ 480 nm ## @ 375 nm

To investigate the sustained drug release behavior, the drug-loaded hydrogels were placed in separate glass vials containing 3 mL of phosphate-buffered saline (PBS, 10 mM, pH 4) and incubated at 37 °C.

At predetermined time intervals, 400 µL aliquots were withdrawn from each vial and replaced with an equal volume of fresh PBS to maintain a constant total volume and sink conditions. For CaDG hydrogels, the sampling was performed daily at consistent time points to preserve uniform interval durations across experiments. The absorbance of the collected samples was recorded at 480 nm and 375 nm for Dox and CPT, respectively. To ensure accuracy, all release experiments were conducted in triplicate, and the average values along with standard deviation error bars were used to plot the sustained release profiles. The cumulative percentage of drug release was calculated using the following equation:

$$\text{The cumulative release of drug (\%)} = \frac{M_t}{M_\infty} \times 100$$

Here, M_t and M_∞ represent the amount of drug released at a given time t and the total amount of drug initially encapsulated within the hydrogel, respectively. A linear correlation between the drug concentration and absorbance was obtained from the calibration plots of both drugs. Hence, for simplicity, the absorbance values were directly utilized to determine the cumulative drug release profile.

To assess the anti-leakage stability of the drug-loaded hydrogels, the samples were stored at 4 °C and periodically analyzed over a 28-day period. At each fixed interval, the hydrogels were gently washed with PBS (pH 7.4), and the extent of drug leakage was quantified by measuring the UV-visible absorbance of the resulting supernatant.

3.4.4. The cellular response to the treatment groups

The cytotoxicity of the treatment groups was evaluated using the MTT (3-(4,5-dimethylthiazol-2-yl)-2,5-diphenyltetrazolium bromide) assay. MDA-MB-231 and HEK-293 cells were seeded in 96-well plates at a density of 2×10^4 cells per well and incubated for 24 h to allow cell adherence. Upon reaching approximately 70% confluency, the cells were exposed to six different treatment concentrations ranging from 200 µM to 0 µM and incubated for an additional 24 h. After treatment, MTT solution (10 mg mL^{-1}) was added to each well and incubated for

4 h to facilitate the formation of formazan crystals. The resulting crystals were then solubilized in 200 µL of DMSO per well, and the absorbance was measured at 570 nm using a microplate reader. Wells treated with 0 µM served as the control group for calculating relative cell viability. The cell viability in percentage was obtained using the following equation.

$$\%\ viable\ cells = \frac{(A570 - A690)\ of treated\ cells}{(A570 - A690)\ of\ control\ cells} \times 100$$

3.4.5. The effect of the treatment groups on MDA-MB-231 spheroids

MDA-MB-231 tumor spheroids were generated by seeding 5,000 cells per well onto an agarose-coated 96-well plate, followed by centrifugation at 1,200 rpm for 5 minutes to promote cell aggregation and facilitate spheroid formation through enhanced cell–cell interactions. The spheroids were then incubated in a humidified atmosphere containing 5% CO_2 at 37 ℃. The culture medium was replaced every two days, and spheroid growth was maintained for approximately 7 days. Subsequently, the matured spheroids were treated with camptothecin (CPT)-loaded formulations at concentrations of 2 µM and 5 µM for 48 hours. Post-treatment morphological alterations were observed using a brightfield digital inverted fluorescence microscope, and representative images were captured for analysis.

3.4.6. Examining cellular apoptosis induced by the treatment groups in the spheroids using the AO/PI staining method

Cellular apoptosis and necrosis were evaluated using the acridine orange/propidium iodide (AO/PI) dual staining method. AO and PI were prepared at concentrations of 15 µg mL^{-1} and 30 µg mL^{-1}, respectively, and subsequently mixed with the cell culture medium to stain the treated spheroids. The spheroids were incubated in the staining solution for 30 minutes under standard culture conditions. After incubation, the samples were gently washed with PBS and examined using digital

inverted fluorescence microscope to visualize live (green) and dead (red) cell populations.

3.4.7. Statistical Analysis

All the biological experiments were performed in three independent replicates (n=3). The data were represented as mean ± S.E. Statistical analysis were performed using GraphPad Prism 9 (GraphPad Software, San Diego, CA, USA). The significance was obtained by using two-way ANOVA followed by an appropriate multiple comparison test.

3.5. References

1. Vargason, A.M., Anselmo et al. (2021), The evolution of commercial drug delivery technologies, Nat Biomed Eng, 5, 951–967 (DOI: 10.1038/s41551-021-00698-w.)

2. Langer, R. (1993), Polymer-controlled drug delivery systems. Acc. Chem. Res., 26, 537–542. (DOI: 10.1021/ar00034a004.)

3. Pakulska, M.M., Miersch, et al. (2016), Designer protein delivery: From natural to engineered affinity-controlled release systems, Science, 351, aac4750. (DOI: 10.1126/science.aac4750.)

4. Kamaly, N., Yameen et al. (2016), Degradable Controlled-Release Polymers and Polymeric Nanoparticles: Mechanisms of Controlling Drug Release, Chem. Rev., 116, 2602–2663 (DOI: 10.1021/acs.chemrev.5b00346.)

5. Senapati, S., Mahanta et al. (2018), Controlled drug delivery vehicles for cancer treatment and their performance, Sig Transduct Target Ther, 3, 7 (DOI: 10.1038/s41392-017-0004-3.)

6. Juthani, R., Punatar et al. (2024), New light on chemotherapy toxicity and its prevention, BJC Rep, 2, 41 (DOI: 10.1038/s44276-024-00064-8.)

7. Woodring, R.N., Gurysh et al. (2023), Drug Delivery Systems for Localized Cancer Combination Therapy, ACS Appl. Bio Mater., 6, 934–950 (DOI: 10.1021/acsabm.2c00973.)

8. Yoon, M.S., Lee et al. (2020), Recent Advances and Challenges in Controlling the Spatiotemporal Release of Combinatorial Anticancer Drugs from Nanoparticles, Pharmaceutics, 12, 1156 (DOI: 10.3390/pharmaceutics12121156.)

9. Lounkine, E., Keiser et al. (2012), Large-scale prediction and testing of drug activity on side-effect targets, Nature, 486, 361–367 (DOI: 10.1038/nature11159.)

10. Ashley, G.W., Henise et al. (2013), Hydrogel drug delivery system with predictable and tunable drug release and degradation rates, Proceedings of the National Academy of Sciences, 110, 2318–2323 (DOI: 10.1073/pnas.1215498110.)

11. Trucillo, P. (2022), Drug Carriers: A Review on the Most Used Mathematical Models for Drug Release, Processes, 10, 1094 (DOI: 10.3390/pr10061094.)

12. Lin, C.-C.,, Metters et al. (2006), Hydrogels in controlled release formulations: Network design and mathematical modeling, Advanced Drug Delivery Reviews, 58, 1379–1408 (DOI: 10.1016/j.addr.2006.09.004.)

13. Amsden, B. (1998), Solute Diffusion within Hydrogels, Mechanisms and Models. Macromolecules, 31, 8382–8395 (DOI: 10.1021/ma980765f.)

14. Axpe, E., Chan et al. (2019), A Multiscale Model for Solute Diffusion in Hydrogels, Macromolecules, 52, 6889–6897 (DOI: 10.1021/acs.macromol.9b00753.)

15. Laracuente, M.-L., Yu et al. (2020), Zero-order drug delivery: State of the art and future prospects, Journal of Controlled Release, 327, 834–856 (DOI: 10.1016/j.jconrel.2020.09.020.)

16. Uhrich, K.E., Cannizzaro et al. (1999), Polymeric Systems for Controlled Drug Release, Chem. Rev., 99, 3181–3198 (DOI: 10.1021/cr940351u.)

17. Neubi, G.M.N., Opoku-Damoah et al. (2018), Bio-inspired drug delivery systems: an emerging platform for targeted cancer therapy, Biomaterials Science, 6, 958–973 (DOI: 10.1039/C8BM00175H.)

18. Xu, Y., Chen et al. (2025), Synthetic Polymers for Drug, Gene, and Vaccine Delivery, Polymer Science & Technology, 1, 171–220 (DOI: 10.1021/polymscitech.5c00010.)

19. Lee, J.H., Yeo et al. (2015), Controlled drug release from pharmaceutical nanocarriers, Chemical Engineering Science, 125, 75–84 (DOI: 10.1016/j.ces.2014.08.046.)

20. Zhu, Q., Qi et al. (2016), Extracellular control of intracellular drug release for enhanced safety of anti-cancer chemotherapy, Sci Rep, 6, 28596 (DOI: 10.1038/srep28596.)

21. Cera, L., Schalley et al. (2018), Under Diffusion Control: from Structuring Matter to Directional Motion, Advanced Materials, 30, 1707029 (DOI: 10.1002/adma.201707029.)

22. Sokolsky-Papkov, M., Agashi et al. (2007), Polymer carriers for drug delivery in tissue engineering, Advanced Drug Delivery Reviews, 59, 187–206 (DOI: 10.1016/j.addr.2007.04.001.)

23. Pappalardo, D., Mathisen et al. (2019), Biocompatibility of Resorbable Polymers: A Historical Perspective and Framework for the Future, Biomacromolecules, 20, 1465–1477 (DOI: 10.1021/acs.biomac.9b00159.)

24. Zhang, X., Chen et al. (2023), Bioinspired oral delivery devices, Nat Rev Bioeng, 1, 208–225 (DOI: 10.1038/s44222-022-00006-4.)

25. Saboktakin, M., Tabatabaei et al. (2015), Supramolecular hydrogels as drug delivery systems, International Journal of Biological Macromolecules, 75, 426–436 (DOI: 10.1016/j.ijbiomac.2015.02.006.)

26. Zhang, X., Zhuo et al. (2025), Supramolecular Polymers for Drug Delivery, Chem. Eur. J., 31, e202404617. (DOI: 10.1002/chem.202404617)

27. Bera, S., Datta et al. (2023), An injectable supramolecular hydrogel as a self-drug-delivery system for local chemoimmunotherapy against melanoma, Biomater. Sci., 11, 5618–5633 (DOI: 10.1039/D3BM00758H.)

28. Roh, Y.H., Ruiz et al. (2011), Engineering DNA-based functional materials, Chem. Soc. Rev., 40, 5730–5744 (DOI: 10.1039/C1CS15162B.)

29. Wang, D., Hu et al. (2017), Bioresponsive DNA Hydrogels: Beyond the Conventional Stimuli Responsiveness, Acc. Chem. Res., 50, 733–739 (DOI: 10.1021/acs.accounts.6b00581.)

30. Wang, D., Cui et al. (2020), Transformation of Biomass DNA into Biodegradable Materials from Gels to Plastics for Reducing Petrochemical Consumption, J. Am. Chem. Soc., 142, 10114–10124 (DOI: 10.1021/jacs.0c02438.)

31. Sarma, S., Thakur et al. (2024), Chromatin inspired bio-condensation between biomass DNA and guanosine monophosphate produces all-nucleic hydrogel as a hydrotropic drug carrier, Commun Chem, 7, 261 (DOI: 10.1038/s42004-024-01353-6.)

32. Li, K., Yatsunyk et al. (2021), Water spines and networks in G-quadruplex structures, Nucleic Acids Res, 49, 519–528 (DOI: 10.1093/nar/gkaa1177.)

33. Bisht, A., Avinash et al. (2025), A comprehensive review on doxorubicin: mechanisms, toxicity, clinical trials, combination therapies and nanoformulations in breast cancer, Drug Deliv. and Transl. Res., 15, 102–133 (DOI: 10.1007/s13346-024-01648-0.)

34. Rivankar, S. (2014), An overview of doxorubicin formulations in cancer therapy, Journal of Cancer Research and Therapeutics, 10, 853 (DOI: 10.4103/0973-1482.139267.)

35. Pérez-Ortega, H.U., Córdova-Espíritu et al. (2025), Camptothecin in Cancer Therapy: Current Challenges and Emerging Strategies with Nanoemulsions, Pharmaceutics, 17, 1414 (DOI: 10.3390/pharmaceutics17111414.)

36. Gong, J., Zhang et al. (2025), Camptothein-Based Anti-Cancer Therapies and Strategies to Improve Their Therapeutic Index, Cancers, 17, 1032 (DOI: 10.3390/cancers17061032.)

37. Duan, Y., Liu et al. (2024), The Role of the CPT Family in Cancer: Searching for New Therapeutic Strategies, Biology, 13, 892 (DOI: 10.3390/biology13110892.)

38. Detellier, C.,, Laszlo et al. (1980), Role of alkali metal and ammonium cations in the self-assembly of the 5’-guanosine monophosphate dianion, J. Am. Chem. Soc., 102, 1135–1141 (DOI: 10.1021/ja00523a033.)

39. Harraz, D.M., Davis et al. (2018), A self-assembled peroxidase from 5′-GMP and heme, Chem. Commun., 54, 1587–1590 (DOI: 10.1039/C7CC09900B.)

40. Lu, S., Wang et al. (2010), Insoluble and Flexible Silk Films Containing Glycerol, Biomacromolecules, 11, 143–150 (DOI: 10.1021/bm900993n.)

41. De Giglio, E., Bonifacio et al. (2015), Exploiting a new glycerol-based copolymer as a route to wound healing: Synthesis, characterization and biocompatibility assessment, Colloids and Surfaces B: Biointerfaces, 136, 600–611 (DOI: 10.1016/j.colsurfb.2015.09.048.)

42. Koca Fındık, B., Jafari et al. (2024), Binding of Phosphate Species to Ca2+ and Mg2+ in Aqueous Solution, J. Chem. Theory Comput., 20, 4298–4307 (DOI: 10.1021/acs.jctc.4c00218.)

43. Thakur, N., Sharma et al. (2019), Biocompatible Fe3+ and Ca2+ Dual Cross-Linked G-Quadruplex Hydrogels as Effective Drug Delivery System for pH-Responsive Sustained Zero-Order Release of Doxorubicin, ACS Appl. Bio Mater., 2, 3300–3311 (DOI: 10.1021/acsabm.9b00334.)

44. Chakraborty, A., Rani et al. (2025), Guanosine Monophosphate Induced Solubilization of Folic Acid Leading to Hydrogel Formation for Targeted Delivery of Hydrophilic and Hydrophobic Drugs, ACS Appl. Mater. Interfaces, 17, 11848–11860 (DOI: 10.1021/acsami.4c21306.)

45. Panda, M., Walmsley et al. (2011), Circular Dichroism Study of Supramolecular Assemblies of Guanosine 5′-Monophosphate, J. Phys. Chem. B, 115, 6377–6383 (DOI: 10.1021/jp201630g.)

46. Mohanty, J., Barooah et al. (2013), Thioflavin T as an Efficient Inducer and Selective Fluorescent Sensor for the Human Telomeric G-Quadruplex DNA, J. Am. Chem. Soc., 135, 367–376 (DOI: 10.1021/ja309588h.)

47. Thakur, N., Sarma et al. (2025), Acidic Amino Acid Induced 5′-Guanosine Monophosphate Fibrillar Nanozyme: A Highly Efficient Metal-Free Intrinsic Peroxidase Mimic, Nano Lett., 25, 15407–15415 (DOI: 10.1021/acs.nanolett.5c04390.)

48. Sarma, S., Jain et al. (2025), Supramolecular Self-Assembly of Polyaniline Embedded Enzyme-Mimicking GMP-Condensate Hydrogel for Electrochromic Energy Storage Applications, ACS Appl. Mater. Interfaces, 17, 48532–48546 (DOI: 10.1021/acsami.5c08151.)

49. Thakur, N., Chaudhary et al. (2021), Ion Conductive Phytic Acid-G Quadruplex Hydrogel as Electrolyte for Flexible Electrochromic Device, ChemNanoMat, 7, 613–619 (DOI: 10.1002/cnma.202100072.)

50. Possenti, E., Colombo et al. (2021), Time-Resolved ATR–FTIR Spectroscopy and Macro ATR–FTIR Spectroscopic Imaging of Inorganic Treatments for Stone Conservation, Anal. Chem., 93, 14635–14642 (DOI: 10.1021/acs.analchem.1c02392.)

51. Nosenko, V., Strutynska et al. (2015), Structure of Biocompatible Coatings Produced from Hydroxyapatite Nanoparticles by Detonation Spraying, Nanoscale Res Lett, 10, 464 (DOI: 10.1186/s11671-015-1160-4.)

52. Yuk, H., Wu et al. (2022), Hydrogel interfaces for merging humans and machines, Nat Rev Mater, 7, 935–952 (DOI: 10.1038/s41578-022-00483-4.)

53. Carvalho, J., Mergny et al. (2020), G-quadruplex, Friend or Foe: The Role of the G-quartet in Anticancer Strategies, Trends in Molecular Medicine, 26, 848–861 (DOI: 10.1016/j.molmed.2020.05.002.)

54. Spiegel, J., Adhikari et al. (2020), The Structure and Function of DNA G-Quadruplexes, Trends in Chemistry, 2, 123–136 (DOI: 10.1016/j.trechm.2019.07.002.)

55. Kciuk, M., Gielecińska et al. (2023), Doxorubicin—An Agent with Multiple Mechanisms of Anticancer Activity, Cells, 12, 659 (DOI: 10.3390/cells12040659.)

56. Nam, K., Kim et al. (2023), Crystallinity-tuned ultrasoft polymeric DNA networks for controlled release of anticancer drugs, Journal of Controlled Release, 355, 7–17 (DOI: 10.1016/j.jconrel.2023.01.056.)

57. Huang, Q., Wang et al. (2013), Evolution in medicinal chemistry of E-ring-modified Camptothecin analogs as anticancer agents, European Journal of Medicinal Chemistry, 63, 746–757 (DOI: 10.1016/j.ejmech.2013.01.058.)

58. Stockert, J.C., Blázquez-Castro et al. (2023), Updating Ortho- and Metachromatic Acridine Orange Fluorescence in Cytochemical Chromosome Staining: A Proposal for Understanding Its Differential Fluorescence on Double- and Single-Stranded Nucleic Acids Substrates Based on Intercalation, Chemosensors, 11, 540 (DOI: 10.3390/chemosensors11100540.)

59. Pinton, P., Giorgi et al. (2008), Calcium and apoptosis: ER-mitochondria Ca2+ transfer in the control of apoptosis, Oncogene, 27, 6407–6418 (DOI: 10.1038/onc.2008.308.)

60. Pörn-Ares, M.I., Ares et al. (1998), Calcium Signalling and the Regulation of Apoptosis, Toxicology in Vitro, 12, 539–543 (DOI: 10.1016/S0887-2333(98)00032-0.)

61. Lee, J., Park, S., Lee et al. (2023), Development of Silk Fibroin-Based Non-Crosslinking Thermosensitive Bioinks for 3D

Bioprinting, Polymers, 15, 3567 (DOI: 10.3390/polym15173567)

62. Lin, C., Chiu, J. (2021), Glycerol-modified γ-PGA and gellan composite hydrogel materials with tunable physicochemical and thermal properties for soft tissue engineering application, Polymer, 230, 124049 (DOI: 10.1016/j.polymer.2021.124049.)

Chapter 4

4. Enzyme-Mimicking "All-Nucleotide" G-Quadruplex Hydrogel as a Dual-Function Microreactor for Biomimetic Cascade Catalysis

4.1. Introduction

Biological systems harness the spatial organization of macromolecules to create confined microenvironments that regulate complex chemical transformations with precision and efficiency. *[1,2]* In eukaryotic cells, such compartmentalization is achieved through two primary strategies: membrane-bound organelles formed by lipid bilayers *[3]*, and membraneless compartments, where macromolecules spontaneously condense into dense phases via liquid-liquid phase separation (LLPS) *[4]*. These biomolecular condensates function as microreactors that enhance local substrate concentrations and facilitate efficient enzymatic cascade reactions through substrate and product enrichment. *[5,6]* Inspired by these strategies, significant research efforts have been focused on developing synthetic cell analogues as functional platforms for cell-like biocatalytic cascades. *[7]*

Among the synthetic systems, supramolecular hydrogels have emerged as promising biomimetic microreactors due to their hydrated, tissue-like mechanical properties and tuneable architectures. These hydrogels recapitulate key intracellular features, such as macromolecular confinement, molecular crowding, and dynamic interactions. Their fibrillar, porous microenvironments enable seamless encapsulation of bioactive macromolecules like native enzymes with their preserved activity. *[8-12]* Thus, supramolecular hydrogels offer superior advantages over rigid porous systems like MOFs *[13]*,

providing the dynamic features essential for synthetic biocatalytic microreactors *[14]*. However, most reported hydrogel systems depend on complex synthetic components *[15]*, external crosslinkers *[16]*, or metal ions *[17]* to achieve catalytic function. These limitations compromise their simplicity, biocompatibility, and relevance to primitive biological systems. Therefore, developing minimalistic, fully biomolecule-based hydrogels that integrate structural organization with catalytic activity remains a key challenge, advancing biomimetic catalytic systems.

Nucleotides, as fundamental building blocks of life, offer an ideal platform for constructing hierarchical synthetic condensates. Their multiple interaction sites enable both biocatalytic functionality and the formation of biomimetic crowded microenvironments. *[18,19]* In particular, guanosine monophosphate (5′-GMP) exhibits a strong propensity to self-assemble into non-covalent superstructures, including G-monomer aggregates, G-dimers, and G-quadruplex (G4) motifs, driven by Hoogsteen hydrogen bonding and π–π stacking interactions. Notably, G4 assemblies further organize into higher-order columnar scaffolds, enabling functional materials. *[20-23]* Our recent study demonstrated that organic acid- and amino acid-induced GMP fibrillar condensates exhibit intrinsic peroxidase-mimetic activity by stabilizing reactive intermediates, elevating local substrate concentrations within the fibrillar matrix, and driving efficient transformations. *[24,25]* Despite these advances, nucleotide-based assemblies typically require external cofactors and the potential of fully nucleotide-driven, hierarchical condensates for integrated catalysis is largely underexplored.

Herein, we report a minimalistic “all-nucleotide” condensation strategy that leverages cooperative interactions between guanosine 5′-monophosphate (GMP) and adenosine phosphate derivatives (AMP, ADP, and ATP) to generate hierarchically organized supramolecular networks. While GMP serves as the primary structural unit, forming G-

quadruplex assemblies, the adenosine phosphate derivatives act as modulators of the assembly process through their phosphate multiplicity and intrinsic acidity. While AMP is unable to proceed this condensation, both ADP and ATP drive hierarchical biomolecular condensation. This spontaneous biomolecular condensation mimics a biogenic phase separation pathway, enabling a concentration-dependent transition from liquid-like spherical intermediates to fibrillar networks. *[24,26]* Interestingly, upon higher-order self-assembly, the resulting ADP-GMP (ADG) and ATP-GMP (ATG) fibrillar condensates form self-standing, stable hydrogels, providing physical evidence of extensive organization.

Unlike conventional hydrogel-based catalytic platforms that often rely on immobilized enzymes or metal cofactors *[27-30]*, the proposed "all-nucleotide" ADG/ATG system derives its catalytic functionality directly from the G4-rich architecture. The stacked G4 domains create a microenvironment capable of stabilizing reactive intermediates, thereby enabling intrinsic peroxidase-mimicking activity in a completely metal-free and non-proteinaceous system. *[24]* A key novelty of this condensate/hydrogel lies in its dual functionality for biocatalytic applications. The ADG hydrogel acts as a biomimetic microenvironment, providing hydrated confinement for enzyme encapsulation and stabilization, while simultaneously functioning as an active catalytic scaffold that mimics enzymatic activity.[31] To demonstrate this, the hydrogel efficiently hosts multiple enzymes, including β-galactosidase and glucose oxidase, enabling two- and three-step cascade reactions in which enzymatic transformations are seamlessly coupled with hydrogel-mediated catalysis. The confined microenvironment enhances substrate channelling, reduces diffusion limitations, and improves overall reaction kinetics.[7,32] This integration of structural confinement and intrinsic catalysis within a minimalistic platform establishes a versatile route to biogenic artificial microreactors for complex biochemical transformations.[33,34] Collectively, the simplicity, modularity, and multifunctionality of the "all-nucleotide" hydrogel provide new opportunities for designing

biomimetic catalytic systems based on condensation-driven self-assembly.

4.2. Results and Discussions

4.2.1. Design Concept and Biogenic Condensation

Inspired by biomolecular condensation in cellar milieu, we designed a "all-nucleotide" platform that undergoes spontaneous condensation and hierarchical self-assembly to form structurally and functionally relevant architectures.[4,35] Guanosine 5'-monophosphate (GMP) was selected as the core building block due to its propensity for acid-triggered self-assembly into G-quadruplexes (G4s) via Hoogsteen hydrogen bonding and π-π stacking.[24,36] An all-nucleotide matrix was created, and assembly dynamics were modulated, using adenosine phosphate derivatives (AMP, ADP and ATP) as anticipated cooperative inducers that enhance intermolecular interactions upon integration. This simple two-component system enables controlled condensation and provides a biomimetic framework for studying structure-function relationships in nucleotide-based assemblies (Figure 1a).

Based on this minimalistic design strategy, a spontaneous biogenic condensation occurred upon simple mixing of the two nucleotide constituents under aqueous physiological conditions. Equimolar (100 μM) solutions of GMP-Na2 were mixed with AMP-Na2, ADP-Na2, and ATP-Na2, respectively, yielding three assembly systems: AMG (AMP-GMP), ADG (ADP-GMP), and ATG (ATP-GMP). After 12 hours of incubation, the Tyndall effect was observed in each condensation, confirming colloidal assembly formation (Figure S1). No turbidity or precipitation was observed post-condensation, owing to the high-water solubility of the disodium nucleotide salts.

Condensation morphology was evaluated using FE-SEM micrographs, revealing worm-like structures in the AMG system, whereas fully matured fibrillar morphologies were observed in both ADG and ATG systems (Figure 1b-1d). These findings indicate the

superior cooperative influence of ADP and ATP in promoting condensation. This fibrillar assembly is likely governed by the well-established GMP self-assembly process. *[24-26]* Accordingly, increasing GMP concentration was anticipated to drive higher-order assembly by enhancing G4 stacking and intermolecular interactions.*[37]*

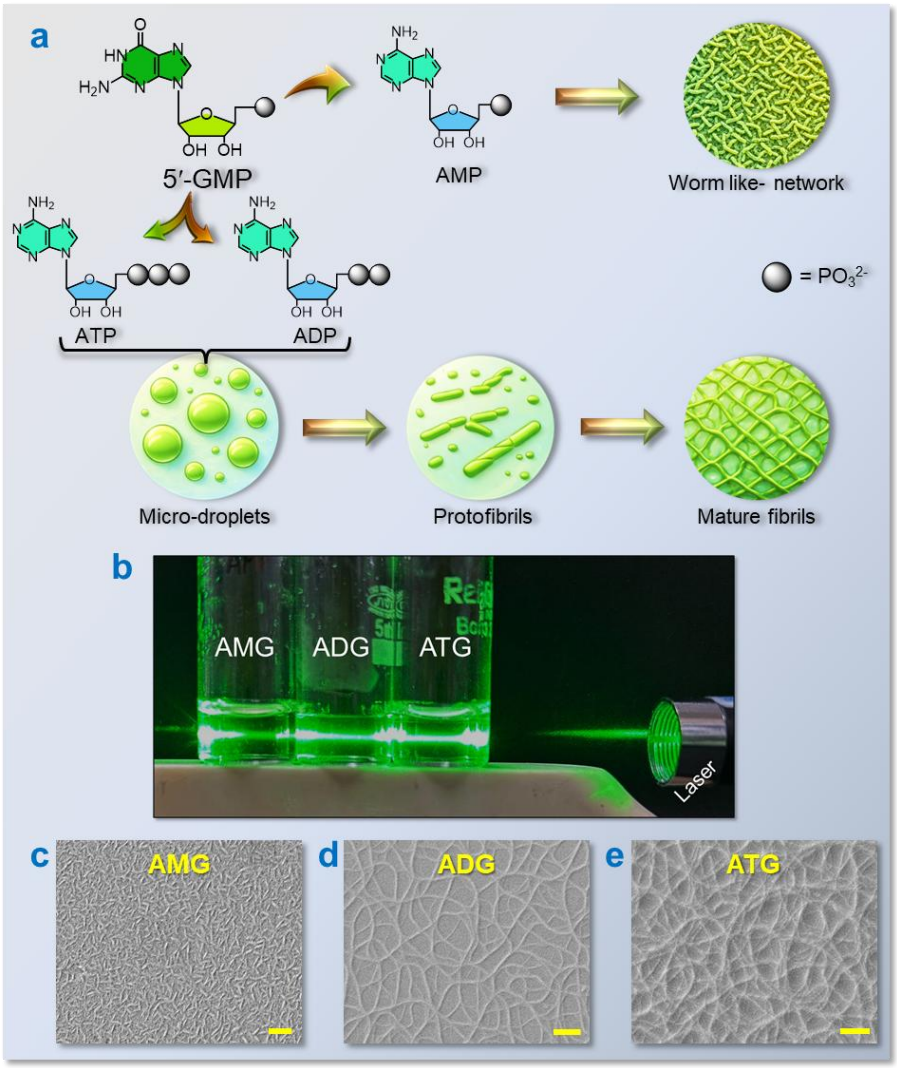


Figure 4.1. *Design concept and morphological outcomes of all-nucleotide assemblies.* ***(a)*** *Schematic illustration of the condensation strategy showing the interaction of guanosine 5'-monophosphate (5'-GMP) with adenosine phosphate derivatives (AMP, ADP, and ATP). While AMP-GMP (AMG) leads to the formation of worm-like networks, ADP-GMP (ADG) and ATP-GMP (ATG) systems undergo hierarchical pathway (spherical intermediates → protofibrils → fibrillar networks).* ***(b)*** *Photographs demonstrating the Tyndall effect in AMG, ADG, and ATG systems (left to right), confirming their colloidal nature. Assembly concentration: ~100 μM.* ***(c-e)*** *FE-*

SEM micrographs of AMG, ADG, and ATG assemblies showing distinct morphologies, where AMG exhibits disordered worm-like structures, while ADG and ATG display interconnected fibrillar networks. (Scale bars ~ 1 μm)

4.2.2. Morphological Evolution of Nucleotide Assemblies

To elucidate the origin of fibrillar matrix formation and validate the proposed design strategy, we systematically investigated the morphological evolution of each assembly system as a function of GMP concentration using confocal laser scanning microscopy (CLSM). Both ADG and ATG systems exhibited hierarchical morphological evolution with increasing GMP concentrations from 10-100 μM, whereas the AMG system showed minimal changes in self-assembly.

In the ADG and ATG systems, growth initiated from spherical intermediate assemblies at low GMP concentrations of 10 μM, indicative of the formation of a dense nucleotide-rich phase, analogous to biomolecular condensates (**Figure 4.2 a, 4.2 A**). At 30 μM GMP, these droplets coalesced into larger aggregates, reflecting their dynamic liquid-like nature (**Figure 4.2 b, 4.2 B**). At intermediate GMP concentrations (~50 μM), the droplets transitioned to short protofibril structures, marking the onset of anisotropic growth driven by enhanced G-quadruplex stacking and π-π interactions (**Figure 4.2 c, 4.2 C**). Further increase to 70 μM produced interconnected fractal-like networks (**Figure 4.2 d, 4.2 D**), which evolved into dense, highly entangled fibrillar architectures at 100 μM (**Figure 4.2 e, 4.2 E**). These observations establish the spherical intermediates as transient precursors in the hierarchical assembly pathway leading to mature fibrillar condensates at higher GMP concentrations. To probe the cargo-enrichment capability of the transient spherical intermediates, fluorescence colocalization experiments were performed using Thioflavin T (ThT) and the hydrophobic probe Nile Red. At low GMP concentrations, the spherical intermediates exhibited strong Nile Red fluorescence, indicating the presence of hydrophobic microdomains capable of preferential cargo partitioning (**Figure 4.3 a,b**), whereas at intermediate GMP concentrations, the mature fibrillar condensates

selectively stained with ThT while residual spherical intermediates retained Nile Red fluorescence (**Figure 4.3 c,d**), demonstrating a transition from the phase separated spherical intermediates to G4-rich fibrillar networks.

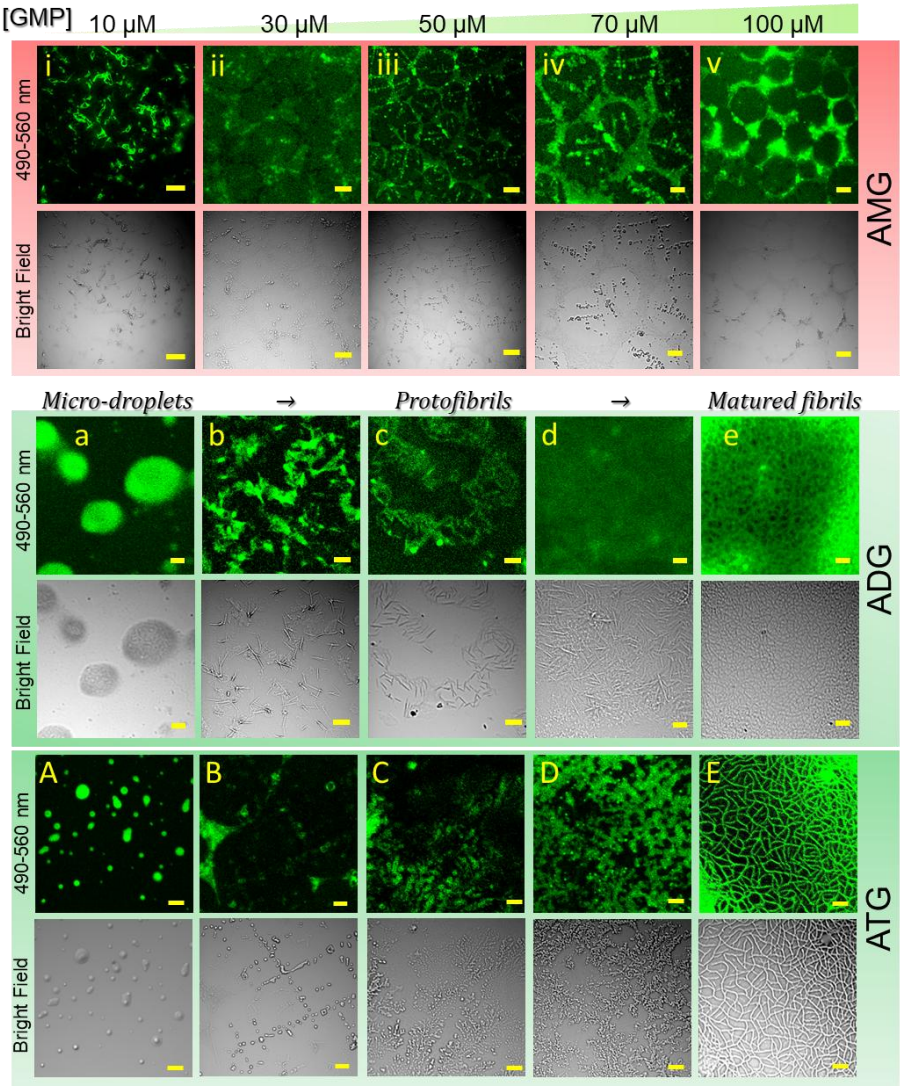


Figure 4.2. *Concentration-dependent morphological evolution of nucleotide condensates varying GMP concentration and keeping the adenosine monophosphate derivatives constant at 100 μM.* ***(i-v)*** *Morphological evolution of AMG system showing only aggregates getting denser with increasing GMP concentration. Morphological evolution of* ***(a-e)*** *for ADG system and* ***(A-E)*** *for ATG system to establish a concentration-dependent hierarchical pathway (spherical intermediates → protofibrils → fibrillar networks). (Scale bar ~ 5 μm)*

In contrast, the AMG system showed no such hierarchical condensation, even at higher concentrations. Instead, it maintained a

similar morphology with denser aggregate-like features throughout, displaying predominantly short, worm-like or sparsely distributed fibrillar structures without forming continuous networks (**Figure 4.2 i-v**). This indicates that AMP, with a monophosphate functionality, limits hierarchical G-quadruplex stacking, whereas ADP and ATP, with their higher phosphate content, promote efficient condensation and robust fibrillar networks. Collectively, these findings establish a concentration-dependent hierarchical pathway (spherical intermediates → protofibrils → fibrillar networks) governed by multivalent interactions and nucleotide composition, closely mimicking biomolecular condensation in cellular systems (**Figure 4.1 a**). Therefore, comprehensive concentration-dependent spectroscopic analysis was performed to elucidate the underlying molecular interactions and chiroptical properties.

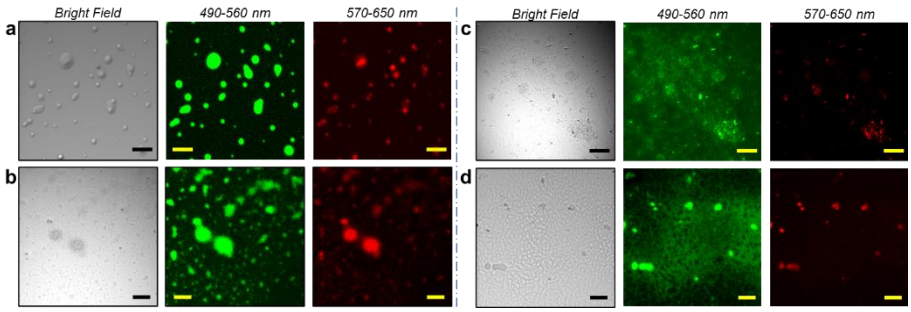


Figure 4.3. *Fluorescence labelling and cargo-enrichment studies of the GMP-concentration-dependent evolution from spherical intermediates to fibrillar assemblies. Bright-field and confocal fluorescence images of ADG* ***(a, c)*** *and ATG* ***(b, d)*** *condensates prepared at low (10 μM;* ***a, b****) and intermediate (50 μM;* ***c, d****) GMP concentrations and stained with Thioflavin T (ThT, green) and Nile Red (red). At 10 μM GMP, the spherical intermediates show strong ThT and Nile Red fluorescence, indicating hydrophobic interiors capable of cargo enrichment and supporting the existence of transient phase-separated spherical intermediates enriched with amphiphilic cargo. At 50 μM GMP, the fibrillar network shows predominantly ThT fluorescence, indicating the development of G-quadruplex-rich fibrillar assemblies, whereas residual spherical intermediates retain both ThT and Nile Red signals, indicating retained hydrophobic interiors. These results suggest that the spherical intermediates act as transient precursors that progressively reorganize into ordered fibrillar assemblies. Scale bars: 5 μm. Dye Concentration ~ 5μM.*

4.2.3. Spectroscopic Characterizations and Molecular mechanism of Condensation

To elucidate the molecular origin of hierarchical fibrillation and growth mechanism of the assemblies, spectroscopic analyses were performed by systematically varying the concentration of GMP, the primary building block of the assembly. UV-visible spectroscopy revealed characteristic absorption bands of GMP (~252 nm) and adenosine derivatives (~258 nm) in close proximity, along with a distinct shoulder at ~275 nm for GMP arising from secondary electronic transitions. Upon mixing, a hypochromic effect at ~275 nm was observed, indicating the onset of intermolecular interactions and early-stage aggregation. Job's plot analysis in this region confirmed a 1:1 stoichiometric ratio between GMP and the adenosine phosphate derivatives, suggesting the formation of well-defined supramolecular complexes (**Figure 4.3**).*[38]*

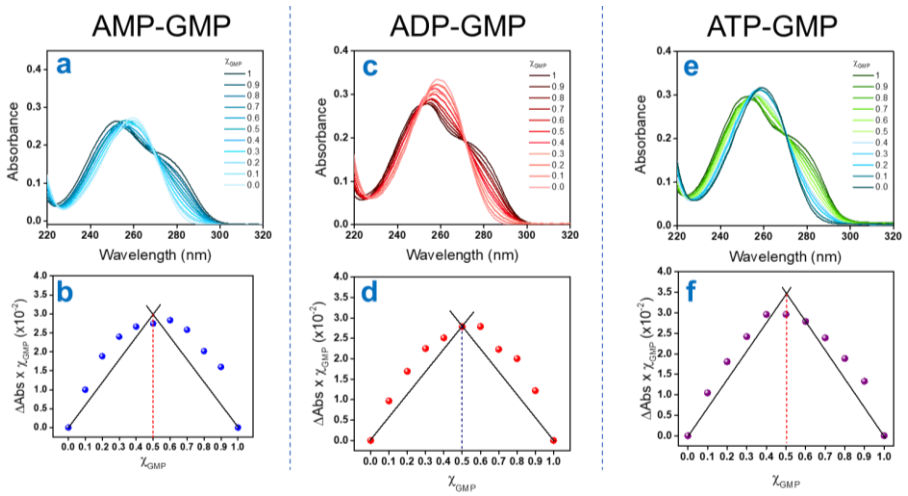


Figure 4.4. *UV-visible absorption spectra and corresponding Job's plots for* ***(a, b)*** *AMP-GMP,* ***(c, d)*** *ADP-GMP, and* ***(e, f)*** *ATP-GMP systems. Stock solutions of GMP and adenosine phosphate derivatives were prepared at 100 μM, and their stoichiometric ratios were systematically varied. ΔAbs was calculated by subtracting the absorbance at each stoichiometric ratio from the maximum observed absorbance*

To probe the structural organization and chiroptical properties of the assemblies, circular dichroism (CD) spectroscopy was employed. The ADG and ATG assemblies exhibited characteristic signatures of antiparallel G-quadruplex structures, with positive Cotton bands at ~300

and ~225 nm and a negative band near 260 nm, confirming the formation of ordered G-quartet stacking (**Figure 4.4 b, c**).*[39,40]* In contrast, the AMG system displayed negligible ellipticity, indicating the absence of significant chiral ordering (**Figure 4.4 a**). Concentration-dependent CD analysis further revealed a progressive enhancement in G4 ellipticity with increasing GMP concentration, establishing that GMP-driven stacking governs the growth of ordered supramolecular architectures, while adenosine derivatives primarily modulate the assembly environment. The maximum chiroptical response observed at a 1:1 stoichiometric ratio highlights the cooperative nature of the interactions and establishes this ratio as optimal for efficient condensation and ordered assembly formation.

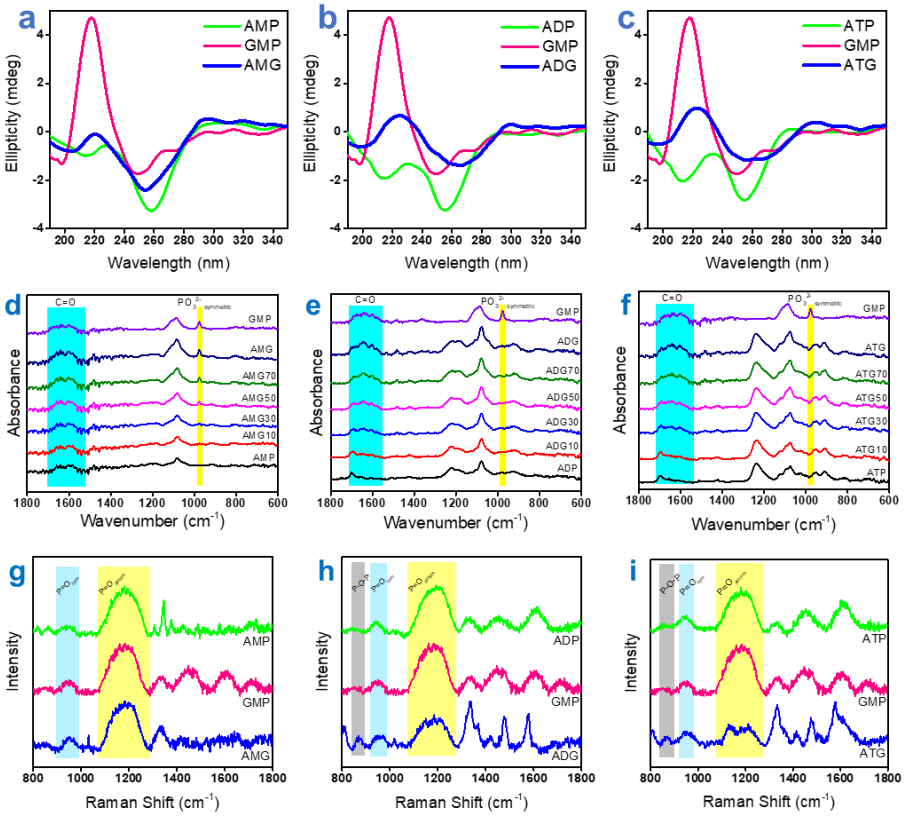


Figure 4.5. *Spectroscopic characterization of G-quadruplex formation and molecular interactions in nucleotide assemblies.* ***(a-c)*** *Circular dichroism (CD) spectra of AMG, ADG, and ATG systems, respectively, showing the chiroptical signatures of the assemblies. (all concentrations were 100 μM)* ***(d-f)*** *ATR-FTIR absorbance spectra of AMG, ADG, and ATG assemblies, respectively, recorded at varying GMP concentrations. Highlighted regions correspond to phosphate (PO_3^{2-}) stretching vibrations and carbonyl (C=O) bands, illustrating progressive spectral changes and*

enhanced intermolecular interactions in ADG and ATG systems compared to AMG. Resonance Raman spectra comparing pristine nucleotides and their corresponding condensates. ***(g)*** *AMP, GMP, and AMP-GMP (AMG) system showing phosphate asymmetric (yellow) and symmetric (blue) stretching bands, with negligible spectral changes upon assembly.* ***(h)*** *ADP, GMP, and ADP-GMP (ADG) and* ***(i)*** *ATP, GMP, and ATP-GMP (ATG) systems exhibiting significant attenuation of the phosphate asymmetric stretching band (yellow) and the emergence of a new P–O–P band (grey), indicating enhanced intermolecular interactions and increased structural rigidity upon condensation.*

As this is an "all-nucleotide" condensation process accompanied by G-quadruplex formation, the involvement of functional groups from both constituents was investigated using ATR-FTIR spectroscopy (**Figure 4.4 d-f**). In the IR spectrum, the pristine GMP spectrum showed PO_3^{2-} symmetric and asymmetric stretching vibrations at ~978 and ~1086 cm^{-1}, respectively, while adenosine derivatives exhibited distinct phosphate bands depending on their phosphate multiplicity.[41] Upon increasing GMP concentration and condensate formation, significant perturbations in the 978 cm^{-1} phosphate band of GMP were observed for ADG and ATG systems, indicating strong intermolecular interactions between phosphate groups of GMP and ADP/ATP. In contrast, minimal spectral changes were observed for the AMG system, suggesting weaker interactions and limited structural reorganization. Additionally, the broadening of the C=O stretching band (~1642 cm^{-1}) with increasing GMP concentration supports enhanced hydrogen bonding and G4 stacking in ADG and ATG systems. To further validate the involvement of phosphate moieties, resonance Raman spectroscopy was performed with emphasis on the phosphate stretching region (**Figure 4.4 g-i**). The ADG and ATG condensates exhibited pronounced attenuation and broadening of the PO_3^{2-} asymmetric stretching band relative to the pristine nucleotides, consistent with increased vibrational coupling arising from multivalent phosphate interactions during ADP/GMP and ATP/GMP condensation. Conversely, negligible spectral changes were observed for the AMG system in the same region, suggesting minimal interaction between the phosphate moieties upon AMP/GMP

condensation. Notably, the emergence of a weak band around ~870 cm^{-1} in ADG and ATG condensates is attributed to P–O–P bridging interactions, indicative of increased structural rigidity within the ordered network.[42] Collectively, these spectroscopic observations provide direct evidence for the critical role of multivalent phosphate interactions in driving G4-mediated condensation and hierarchical assembly. These observations were further corroborated by zeta potential measurements. Pristine nucleotides exhibited negative surface potentials in the range of −25 to −35 mV due to their phosphate-rich surfaces. Upon condensation, ADG and ATG assemblies showed a significant shift toward less negative values (−12.53 mV and −4.23 mV, respectively), whereas AMG displayed only a modest change (−22.51 mV) (**Figure 4.5**). This reduction in surface charge indicates effective masking of negatively charged phosphate groups through multivalent interactions, leading to the formation of compact and ordered supramolecular networks in ADG and ATG systems.

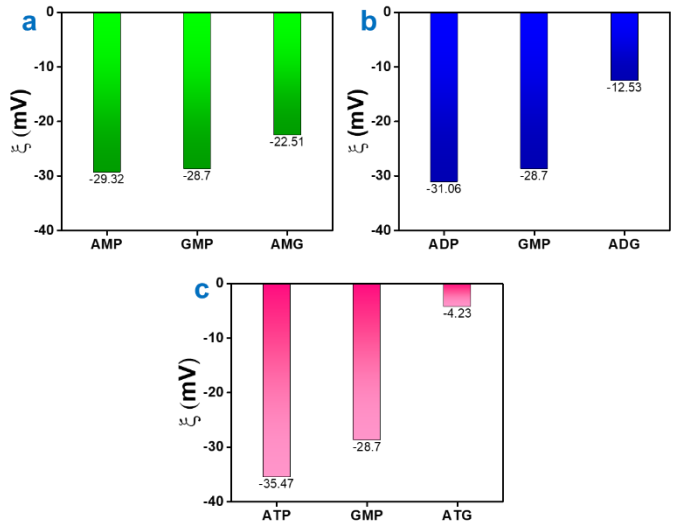


Figure 4.6. *Zeta potential values of the pristine nucleotides and corresponding condensates, illustrating changes in surface charge upon condensation.* ***(a)*** *AMP, GMP, and AMP-GMP (AMG);* ***(b)*** *ADP, GMP, and ADP-GMP (ADG); and* ***(c)*** *ATP, GMP, and ATP-GMP (ATG) systems. All values are reported in mV.*

The extent of π-π stacking and G-driven self-association was quantitatively evaluated using a Thioflavin T (ThT) fluorescence assay. ThT interacts with ordered supramolecular structures through end

stacking, groove binding, or intercalation within GMP channels, restricting intramolecular torsional motion and enhancing fluorescence (**Figure 4.6 a**).*[43.44]* The ThT-loaded condensates exhibited a characteristic emission at ~450 nm (λ_{ex} = 350 nm).*[24]* At an optimal concentration (100 μM), the fluorescence intensity followed the order ADG > ATG > AMG. While ADG and ATG showed comparable FL/FL_0 ratios, AMG exhibited significantly lower enhancement, consistent with minimal stacking as supported by CD and FTIR results (**Figure 4.6 b**). To further establish the role of GMP in governing stacking, concentration-dependent fluorescence studies were carried out. The AMG system showed nearly constant fluorescence intensity across the GMP concentration range (10-100 μM) (**Figure 4.6 c**), whereas ADG and ATG systems exhibited a linear increase in fluorescence intensity with increasing GMP concentration, confirming that stacking and network formation are primarily governed by GMP (**Figure 4.6 d, 4.6 e**). This also reflects the hierarchical development of ordered networks in ADG and ATG systems, while such ordering is absent in the AMG system. Temperature-dependent fluorescence studies further revealed differences in stacking stability. With increasing temperature, fluorescence intensity decreased due to disruption of weakly stacked G-quartets. Notably, the ADG system retained relatively higher fluorescence intensity compared to ATG, indicating a more stable and higher-order stacked architecture (**Figure 4.6 f**). Control experiments varying ADP and ATP concentrations at constant GMP showed only marginal increases in fluorescence intensity, suggesting that adenosine phosphate derivatives play a secondary role in stacking. However, across the entire concentration range (10-100 μM), ADG consistently exhibited higher fluorescence intensity than ATG, indicating more efficient stacking and network formation.

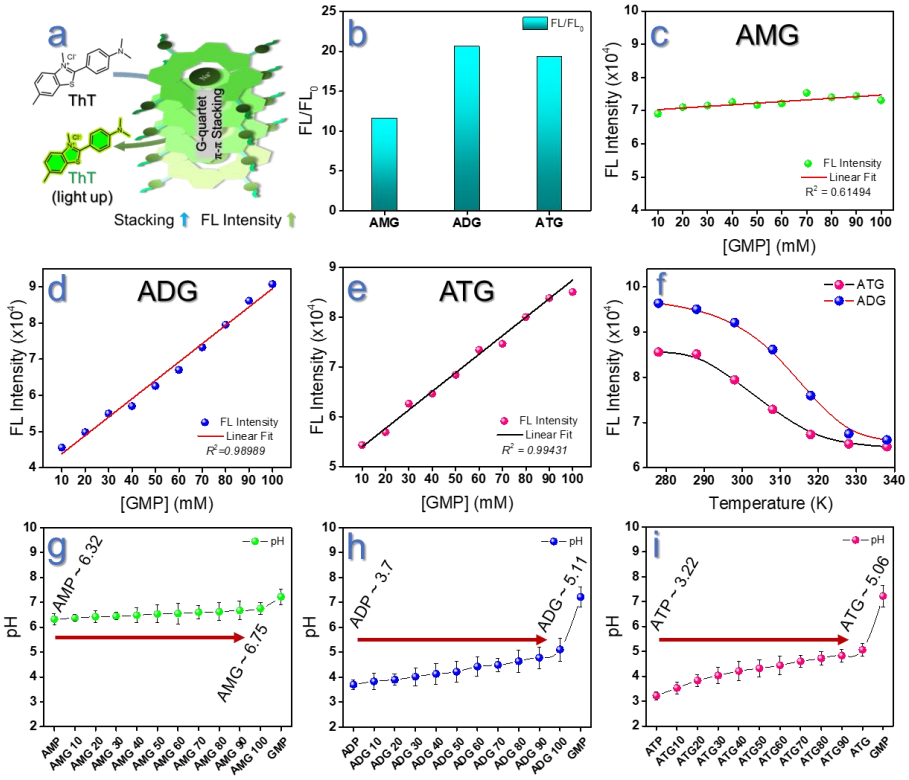


Figure 4.7. *Evaluation of π-π stacking and hierarchical assembly using Thioflavin T (ThT) fluorescence.* ***(a)*** *Schematic illustration of ThT interaction with G-quadruplex channels,* ***(b)*** *Corresponding FL/FL₀ ratio indicating relative fluorescence enhancement compared to free ThT and ThT-loaded AMG, ADG, and ATG condensates at optimal concentration (100 μM),* ***(c-e)*** *Concentration-dependent fluorescence response of AMG, ADG and ATG condensates respectively, with increasing GMP concentration,* ***(f)*** *Temperature-dependent fluorescence behaviour showing reduced intensity upon thermal disruption of G-quartet stacking, with ADG retaining higher stability than ATG.* ***(g-i)*** *Control pH titrations showing the variation in pH with increasing GMP concentration (10-100 μM) at a fixed concentration of adenosine phosphate derivatives (100 μM). The nomenclature AMG10-AMG100 denotes GMP concentrations from 10 to 100 μM in the AMG system, with analogous notation used for ADG and ATG systems.*

Given the strong pH sensitivity of G-quadruplex assembly, we hypothesized that the observed differences in condensation behaviour originate from the intrinsic acidity of the adenosine phosphate derivatives. Previous studies have established that mildly acidic conditions (pH ~3.5-4.5) favour efficient G4 formation. Accordingly, concentration-dependent pH titrations were performed, and the results are shown in **Figure 4.6 g-i**. ADP (pH 3.7) and ATP (pH 3.22) lie within

or near this optimal range, whereas AMP exhibits a near-neutral pH (6.32), which is unfavourable for G4 assembly. Upon addition of GMP, the pH of ADG and ATG systems increased to ~5.11 and ~5.06, respectively, indicating dynamic proton redistribution, while the AMG system remained at a higher pH (~6.75), maintaining an unfavourable environment for G4 formation. Notably, ADP exhibits a more optimal pH alignment than ATP, which rationalizes its ability to form more stable and higher-order stacked assemblies, consistent with fluorescence and morphological observations.

Collectively, these results establish a cooperative condensation mechanism governed by the interplay of π-π stacking, multivalent phosphate interactions, and pH modulation. As the primary structural unit, GMP forms G-quadruplex (G4) assemblies via stacking and Hoogsteen hydrogen bonding (**Figure 4.8**). ADP and ATP, with their higher phosphate content and intrinsic acidity, generate a favourable microenvironment that enhances proton-mediated interactions and efficient G4 stacking. Notably, ADP yields more stable, higher-order stacking than ATP due to better pH alignment within the optimal G4 assembly window. The assembly follows a hierarchical pathway: phase separation drives spherical intermediate formation, followed by protofibril nucleation and interconnected fibrillar networks. Spectroscopic and fluorescence studies showed that the GMP concentration controls stacking extent, while adenosine derivatives modulate the assembly environment without directly participating in self-assembly. In contrast, AMP shows limited condensation due to its lower charge density and near-neutral pH, yielding less organized structures. Overall, this reveals a GMP-driven, pH-regulated, phosphate-assisted pathway to stable "all-nucleotide" supramolecular networks *[24, 26, 45-48]*

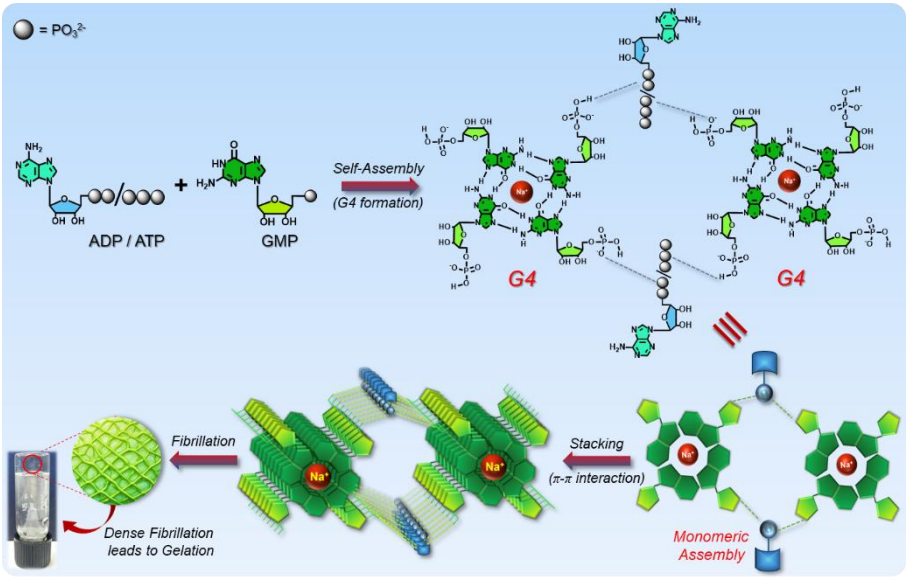


Figure 4.8. *Proposed mechanistic illustration of GMP-driven G-quadruplex formation and π-π stacking, facilitated by multivalent phosphate interactions, leading to hierarchical fibrillar assembly and hydrogel formation.*

4.2.4. Hierarchical Fibrillation Driving Hydrogel Formation

Prompted by the hierarchical assembly behaviour observed in the ADG and ATG systems, the potential for interconnected fibrillar networks to induce macroscopic gelation was investigated. Notably, both ADG and ATG systems, which exhibited dense and highly entangled fibrillar architectures at higher concentrations (x 1000) of constituents, underwent a sol-to-gel transition, forming self-supporting hydrogels (**Figure 4.8 a**). In contrast, the AMG system, characterized by disordered worm-like or sparsely distributed structures, failed to form a stable gel and remained as a weakly aggregated solution. Both ADG and ATG systems demonstrated robust gelation over a wide concentration range, with minimum gelation concentrations of 50 mM for ADP/ATP and 80 mM for GMP (**Figure 4.8 b**). This broad gelation window can be attributed to enhanced fibrillation at higher GMP concentrations, where dense and interconnected fibrillar networks facilitate hydrogel formation through effective network percolation.

The mechanical stability of the hydrogels was further evaluated using oscillatory rheology. Solid-like viscoelastic behaviour was displayed by both ADG and ATG hydrogels, with storage modulus (G″)

exceeding loss modulus (G′) across a broad linear viscoelastic regime (strain: 0.1-100%; **Figure 4.8 c**) and angular frequency range (0.1-100 rad.s^{-1}; **Figure 4.8 d**). Rapid reversible gel-sol-gel self-healing was also exhibited by the hydrogels (**Figure 4.9 a,b**), confirming the network formation via dynamic non-covalent interactions into robust, well-developed gel architectures. Collectively, these findings provide strong evidence that favourable condensation in ADG and ATG systems leads to uniform fibrillar assembly, which transitions into mechanically robust hydrogels at higher concentrations. In contrast, the limited condensation efficiency in the AMG system results in the absence of gelation, even at elevated concentrations, highlighting the critical role of multivalent interactions and hierarchical fibrillation in driving hydrogel formation.

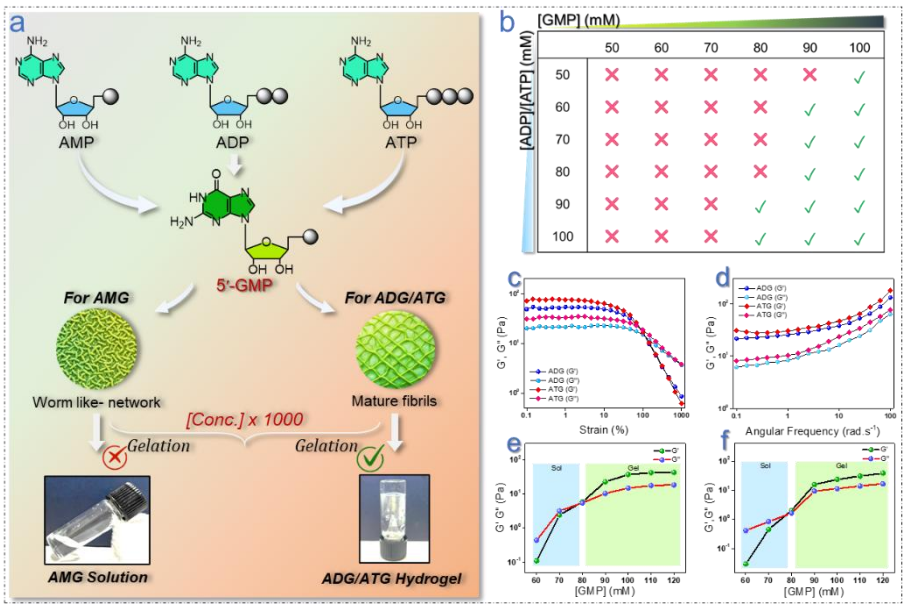


Figure 4.9. *Hydrogel formation and rheological characterization of nucleotide condensates.* ***(a)*** *Schematic illustration of concentration-dependent gelation, showing that GMP-driven fibrillation in ADG and ATG systems leads to the formation of self-supporting hydrogels, whereas AMG forms only worm-like networks and remains in the sol state.* ***(b)*** *Diagram depicting gelation (✓) and non-gelation (✗) as a function of concentration, highlighting the critical threshold required for hydrogel formation.* ***(c)*** *Amplitude (strain) sweep measurements showing storage modulus (G') and loss modulus (G"), demonstrating a wide linear viscoelastic region.* ***(d)*** *Frequency sweep measurements confirming dominant elastic behaviour (G' > G") over a broad frequency range.* ***(e, f)*** *GMP concentration-dependent rheological analysis indicating the minimum and optimal gelation concentrations for ADG and ATG systems.*

Based on the morphological and spectroscopic analyses, GMP was identified as the primary structural unit driving the fibrillar assemblies in both ADG and ATG systems. To further validate its role in gelation, concentration-dependent gelation studies were performed by varying the GMP concentration. At lower GMP concentrations (<80 mM), both systems remained in the sol state. A sol-to-gel cross-over transition was observed at ~80 mM GMP, marking the critical gelation threshold. Upon further increasing the GMP concentration (>80 mM), stable hydrogels were formed, with optimal gel strength observed at 100 mM GMP for both ADG and ATG systems (**Figure 4.8 e, f**).

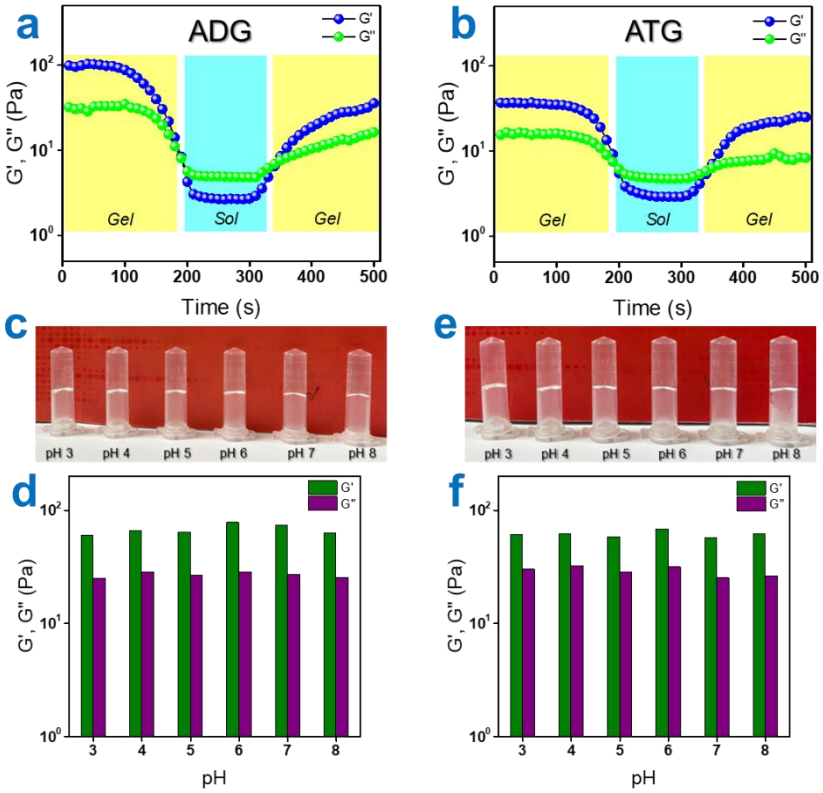


Figure 4.10. *Self-recovery behaviour of* ***(a)*** *ADG and* ***(b)*** *ATG hydrogels evaluated by time-dependent oscillatory rheology. The test involved a strain sweep from 1% to 1000% (0-200 s), followed by a constant high strain of 1000% (200-300 s), and subsequent strain recovery from 1000% to 1% (300-500 s). pH-dependent stability of ADG and ATG hydrogels in buffered media.* ***(c, e)*** *Digital photographs showing the structural integrity of ADG and ATG hydrogels, respectively, across different pH conditions.* ***(d, f)*** *Corresponding rheological measurements displaying storage (G') and loss (G") moduli at a constant strain of 1% and angular frequency of 10 rad* s^{-1}.

Citrate buffer was used for pH 3-5 and phosphate buffer for pH 6-8, with pH adjusted using 1 M HCl and 1 M NaOH.

Furthermore, the critical role of intrinsic pH modulation by ADP and ATP in governing gelation was evident from controlled studies performed in buffered media. ADG and ATG hydrogels were prepared over a broad pH range (pH 3-8), and all samples remained stable with comparable mechanical properties (**Figure 4.9 c-f**). This indicates that the external pH of the medium does not dictate the self-assembly or gelation process. Instead, the local pH environment generated by the adenosine phosphate derivatives played a dominant role in regulating assembly. These findings highlight that the intrinsic acidity and multivalent phosphate groups of ADP and ATP facilitate proton-mediated interactions and hydrogen bonding with G-quartet structures, thereby promoting and stabilizing both the condensates and the resulting hydrogels at higher concentrations.

4.2.5. Intrinsic Peroxidase Mimicking Activity

The formation of mechanically robust hydrogels in the ADG and ATG systems, driven by dense and interconnected fibrillar networks, establishes a confined and highly organized microenvironment capable of hosting chemical transformations. Such hierarchical architectures, composed of π-π stacked G-quadruplex domains and multivalent phosphate interactions, provide a high local concentration of functional groups and facilitate efficient molecular interactions within the network. Importantly, these features closely resemble enzyme-like active environments, where structural confinement and molecular organization play a critical role in catalytic efficiency. Notably, G4 assemblies are known to exhibit intrinsic catalytic properties due to their amphiphilic nature and ability to stabilize radical intermediates within stacked channels. The extended fibrillar network further enhances substrate accessibility and retention, thereby promoting catalytic efficiency. Based on these features, we hypothesized that ADG and ATG hydrogels possess intrinsic peroxidase-mimicking activity (**Figure 4.10 a**).

Accordingly, the oxidation of 3,3′,5,5′-tetramethylbenzidine (TMB) by H_2O_2 was monitored in the absence and presence of the hydrogels. A significant increase in absorbance at λ_{max} ~ 652 nm, corresponding to the formation of the oxidized TMB radical cation ($TMB^{\bullet+}$), was observed in the presence of both ADG and ATG hydrogels compared to the catalyst-free system, confirming their intrinsic peroxidase-like activity. As a control, the reaction kinetics were monitored at 652 nm in the presence of the hydrogels and their individual constituents (**Figure 4.10 c**). The hydrogels exhibited significantly higher reaction rates than their respective components, highlighting the enhanced catalytic efficiency arising from micro-confinement within the gel matrix (**Figure 4.10 b**). Notably, the ADG hydrogel showed a higher catalytic rate than the ATG system, consistent with its more extensive G-quadruplex stacking and higher structural organization. Since GMP concentration governs the extent of G-quadruplex (G4) formation, its influence on peroxidase-like activity was systematically investigated by preparing ADG hydrogels with varying GMP concentrations. A clear increase in kinetic reaction velocity was observed with increasing GMP content, indicating a direct correlation between G4 formation and catalytic efficiency (**Figure 4.10 d**). This trend confirms that the density of stacked G-quartet structures plays a critical role in governing peroxidase-like activity, with higher G4 content providing more effective catalytic sites within the hydrogel matrix.

To further quantify the intrinsic peroxidase-mimicking activity, detailed kinetic studies were carried out for the ADG hydrogel, identified as the most efficient catalytic system. The catalytic kinetics were evaluated by systematically varying the concentrations of TMB (0.05-1 mM) and H_2O_2 (1-12 mM), while monitoring the time-dependent increase in absorbance at 652 nm. The reaction profiles followed classical Michaelis-Menten behaviour for both substrates (**Figures 4.10 e, f**), indicating enzyme-like catalytic performance. The corresponding Lineweaver-Burk plots (***insets* of Figures 4.10 e, f**) were

used to extract the kinetic parameters, including the Michaelis constant (K_M) and maximum reaction velocity (V_{max}).*[52,53]* The relatively low K_M values obtained for TMB (0.2695 mM) and H_2O_2 (2.7158 mM) indicate strong substrate affinity within the hydrogel matrix, likely facilitated by the confined microenvironment and efficient substrate accessibility. The V_{max} values were determined to be 2.88×10^{-7} Ms^{-1} for TMB and 4.47×10^{-8} Ms^{-1} for H_2O_2, which are comparable to or exceed those reported for many metal-free peroxidase mimics (**Table 4.1**), highlighting the high catalytic efficiency of the system. Furthermore, the ADG hydrogel exhibited a specific activity of 1.5 $U.mg^{-1}$ (**Figure 4.10 g**), demonstrating its effective catalytic turnover under optimized conditions. Notably, despite being a noncovalently assembled system, the hydrogel maintained robust catalytic performance over a broad temperature range (278-313 K), with optimal activity observed at 303 K (**Figure 4.10 h**). This thermal resilience emphasizes the structural stability of the G-quadruplex-based fibrillar network and its suitability as an enzyme mimicking system.

Table 4.1. Comparison of the kinetic constants of ADG hydrogel with recently reported metal-free peroxidase-mimicking systems and benchmark catalysts.

Catalyst	**K_M (mM)**		**V_{max} (10^{-8} M.s^{-1})**		**References**
	TMB	H_2O_2	TMB	H_2O_2	
HRP	0.434	3.7	10	8.71	[56]
Fe_3O_4	0.098	154	3.44	9.78	[56]
Boron-doped graphdiyne nanosheet (B-GDY)	0.28	0.94	2.97	4.55	[57]
Graphdiyne oxide (GDYO)	0.62	2.59	0.19	0.17	[58]
Graphene Oxide (GO)	0.02	3.99	0.34	0.38	[59]
Multi-hydroxylated [70] fullerenes (MHF)	0.597	2.95	0.297	0.143	[60]
Modified GCN (AKCN)	0.601	0.79	4.22	6.78	[61]
$C_{60}[C(COOH)_2]_2$	0.23	24.58	0.035	0.04	[62]
Aspartic Acid-GMP Hydrogel	0.3785	0.3778	3.17	19.4	[24]
ADP-GMP (ADG) Hydrogel	**0.2695**	**2.7158**	**0.288**	**4.47**	**This Work**

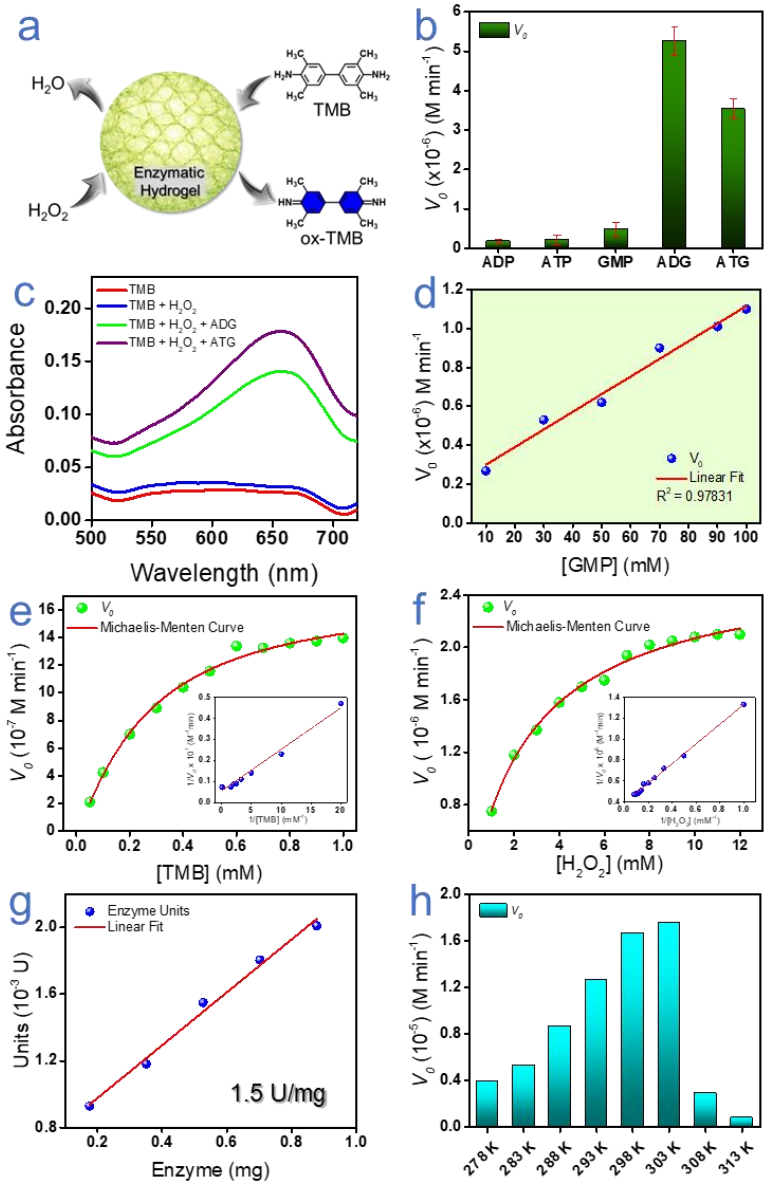


Figure 4.11. *Intrinsic peroxidase-mimicking activity and kinetic analysis of nucleotide hydrogels.* ***(a)*** *Schematic illustration of the intrinsic peroxidase-like catalytic mechanism.* ***(b)*** *Comparative kinetic analysis of ADG and ATG hydrogels relative to their individual nucleotide constituents, highlighting enhanced catalytic performance upon gelation.* ***(c)*** *Control experiments for peroxidase-like activity showing UV-visible spectra under different conditions. Significant absorption is observed only for ADG + TMB + H_2O_2 and ATG + TMB + H_2O_2 systems, with the ADG hydrogel exhibiting higher catalytic activity than ATG.* ***(d)*** *Concentration-dependent enhancement in catalytic velocity with increasing GMP content in the ADG hydrogel, highlighting the critical role of G-quadruplex (G-quartet) structures in governing catalytic activity.* ***(e, f)*** *Michaelis-Menten kinetic curves and corresponding Lineweaver-Burk plots (insets) of the ADG hydrogel with respect to varying concentrations of* ***(e)*** *TMB (0.05 - 1 mM) and* ***(f)*** *H_2O_2 (1 - 12 mM).* ***(g)*** *Specific activity profile of the ADG hydrogel using TMB*

as the substrate. ***(h)*** *Temperature-dependent catalytic activity demonstrating the broad operational stability of the ADG hydrogel as a peroxidase mimic.*

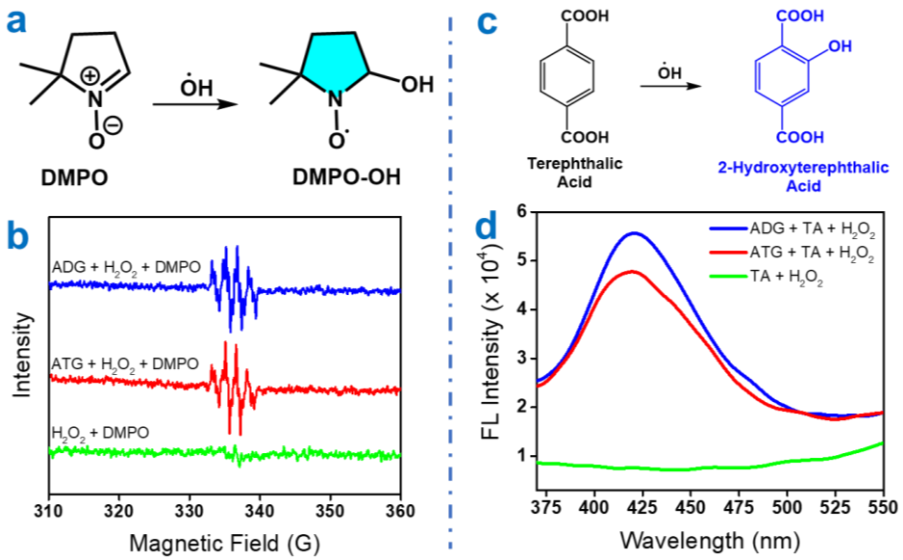


Figure 4.12. *Hydroxyl radical (•OH)-mediated reaction pathway underlying the peroxidase-like activity of ADG and ATG condensates.* ***(a)*** *Schematic reaction showing 5,5-dimethyl-1-pyrroline N-oxide (DMPO) as a spin-trapping agent.* ***(b)*** *Electron paramagnetic resonance (EPR) spectra obtained, showing a characteristic four-line signal corresponding to the DMPO–•OH adduct in the presence of ADG and ATG systems.* ***(c)*** *Schematic illustration of the conversion of terephthalic acid to fluorescent 2-hydroxyterephthalic acid upon reaction with hydroxyl radicals (•OH).* ***(d)*** *Control experiments showing significantly enhanced •OH generation in the presence of ADG and ATG catalysts, with ADG exhibiting higher activity than ATG.*

To confirm the indispensable role of G4 assembly, control experiments were performed using nucleotide combinations incapable of higher-order self-assembly. Individual nucleotides and the AMP-GMP condensate, both lacking ordered G4 formation, showed negligible catalytic activity (**Figure 4.13 a**), demonstrating that simple nucleotide mixing is insufficient for catalytic function. Additionally, deliberate disruption of the G4 network by concentrated NaOH treatment, which destabilizes Hoogsteen hydrogen bonding and dismantles the stacked G-quartet framework*[26]*, caused hydrogel collapse and a significant loss of catalytic activity (**Figure 4.13 b,c**). These results collectively confirm that intact G4-rich supramolecular architecture is essential for peroxidase-like activity, with the stacked G-quartet network serving as the structural basis of catalysis.

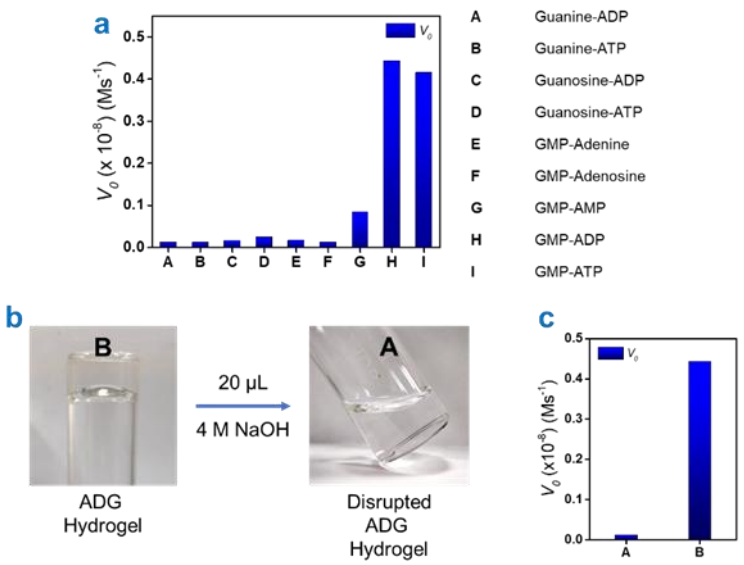


Figure 4.13. *Control experiments demonstrating the critical role of G-quadruplex assembly in the intrinsic peroxidase-like activity of ADG hydrogels.* ***(a)*** *Comparison of the catalytic velocities of non G4-forming nucleotide/nucleoside mixtures. Negligible activity was observed for the simple nucleotide mixtures and the AMP-GMP mixture, whereas significantly enhanced catalytic activity was obtained for ADG and ATG condensates, confirming the necessity of higher-order G4 assembly.* ***(b)*** *Digital photographs showing the disruption of the ADG hydrogel (B) upon treatment with concentrated NaOH (4 M), which destabilizes the G-quadruplex network (A) under highly basic conditions.* ***(c)*** *Corresponding catalytic velocities before (B) and after (A) G4 disruption, showing a significant loss in activity upon hydrogel disassembly. These results establish that the integrity and density of the stacked G-quartet network are essential for the emergence of peroxidase-like catalytic activity.*

Peroxidase-like activity generally proceeds via either hydroxyl (•OH) radical generation or an electron transfer pathway.*[49,50]* To probe the catalytic mechanism, electron paramagnetic resonance (EPR) spectroscopy was employed using DMPO as a spin-trapping agent. A characteristic quartet signal with an intensity ratio of 1:2:2:1, corresponding to the DMPO-OH adduct, was observed for both ADG and ATG systems, confirming the generation and involvement of •OH radicals in the catalytic process (**Figure 4.12 a, b**).*[51]* The extent of •OH radical generation was further quantified using a terephthalic acid (TA) assay, where reaction with •OH produces a fluorescent adduct (**Figure 4.12 a**).*[24]* Under identical conditions, the ADG system exhibited higher fluorescence intensity than ATG, indicating a greater

•OH generation capability and correlating with its superior catalytic performance (**Figure 4.12 d**). Thus, the proposed mechanistic pathway governing the enhanced catalytic performance of the G-quartet-based ADG and ATG hydrogels is summarized in **Figure 4.14**.

The catalytic activity of the ADG and ATG hydrogels is associated with their G4-rich supramolecular organization, as indicated by the correlation between GMP concentration, G4-associated spectroscopic responses, and catalytic reaction velocity. EPR spectroscopy and the terephthalic acid assay further demonstrate the generation of hydroxyl radicals. These observations suggest that radical-mediated oxidation contributes to the peroxidase-mimicking activity of the nucleotide assemblies. Nevertheless, the exclusive catalytic contribution of G4 structures has not been conclusively established, as the possible involvement of other supramolecular interactions and nonspecific peroxide decomposition cannot be completely excluded.

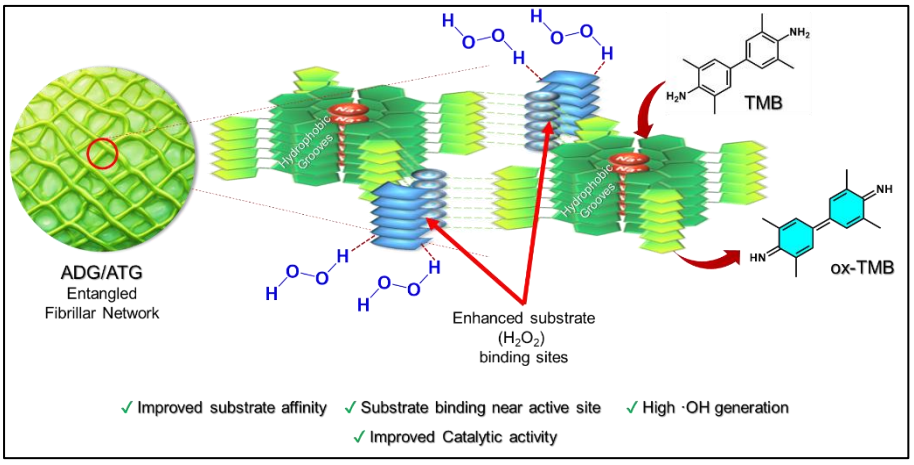


Figure 4.14. *Schematic illustration of enhanced substrate affinity and catalytic efficiency within ADG/ATG fibrillar hydrogel networks. The coexistence of multivalent phosphate groups from GMP and ADP/ATP increases the availability of H_2O_2 binding sites, promoting efficient •OH radical generation. Concurrently, π–π stacked G-quadruplex (G4) domains provide hydrophobic grooves that facilitate the encapsulation and enrichment of aromatic substrates such as TMB, increasing their local concentration near catalytic sites. The combined effects of multivalent interactions, substrate confinement, and G4-mediated stacking create a cooperative catalytic microenvironment, thereby enhancing intrinsic peroxidase-like activity.[24]*

4.2.6. Enabling Biocatalytic Cascade with "All-Nucleotide" Hydrogel

The hydrated and micro-confined architecture of the ADG hydrogel provides an ideal platform for enzyme encapsulation and multi-step biocatalysis, building upon its intrinsic peroxidase-like activity. Formed through the simple co-assembly of nucleotide constituents under aqueous conditions, this minimalistic matrix enables efficient co-encapsulation of multiple enzymes while preserving their native activity.*[54]* The confined network promotes enhanced substrate channelling through molecular proximity, thereby facilitating cascade transformations. A key distinguishing feature of the ADG hydrogel is its dual functionality: it acts not only as a biomimetic microenvironment for enzyme immobilization but also as an active catalytic scaffold that mimics horseradish peroxidase (HRP). This integration of structural confinement with intrinsic catalytic activity creates a synergistic platform that enhances cascade efficiency beyond conventional systems.*[7]* To validate this concept, β-galactosidase (*β-Gal*) and glucose oxidase (*GOx*) were co-encapsulated within the hydrogel matrix, enabling seamless coupling between enzymatic reactions and hydrogel-mediated catalysis (**Figure 4.15 a**).

The cascade capability of the system was demonstrated using two sequential reaction designs. In the two-component cascade (**Figure 4.15 b**), *GOx* catalyses the oxidation of glucose to gluconic acid, generating H_2O_2 in situ, which is subsequently utilized by the hydrogel to oxidize the chromogenic substrate TMB, producing a characteristic absorbance at 652 nm.*[24,49]* Extending this concept, a three-component cascade (**Figure 4.15 c**) was constructed using lactose as the initial substrate, where *β-Gal* hydrolyses lactose into glucose and galactose, followed by *GOx*-mediated H_2O_2 generation and subsequent hydrogel-driven TMB oxidation.*[32]* To evaluate the effect of the crowded microenvironment provided by the ADG hydrogel, a controlled two-step cascade experiment was performed in parallel using native horseradish peroxidase (HRP) under identical conditions. Notably, the

ADG hydrogel exhibited significantly higher reaction rates compared to the HRP system, highlighting the critical role of the confined microenvironment in enhancing catalytic efficiency beyond that of the free enzyme (**Figure 4.16**).

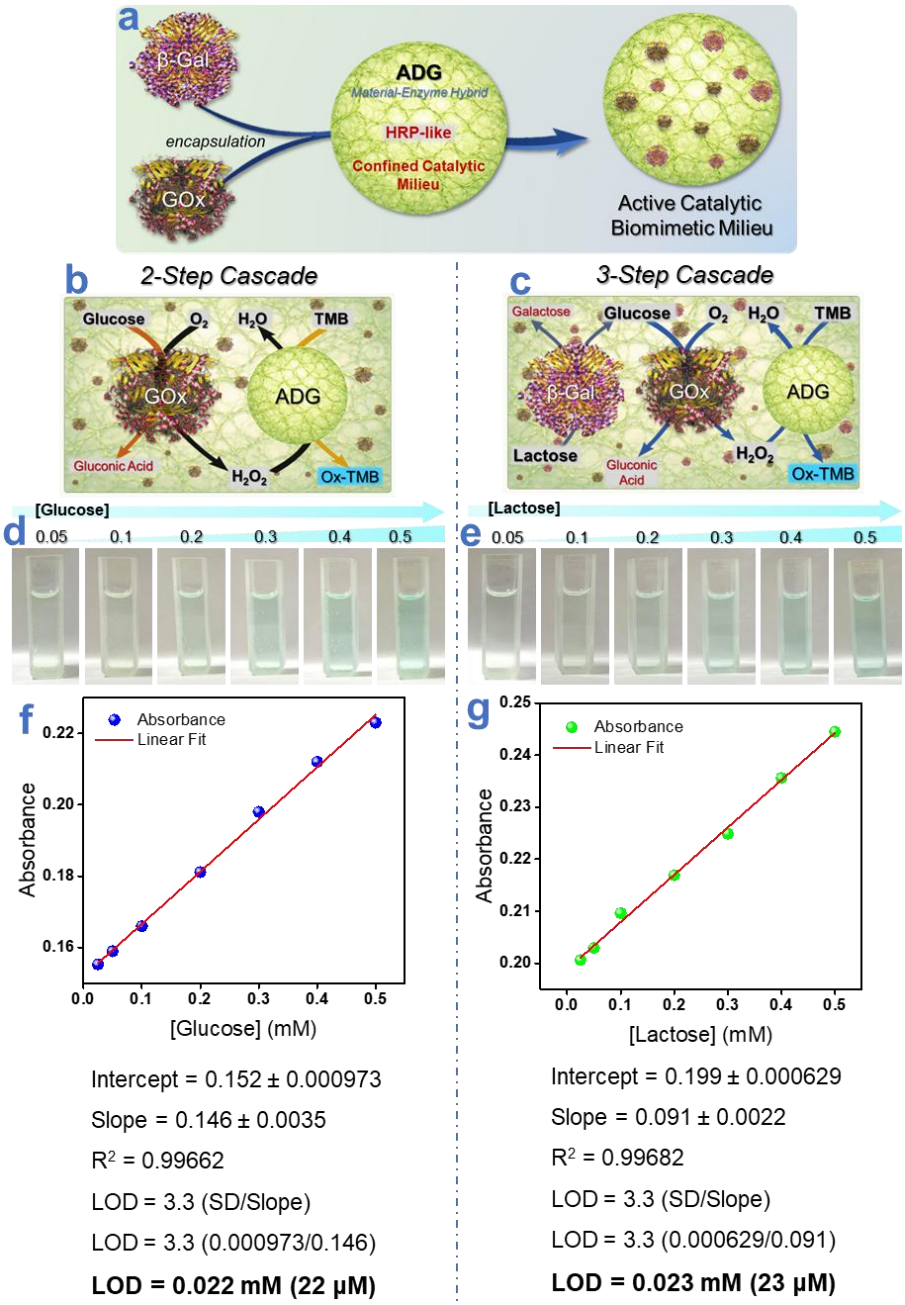


Figure 4.15. *Multi-enzyme cascade catalysis within the ADG hydrogel microreactor.* ***(a)*** *Schematic illustration of enzyme encapsulation (β-galactosidase and glucose oxidase) within the ADG hydrogel, highlighting its dual role as a confined catalytic milieu and intrinsic HRP-like scaffold.* ***(b)*** *Two-enzyme cascade system where GOx catalyses glucose oxidation to generate H_2O_2, which is subsequently utilized by the*

hydrogel to oxidize TMB to ox-TMB. ***(c)*** *Three-enzyme cascade system involving β-Gal-mediated hydrolysis of lactose to glucose, followed by GOx-generated H_2O_2 and hydrogel-catalysed TMB oxidation.* ***(d,e)*** *Photographic images showing concentration-dependent colorimetric response for glucose and lactose for 2-step and 3-step cascades respectively.* ***(f,g)*** *Calibration plots showing the linear relationship between absorbance and substrate concentration (both glucose and lactose) at a fixed reaction time (30 min) and constant TMB concentration (1 mM) for both cascade systems, along with corresponding limits of detection (LOD).*

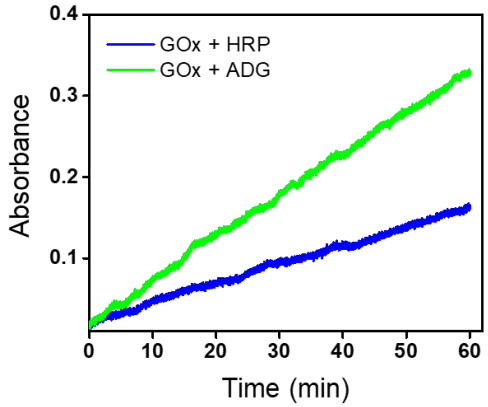


Figure 4.16. *Control experiment highlighting the role of the confined microenvironment in the ADG hydrogel. A two-step cascade reaction involving GOx was performed under identical conditions using either native HRP or the ADG hydrogel as the peroxidase mimic. A significantly higher reaction rate was observed for the GOx-ADG hydrogel system, demonstrating the enhanced catalytic efficiency arising from the crowded and confined microenvironment. Experimental conditions: glucose (0.5 mM), GOx (0.1 mg mL^{-1}), and HRP (0.1 mg mL^{-1}).*

To quantitatively assess the efficiency of the cascade systems, kinetic analyses were performed by monitoring the substrate concentration-dependent increase in the absorbance at 652 nm. In both the two- and three-enzyme cascades, a progressive increase in reaction rate was observed with increasing substrate concentration, exhibiting a linear response over the investigated range (**Figure 4.15 f, g**). For each measurement, the substrate was introduced into the catalytic matrix and incubated for a fixed duration, ensuring consistent comparison across concentrations. Correspondingly, a pronounced increase in the characteristic blue colour of oxidized TMB (ox-TMB) was observed, confirming effective catalytic turnover in both cascade systems (**Figure 4.15 d, e**). The linear dependence of absorbance on substrate

concentration enables quantitative analysis, allowing estimation of the limits of detection (LOD) for the system. The calculated LOD values were 22 μM for glucose and 23 μM for lactose, demonstrating the potential of the cascade platform as a sensitive biocatalytic sensor. The enhanced catalytic performance can be attributed to the confined hydrogel environment, which reduces diffusion distances and facilitates efficient transfer of reactive intermediates, particularly H_2O_2, between sequential catalytic steps. Although the three-enzyme cascade exhibited slightly lower reaction rates compared to the two-enzyme system, likely due to the additional kinetic barrier associated with lactose hydrolysis, it maintained a strong linear correlation between substrate concentration and absorbance. This indicates efficient coupling between the enzymatic reactions and hydrogel-mediated catalysis. Collectively, these results establish the ADG hydrogel as an integrated catalytic microreactor, where spatial confinement and intrinsic peroxidase-like activity synergistically enhance cascade kinetics and enable sensitive substrate detection.

The catalytic experiments were performed at pH 4.4, which favours the peroxidase-like activity of G4-associated assemblies but does not represent normal physiological extracellular or cytosolic conditions. Mildly acidic conditions of this kind may, however, be relevant to certain acidic biological compartments, such as endosomes and lysosomes, and to pathological microenvironments such as tumour tissue. Catalytic studies at pH 7.4 and under other biologically relevant conditions will be necessary to establish the broader biomedical applicability of these assemblies.

4.3. Conclusion

In summary, our minimalistic “all-nucleotide” platform enables pH-regulated biomolecular condensation, yielding hierarchically structured G-quadruplex (G4)-based supramolecular fibrillar assemblies that transition into hydrogels upon higher-order organization. By systematically tuning phosphate multiplicity and intrinsic acidity across

adenosine mono/di/triphosphate derivatives, we demonstrate that multivalent phosphate interactions and localized pH gradients orchestrate GMP-driven G4 stacking. Among these, ADP-GMP and ATP-GMP condensates (ADG and ATG) displayed pronounced hierarchical self-assembly, propelled by escalating phosphate valency. Kinetic morphological evolution revealed a concentration-dependent shift from phase-separated droplets to fibrillar networks, unveiling a novel "all-nucleotide" small-biomolecule condensation under physiological conditions. These assemblies further evolved into hydrogels at elevated concentrations, manifesting robust biocatalytic activity. Both ADG and ATG hydrogels functioned as efficient, metal-free peroxidase mimics, with ADG exhibiting superior performance through elevated substrate affinity, catalytic efficiency, and a hydroxyl radical-generating mechanism. Crucially, G4 moieties emerged as pivotal for this enhanced catalysis. Furthermore, these hydrogels uniquely integrate dual roles as catalytic scaffolds and biomimetic microenvironments, facilitating seamless encapsulation of multiple enzymes and accelerating multi-step cascade reactions with superior kinetics and ultralow detection limits. We successfully implemented both dual- and triple-enzyme cascade systems, underscoring the "all-nucleotide" hydrogel's prowess in biocatalysis, offering greater efficiency and physiological compatibility compared to harsh, rigid synthetic constructs reported earlier. This approach unlocks new pathways for programmable, metal-free catalytic materials and biomimetic microreactors, with broad potential in biosensing, artificial enzymatic systems, and protocell-inspired functional materials.

4.4. Experimental Section

4.4.1. Synthesis of the condensates and hydrogels

Condensates were prepared by mixing equimolar aqueous solutions (100 μM each) of adenosine phosphate disodium salts (AMP-Na_2, ADP-Na_2, or ATP-Na_2) with guanosine monophosphate disodium salt (GMP-Na_2). The resulting homogeneous solutions were incubated

at 25 °C for 12 h, after which condensate formation was confirmed by the appearance of a Tyndall effect under laser illumination. The samples were directly drop-cast onto glass slides for morphological analysis and used as-prepared for spectroscopic characterization. Concentration-dependent studies were performed by varying GMP concentration while maintaining a constant concentration of the corresponding adenosine phosphate derivative. For fluorescence and confocal imaging, samples were stained with Thioflavin T (5 μM). For pH titration and zeta potential measurements, samples were prepared at 1 mM concentration for both components under otherwise identical conditions.

Hydrogels were prepared by dissolving GMP-Na_2 (100 mM) and ADP-Na_2 or ATP-Na_2 (100 mM) in water (1 mL), followed by gentle heating with stirring until a clear solution was obtained. Upon standing undisturbed for 10 min at room temperature, self-supporting, transparent ADG and ATG hydrogels were formed, respectively. These hydrogels were used for rheological measurements, while diluted samples were employed for enzyme kinetics and cascade catalysis studies.

4.4.2. Characterizations

Microscopic Characterizations: Confocal laser scanning microscopy (CLSM) was performed using an Olympus IX-83 microscope equipped with a multiline Ar gas laser (λ_{ex} = 405 nm). For imaging, condensates were prepared by mixing aqueous solutions of the respective nucleotide constituents at desired concentrations, followed by vortexing for 5 min to ensure homogeneous mixing. Thioflavin T (ThT, ethanolic solution) was then added, and the samples were incubated for 1 h to allow efficient dye incorporation. The samples were subsequently drop-cast onto thoroughly cleaned glass slides and allowed to incubate and partially dry at 25 °C prior to imaging. Field emission scanning electron microscopy (FE-SEM) was carried out using a Carl Zeiss Supra 55 microscope. Samples were prepared following a similar protocol, excluding the ThT staining step, and were dried and sputter-coated with a thin Au layer prior to imaging.

Spectroscopic Characterization: UV-visible absorption spectra (220-320 nm) were recorded using a Varian Cary 100 Bio spectrophotometer, while circular dichroism (CD) spectra (190-350 nm) were obtained using a JASCO J-815 spectropolarimeter with a 2 mm path-length quartz cuvette. CD measurements were performed at a scan rate of 50 nm min^{-1}, and baseline correction was carried out using Milli-Q water. Steady-state fluorescence spectra were recorded on a Horiba JobinYvon Fluoromax-4P spectrofluorometer (model FM-100). All measurements were conducted using samples at their respective condensate concentrations.

Zeta Potential Measurements and pH Titration: Zeta potential measurements were performed using a Nanoplus Zeta Potential Analyzer equipped with a quartz flow cell. Samples were prepared at a concentration of 1 mM for each constituent, with GMP concentration varied accordingly, and incubated for 12 h to ensure complete condensation. pH measurements and titrations were carried out using a LABMAN LMPH10 pH meter calibrated with standard buffers.

Rheological Measurements: Rheological properties of the hydrogels were measured using an Anton Paar Physica MCR 301 rheometer. Dynamic strain (amplitude) sweep experiments were conducted at a constant angular frequency of 10 rad s^{-1}, while frequency sweep measurements were performed over a range of angular frequencies at a fixed strain of 1%, within the linear viscoelastic region. All measurements were carried out at 25 °C using appropriate plate geometry.

4.4.3. Enzyme Kinetics and Catalytic Assays

Enzymatic kinetics and cascade biocatalytic assays were monitored by recording time-dependent absorbance changes using a Varian Cary 100 Bio UV-visible spectrophotometer with a quartz cuvette (~10 mm path length). Electron paramagnetic resonance (EPR) spectra were recorded on a JEOL JES-FA200 ESR spectrometer immediately after the addition of H_2O_2 to a pre-mixed solution of hydrogel and DMPO. The

terephthalic acid (TA) fluorescence assay for hydroxyl radical detection was performed using the same fluorometer. Hydrogel, terephthalic acid, and H_2O_2 were mixed simultaneously and incubated for 20 min to allow radical formation, after which fluorescence spectra were recorded.

4.4.4. Enzyme Kinetics and Mechanism

Peroxidase-like activity was evaluated using diluted hydrogel samples to ensure efficient substrate diffusion and binding. Kinetic measurements were performed in acetate buffer (0.01 M, pH 4.4) with a total reaction volume of 3 mL, containing 100 µL hydrogel and varying concentrations of TMB and H_2O_2. The reaction was initiated by the addition of H_2O_2, followed by thorough mixing and incubation for 10 min at room temperature. The oxidation of TMB to ox-TMB was monitored by recording the time-dependent absorbance at 652 nm, and the initial reaction rates were calculated accordingly. Steady-state kinetic parameters were determined from two sets of experiments: (i) varying TMB concentration (0.05-1 mM) at fixed H_2O_2 concentration (10 mM) and constant hydrogel (100µL/3mL) content, and (ii) varying H_2O_2 concentration (1-12 mM) at fixed TMB (1 mM) and hydrogel concentrations (100µL/3mL). The kinetic parameters, including Michaelis constant (K_M) and maximum reaction velocity (V_{max}), were obtained using the Lineweaver-Burk form of the Michaelis-Menten equation:[53]

$$\frac{1}{V} = \frac{K_M}{V_{max}[S]} + \frac{1}{V_{max}}$$

where V is the initial reaction rate, [S] is the substrate concentration, K_M is the Michaelis constant, and V_{max} is the maximum reaction velocity.

Specific activity (SA) was evaluated by varying the hydrogel volume while keeping TMB (1 mM) and H_2O_2 (5 mM) concentrations constant in acetate buffer (1 mL, pH 4.4). The initial rates were determined as described above, and SA was calculated using:[55]

$$SA = \left[v/(\varepsilon \times l) \times \left(\frac{\Delta A}{\Delta t}\right)\right]/m$$

where V is the total reaction volume (μL), ε is the molar extinction coefficient of TMB (39,000 M^{-1} cm^{-1}), l is the optical path length (cm), ΔA/Δt is the initial rate of absorbance change, and m is the mass of hydrogel (mg).

Hydroxyl radical (•OH) generation was investigated using electron paramagnetic resonance (EPR) spectroscopy with DMPO (1 mM) as a spin-trapping agent. The reaction conditions were identical to the kinetic assays, with DMPO replacing TMB. After incubation for 10 min, the solution was transferred to a quartz capillary and immediately analysed using an EPR spectrometer. Quantification of •OH generation was further performed using a terephthalic acid (TA) fluorescence assay. A mixture of 0.5 mL terephthalic acid solution (1 mM in 1 M NaOH), 4.3 mL buffer containing H_2O_2 (10 mM), and 100 μL hydrogel was incubated for 15 min. Fluorescence measurements were recorded by exciting at 315 nm, and emission spectra were collected at defined time intervals to monitor the formation of the fluorescent hydroxylated product.

4.4.5. Enzymatic Cascade Synthesis and Catalytic Activity

Enzymatic cascade reactions were carried out under mild, physiologically relevant conditions. Glucose oxidase (GOx) stock solution (1 mg mL^{-1}) was prepared in phosphate-buffered saline (PBS, 0.01 M, pH 7.4) containing 150 mM NaCl. β-Galactosidase (β-Gal) stock solution (500 U mL^{-1}) was prepared in Tris-HCl buffer (0.05 M, pH 7.0) supplemented with NaCl (100 mM) and $MgCl_2$ (2 mM). ADG hydrogels were prepared as described above, and enzyme solutions were incorporated during gel formation to calibrate a total hydrogel volume of 1 mL. For the two-enzyme cascade, GOx was encapsulated at an optimal concentration of 0.1 mg mL^{-1}. For the three-enzyme cascade, β-Gal (50 U mL^{-1}) and GOx (0.1 mg mL^{-1}) were co-encapsulated within

the hydrogel matrix. The enzyme-loaded hydrogels were aged for 12 h to ensure efficient encapsulation and stabilization.

Catalytic reactions were initiated by adding 100 μL of enzyme-loaded hydrogel into acetate buffer (0.01 M, pH 4.4) (3 mL of total reaction volume) containing TMB (1 mM) and varying concentrations of substrate: glucose (0.025-0.5 mM) for the two-step cascade and lactose (0.025-0.5 mM) for the three-step cascade. The reaction mixtures were thoroughly mixed and incubated at 25 °C for 1 h. The formation of oxidized TMB was quantified by measuring absorbance at 652 nm. Calibration curves were constructed from the linear relationship between absorbance and substrate concentration, and the limits of detection (LOD) for glucose and lactose were determined accordingly.

4.5. References

1. Zhang, Y., Narlikar et al. (2021), Enzymatic Reactions inside Biological Condensates, Journal of Molecular Biology, 433, 166624 (DOI: 10.1016/j.jmb.2020.08.009.)

2. Lim, S., Clark et al. (2024), Phase-separated biomolecular condensates for biocatalysis, Trends in Biotechnology, 42, 496–509 (DOI: 10.1016/j.tibtech.2023.10.003.)

3. Tero, R., Fukumoto et al. (2017), Formation of Cell Membrane Component Domains in Artificial Lipid Bilayer, Sci Rep, 7, 17905 (DOI: 10.1038/s41598-017-18242-9.)

4. Banani, S.F., Lee et al. (2017), Biomolecular condensates: organizers of cellular biochemistry, Nat Rev Mol Cell Biol, 18, 285–298 (DOI: 10.1038/nrm.2017.7.)

5. Gil-Garcia, M., Benítez-Mateos et al. (2024), Local environment in biomolecular condensates modulates enzymatic activity across length scales, Nat Commun, 15, 3322 (DOI: 10.1038/s41467-024-47435-w.)

6. Netzer, A., Katzir, et al. (2023), Emergent properties of melanin-inspired peptide/RNA condensates, Proc. Natl. Acad. Sci. U. S. A., 120, e2310569120. (DOI: 10.1073/pnas.2310569120.)

7. Vázquez-González, M., Wang et al. (2020), Biocatalytic cascades operating on macromolecular scaffolds and in confined environments, Nat Catal, 3, 256–273 (DOI: 10.1038/s41929-020-0433-1.)
8. Das, N., Maity et al. (2023), Chemical Transformations in Supramolecular Hydrogels, ACS Catal., 13, 5544–5570 (DOI: 10.1021/acscatal.3c00411.)
9. Smith, D.K. (2025), Supramolecular Gels as Active Tools for Reaction Engineering, Angew. Chem. Int. Ed., 137, e202502053. (DOI: 10.1002/ange.202502053.)

10. Rizzo, C., Marullo et al. (2021), Catalysis in Supramolecular Systems: the Case of Gel Phases, European Journal of Organic Chemistry, 2021, 3148–3169 (DOI: 10.1002/ejoc.202100372.)

11. Gao, F., Yang et al. (2024), Bioinspired Supramolecular Hydrogel from Design to Applications, Small Methods, 8, 2300753 (DOI: 10.1002/smtd.202300753.)

12. Shigemitsu, H., Hamachi et al. (2017), Design Strategies of Stimuli-Responsive Supramolecular Hydrogels Relying on Structural Analyses and Cell-Mimicking Approaches, Acc. Chem. Res., 50, 740–750 (DOI: 10.1021/acs.accounts.7b00070.)

13. Gröger, H., Allahverdiyev, et al. (2024), Merging MOF Chemistry & Biocatalysis: A Perspective for Achieving Efficient Organic Synthetic Processes and Applications in the Chemical Industry?, Adv. Funct. Mater., 34, 2304794. (DOI: 10.1002/adfm.202304794.)

14. Chen, J., Wang et al. (2023), Dynamic supramolecular hydrogels mediated by chemical reactions, Chem. Commun., 59, 14236–14248 (DOI: 10.1039/D3CC04353C.)

15. Wang, X., Wang et al. (2021), Enzyme-Laden Bioactive Hydrogel for Biocatalytic Monitoring and Regulation, Acc. Chem. Res., 54, 1274–1287 (DOI: 10.1021/acs.accounts.0c00832.)

16. Zhang, X., Zhang et al. (2024), DNA-Free Guanosine-Based Polymer Nanoreactors with Multienzyme Activities for Ferroptosis–Apoptosis Combined Antitumor Therapy, ACS Nano, 18, 33531–33544 (DOI: 10.1021/acsnano.4c11275.)

17. Huang, J., Jiao et al. (2021), Immobilizing Enzymes on Noble Metal Hydrogel Nanozymes with Synergistically Enhanced Peroxidase Activity for Ultrasensitive Immunoassays by Cascade Signal Amplification, ACS Appl. Mater. Interfaces, 13, 33383–33391 (DOI: 10.1021/acsami.1c09100.)

18. Lopez, A., Liu et al. (2017), Self-Assembly of Nucleobase, Nucleoside and Nucleotide Coordination Polymers: From Synthesis to Applications, ChemNanoMat, 3, 670–684 (DOI: 10.1002/cnma.201700154.)

19. Peters, G.M., Davis et al. (2016), Supramolecular gels made from nucleobase, nucleoside and nucleotide analogs, Chem. Soc. Rev., 45, 3188–3206 (DOI: 10.1039/C6CS00183A.)

20. Detellier, C., Laszlo et al. (1980), Role of alkali metal and ammonium cations in the self-assembly of the 5'-guanosine monophosphate dianion, J. Am. Chem. Soc., 102, 1135–1141 (DOI: 10.1021/ja00523a033.)

21. Otero, R., Schöck et al. (2005), Guanine Quartet Networks Stabilized by Cooperative Hydrogen Bonds, Angew. Chem. Int. Ed., 44, 2270–2275 (DOI: 10.1002/anie.200461586.)

22. Rosenzweig, B.A., Hamilton et al. (2009), Self-Assembly of a Four-Helix Bundle on a DNA Quadruplex, Angew. Chem. Int. Ed., 48, 2749–2751 (DOI: 10.1002/anie.200804849.)

23. Sahu, T.K., Aneja, et al. (2026), Intermingled Coordination Environments Enable Defect-Engineered Metal–Polyphenol/G-Quadruplex Hydrogel for Enhanced N_2-to-NH_3 Photoconversion, Small, 22, e14925. (DOI: 10.1002/smll.202514925.)

24. Thakur, N., Sarma et al. (2025), Acidic Amino Acid Induced 5′-Guanosine Monophosphate Fibrillar Nanozyme: A Highly Efficient Metal-Free Intrinsic Peroxidase Mimic, Nano Lett., 25, 15407–15415 (DOI: 10.1021/acs.nanolett.5c04390.)

25. Sarma, S., Jain et al. (2025), Supramolecular Self-Assembly of Polyaniline Embedded Enzyme-Mimicking GMP-Condensate Hydrogel for Electrochromic Energy Storage Applications, ACS Appl. Mater. Interfaces, 17, 48532–48546 (DOI: 10.1021/acsami.5c08151.)

26. Sarma, S., Thakur et al. (2024), Chromatin inspired bio-condensation between biomass DNA and guanosine monophosphate produces all-nucleic hydrogel as a hydrotropic drug carrier, Commun Chem, 7, 261 (DOI: 10.1038/s42004-024-01353-6.)

27. Liang, J., Mazur et al. (2019), Peptide-induced super-assembly of biocatalytic metal–organic frameworks for programmed enzyme cascades, Chem. Sci., 10, 7852–7858 (DOI: 10.1039/C9SC02021G.)

28. Weng, Y., Song et al. (2021), Hybrid hydrogel reactor with metal–organic framework for biomimetic cascade catalysis, Chemical Engineering Journal, 425, 131482 (DOI: 10.1016/j.cej.2021.131482.)

29. Elani, Y., Law et al. (2014), Vesicle-based artificial cells as chemical microreactors with spatially segregated reaction pathways, Nat Commun, 5, 5305 (DOI: 10.1038/ncomms6305.)

30. Wilner, O.I., Shimron et al. (2009), Self-Assembly of Enzymes on DNA Scaffolds: En Route to Biocatalytic Cascades and the Synthesis of Metallic Nanowires, Nano Lett., 9, 2040–2043 (DOI: 10.1021/nl900302z.)

31. Klermund, L., Castiglione et al. (2018), Polymersomes as nanoreactors for preparative biocatalytic applications: current challenges and future perspectives, Bioprocess Biosyst Eng, 41, 1233–1246 (DOI: 10.1007/s00449-018-1953-9.)

32. Chen, W.-H., Vázquez-González et al. (2018), Biocatalytic cascades driven by enzymes encapsulated in metal–organic framework nanoparticles, Nat Catal, 1, 689–695 (DOI: 10.1038/s41929-018-0117-2.)

33. Trantidou, T., Friddin et al. (2017), Engineering Compartmentalized Biomimetic Micro- and Nanocontainers, ACS Nano, 11, 6549–6565 (DOI: 10.1021/acsnano.7b03245.)

34. Tu, Y., Peng et al. (2016), Mimicking the Cell: Bio-Inspired Functions of Supramolecular Assemblies, Chem. Rev., 116, 2023–2078 (DOI: 10.1021/acs.chemrev.5b00344.)

35. Kilgore, H.R., Young et al. (2022), Learning the chemical grammar of biomolecular condensates, Nat Chem Biol, 18, 1298–1306 (DOI: 10.1038/s41589-022-01046-y.)

36. Harraz, D.M., Davis et al. (2018), A self-assembled peroxidase from 5′-GMP and heme, Chem. Commun., 54, 1587–1590 (DOI: 10.1039/C7CC09900B.)

37. Davis, J.T., Spada et al. (2007), Supramolecular architectures generated by self-assembly of guanosine derivatives, Chem. Soc. Rev., 36, 296–313 (DOI: 10.1039/B600282J.)

38. Chakraborty, A., Rani et al. (2025), Guanosine Monophosphate Induced Solubilization of Folic Acid Leading to Hydrogel Formation for Targeted Delivery of Hydrophilic and Hydrophobic Drugs, ACS Appl. Mater. Interfaces, 17, 11848–11860 (DOI: 10.1021/acsami.4c21306.)

39. Panda, M., Walmsley et al. (2011), Circular Dichroism Study of Supramolecular Assemblies of Guanosine 5′-Monophosphate, J. Phys. Chem. B, 115, 6377–6383 (DOI: 10.1021/jp201630g.)

40. del Villar-Guerra, R., Trent et al. (2018), G-Quadruplex Secondary Structure Obtained from Circular Dichroism Spectroscopy, Angew. Chem. Int. Ed., 57, 7171–7175 (DOI: 10.1002/anie.201709184.)

41. Syberg, F., Suveyzdis et al. (2012), Time-resolved Fourier Transform Infrared Spectroscopy of the Nucleotide-binding Domain from the ATP-binding Cassette Transporter MsbA: ATP HYDROLYSIS IS THE RATE-LIMITING STEP IN THE CATALYTIC CYCLE*, J. Biol. Chem., 287, 23923–23931 (DOI: 10.1074/jbc.M112.359208.)

42. Rimai, L., Cole et al. (1969), Studies of Raman Spectra of Water Solutions of Adenosine Tri-, Di-, and Monophosphate and Some Related Compounds, Biophysical Journal, 9, 320–329 (DOI: 10.1016/S0006-3495(69)86389-7.)

43. Renaud de la Faverie, A., Guédin, et al. (2014), Thioflavin T as a fluorescence light-up probe for G4 formation, Nucleic Acids Res., 42, e65 (DOI: 10.1093/nar/gku111)

44. Mohanty, J., Barooah et al. (2013), Thioflavin T as an Efficient Inducer and Selective Fluorescent Sensor for the Human Telomeric G-Quadruplex DNA, J. Am. Chem. Soc., 135, 367–376 (DOI: 10.1021/ja309588h.)

45. Davis, J.T. (2004), G-Quartets 40 Years Later: From 5′-GMP to Molecular Biology and Supramolecular Chemistry, Angew. Chem. Int. Ed., 43, 668–698 (DOI: 10.1002/anie.200300589.)

46. Bochman, M.L., Paeschke et al. (2012), DNA secondary structures: stability and function of G-quadruplex structures, Nat Rev Genet, 13, 770–780 (DOI: 10.1038/nrg3296.)

47. Tao, Y.H., Schulke et al. (2024), Hydration water drives the self-assembly of guanosine monophosphate, Biophysical Journal, 123, 931–939 (DOI: 10.1016/j.bpj.2024.03.005.)

48. Wu, G., Kwan et al. (2009), Helical Structure of Disodium 5′-Guanosine Monophosphate Self-Assembly in Neutral Solution, J. Am. Chem. Soc., 131, 3180–3182 (DOI: 10.1021/ja809258y.)

49. Singh, S., Mukherjee et al. (2023), Coacervate-Based Plexcitonic Assembly toward Peroxidase-like Activity and Ultrasensitive Glucose Sensing, ACS Appl. Mater. Interfaces, 15, 25524–25535 (DOI: 10.1021/acsami.3c02863.)

50. Adeniyi, O., Sicwetsha et al. (2020), Nanomagnet-Silica Nanoparticles Decorated with Au@Pd for Enhanced Peroxidase-Like Activity and Colorimetric Glucose Sensing, ACS Appl. Mater. Interfaces, 12, 1973–1987 (DOI: 10.1021/acsami.9b15123.)

51. Li, Z., Liu et al. (2023), Regulating the N Coordination Environment of Co Single-Atom Nanozymes for Highly Efficient Oxidase Mimics, Nano Lett., 23, 1505–1513 (DOI: 10.1021/acs.nanolett.2c04944.)

52. Zheng, J.-J., Zhu et al. (2024), Optimizing the standardized assays for determining the catalytic activity and kinetics of peroxidase-like nanozymes, Nat Protoc, 19, 3470–3488 (DOI: 10.1038/s41596-024-01034-7.)

53. Jiang, B., Duan et al. (2018), Standardized assays for determining the catalytic activity and kinetics of peroxidase-like nanozymes, Nat Protoc, 13, 1506–1520 (DOI: 10.1038/s41596-018-0001-1.)

54. Ariaeenejad, S., Motamedi et al. (2026), Enzyme immobilization on hydrogels: An overview on methods, interactions, and divers applications, International Journal of Biological Macromolecules, 336, 149325 (DOI: 10.1016/j.ijbiomac.2025.149325.)

55. Zhu, S., He et al. (2024), Enhanced Peroxidase-like Activity of Ruthenium-Modified Single-Atom-Thick A Layers in MAX Phases for Biomedical Applications, ACS Nano, 18, 29522–29534 (DOI: 10.1021/acsnano.4c05753.)

56. Gao, L., Zhuang, J., Nie, L. et al. (2007), Intrinsic peroxidase-like activity of ferromagnetic nanoparticles, Nature Nanotech, 2, 577–583 (DOI: 10.1038/nnano.2007.260.)

57. Bi, X., Bai, Q., Wang, L. et al. (2022), Boron doped graphdiyne: A metal-free peroxidase mimetic nanozyme for antibacterial application, Nano Res., 15, 1446–1454 (DOI: 10.1007/s12274-021-3685-4.)

58. Ma, W., Xue, et al. (2020), Graphdiyne oxide: a new carbon nanozyme, Chem. Commun., 56, 5115-5118 (DOI: 10.1039/D0CC01840F.)
59. Song, Y., Qu, et al. (2010), Graphene Oxide: Intrinsic Peroxidase Catalytic Activity and Its Application to Glucose Detection, Adv. Mater., 22, 2206-2210 (DOI: 10.1002/adma.200903783.)
60. Sun, Z., Zhou, et al. (2023), Metal-Free Peroxidase-Mimetic Nanocatalysts for Chemodynamic Vascular-Disrupting Cancer Therapy, Adv. Healthc. Mater., 12, 2301306 (DOI: 10.1002/adhm.202301306.)
61. Zhang, P., Sun, D., Cho, A. et al. (2019), Modified carbon nitride nanozyme as bifunctional glucose oxidase-peroxidase for metal-free bioinspired cascade photocatalysis, Nat. Commun., 10, 940 (DOI: 10.1038/s41467-019-08731-y.)
62. Li, R., Zhen, et al. (2013), A novel glucose colorimetric sensor based on intrinsic peroxidase-like activity of C_{60}-carboxyfullerenes, Biosens. Bioelectron., 47, 502-507 (DOI: 10.1016/j.bios.2013.03.057.)

Chapter 5

5. Engineering a Nucleotide-Based Artificial Metalloenzyme through Supramolecular Confinement of a Copper-Histidine Cofactor

5.1. Introduction

Metalloenzymes achieve extraordinary catalytic efficiency and substrate specificity through the synergistic interplay between precisely organized amino acid residues and metal cofactors embedded within dynamic protein scaffolds. Beyond anchoring the catalytic center, the protein matrix establishes a well-defined secondary coordination environment that governs substrate recognition, electron transfer, and catalytic turnover. However, the structural fragility of proteins under non-native conditions frequently causes irreversible deactivation, limiting their practical utility in biotechnological and industrial applications.*[1-3]* These constraints have driven considerable interest in developing artificial metalloenzymes that emulate the structural and functional characteristics of natural enzymes while offering enhanced robustness and tunability.*[4-8]* Existing strategies have largely relied on rigid synthetic supports, including nanoparticles, metal-organic frameworks, and covalent hybrid materials to immobilize catalytic centers. Although such systems improve stability, they generally fail to reproduce the dynamic, hierarchically organized microenvironment that underpins the remarkable efficiency of natural metalloenzymes, underscoring the need for alternative biomimetic design strategies.*[9-13]*

Among metalloenzyme families, multicopper oxidases constitute an important class of biocatalysts that catalyze aerobic

oxidation reactions essential for cellular metabolism by exploiting cooperative electronic communication between multiple copper centers to activate molecular oxygen.*[14]* In particular, dicopper metalloenzymes, exemplified by catechol oxidase that have attracted considerable attention owing to their well-defined metal coordination architecture and unique oxygen activation mechanism. The catalytic center of catechol oxidase comprises a binuclear copper site in which each Cu(II) ion is coordinated by three histidine residues, forming a coordinatively unsaturated environment that enables reversible oxygen binding, efficient electron transfer, and generation of reactive copper-oxygen intermediates that drive the selective oxidation of catechols to o-quinones. Critically, the surrounding protein matrix not only preserves the precise geometry of the dicopper center but also provides a dynamic secondary coordination sphere that regulates substrate accessibility, stabilizes reactive intermediates, and facilitates rapid catalytic turnover.*[15-17]* Inspired by this architecture, numerous synthetic catechol oxidase mimics based on discrete copper complexes have been developed.*[18-22]* However, although many reproduce the primary coordination environment of the dicopper active site, they lack the hierarchical organization and confined microenvironment provided by the protein scaffold resulting in diminished catalytic efficiency and limited functional resemblance to the native enzyme.

A defining feature of natural enzymes is that catalytic activity arises not solely from the metal active site but from the precisely organized three-dimensional protein scaffold that positions functional groups, regulates substrate access, and stabilizes intermediates through an adaptive network of noncovalent interactions. Reproducing such tertiary architectures without proteins remains one of the central challenges in artificial enzyme design.*[1,23-25]* Biomolecular self-assembly offers a compelling bottom-up strategy in this regard, whereby small molecular building blocks spontaneously organize into ordered supramolecular structures through reversible noncovalent interactions, retaining structural adaptability without requiring complex molecular

engineering.*[26-28]* Among available building blocks, nucleotides are particularly attractive due to their intrinsic capacity to self-assemble into hydrated, hierarchical networks that resemble the dynamic microenvironments of native enzymes.*[29-30]* 5′-Guanosine monophosphate (5′-GMP), in particular, possesses both Watson-Crick and Hoogsteen hydrogen-bonding motifs that enable its hierarchical organization into G-quartets, nanofibers, and extended supramolecular hydrogels.*[31,32]* This structural versatility, combined with the ability to coordinate metal ions and complexes, provides an ideal platform for constructing biomimetic catalytic scaffolds with tunable architectures and confined reaction microenvironments. Moreover, the dynamic and reversible nature of noncovalent interactions within GMP assemblies imparts structural flexibility analogous to native protein matrices, facilitating substrate diffusion while stabilizing catalytically active species. Integrating metal-based active sites within such nucleotide-directed supramolecular frameworks therefore represents a promising strategy to recreate enzyme-like coordination environments using minimal biomolecular components.*[33-36]*

Herein, we report a de novo supramolecular strategy for constructing a biomimetic dicopper catalytic system by integrating a Copper-Histidine (CuH) complex within a self-assembled 5′-GMP nanofibrous hydrogel through spontaneous noncovalent condensation. This one-pot assembly, employing only unmodified biomolecular building blocks, transforms a soluble CuH complex into a hierarchically organized supramolecular hydrogel (CuHG) that closely emulates the structural organization of natural dicopper metalloenzymes. Within this architecture, the CuH complex functions as the catalytic active center, while the GMP nanofibrillar network serves as a dynamic protein surrogate, providing a confined microenvironment that stabilizes the metal center and promotes efficient substrate access and electron transfer. Unlike conventional platforms that passively immobilize metal complexes on rigid supports, the supramolecular organization of CuHG actively modulates the copper coordination environment by stabilizing

both Cu(I) and Cu(II) oxidation states, facilitating reversible redox cycling and formation of reactive copper-oxygen intermediates essential for catalytic oxidation. The hydrogel consequently exhibits efficient catechol oxidase-like activity, selectively catalyzing the oxidation of 3,5-di-tert-butylcatechol to the corresponding 3,5-di-tert-butyl-o-benzoquinone with enzyme-like kinetics, enhanced catalytic efficiency, and remarkable thermal stability.

Building on the nucleotide-containing supramolecular metalloenzymes reported by Xu et al., *[49]* this work introduces a distinct strategy in which an unmodified Cu-histidine complex is incorporated within a self-assembled 5′-GMP G-quadruplex hydrogel. Unlike earlier systems based on Fmoc-modified amino acids, the present platform uses only unmodified biomolecular components to build a hydrogel catalytic microenvironment that supports di-copper oxidase-like activity. It thus offers a minimalist, protein-free platform for designing artificial metalloenzymes through biomolecular self-assembly.

5.2. Result and Discussion

5.2.1. Design Strategy, Biomimetic Inspiration and Spontaneous Self-Assembly of the CuHG Hydrogel

The CuHG hydrogel was designed by emulating the structural organization of catechol oxidase, wherein a binuclear copper active site embedded within a dynamic protein scaffold governs substrate recognition, oxygen activation, and electron transfer. Reproducing such functionality demands not only recreating the primary copper coordination environment but also establishing a secondary coordination sphere capable of stabilizing reactive intermediates and facilitating efficient catalysis.*[37]* We hypothesized that a self-assembled nucleotide scaffold could serve as a protein surrogate, providing a confined yet dynamic microenvironment to organize and stabilize a biomimetic copper catalytic center through cooperative noncovalent interactions.

Accordingly, a Copper-Histidine (CuH) complex was selected as the catalytic motif, as histidine constitutes the primary ligand coordinating dicopper active sites in native catechol oxidases. 5′-GMP was chosen as the structural scaffold owing to its intrinsic capacity to hierarchically self-assemble via Hoogsteen hydrogen bonding, π-π stacking, and electrostatic interactions into extended G-quadruplex-rich nanofibrous architectures. We envisioned that spontaneous condensation of these two biomolecular components would spatially confine the CuH complex within the nucleotide network, emulating the catalytic microenvironment of the native enzyme.(**Figure 5.1.**)

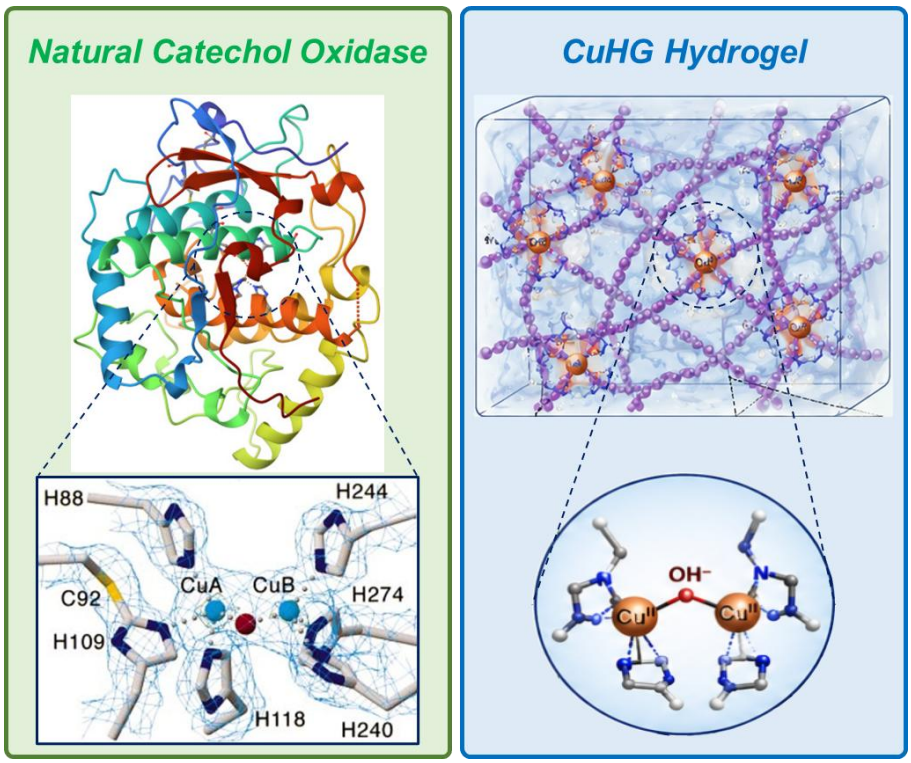


Figure 5.1. *Structural comparison between the dicopper active site of native catechol oxidase (left) and the biomimetic CuHG hydrogel (right). While the natural enzyme employs a histidine-coordinated dicopper center embedded within a protein scaffold, the CuHG hydrogel recreates an analogous microenvironment via G-quadruplex nanofibrillar confinement of the Cu-His complex, stabilizing a hydroxide/oxygen-bridged dicopper active site that mirrors the native catalytic architecture.*[37]

The CuH complex was prepared in aqueous solution under physiological conditions at a Cu(II):histidine stoichiometric ratio of 1:2, yielding a soluble coordination complex.*[38]* Subsequent addition of 5′-

GMP in equimolar proportion to histidine triggered spontaneous supramolecular condensation, rapidly transforming the homogeneous precursor solution into a self-supporting CuHG hydrogel without requiring external crosslinkers or chemical modification of either component (**Figure 5.2**). This self-assembly process drives the hierarchical organization of GMP into an interconnected nanofibrous network while simultaneously entrapping and stabilizing the CuH complex within the growing scaffold. Stable hydrogel formation was observed only at a specific composition of Cu(II), histidine and 5′-GMP. In the optimized formulation, Cu(II) and histidine were combined at a 1:2 molar ratio to form the soluble Cu-His complex, and 5′-GMP was then added at a concentration equimolar to histidine. This composition appears to be important for establishing the interconnected supramolecular network, although additional interactions between Cu(II) and GMP may also contribute to the assembly process.

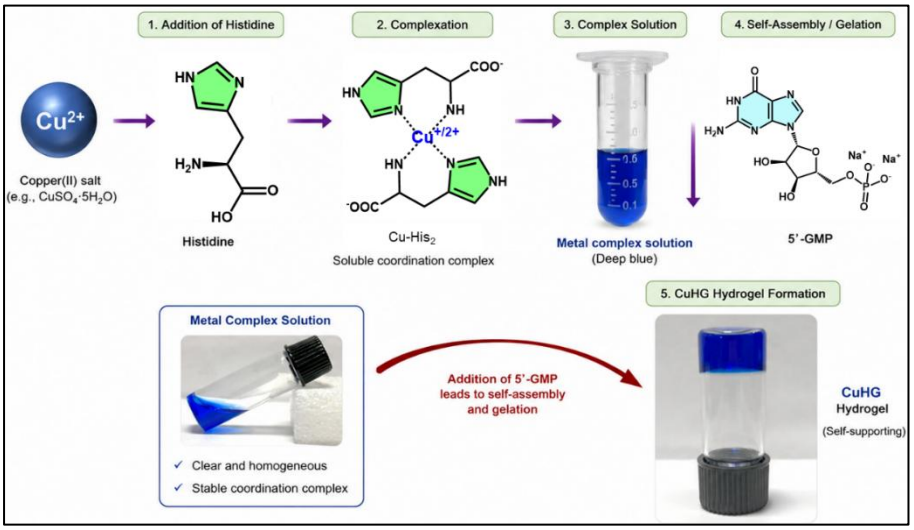


Figure 5.2. *Schematic illustration of the spontaneous formation of the CuHG hydrogel through CuH complexation and nucleotide-directed self-assembly. Cu^{2+} ions initially coordinate with histidine to form a soluble CuH complex, producing a homogeneous deep-blue solution. Subsequent addition of 5′-guanosine monophosphate (5′-GMP) triggers spontaneous supramolecular self-assembly through G-quadruplex formation, resulting in a self-supporting CuHG hydrogel.*

5.2.2. Structural and Coordination Environment of the Artificial Active Site

Following the successful formation of the CuHG hydrogel, a comprehensive structural and spectroscopic investigation was undertaken to elucidate how supramolecular self-assembly influences the coordination environment of the CuH catalytic center. Since the catalytic efficiency of natural di-copper oxidases arises from the intimate interplay between the primary metal coordination sphere and the surrounding protein matrix, it was essential to determine whether the nucleotide-derived hydrogel merely immobilizes the metal complex or actively modulates its local electronic environment.

To investigate whether the self-assembled 5′-GMP hydrogel preserves the coordination environment of the CuH complex upon supramolecular confinement, UV-visible absorption spectroscopy was performed (**Figure 5.3 a**). The CuH complex exhibits a characteristic broad d-d transition centered at approximately 630 nm, which is typical of Cu coordinated by nitrogen donor ligands.*[39]* Upon increasing the concentration of 5′-GMP, the absorption intensity at 630 nm progressively increased while the position of the absorption maximum remained essentially unchanged (**Figure 5.3 b**). The preservation of λ_{max} indicates that the primary coordination geometry surrounding the copper center is retained during hydrogel formation, whereas the systematic enhancement in absorbance suggests progressively greater incorporation and stabilization of the CuH complex within the growing supramolecular network. Notably, the highest absorbance was observed at the optimum gelation composition, implying maximal confinement of the CuH complex within the hierarchically assembled GMP matrix.*[40]* The absence of any significant spectral shift or band broadening further suggests that the hydrogel does not perturb the intrinsic coordination environment of the CuH complex but instead provides a structurally homogeneous microenvironment.

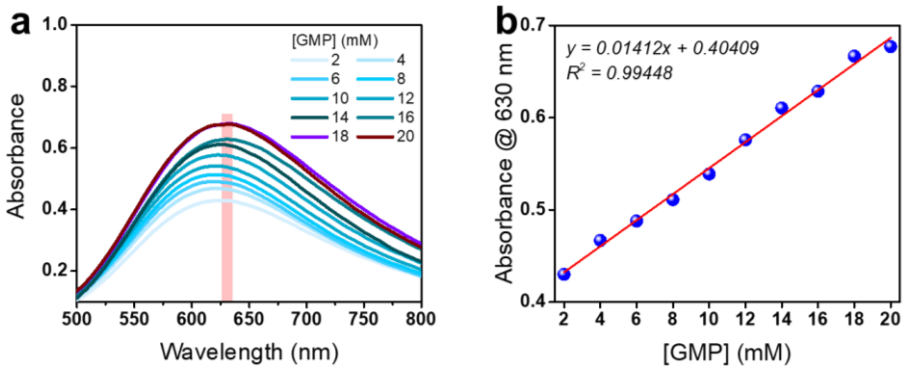


Figure 5.3. *UV-visible characterization of the CuHG hydrogel.* ***(a)*** *UV-Vis absorption spectra of the CuH complex upon increasing 5'-GMP concentration, showing progressive enhancement of the characteristic Cu(II) absorption band at ~630 nm.* ***(b)*** *Linear correlation between the absorbance at 630 nm and GMP concentration, indicating the preservation and stabilization of the CuH complex within the self-assembled hydrogel matrix.*

The metal coordination micro-environment of the CuHG hydrogel were first examined by X-ray photoelectron spectroscopy (XPS). The survey spectra of histidine, the CuH complex, and CuHG hydrogel confirmed the successful incorporation of copper into the supramolecular matrix while retaining the characteristic C, N, O, and Cu signals expected from the constituent biomolecular components (**Figure 5.4 a**). The Cu2p spectra provide direct evidence for changes in the copper oxidation state upon hydrogel formation (**Figure 5.4 b**). The CuH complex predominantly exhibits the characteristics peaks at 952.47 eV ($Cu^{+}2p_{1/2}$) and 932.77 eV ($Cu^{+}2p_{3/2}$) associated with Cu(I). On the other hand, the CuHG hydrogel displays additional contributions with peaks at 953.39 eV ($Cu^{2+}2p_{1/2}$) and 934.16 eV ($Cu^{2+}2p_{1/2}$) corresponding to Cu(II), along with peaks at 951.96 eV ($Cu^{+}2p_{1/2}$) and 934.16 eV ($Cu^{+}2p_{3/2}$), demonstrating the coexistence of both oxidation states within the supramolecular network.*[41-43]* The stabilization of mixed Cu(I)/Cu(II) species is particularly significant because catalytic oxidation by catechol oxidase proceeds through continuous redox cycling between these oxidation states during oxygen activation and substrate oxidation. The ability of the hydrogel to stabilize both copper oxidation states therefore indicates that the nucleotide matrix actively

regulates the electronic structure of the catalytic center rather than acting as a passive support.

To gain further insight into the coordination environment surrounding the catalytic center, high-resolution N_{1s} spectra were analyzed (**Figure 5.4 c**). Free histidine exhibits two characteristic nitrogen environments corresponding to the imidazole nitrogen (N_{π}) and amino/imidazole nitrogen (NH/N_{τ}). Upon coordination with Cu(II), the relative intensities and binding energies of these components change, confirming the participation of histidine nitrogen atoms in metal coordination. Interestingly, after incorporation into the CuHG hydrogel, the N_{1s} spectrum undergoes a further mild shift toward lower binding energies accompanied by subtle changes in peak intensity, indicating that the surrounding nucleotide network modifies the electronic environment of the coordinated histidine ligands.*[44]* These observations indicate that incorporating the Cu-His complex into the GMP hydrogel alters the local electronic environment of the coordinated histidine ligands. This is consistent with additional interactions between the Cu-His complex and the surrounding nucleotide-rich scaffold, which may help stabilize the catalytic center. XPS alone cannot establish the structural organization of a secondary coordination sphere, but the observed changes in chemical state support an altered coordination microenvironment within the hydrogel. X-ray absorption spectroscopy (XAS) will be needed to determine this environment precisely. *[44,49, 50]*

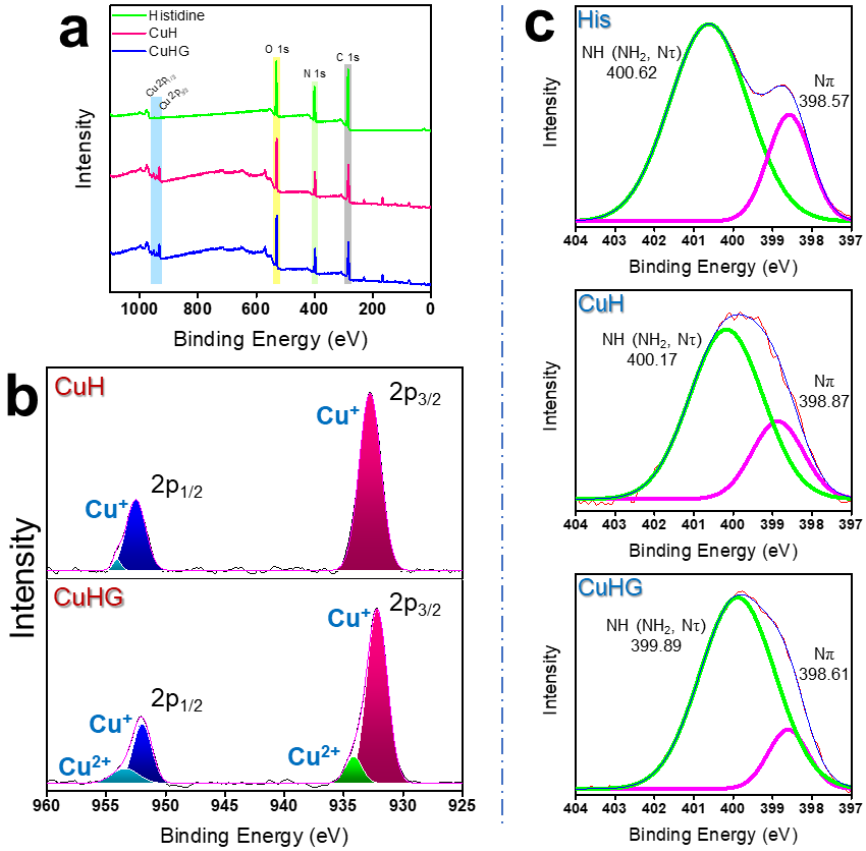


Figure 5.4. ***(a)*** *XPS survey spectra of histidine, the CuH complex, and the CuHG hydrogel confirming the incorporation of copper into the supramolecular matrix.* ***(b)*** *High-resolution Cu_{2p} spectra revealing the coexistence of Cu(I) and Cu(II) species in the CuHG hydrogel, indicative of a redox-active catalytic center stabilized by the self-assembled GMP scaffold.* ***(c)*** *High-resolution N_{1s} spectra showing modulation of the histidine nitrogen coordination environment upon Cu complexation and hydrogel formation.*

Thermogravimetric analysis (TGA) further revealed that incorporation of the CuH complex into the GMP network enhances the thermal robustness of the catalyst (**Figure 5.5 a**). Compared with the free CuH complex, the CuHG hydrogel exhibits delayed thermal degradation and higher residual mass, reflecting stronger intermolecular interactions and improved structural integrity arising from the hierarchical supramolecular network. This enhanced thermal stability demonstrates that the self-assembled fibrillar scaffold effectively protects the catalytic center under elevated temperatures, a characteristic frequently associated with robust enzyme mimics.

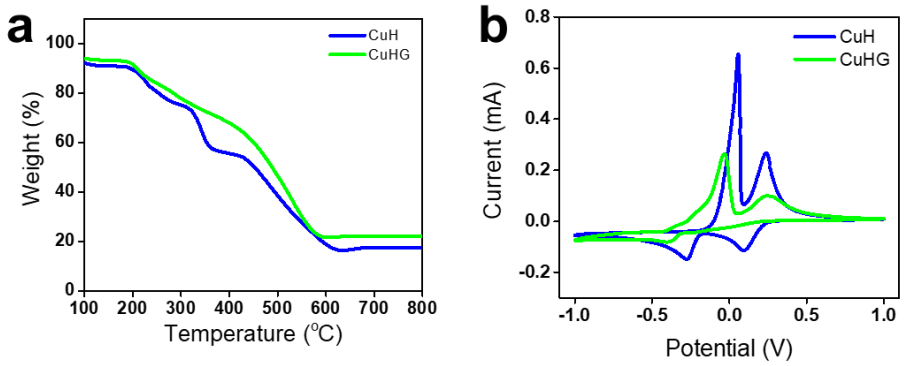


Figure 5.5. (a) *TGA graphs and* ***(b)*** *Cyclic Voltammogram of CuH complex and CuHG hydrogel respectively.*

Electrochemical characterization by cyclic voltammetry (CV) provides additional evidence that supramolecular confinement alters the redox behavior of the copper center (**Figure 5.5 b**). Whereas the CuH complex displays relatively high electrochemical responses, the CuHG hydrogel exhibits a significantly more pronounced and quasi-reversible Cu(II)/Cu(I) redox couple with enhanced peak currents and reduced polarization. These observations indicate that incorporation of the Cu-His complex into the GMP hydrogel modifies its electrochemical response and redox behavior. The enhanced peak currents and changes in the voltametric profile suggest altered accessibility and electrochemical behavior of the copper centers within the supramolecular matrix. However, further quantitative analysis of scan-rate-dependent peak separation and electron-transfer kinetics would be required to establish whether the hydrogel directly facilitates faster heterogeneous electron transfer.

Collectively, these results demonstrate that the self-assembled 5′-GMP network not only preserves the structural integrity of the CuH complex but also provides a confined, protein-like coordination environment that enhances its stability and electronic organization. Such supramolecular confinement establishes the structural foundation for efficient Cu(I)/Cu(II) redox cycling and the enzyme-like catalytic behavior of the CuHG hydrogel.

Following the formation of the Cu-His complex, the addition of 5′-GMP may introduce additional interactions between the nucleotide and the copper-containing coordination complex. Although the spectroscopic observations support the retention of the histidine-associated copper environment after hydrogel formation, possible coordination or electrostatic interactions between GMP and Cu(II) cannot be ruled out. Therefore, the CuHG system is considered a supramolecular assembly in which the Cu-His complex is incorporated into a GMP-rich network, potentially accompanied by additional interactions between the nucleotide scaffold and the metal center.

5.2.3. Hierarchical Organization of the Hydrogel Scaffold

To visualize the intrinsic architecture of the CuHG hydrogel, the sample was diluted 100-fold prior to FE-SEM analysis, enabling clear observation of the self-assembled network. The micrographs reveal a highly interconnected nanofibrillar morphology composed of uniformly distributed, branched fibers, indicative of hierarchical supramolecular organization (**Figure 5.6 a**). EDX analysis confirms the presence of C, N, O, P, and Cu, verifying the successful incorporation of the CuH complex within the GMP scaffold (**Figure 5.6 b**). Furthermore, the fibrils exhibit a narrow diameter distribution with an average diameter of 225.14 ± 49.9 nm, demonstrating controlled self-assembly (**Figure 5.6 c**). This well-defined nanofibrous architecture provides the structural framework necessary to spatially confine the catalytic centers and mimic the protein scaffold of natural metalloenzymes.

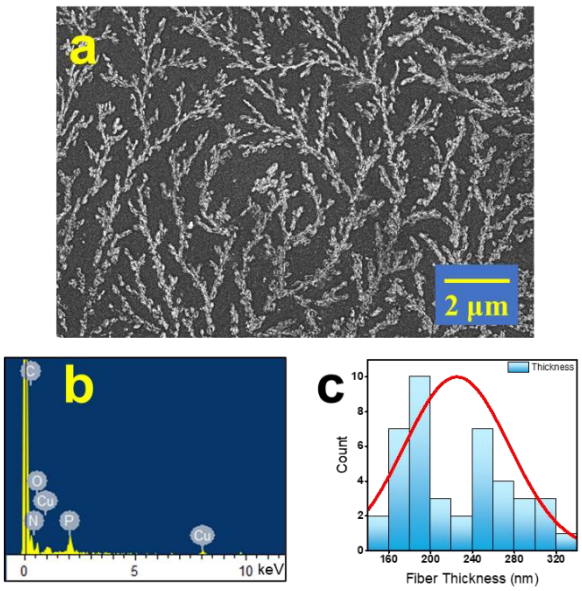


Figure 5.6. *Hierarchical organization of the CuHG hydrogel scaffold.* ***(a)*** *FE-SEM image of the 100-fold diluted CuHG hydrogel showing an interconnected nanofibrillar network.* ***(b)*** *EDX spectrum confirming the elemental composition (C, N, O, P, and Cu) of the hydrogel scaffold.* ***(c)*** *Diameter distribution of the nanofibers, revealing a uniform fibrillar architecture with an average fiber diameter of 225.14 ± 49.9 nm, indicative of controlled supramolecular self-assembly.*

To investigate the supramolecular organization of the nucleotide scaffold, the secondary structure of the CuHG hydrogel was examined by circular dichroism (CD) spectroscopy. Since the intrinsic chirality of L-histidine contributes significantly to the CD signal, an equimolar mixture of D- and L-histidine was employed during these measurements to eliminate the chiral contribution of the amino acid and selectively probe the structural organization of the GMP network. As shown in **Figure 5.7 a**, pristine GMP exhibited only weak ellipticity, whereas the CuHG hydrogel displayed a characteristic negative Cotton effect centered at ~250 nm, which is a well-established spectroscopic signature of G-quartet/G-quadruplex assemblies.*[45,46]* The formation of G-quadruplex domains was further corroborated using the Thioflavin T (ThT) fluorescence assay. While free ThT exhibited negligible fluorescence, the CuHG hydrogel produced a substantial enhancement in fluorescence intensity, indicating efficient binding of ThT to the ordered G-quartet structures present within the hydrogel network (**Figure 5.7 b**). Quantitative analysis of the fluorescence enhancement,

expressed as the FL/FL$_0$ ratio, revealed values that fall well within the range reported for established G-quadruplex-based supramolecular assemblies, providing further evidence for the successful formation of a G-quadruplex-rich scaffold (**Figure 5.7 c**).*[47,48]*

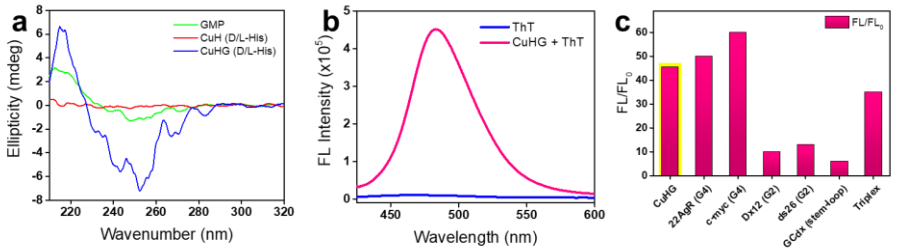


Figure 5.7. *Structural characterization of the G-quadruplex framework in the CuHG hydrogel.* ***(a)*** *Circular dichroism (CD) spectra of histidine, 5'-GMP, and the CuHG hydrogel, showing the characteristic negative ellipticity at ~250 nm indicative of G-quadruplex formation.* ***(b)*** *Thioflavin T (ThT) fluorescence spectra demonstrating selective binding of ThT to the G-quadruplex-rich CuHG hydrogel.* ***(c)*** *Relative fluorescence enhancement (FL/FL$_0$) of ThT in the CuHG hydrogel compared with reported G-quadruplex assemblies, confirming the formation of an ordered G-quadruplex secondary structure within the supramolecular scaffold.*

Given the strong pH dependence of 5′-GMP self-assembly, we hypothesized that CuHG hydrogel formation is primarily governed by pH modulation induced by Copper-Histidine complexation. While free histidine exhibits a basic aqueous pH (~8.1) and is unable to initiate the self-assembly of 5′-GMP, coordination with Cu^{2+} markedly lowers the solution pH to approximately 3.75 owing to metal binding through the imidazole and amino functionalities. Notably, this pH lies within the optimal mildly acidic range (pH ~3.5-4.5) reported for efficient G-quadruplex formation.*[34]* The acidic environment reduces electrostatic repulsion between the negatively charged phosphate groups of GMP, thereby facilitating intermolecular association through Hoogsteen hydrogen bonding and π-π stacking. This cooperative assembly promotes the formation of planar G-quartets, which subsequently stack into columnar G-quadruplex structures and further organize into an interconnected nanofibrillar network. Thus, the CuH complex performs a dual role by serving as the catalytic precursor while simultaneously

directing the hierarchical self-assembly of GMP into a G-quadruplex-rich secondary structure that spatially confines and stabilizes the catalytic center within a protein-like supramolecular scaffold.

5.2.4. Mechanical Properties of the CuHG hydrogel

To investigate the mechanical behavior of the CuHG hydrogel, oscillatory rheological measurements were performed. The amplitude sweep revealed a well-defined linear viscoelastic region (0.1-216% strain), where the storage modulus (G′) remained significantly higher than the loss modulus (G″), confirming the predominance of elastic behavior and the formation of a mechanically stable nanofibrillar network (**Figure 5.8 a**). Beyond the yield strain (~300%), the crossover of G′ and G″ indicated disruption of the supramolecular network. Similarly, the frequency sweep demonstrated the consistent dominance of G′ over G″ across the investigated frequency range (0.1-100 rad s^{-1}), indicating that the hydrogel retains its structural integrity under dynamic mechanical deformation (**Figure 5.8 b**).

The dynamic nature of the CuHG network was further evaluated by alternating low (1%) and high (1000%) strain cycles. Under high strain, the hydrogel underwent reversible network disruption, whereas restoring the strain to 1% resulted in rapid recovery of the storage modulus over five consecutive cycles, demonstrating excellent thixotropic behavior and injectability (**Figure 5.8 c**). Consistent with these findings, the hydrogel exhibited rapid gel-sol-gel transitions and efficient self-healing (**Figure 5.8 d**), confirming that the nanofibrillar scaffold is stabilized by reversible non-covalent interactions. Such dynamic mechanical adaptability closely resembles the behavior of natural protein scaffolds, enabling the CuHG hydrogel to maintain a stable catalytic microenvironment while undergoing reversible structural rearrangements.

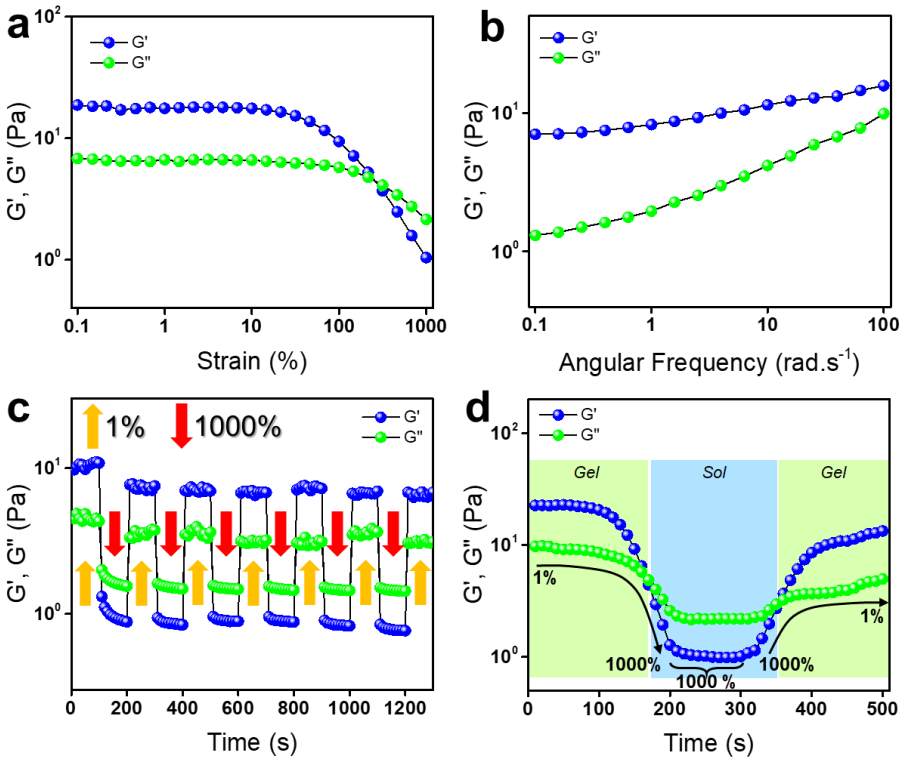


Figure 5.8. *Rheological characterization of the CuHG hydrogel.* ***(a)*** *Dynamic strain sweep,* ***(b)*** *frequency sweep at 1% strain,* ***(c)*** *thixotropic loop measurements at an angular frequency of 10 rad* s^{-1}*, and* ***(d)*** *time-dependent oscillatory rheology demonstrating reversible gel-sol-gel transition and rapid self-recovery of the CuHG hydrogel under alternating low (1%) and high (1000%) strain.*

5.2.5. Catechol Oxidase-Like Catalytic Activity

Having established that the CuHG hydrogel recreates a hierarchically organized G-quadruplex nanofibrillar scaffold capable of stabilizing the CuH active site within a protein-like secondary coordination environment, we next investigated whether this biomimetic architecture could reproduce the catalytic function of natural catechol oxidase. In native catechol oxidases, a dicopper center embedded within a dynamic protein matrix cooperatively activates molecular oxygen and selectively oxidizes catechols to o-quinones, with the protein scaffold critically regulating substrate accessibility, intermediate stabilization, and electron transfer. Inspired by this structural-functional synergy, the CuHG hydrogel was designed such that the CuH complex mimics the catalytic copper center, while the self-assembled G-quadruplex-rich GMP network serves as a protein surrogate, generating a confined

microenvironment analogous to the enzyme's secondary coordination sphere. The oxidation of 3,5-di-tert-butylcatechol (DTBC) to 3,5-di-tert-butyl-o-benzoquinone (DTBQ) was employed as the benchmark reaction to evaluate this catalytic mimicry (**Figure 5.9 a**).*[43,49]*

Upon incubation with the hydrogel, a time-dependent increase in the characteristic DTBQ absorption band at ~405 nm confirmed continuous DTBC oxidation (**Figure 5.9 b**). To verify oxidase-type reactivity, controlled experiments under aerobic and anaerobic (N_2) conditions were performed with all other parameters held constant. Negligible product formation was observed under N_2 after 30 minutes, confirming strict O_2 dependence consistent with the mechanism of native catechol oxidases (**Figure 5.9 c**). Comparative evaluation of all precursor components and the free CuH complex revealed negligible catalytic velocities relative to the intact CuHG hydrogel, demonstrating that supramolecular confinement within the GMP nanofibrillar scaffold is essential for efficient substrate oxidation (**Figure 5.9 d**).

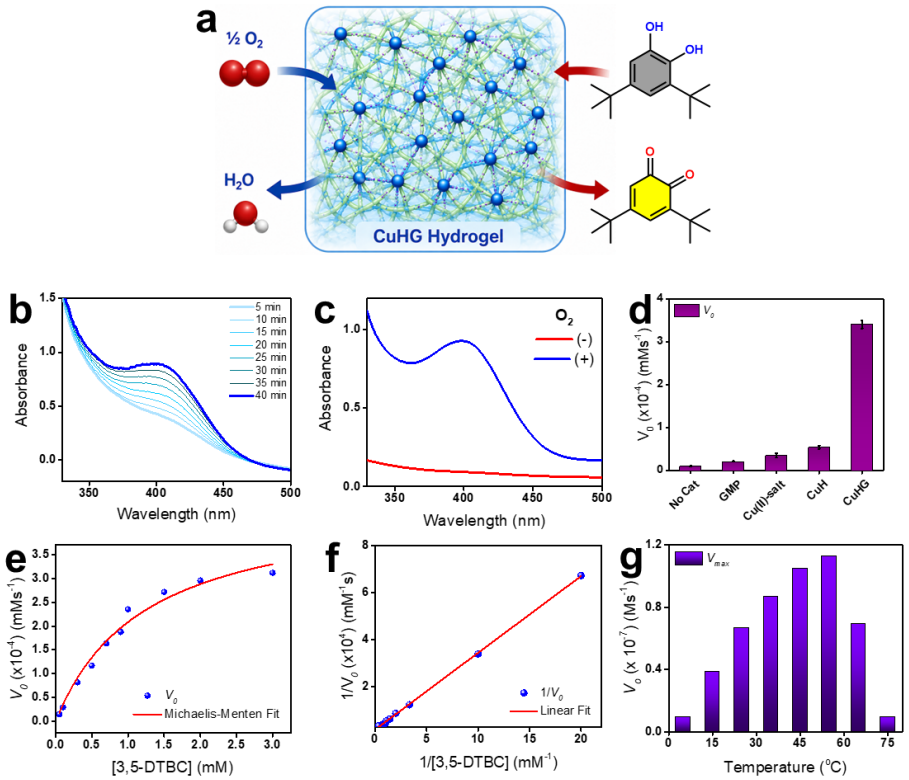


Figure 5.9. *Catechol oxidase-like catalytic activity of the CuHG hydrogel.* ***(a)*** *Schematic representation of the CuHG hydrogel-catalyzed oxidation of 3,5-di-tert-*

butylcatechol (DTBC) to 3,5-di-tert-butyl-o-benzoquinone (DTBQ) using molecular oxygen. ***(b)*** *Time-dependent UV-vis spectra showing DTBQ formation.* ***(c)*** *Control experiments demonstrating the catalytic activity of the CuHG hydrogel in presence of* O_2. ***(d)*** *Relative catalytic activity of CuHG compared with the pristine components including CuH complex.* ***(e)*** *Michaelis-Menten kinetics and* ***(f)*** *corresponding Lineweaver-Burk plot for DTBC oxidation.* ***(g)*** *Catalytic activity of the CuHG hydrogel over a wide range of temperature.*

Catalytic efficiency was quantitatively assessed via Michaelis-Menten kinetics by varying DTBC concentration. The system exhibited characteristic enzyme-like saturation behavior, and kinetic parameters were extracted from the corresponding Lineweaver-Burk plot (**Figure 5.9 e, f**). A low K_M of 1.25 mM indicates high substrate affinity, while a V_{max} of 4.66×10^{-4} mMs^{-1} reflects robust catalytic turnover. The hydrogel further retained activity across a broad temperature range (15-60 °C) with minimal performance loss, underscoring the structural integrity of the confined active sites (**Figure 5.9 g**). Collectively, these results demonstrate that the G-quadruplex scaffold not only stabilizes the dicopper-inspired active center but also furnishes a protein-like microenvironment that facilitates efficient oxygen activation and substrate oxidation, faithfully reproducing the key functional hallmarks of natural catechol oxidase.

5.2.6. Mechanistic Role of Supramolecular Confinement: Stabilizing the Active Site

To gain mechanistic insight into the origin of the enhanced catechol oxidase-like activity, in situ electrospray ionization mass spectrometry (ESI-MS) was performed under catalytic conditions in the presence of molecular oxygen to probe the nature of the active catalytic species. As shown in **Figure 5.10**, the CuH complex alone predominantly exhibited a signal corresponding to a $(Cu\text{-}His)_2$ dimer, indicating that although the dicopper complex is formed, it lacks further activation by molecular oxygen. In contrast, the CuHG hydrogel displayed a distinct oxygen-containing dicopper species, corresponding to a bridging oxygen-bound Cu-His dimer, closely resembling the

oxygen-bridged active center reported for natural catechol oxidase. The emergence of this oxygen-bridged intermediate provides direct experimental evidence that the supramolecular hydrogel promotes the formation and stabilization of the catalytically active dicopper species during the oxidation reaction.

The formation of this oxygen-bridged intermediate highlights the crucial role of supramolecular confinement provided by the hierarchically assembled GMP nanofibrillar scaffold. Beyond simply immobilizing the CuH complex, the G-quadruplex network creates a confined catalytic microenvironment that spatially organizes the dicopper centers, facilitates oxygen binding between the two copper ions, and stabilizes the reactive oxygen-bridged intermediate through secondary coordination sphere interactions. Such stabilization closely parallels the structural role of the protein matrix in natural catechol oxidase, where the surrounding residues precisely orient the dicopper center and promote efficient oxygen activation and electron transfer. Consequently, the CuHG hydrogel exhibits significantly enhanced catalytic efficiency compared with the free CuH complex, demonstrating that the improved enzyme-like activity originates not only from the presence of the Copper-Histidine active site but also from its stabilization within the nucleotide-derived supramolecular scaffold. These findings provide direct mechanistic evidence that the G-quadruplex hydrogel functions as a biomimetic protein matrix, recreating the structural environment necessary to stabilize the catalytically competent oxygen-bridged dicopper intermediate responsible for efficient catechol oxidation.

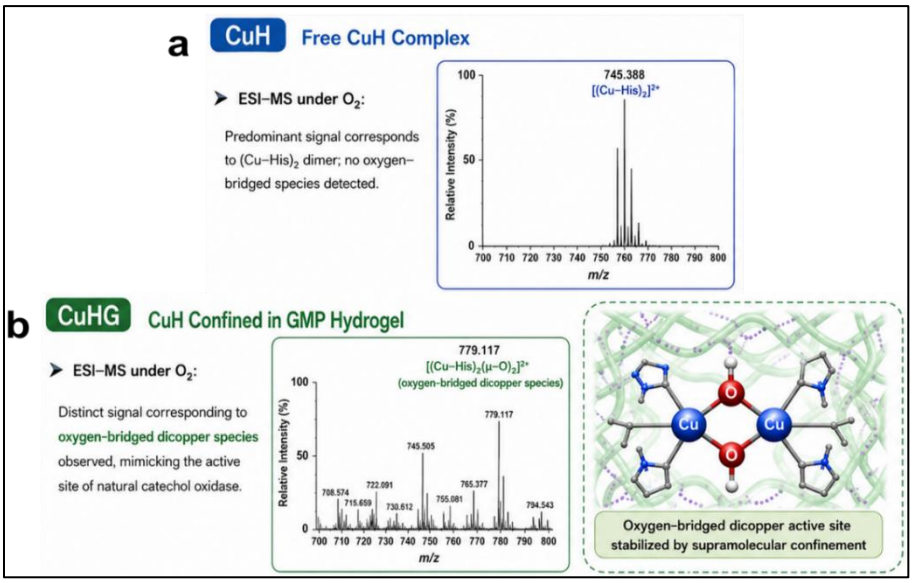


Figure 5.10. *Mechanistic role of supramolecular confinement in stabilizing the catalytically active dicopper intermediate. Comparison of the in-situ ESI-MS spectra of the free CuH complex and the CuHG hydrogel under aerobic catalytic conditions. The free CuH complex predominantly exhibits a (Cu-His)₂ dimer, whereas the CuHG hydrogel stabilizes an oxygen-bridged dicopper intermediate, closely resembling the active site of natural catechol oxidase.*

5.3. Conclusion and Future Scope

This chapter demonstrates a minimalist biomimetic strategy for constructing a protein-free artificial metalloenzyme through the spontaneous self-assembly of a Copper-Histidine (CuH) complex within a 5′-GMP-derived G-quadruplex hydrogel. The hierarchically organized nanofibrillar scaffold successfully recreates the structural and functional attributes of natural catechol oxidase by providing a dynamic secondary coordination environment that stabilizes the dicopper catalytic center. Structural, spectroscopic, electrochemical, and rheological investigations confirmed the formation of a robust G-quadruplex framework, stabilization of mixed Cu(I)/Cu(II) oxidation states, excellent mechanical resilience, and efficient self-recovery. The CuHG hydrogel exhibited oxygen-dependent catechol oxidase-like activity with high substrate affinity, broad thermal stability, and enzyme-like catalytic kinetics. Furthermore, in situ ESI-MS revealed the formation of an oxygen-bridged dicopper intermediate within the hydrogel,

providing direct mechanistic evidence that supramolecular confinement stabilizes the catalytically active species responsible for enhanced catalytic performance.

Although these findings establish the CuHG hydrogel as a promising biomimetic catalytic platform, a comprehensive understanding of the relationship between the supramolecular scaffold, the coordination environment, and catalytic activity remains to be established. Ongoing investigations employing advanced structural characterization techniques, including X-ray absorption spectroscopy (EXAFS), electron paramagnetic resonance (EPR) spectroscopy, and molecular dynamics (MD) simulations, will provide atomic-level insight into the coordination geometry, electronic structure, and dynamic stabilization of the Cu active site within the G-quadruplex scaffold. These studies will establish a detailed structure–activity relationship, enabling a deeper mechanistic understanding of how supramolecular confinement governs the stability, redox behavior, and catalytic efficiency of the artificial metalloenzyme.

5.4. Experimental Section

5.4.1. Synthesis of CuHG hydrogel

A homogeneous, transparent solution was first prepared by dissolving 100 mM Copper(II) sulfate pentahydrate and 200 mM L-histidine in deionized water. The mixture was mildly heated to 45°C for 5 minutes, followed by the addition of 200 mM $GMPNa_2$ under continuous stirring, yielding another homogeneous, transparent solution. The resulting solution was kept undisturbed for 5-10 minutes, leading to the formation of a dark blue colored transparent hydrogel. This hydrogel was stable and rigid, forming reproducibly within a defined pH range. Subsequently, the hydrogel was freeze-dried to obtain a xerogel suitable for solid-state characterization and catalytic studies. For dilute-phase spectroscopic and microscopic analyses, the hydrogel was dispersed in deionized water and incubated to achieve equilibrium swelling.

5.4.2. Characterizations

5.4.2.1. Microscopic Characterizations

For microscopic imaging, the prepared hydrogels were diluted 100-fold and subsequently drop-cast onto thoroughly cleaned glass slides, then allowed to partially dry at 25 °C prior to imaging. Field emission scanning electron microscopy (FE-SEM) was performed using a Carl Zeiss Supra 55 instruments. Fibrillar morphology, including fiber diameter and length distributions, was quantified from the acquired FE-SEM micrographs using ImageJ software.

5.4.2.2. Spectroscopic Characterization

Spectroscopic characterizations were performed as follows. UV-visible absorption spectra were recorded on a Varian Cary 100 Bio spectrophotometer using samples diluted 100-fold with Milli-Q water. Circular dichroism (CD) spectra were acquired using a JASCO J-815 spectropolarimeter with a 10 mm path-length quartz cuvette at a scan rate of 50 nm min^{-1}; baseline correction was performed using Milli-Q water as reference. Steady-state fluorescence spectra were recorded on a Horiba Jobin Yvon FluoroMax-4P spectrofluorometer. For the Thioflavin T (ThT) fluorescence assay, ThT dye was added to the hydrogel samples at an appropriate concentration and allowed to incubate for a defined period to facilitate dye integration into the fibrillar network, resulting in characteristic fluorescence enhancement.

5.4.2.3. pH Measurement

pH measurements of the diluted (10-times) metal complex solutions and hydrogels were carried out using a LABMAN LMPH10 pH meter calibrated with standard buffers.

5.4.2.4. Rheological Measurements

Rheological properties of the hydrogels were measured using an Anton Paar Physica MCR 301 rheometer. Dynamic strain (amplitude) sweep experiments were conducted at a constant angular frequency of 10 $rad.s^{-1}$, while frequency sweep measurements were performed over a range of angular frequencies at a fixed strain of 1%, within the linear viscoelastic

region. All measurements were carried out at 25 °C using appropriate plate geometry.

5.4.2.5. Enzyme Kinetics and Catalytic Assays

Enzymatic kinetics and biocatalytic assays were monitored by recording time-dependent absorbance changes using a Varian Cary 100 Bio UV-visible spectrophotometer with a quartz cuvette (10 mm path length). Initial reaction velocities were determined from the linear portion of the absorbance versus time profiles, and the Michaelis-Menten kinetic parameters (K_M and V_{max}) were derived by fitting the data to the Michaelis-Menten equation. To elucidate the mechanistic basis of the active catalytic center, reaction intermediates and products were identified using liquid chromatography-mass spectrometry (LC-MS) on a Waters ACQUITY H-Class Plus UPLC system coupled to a Xevo G3 QTOF mass spectrometer. Samples were directly collected from the enzymatic reaction mixture under catalytic conditions and analyzed without further purification to capture transient intermediates.

5.4.3. Enzyme Kinetics

Catechol oxidase-like activity was evaluated using diluted hydrogel samples to ensure efficient substrate diffusion and accessibility to the active sites. Kinetic measurements were performed in HEPES buffer (10 mM, pH 6.8) with a total reaction volume of 3 mL, containing 1.5 mg of dried hydrogel (0.5 mg mL^{-1}) and varying concentrations of 3,5-di-tert-butylcatechol (DTBC). The reaction was initiated by the addition of DTBC followed by thorough mixing, and the oxidation of DTBC to 3,5-di-tert-butylquinone (DTBQ) was monitored by recording time-dependent absorbance at 405 nm over a 10 min incubation period at room temperature (25 °C). Initial reaction velocities were extracted from the linear region of the absorbance versus time profiles.

Steady-state kinetic parameters were determined by varying the DTBC concentration over the range of 0.1-3 mM while maintaining a constant hydrogel content (0.5 mg mL^{-1}). The Michaelis constant (K_M) and maximum reaction velocity (V_{max}) were obtained by fitting the data

to the Lineweaver-Burk double-reciprocal form of the Michaelis-Menten equation:

$$\frac{1}{V} = \frac{K_M}{V_{max}[S]} + \frac{1}{V_{max}}$$

where V is the initial reaction velocity, [S] is the substrate concentration, K_M is the Michaelis constant, and V_{max} is the maximum reaction velocity.

5.5. References

1. Wang, T., Fan, X., Hou, C. et al. (2018), Design of artificial enzymes by supramolecular strategies, Current Opinion in Structural Biology, 51, 19-27 (DOI: 10.1016/j.sbi.2018.02.003.)

2. Wiester, M.J., Ulmann, P.A., Mirkin, C.A. (2011), Enzyme Mimics Based Upon Supramolecular Coordination Chemistry, Angewandte Chemie International Edition, 50, 114-137 (DOI: 10.1002/anie.201000380.)

3. Meeuwissen, J., Reek, J.N.H. (2010), Supramolecular catalysis beyond enzyme mimics, Nature Chem, 2, 615-621 (DOI: 10.1038/nchem.744.)

4. Makam, P., Yamijala, S.S.R.K.C., Tao, K. et al. (2019), Non-proteinaceous hydrolase comprised of a phenylalanine metallo-supramolecular amyloid-like structure, Nat Catal, 2, 977-985 (DOI: 10.1038/s41929-019-0348-x.)

5. Liu, S., Du, P., Sun, H. et al. (2020), Bioinspired Supramolecular Catalysts from Designed Self-Assembly of DNA or Peptides, ACS Catal., 10, 14937-14958 (DOI: 10.1021/acscatal.0c03753.)

6. Liu, Q., Wang, H., Shi, X. et al. (2017), Self-Assembled DNA/Peptide-Based Nanoparticle Exhibiting Synergistic Enzymatic Activity, ACS Nano, 11, 7251-7258 (DOI: 10.1021/acsnano.7b03195.)

7. Rufo, C.M., Moroz, Y.S., Moroz, O.V. et al. (2014), Short peptides self-assemble to produce catalytic amyloids, Nature Chem, 6, 303-309 (DOI: 10.1038/nchem.1894.)

8. Solomon, L.A., Kronenberg, J.B., Fry, H.C. (2017), Control of Heme Coordination and Catalytic Activity by Conformational Changes in Peptide-Amphiphile Assemblies, J. Am. Chem. Soc., 139, 8497-8507 (DOI: 10.1021/jacs.7b01588.)

9. Lyu, Y., Scrimin, P. (2021), Mimicking Enzymes: The Quest for Powerful Catalysts from Simple Molecules to Nanozymes, ACS Catal., 11, 11501-11509 (DOI: 10.1021/acscatal.1c01219.)

10. Kang, T., Kim, Y.G., Kim, D. et al. (2020), Inorganic nanoparticles with enzyme-mimetic activities for biomedical applications, Coordination Chemistry Reviews, 403, 213092 (DOI: 10.1016/j.ccr.2019.213092.)

11. Fu, Q., Tian, S., Wang, S. et al. (2025), Advances in Metal–Organic Framework-Based Nanozymes for Biosensing and Point-of-Care Testing Applications, ACS Appl. Nano Mater., 8, 17339-17355 (DOI: 10.1021/acsanm.5c02319.)

12. Zhang, Y., Zhang, C., Qian, W. et al. (2024), Recent advances in MOF-based nanozymes: Synthesis, activities, and bioapplications, Biosensors and Bioelectronics, 263, 116593 (DOI: 10.1016/j.bios.2024.116593.)

13. Liang, M., Yan, X. (2019), Nanozymes: From New Concepts, Mechanisms, and Standards to Applications, Acc. Chem. Res., 52, 2190-2200 (DOI: 10.1021/acs.accounts.9b00140.)

14. Solomon, E.I., Sundaram, U.M., Machonkin, T.E. (1996), Multicopper Oxidases and Oxygenases, Chem. Rev., 96, 2563-2606 (DOI: 10.1021/cr950046o.)

15. Solomon, E.I. (2016), Dioxygen Binding, Activation, and Reduction to H2O by Cu Enzymes, Inorg. Chem., 55, 6364-6375 (DOI: 10.1021/acs.inorgchem.6b01034.)

16. Jones, S.M., Solomon, E.I. (2015), Electron transfer and reaction mechanism of laccases, Cell. Mol. Life Sci., 72, 869-883 (DOI: 10.1007/s00018-014-1826-6.)

17. Heppner, D.E., Kjaergaard, C.H., Solomon, E.I. (2013), Molecular Origin of Rapid versus Slow Intramolecular Electron Transfer in the Catalytic Cycle of the Multicopper Oxidases, J. Am. Chem. Soc., 135, 12212-12215 (DOI: 10.1021/ja4064525.)

18. Thanneeru, S., Milazzo, N., Lopes, A. et al. (2019), Synthetic Polymers To Promote Cooperative Cu Activity for O2 Activation: Poly vs Mono, J. Am. Chem. Soc., 141, 4252-4256 (DOI: 10.1021/jacs.9b01093.)

19. Liang, H., Lin, F., Zhang, Z. et al. (2017), Multicopper Laccase Mimicking Nanozymes with Nucleotides as Ligands, ACS Appl. Mater. Interfaces, 9, 1352-1360 (DOI: 10.1021/acsami.6b15124.)

20. Wang, J., Huang, R., Qi, W. et al. (2019), Construction of a bioinspired laccase-mimicking nanozyme for the degradation and detection of phenolic pollutants, Applied Catalysis B: Environmental, 254, 452-462 (DOI: 10.1016/j.apcatb.2019.05.012.)

21. Makhlynets, O.V., Gosavi, P.M., Korendovych, I.V. (2016), Short Self-Assembling Peptides Are Able to Bind to Copper and Activate Oxygen, Angewandte Chemie International Edition, 55, 9017-9020 (DOI: 10.1002/anie.201602480.)

22. Koval, I.A., Gamez, P., Belle, C. et al. (2006), Synthetic models of the active site of catechol oxidase: mechanistic studies, Chem. Soc. Rev., 35, 814-840 (DOI: 10.1039/B516250P.)

23. Huang, W., Wang, S., Wei, Y. et al. (2025), Design and evolution of artificial enzyme with in-situ biosynthesized non-canonical amino acid, Nat Commun, 16, 8698 (DOI: 10.1038/s41467-025-63733-3.)

24. Hanreich, S., Bonandi, E., Drienovská, I. (2023), Design of Artificial Enzymes: Insights into Protein Scaffolds, ChemBioChem, 24, e202200566 (DOI: 10.1002/cbic.202200566.)

25. Rakotoharisoa, R.V., Seifinoferest, B., Zarifi, N. et al. (2024), Design of Efficient Artificial Enzymes Using Crystallographically Enhanced Conformational Sampling, J. Am. Chem. Soc., 146, 10001-10013 (DOI: 10.1021/jacs.4c00677.)

26. Du, X., Zhou, J., Xu, B. (2014), Supramolecular Hydrogels Made of Basic Biological Building Blocks, Chemistry - An Asian Journal, 9, 1446-1472 (DOI: 10.1002/asia.201301693.)

27. Schmid, S.Y., Lachowski, K., Chiang, H.T. et al. (2023), Mechanisms of Biomolecular Self-Assembly Investigated Through In Situ Observations of Structures and Dynamics, Angewandte Chemie International Edition, 62, e202309725 (DOI: 10.1002/anie.202309725.)

28. Mandal, D., Shirazi, A.N., Parang, K. (2014), Self-assembly of peptides to nanostructures, Org. Biomol. Chem., 12, 3544-3561 (DOI: 10.1039/C4OB00447G.)

29. Sikder, A., Esen, C., O'Reilly, R.K. (2022), Nucleobase-Interaction-Directed Biomimetic Supramolecular Self-Assembly, Acc. Chem. Res., 55, 1609-1619 (DOI: 10.1021/acs.accounts.2c00135.)

30. Peters, G.M., Davis, J.T. (2016), Supramolecular gels made from nucleobase, nucleoside and nucleotide analogs, Chem. Soc. Rev., 45, 3188–3206 (DOI: 10.1039/C6CS00183A.)

31. Harraz, D.M., Davis, J.T. (2018), A self-assembled peroxidase from 5′-GMP and heme, Chem. Commun., 54, 1587-1590 (DOI: 10.1039/C7CC09900B.)

32. Davis, J.T., Spada, G.P. (2007), Supramolecular architectures generated by self-assembly of guanosine derivatives, Chem. Soc. Rev., 36, 296-313 (DOI: 10.1039/B600282J.)

33. Sarma, S., Thakur, N., Varshney, N. et al. (2024), Chromatin inspired bio-condensation between biomass DNA and guanosine monophosphate produces all-nucleic hydrogel as a hydrotropic drug carrier, Commun Chem, 7, 261 (DOI: 10.1038/s42004-024-01353-6.)

34. Thakur, N., Sarma, S., Agarwal, V. et al. (2025), Acidic Amino Acid Induced 5′-Guanosine Monophosphate Fibrillar Nanozyme: A Highly Efficient Metal-Free Intrinsic Peroxidase Mimic, Nano Lett., 25, 15407-15415 (DOI: 10.1021/acs.nanolett.5c04390.)

35. Sarma, S., Jain, N., Bansal, L. et al. (2025), Supramolecular Self-Assembly of Polyaniline Embedded Enzyme-Mimicking GMP-Condensate Hydrogel for Electrochromic Energy Storage Applications, ACS Appl. Mater. Interfaces, 17, 48532-48546 (DOI: 10.1021/acsami.5c08151.)

36. Chakraborty, A., Dash, S., Thakur, N. et al. (2024), Polyoxometalate-Guanosine Monophosphate Hydrogels with Haloperoxidase-like Activity for Antibacterial Performance, Biomacromolecules, 25, 104-118 (DOI: 10.1021/acs.biomac.3c00845.)

37. Klabunde, T., Eicken, C., Sacchettini, J.C. et al. (1998), Crystal structure of a plant catechol oxidase containing a dicopper center, Nat Struct Mol Biol, 5, 1084-1090 (DOI: 10.1038/4193.)

38. Sigel, H., McCormick, D.B. (1971), Structure of the copper(II)-L-histidine 1:2 complex in solution, J. Am. Chem. Soc., 93, 2041-2044 (DOI: 10.1021/ja00737a032.)

39. Hathaway, B.J., Billing, D.E. (1970), The electronic properties and stereochemistry of mono-nuclear complexes of the copper(II) ion, Coordination Chemistry Reviews, 5, 143-207 (DOI: 10.1016/S0010-8545(00)80135-6.)

40. Chakraborty, A., Rani, A., Sinha, P. et al. (2025), Guanosine Monophosphate Induced Solubilization of Folic Acid Leading to Hydrogel Formation for Targeted Delivery of Hydrophilic and

Hydrophobic Drugs, ACS Appl. Mater. Interfaces, 17, 11848-11860 (DOI: 10.1021/acsami.4c21306.)

41. McIntyre, N.S., Cook, M.G. (1975), X-ray photoelectron studies on some oxides and hydroxides of cobalt, nickel, and copper, Anal. Chem., 47, 2208-2213 (DOI: 10.1021/ac60363a034.)

42. Ávila-Torres, Y., Huerta, L., Barba-Behrens, N. (2013), XPS-Characterization of Heterometallic Coordination Compounds with Optically Active Ligands, Journal of Chemistry, 2013, 370637 (DOI: 10.1155/2013/370637.)

43. Singh, A.K., Sharma, D., Singh, D.K. et al. (2025), Oxidase-Like Nanozyme Activity of Ultrathin Copper Metal–Organic Framework Nanosheets with High Specificity for Catechol Oxidation, ChemCatChem, 17, e202401029 (DOI: 10.1002/cctc.202401029.)

44. Feyer, V., Plekan, O., Ptasińska, S. et al. (2012), Adsorption of Histidine and a Histidine Tripeptide on Au(111) and Au(110) from Acidic Solution, J. Phys. Chem. C, 116, 22960-22966 (DOI: 10.1021/jp307463z.)

45. Panda, M., Walmsley, J.A. (2011), Circular Dichroism Study of Supramolecular Assemblies of Guanosine 5′-Monophosphate, J. Phys. Chem. B, 115, 6377-6383 (DOI: 10.1021/jp201630g.)

46. del Villar-Guerra, R., Trent, J.O., Chaires, J.B. (2018), G-Quadruplex Secondary Structure Obtained from Circular Dichroism Spectroscopy, Angewandte Chemie International Edition, 57, 7171-7175 (DOI: 10.1002/anie.201709184.)

47. Renaud de la Faverie, A., Guédin, A., Bedrat, A. et al. (2014), Thioflavin T as a fluorescence light-up probe for G4 formation, Nucleic Acids Res, 42, e65 (DOI: 10.1093/nar/gku111.)

48. Bhasikuttan, A.C., Mohanty, J. (2015), Targeting G-quadruplex structures with extrinsic fluorogenic dyes: promising fluorescence

sensors, Chem. Commun., 51, 7581-7597 (DOI: 10.1039/C4CC10030A.)

49. Xu, S., Wu, H., Liu, S. et al. (2023), A supramolecular metalloenzyme possessing robust oxidase-mimetic catalytic function, Nat Commun, 14, 4040 (DOI: 10.1038/s41467-023-39779-6.)

50. Wright, A. M., Wu, Z., Zhang, G. et al. (2018), A Structural Mimic of Carbonic Anhydrase in a Metal-Organic Framework, Chem, 4, 1-8 (DOI: 10.1016/j.chempr.2018.09.011.)

Chapter 6

6. Supramolecular Self-Assembly of Polyaniline Embedded Enzyme Mimicking GMP-Condensate Hydrogel for Electrochromic Energy Storage Applications

6.1. Introduction

Hydrogels are three-dimensional, solid-like networks formed through the entanglement of supramolecular or polymeric micro- and nanostructures, and their soft, water-rich, tissue-like nature positions them as a natural interfacing material for merging human and machine systems.*[1-3]* By closely mimicking the mechanical and biochemical properties of the extracellular matrix, hydrogels offer the biocompatibility needed to establish stable, conformal contact with biological tissue, making them well-suited for human-machine interfaces and a range of biomedical applications.*[2]* Conductive hydrogels, in particular, hold great potential for flexible electronics with shape-morphing capabilities, making them suitable for applications like artificial muscles, epidermal sensors, and implantable devices.*[4,5]* These hydrogels exhibit a solid-liquid interface, high processability, and tissue-like properties, positioning them as promising materials for human-machine interfaces.*[6-9]* Hydrogels made from conducting polymers combine the high conductivity of these polymers with the excellent flexibility of hydrogels.*[10]* Conducting polymers (CPs) offer remarkable electrical conductivity, responsiveness to stimuli, and biomolecule functionalization, enabling diverse biomedical applications such as biosensors, drug delivery systems, and tissue engineering scaffolds.*[11,12]* However, their low mechanical stiffness limits their

practicality in standalone applications. To overcome this challenge, combining CPs with hydrogels results in conducting polymer hydrogels (CPHs), which are three-dimensional electrically conductive materials with enhanced mechanical properties. These CPHs are ideal for bioelectronics, biosensors, and cell-responsive medical devices.*[13-15]*

Unlike covalently cross-linked polymeric hydrogels, supramolecular hydrogels are free from cytotoxic reagents such as initiators, catalysts, or oxidants, making them ideal for tissue regeneration and engineering applications.*[16-18]* Among naturally occurring gelators, low molecular weight compounds like short peptides, carbohydrates, and nucleic acid fragments stand out due to their inherent biocompatibility.*[19-21]* Nucleic acid building blocks, are particularly promising as supramolecular gelators as they leverage reversible noncovalent interactions such as hydrogen bonding and π-π stacking, which are fundamental to DNA and RNA assembly.*[22]* By mimicking these natural structural principles, researchers can design biocompatible molecular gels tailored for biomedical applications.*[23,24]*

Conventional conductive polymer hydrogels (CPHs) for biomedical and flexible energy storage use insulating polymer matrices, forming interpenetrating networks (IPNs) that reduce conductivity and electrochemical performance.*[25,26]* Additionally, they often lack adequate mechanical strength for culturing soft tissues, self-healing capabilities, and sufficient biocompatibility. As a result, their potential as functional biomaterials remain constrained. To seamlessly integrate electronics with biological systems, electronic components must closely interface with internal structures of biomaterials.*[10,27,28]* Nucleotides' natural capacity for supramolecular assembly allows them to form cohesive nano-fibrillar networks.*[29,30]* Yet to the best of our knowledge, no studies have reported their inherent enzyme mimetic properties. By harnessing these self-assembled nucleotide superstructures' intrinsic enzyme-like catalytic properties, they can

serve as confined matrices for in-situ conductive polymer growth, creating functional biomaterials that bridge biomolecular self-assembly and bioelectronic interfaces.*[4,10]*

Herein, we developed a guanosine monophosphate (GMP) hydrogel condensate self-assembled via camphorsulfonic acid (CSA) induction, which exhibited intrinsic metal-free peroxidase-like activity. The CSA triggered GMP to form G-duplex motifs, which stacked into G-wire nanoarchitectures, creating a fibrillar superstructure. This enzymatic matrix enabled in-situ polymerization of polyaniline (PANI) nanofibers along the G-wires, yielding a conductive hydrogel through extensive fibrillation. The resulting CSA-GMP hydrogel demonstrated stimuli-responsive reconfiguration, achieving a biomolecular interface "all-solid-state supercapacitor" with high energy storage and electrochromic capabilities (**Scheme 6.1**). To our knowledge, this was the first supramolecular biomolecule-based hydrogel supercapacitor. The system integrated conductivity with biocompatibility and tunable mechanics, including self-healing, shape selectivity, and printability, for applications in soft robotics and biomedical devices.

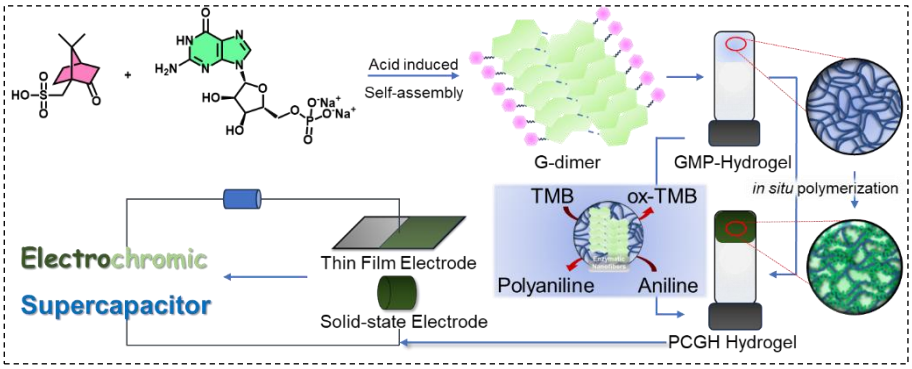


Figure 6.1. *Schematic illustration of the enzymatic GMP molecular hydrogel, which undergoes in situ polymerization of aniline to form a polyaniline-embedded CSA-GMP nanofibrous hydrogel (PCGH) scaffold, used for the fabrication of an electrochromic supercapacitor device.*

6.2. Results and Discussions

6.2.1. Organic Acid induced Self-Assembly of 5′-GMP

Guanosine monophosphate (GMP), a key nucleotide component of DNA secondary structures, can self-assemble via Hoogsteen hydrogen bonding to form various non-covalent superstructures, including G-monomer aggregates, G-dimers, and G-quadruplexes.*[31-33]* GMP-based macrocycles are stabilized by self-complementary hydrogen bonds and rely on ion-dipole interactions, dispersion forces, and interlayer hydrogen bonding to create columnar superstructures.*[34-36]* This self-association is enhanced in mildly acidic aqueous environments, where acidic groups and hydration water molecules promote GMP self-assembly.*[37-40]* Water-soluble organic acids, due to their mild acidity and ability to form hydrogen bonds, can induce GMP condensation. Herein, we report the development of a camphorsulfonic acid (CSA)-induced fibrillar GMP assembly under aqueous physiological conditions (**Figure 6.2 a**). A simple mixing of 1 mM CSA and 1.2 mM GMP resulted in transparent fibrillar assemblies.*[31]* Scanning electron microscopy confirmed the formation of homogeneous fibrils with an average diameter of 34 ± 5 nm (**Figure 6.2 b**).

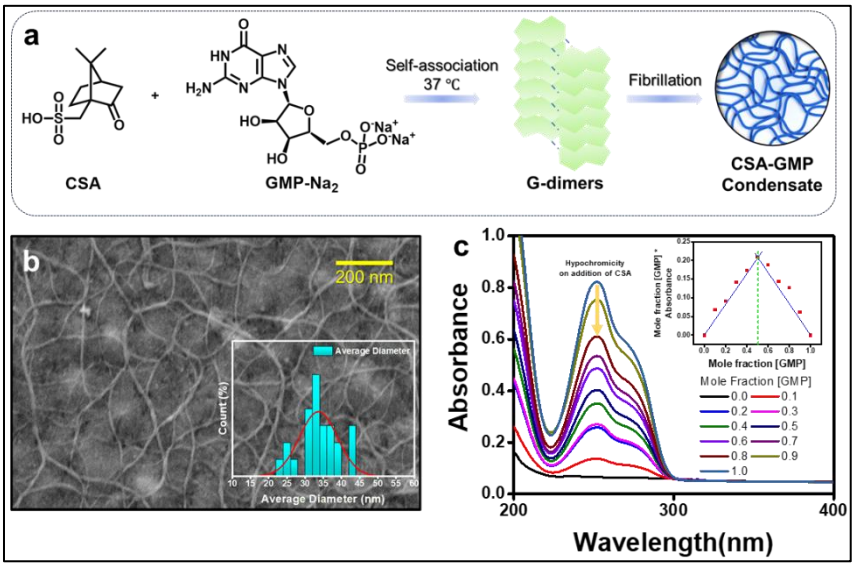


Figure 6.2. (a) *Schematic of CSA and GMP condensation and formation of G-dimers.* ***(b)*** *Scanning electron microscopic image and their respective height distribution graph*

showing the average diameter of the CSA-GMP fibers. ***(c)*** *The UV-visible absorbance spectrum of CSA and GMP at varying molar ratio of same concentration (1 × 10^{-5} M) to observe the hypochromicity of the absorbance peak of GMP at 252 nm due to addition of CSA fraction, inset showing corresponding Job's plot obtained at 252 nm wavelength of maximum absorption which shows the self-assembly molar ratio is 1:1.*

To elucidate the formation mechanism and structure of the acid-induced nucleotide self-assembly, we performed various spectroscopic characterizations. UV-visible spectrophotometry revealed hypochromicity at 252 nm, along with a shoulder at 270 nm, upon addition of CSA to GMP (**Figure 6.2 c**), indicating the formation of an ordered supramolecular assembly at 1:1 stoichiometry (**Figure 6.2 c (inset)**, Job's plot). The formation of stacked G-self-association was quantitatively evaluated using a Thioflavin T (ThT) assay. The fluorogenic dye ThT is stabilized in a rigid, planar structure through end stacking, groove binding, or intercalation due to the non-covalent interactions between ThT and the GMP channel. This stabilization significantly reduces ThT's typical nonradiative torsional relaxation and enhances fluorescence by several folds.*[41,42]* This enhanced fluorescence observed for the CSA-GMP assembly relative to ThT (FL/FL_0) is consistent with the formation of previously reported GMP-stacking DNA structures*[41]* (**Figure 6.3 a**), where ThT intercalation stabilizes the GMP stacked moiety. Furthermore, zeta potential analysis revealed a significant decrease in surface charge as GMP concentration increased (at constant CSA concentration of 100 μM), reaching a minimum at 150 μM GMP (**Figure 6.3 b**). This suggested the interaction of the sulfonated groups of CSA with the phosphate functionalities of the self-assembled GMP fibers, facilitating supramolecular fibrillar network formation. A concentration-dependent pH titration was performed with varying GMP concentrations. The pH of CSA alone was measured at 1.37. Upon the addition of GMP, the pH increased linearly from 2.25 to 3.96 (**Figure 6.3 c**). This indicates that the acidic nature of CSA promotes the self-assembly of GMP, resulting in a mildly acidic pH of approximately 4 at optimal condensation. These findings also suggest proton exchange between the precursors, as the pH of CSA rises

from 1.37 to 4, while the pH of monomeric GMP decreases from 6.2 to 4 during condensation.

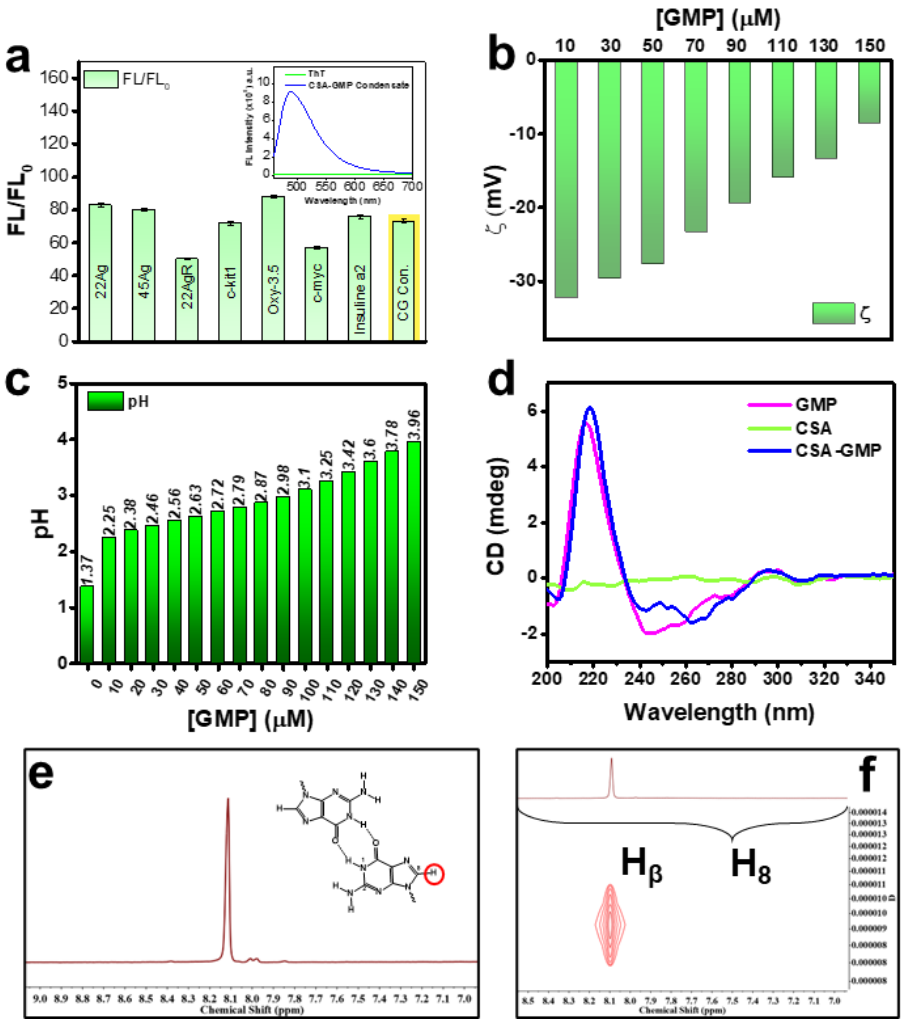


Figure 6.3. ***(a)*** *FL-spectrum of the ThT assay,* ***(b)*** *zeta-potential analysis,* ***(c)*** *Concentration dependent pH titration of the CSA-GMP assembly.* ***(d)*** *CD spectrum of GMP (150 μM), CSA (100 μM) and CSA-GMP assembly showing the characteristics peak region* ***(e)*** *^{1}H-NMR spectrum showing the formation of G-dimers (inset: structural representation of G-dimer).* ***(f)*** *H8 region of a ^{1}H 2D DOSY NMR spectrum of the CSA-GMP assembly in D_2O at 298 K.*

The circular dichroism (CD) spectrum of the CSA-GMP assembly exhibits characteristic peaks indicative of associative GMP self-assembly. While the overall intensity remains similar to that of monomeric GMP, the single negative Cotton band observed at 243 nm in the monomeric form splits into two distinct negative Cotton bands with maxima at 240 nm and 265 nm in the assembly (**Figure 6.3 d**). To

validate this peak splitting, a systematic analysis was performed by varying GMP concentrations while maintaining constant CSA concentration. This approach revealed a pronounced evolution of the two peaks in the same spectral regions. The resonance of CSA-GMP assembly displays three negative Cotton bands at approximately 240 nm, 265 nm, and 310 nm, respectively. This spectral pattern suggests the formation of an associative structure dissimilar to the conventional G-quadruplex. The formation of an exchangeable cation-stabilized, hydrogen-bonded stacked G-dimer can be expected as supported by previous systematic studies.*[43]* To further validate the molecular interactions during self-assembly, individual ^{1}H NMR spectra of GMP, CSA, and the CSA-GMP assembly were acquired and analyzed for structure-to-spectrum correlations. The ^{1}H-NMR analysis of the CSA-GMP assembly (1 mM CSA, 1.5 mM GMP) exhibited a resonance at 8.10 ppm, corresponding to the H8 proton of guanine, showing a downfield shift from the 8.18 ppm signal observed in monomeric GMP, confirming the formation of G-dimeric aggregates (**Figure 6.3 e**). Minor peaks corresponding to G-monomers were detected, with no evidence of G-quadruplex formation. CSA resonances showed minor shifts of 0.5-0.8 ppm, indicating non-covalent interactions, while the lack of significant peak shifts suggests no covalent bonding during condensation. Broadening of the bridging methyl and methyl hydrogel signals near the sulfonyl group was observed, likely due to molecular crowding and self-assembly. For GMP, no significant chemical shift changes were observed in the sugar moiety, but the methyl group near the phosphate showed a 0.1 ppm shift, reflecting changes in the phosphate's electrostatic environment.*[44]* Diffusion-ordered spectroscopy (DOSY) NMR confirmed the presence of aggregates with a translational diffusion coefficient of 2.60064 x 10^{-6} m^2s^{-1}, indicating the formation of 5'-GMP dimers as basic building blocks (**Figure 6.3 f**).*[45]*

Kinetic morphological evaluation, using ThT assay to quantify π-π stacking, revealed a concentration-dependent fibril formation

mechanism (**Figure 6.4**).*[31,46]* At a low GMP concentration (30 μM), small aggregates with an average diameter of 1 μm were formed. These aggregates interconnected to create larger assemblies with an average size of 5-10 μm at GMP concentration of 50 μm. When the GMP concentration was increased to 70 μM, the onset of fibrillation began, producing short rod-like morphologies. At 90 μM GMP, these structures progressively assembled into organized flower-like arrays. At the optimal concentration of 120 μM, a rigid fibrillar network was formed, exhibiting maximum green emission, suggesting extensive π-π stacking.

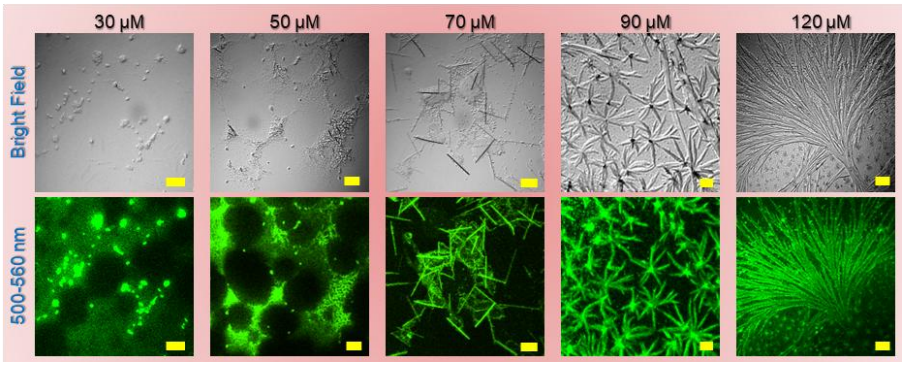


Figure 6.4. *Kinetic morphological evolution of CSA-GMP condensation: Confocal fluorescence images of the progression of green fluorescence along with the fibrillation with the increase in GMP concentration (scale bar: 5 μm).*

The spectroscopic and kinetic morphological data collectively support a model wherein the condensation of GMP molecules is governed by non-covalent interactions, resulting in a CSA-induced, stacked dimeric self-assembly. The pronounced acidity of the assembly (with pH values ranging from approximately 2.2 to 4) facilitates the protonation of the phosphate groups on GMP. This protonation event enables the establishment of hydrogen-bonding interactions between CSA and GMP molecules, as well as Na^+-ion binding (as the precursor is the disodium salt of GMP) within the dimeric stacks.*[47]* These findings are further corroborated by the observed linear reduction in surface charge of monomeric GMPs upon their condensation into stacked dimeric assemblies. In addition to hydrogen bonding, π-π stacking interactions between guanine dimers drive the formation of a fibrillar network, as confirmed by both ThT assays and kinetic

morphological analyses. Unlike conventional biomolecular stacking, the self-assembly of monomeric 5′-GMP is not predominantly dictated by hydrophobic interactions. Instead, the process is enthalpy-driven, with cation binding, hydrogen bonding, and π-π interactions playing pivotal roles.*[48]* Notably, in this acid-induced GMP self-assembly, hydration water significantly influences the thermodynamics of self-association, mediating a delicate balance among hydrophilic solvation, local confinement, and solute-solute interactions between CSA and GMP.*[37]*

At higher concentrations, CSA and GMP molecules self-assemble to form a dense fibrillar network, resulting in a soft, transparent hydrogel that forms instantly upon mixing 100 mM CSA with 150 mM GMP under physiological conditions, without the need of any external stimuli (**Figure 6.5 a**). This hydrogel could be generated across a wide range of CSA (75-175 mM) and GMP (125-200 mM) concentrations, while keeping the other component constant (**Figure 6.5 b**). To investigate the formation mechanism and molecular interactions, powder X-ray Diffraction (pXRD) and Fourier Transform Infrared (FTIR) spectroscopy were performed using the dried hydrogel. pXRD patterns revealed prominent peaks at 2θ = 6.47° (d = 0.73 nm), corresponding to the diameter of GMP self-assemblies, and at 15.80° (d = 1.8 nm) and 16.94° (d = 1.9 nm), indicative of the interplanar spacings between π-π stacked GMP assemblies (**Figure 6.5 c**).*[31,36]* FTIR analysis of the CSA-GMP xerogel with respect to the percussor CSA and GMP reveled the interaction between the functional groups (**Figure 6.5 d**). Marginal shifts of 6-12 cm^{-1} in peaks associated with P=O (1060 cm^{-1}) from the phosphate moiety and C=O (1687 cm^{-1} to 1695 cm^{-1}), C–N (1479 cm^{-1} to 1481 cm^{-1}), and N–H bending (1600 cm^{-1} to 1606 cm^{-1}) in the guanine moiety of GMP, suggesting robust hydrogen bonding during gelation. Notably, the S=O peak (~1395 cm^{-1}) of CSA disappeared in the hydrogel, indicating its involvement in hydrogen bonding. On the other hand, the C=O peak of CSA (1738 cm^{-1}) remained unchanged, suggesting its non-involvement in the self-assembled supramolecular structure. Collectively, these findings demonstrate the

formation of G-dimeric wires that assemble into the CSA-GMP hydrogel. *[32-35]*

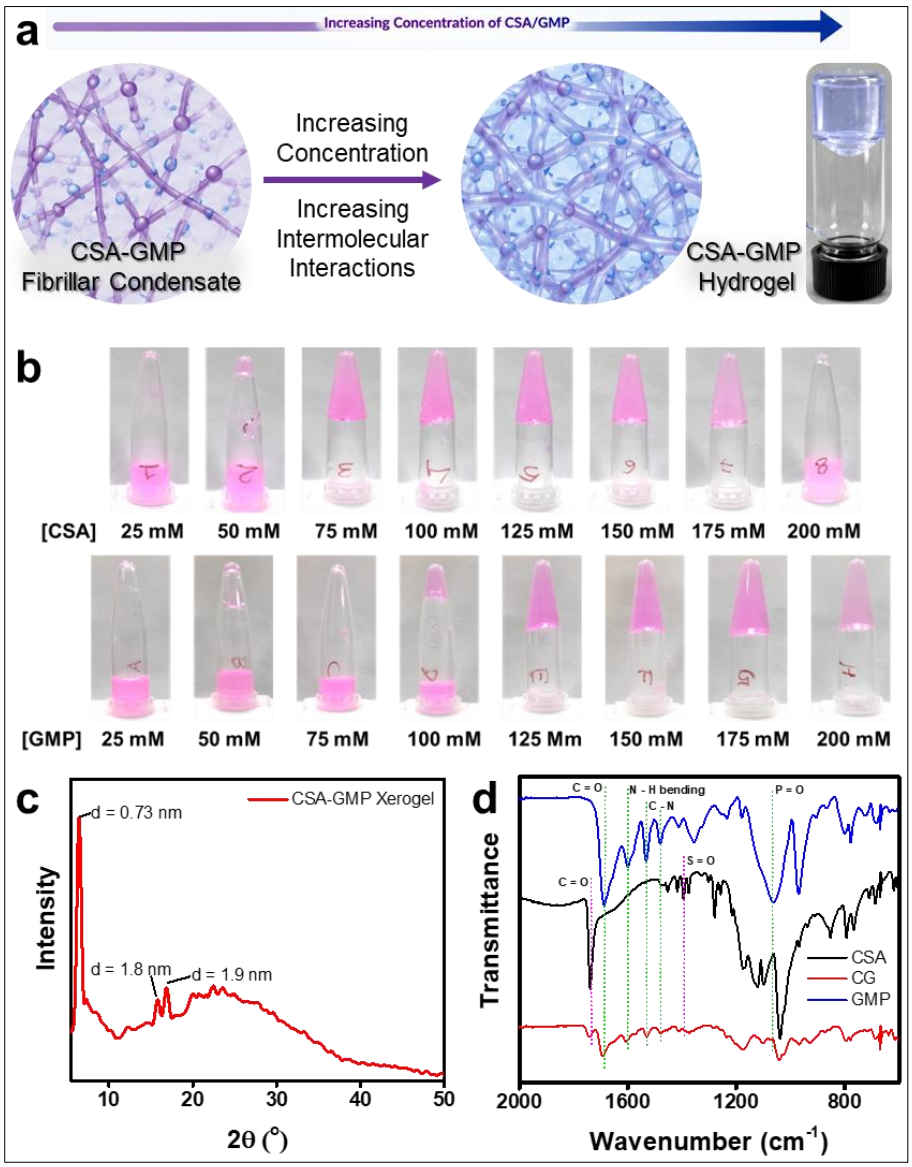


Figure 6.5. (a) *Schematic illustration depicting the concentration-driven transformation of CSA-GMP fibrillar assemblies into a transparent hydrogel matrix.* ***(b)*** *Phase diagram showing the formation of RhB-loaded hydrogels at varying concentrations of the components: CSA concentration varied from 25-200 mM at a fixed GMP concentration of 125 mM, and GMP concentration varied from 25-200 mM at a fixed CSA concentration of 100 mM.* ***(c)*** *Powder X-ray diffraction (pXRD) pattern of the dried CSA-GMP hydrogel (xerogel).* ***(d)*** *Fourier-transform infrared (FTIR) spectra of CSA, GMP, and the CSA-GMP (CG) hydrogel, highlighting intermolecular hydrogen-bonding interactions involving phosphate, carbonyl (C=O), amine (N–H), and hydroxyl (O–H) functional groups.*

6.2.2. Metal-free intrinsic peroxidase activity of the CSA-GMP assemblies

The arrangement of biocatalysts within confined cellular environments facilitates the directed transport of reaction intermediates throughout the cells. Various self-assembled microstructures, including liposomes, microcapsules, polymersomes, aqueous droplets, and fibrillar condensate hydrogels, have been investigated as organized microenvironments that replicate cellular structures.*[49-52]* Previous studies have demonstrated that G-quadruplex-based self-assembled nucleic acid fragments exhibit intrinsic peroxidase activity through the incorporation of a hemin cofactor.*[53,54]* However, a metal-free approach leveraging supramolecular networks without relying on cofactors or metal-active centers remains unexplored. By emulating these confined cellular environments, the synthesized CSA-GMP condensates were utilized as microreactors, leading to a metal-free biomolecular self-assembly that exhibits intrinsic peroxidase activity.*[55]*

To investigate the peroxidase-like activity of the CSA-GMP condensate, we selected a model oxidation reaction utilizing 3,3′,5,5′-Tetramethylbenzidine (TMB) in the presence of H_2O_2 (**Figure 6.6 a**). The enzyme-mimicking properties of the condensate were assessed using UV-visible spectrophotometry, where we monitored the maximum absorbance of oxidized TMB at 652 nm. Upon adding 1 mM TMB and 10 mM H_2O_2 to a 10 mM aqueous solution of CSA-GMP fibrillar condensate, a distinct absorption peak appeared at 652 nm, indicating the formation of oxidized TMB. Additionally, the initially colorless solution of CSA-GMP condensate transformed into a deep blue hue within 60 minutes, accompanied by a linear increase in absorbance at 652 nm (**Figure 6.6 b**). In contrast, in absence of the CSA-GMP condensate, neither TMB alone nor TMB with only H_2O_2 produced a peak at 652 nm (**Figure 6.6 c**), confirming the intrinsic peroxidase activity of the condensate.

Figure 6.6 d illustrates the enzyme activity rate (V_0) as a function of time when using CSA and GMP as catalysts instead of the CSA-GMP condensate. Very low V_0 values were observed in both cases, highlighting the significance of the micro-confined environment provided by the CSA-GMP fibrillar network. To optimize the enzyme-like activity of the CSA-GMP condensate, we examined various reaction parameters, including pH and temperature. Figure **6.6 e** shows that peroxidase-like activity varied with pH in the range of 2-12, peaking around pH 4. Activity sharply decreased at higher pH (>8), likely due to instability in the non-covalently structured CSA-GMP supramolecular confinement. Further investigations into temperature effects on both activity and morphological stability revealed that at lower temperature (<308 K) the enzymatic activity was enhanced, which gradually declined with increasing temperature (**Figure 6.6 f**). Maximum activity was observed at physiological temperature (298 K). This decrease in enzymatic activity with increasing temperature is likely due to the disruption of CSA-GMP condensation, consistent with typical behavior observed in biological supramolecular systems.

The kinetic parameters associated with the peroxidase-like activity of CSA-GMP condensates were evaluated through kinetic experiments with varied concentrations of TMB (0.01-2.5 mM) and H_2O_2 (0.1-10 mM). Changes in absorbance at 652 nm were monitored as a function of time, revealing a typical Michaelis-Menten behavior for both TMB and H_2O_2 (**Figure 6.6 g, h**). The Michaelis constant (K_M) and maximum reaction velocity (V_{max}) were determined using Lineweaver-Burk plots (**Figure 6.6 i, j**). A low K_M value indicates a high affinity between the enzyme and its substrate, suggesting that the enzyme can achieve half of V_{max} at a low substrate concentration. The estimated K_M values for TMB and H_2O_2 were found to be 0.5445 mM and 0.6017 mM, respectively. This high substrate affinity towards a metal-free biomolecular self-assembly is significant and compares favorably to that of metal-based nanozymes and natural enzymes. Additionally, the estimated V_{max} values for TMB and H_2O_2 within the CSA-GMP

microenvironment were 3.87 x 10^{-3} mMs^{-1} and 2.48 x 10^{-2} mMs^{-1}, respectively. The strong affinity of TMB and H_2O_2 for the CSA-GMP confinement suggests effective spatial confinement within the aqueous fibrillar microenvironment, highlighting the high activity of the metal-free enzyme-like nanofibers formed by CSA-induced GMP dimeric superstructures.

Peroxidase-mimic catalysis typically proceeds via two primary catalytic pathways: the generation of hydroxyl radicals (·OH)*[56,57]* and electron transfer processes*[58]*. In our study, the potential formation of ·OH radicals were initially assessed using a fluorescence-based experiment. This involved employing terephthalic acid, a weakly fluorescent molecule, as a probe that reacts with ·OH radicals to produce the strongly fluorescent 2-hydroxyterephthalic acid.*[56]* A significant increase in the fluorescent intensity was observed in the presence of H_2O_2 and CSA-GMP condensates (**Figure 6.7 a**), indicating the generation of ·OH radicals within the catalytic system. Further evidence was obtained using Electron Spin Resonance (ESR) spectroscopy, a powerful technique for identifying and quantifying short-lived radicals. The collected spectra (**Figure 6.7 b**), with 5,5-dimethyl-1-pyrroline N-oxide (DMPO) as a radical trap, showed a four-line signal, indicative of the DMPO-·OH adduct.*[57]* This signal was observed in the presence of CSA-GMP condensates (CG) but not in their absence. This direct evidence suggests that the generation of ·OH radicals play a crucial role in the catalytic pathway of CSA-GMP condensates. The ionic channels within G-dimers can stabilize the generated ·OH radicals, which effectively facilitate substrate oxidation within the aqueous micro-confined environment.

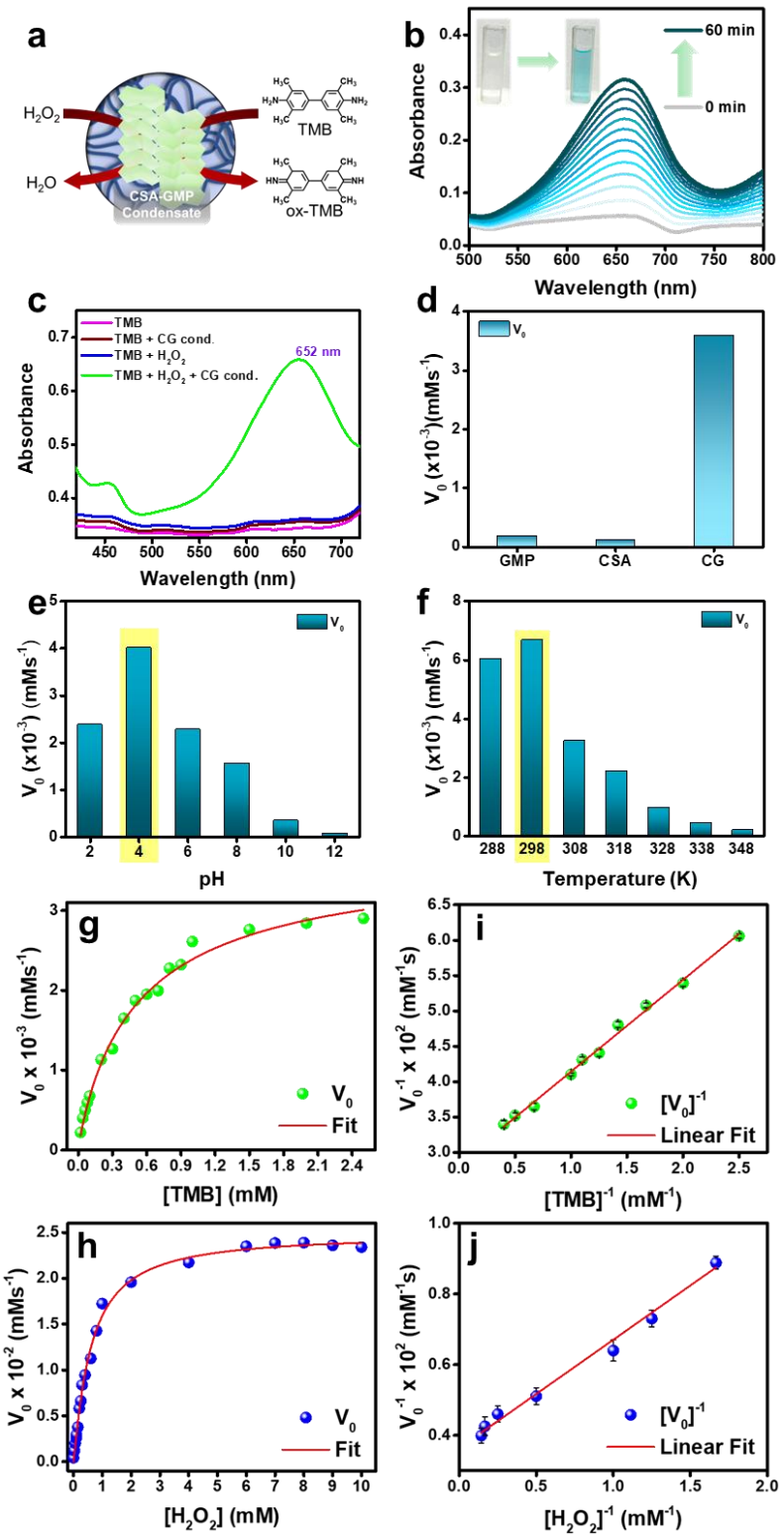


Figure 6.6. ***(a)*** *Schematic illustration showing the peroxidase enzyme-like nano-fibrous CSA-GMP condensate,* ***(b)*** *UV-visible spectrum of the TMB oxidation with respect to time (inset photographs showing the colour change).* ***(c)*** *UV-visible spectra of the controlled experiments of the peroxidase activity of TMB, TMB + CG cond., TMB+H_2O_2 and TMB+H_2O_2+CG cond.* ***(d)*** *The relative peroxidase activity of the CG*

condensate with respect to precursors camphor sulfonic acid (CSA) and guanosine monophosphate (GMP). Optimization of the peroxidase-mimicking activity under different conditions; ***(e)*** *pH and* ***(f)*** *temperature.* ***(g)*** *and* ***(h)*** *Michaelis-Menten plots of CSA-GMP catalyzed TMB oxidations by keeping H_2O_2 and TMB constant, respectively, and* ***(i)*** *and* ***(j)*** *corresponding Lineweaver-Burk plots for TMB and H_2O_2, respectively.*

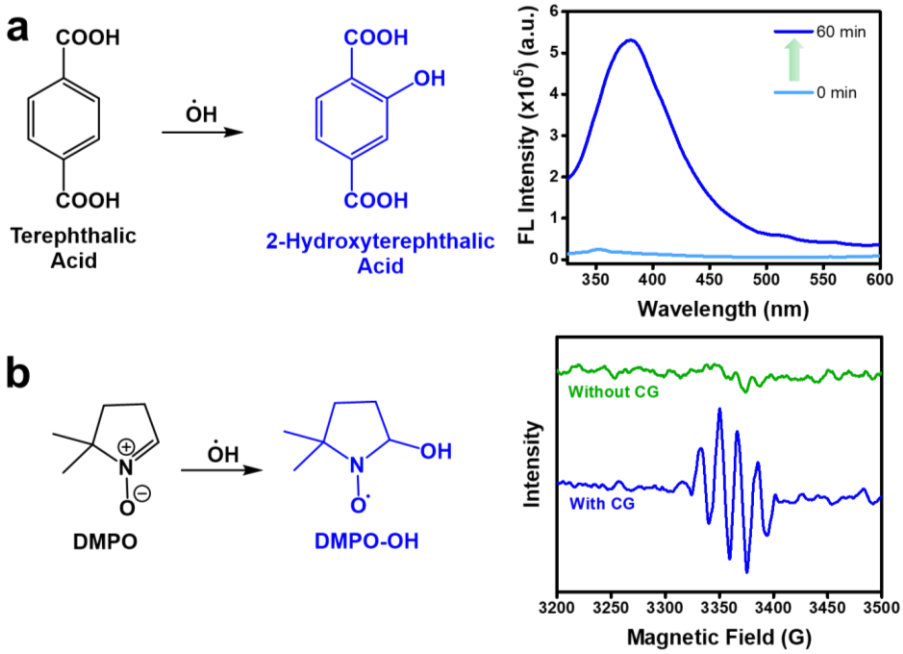


Figure 6.7. *Reaction mechanism determination of the peroxidase activity of CSA-GMP condensate;* ***(a)*** *with terephthalic acid for the detection of ·OH radical and corresponding enhancement in the FL intensity confirming the formation of 2-hydroxyterephthalic acid,* ***(b)*** *with 5,5-dimethyl-1-pyrroline N-oxide (DMPO) as a radical trap, showed a four-line EPR signal indicative of the DMPO-·OH adduct.*

6.2.3. In-situ polymerization of aniline inside the enzymatic CSA-GMP hydrogel

Classical chemical synthesis of polyaniline typically involves aniline, an oxidant, and a strong mineral acid dopant. Kaner et al. developed a method for synthesizing polyaniline nano-fibers (approximately 50 nm in diameter) using camphor-sulfonic acid as the dopant in interfacial polymerization.*[59]* Leveraging the presence of camphor-sulfonic acid (CSA) in CSA-GMP hydrogel, which has an inherent mildly acidic pH (~3.4), the enzyme-mimicking CSA-GMP hydrogel was employed for fabricating nanofibrous conductive materials. As illustrated schematically in **Figure 6.8 a**, the CSA-GMP

hydrogel acts as a catalytic matrix that facilitates the oxidation of aniline by H_2O_2 to form polyaniline. To initiate polymerization, the CSA-GMP hydrogel was gently heated to 50 ℃ until they became transparent solutions. Upon adding equimolar concentrations of aniline and H_2O_2 as an oxidant, interfacial polymerization of aniline started immediately, which upon cooling and aging led to the formation of polyaniline-embedded CSA-GMP nanofibrous hydrogel (PCGH) scaffold. The polymerization of aniline occurred unidirectionally within the matrix, yielding uniform opaque emerald-green colored hydrogel (**Figure 6.8 b**).*[10]* The color change from transparent CSA-GMP hydrogel to emerald green PCGH hydrogel was the initial visual indication of successful polymerization under ambient conditions facilitated by the matrix-assisted processes.*[26]* The resulting PCGH hydrogels were labeled PCGH1, PCGH2, and PCGH3 based on initial aniline concentrations of 0.05 M, 0.10 M, and 0.20 M respectively. Due to the simplicity and ease of processing during the in-situ polymerization within biomolecular condensate, the PCGH hydrogel could be molded in a variety of shapes, including blocks, stars, hearts, and tubes (**Figure 6.8 c**). Additionally, these hydrogels exhibit self-sustaining properties and demonstrate an exceptional weight-bearing capacity of up to 100 g while maintaining a high shear stress of 9.8 kPa as shown in the **Figure 6.8 d**.

Microscopic imaging during templated growth of polyaniline nano-fibers revealed unidirectional polymeric growth aligned with the CSA-GMP fibrillar network. High-resolution Transmission Electron Microscopic (HRTEM) image showed the homogeneous fibrillar network with the nano-fibrillar polyaniline clusterization in between the fibrillar CSA-GMP condensate (**Figure 6.8 e**). Field Emission Scanning Electron Microscopy (FESEM) images demonstrated a homogeneous entangled fibril network within PCGH hydrogel, with an average diameter of 30 ± 5 nm (**Figure 6.8 f**). This size matched with the previously calculated dimensions of CSA-GMP fibers, suggesting the growth of PANI nano-fibers along the CSA-GMP matrix resulting the

formation of dense phase PCGH hydrogels.*[60]* Atomic Force Microscopy (AFM) images further validated the uniformity of the fibrillar network, showing fiber bundling with an average height of 6 ± 2 nm (**Figure 6.8 g**). The observed bundling suggested non-covalent interactions between supramolecular self-assembled GMP templates and polyaniline nano-fibers.

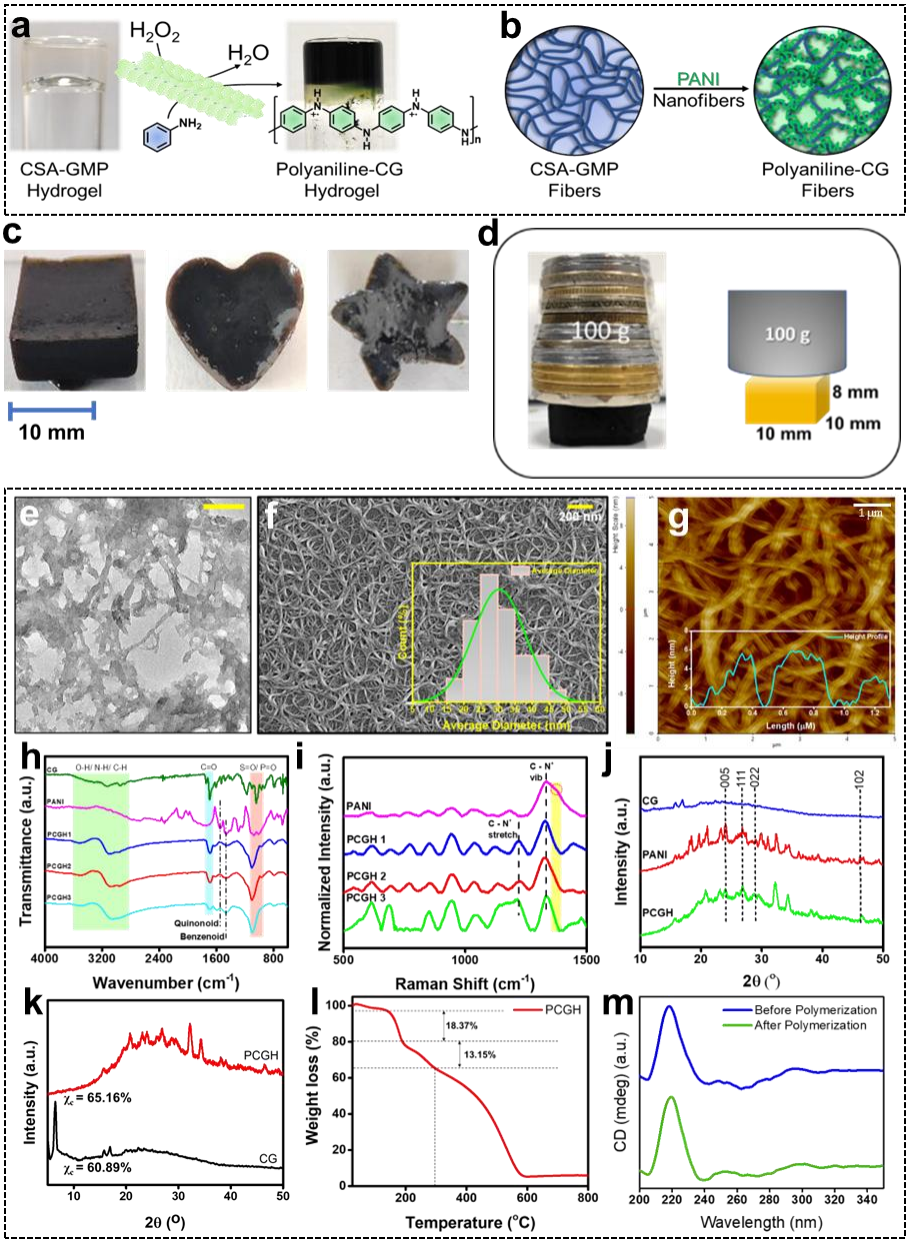


Figure 6.8. (a) *Schematic illustrating the fabrication of PCGH hydrogel by applying CSA-GMP hydrogel as a catalytic matrix for the deposition of PANI nanofibers, (**b**) illustration showing the unidirectional formation of PANI nano-fibers within the template matrix. **(c)** Shape-morphing ability of the PCGH hydrogel. **(d)** Self-sustaining behavior of PCGH and showing the dimension of the gel upon loading stress. **(e)***

HRTEM image showing the entangled fibrillar network (scale bar: 200 nm). ***(f)*** *SEM image with the size distribution inset.* ***(g)*** *AFM image showing the height distribution of the diluted PCGH hydrogel.* ***(h)*** *Fourier transform infrared spectra (FTIR),* ***(i)*** *Raman spectra and* ***(j)*** *X-ray diffraction (XRD) patterns of the CSA-GMP hydrogel (CG), PANI and PCGH hydrogel (all used as lyophilized powder form).* ***(k)*** *Curve showing crystallinity of CG and PCGH3.* ***(l)*** *TGA curve of the PCGH3 xerogel.* ***(m)*** *CD spectrum of the CSA-GMP condensate/hydrogel before and after aniline polymerization showing the structural and chiral integrity of the CSA-GMP condensate.*

The confirmation of the formation of polyaniline nanofibers around the CSA-GMP fibrillar condensate was obtained through a comparative study. *[60]* In this study, aniline polymerization was conducted conventionally using the same concentrations of CSA and H_2O_2, which resulted in dark green-colored precipitates where no nanofiber formation was observed (**Figure 6.9**). This suggests that the CSA-GMP fibrillar matrix not only provides a catalytic scaffold but may also guide aniline polymerization into unidirectional fibrillar growth.

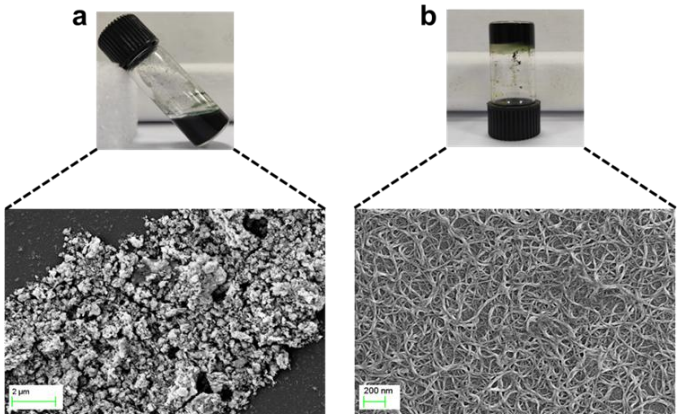


Figure 6.9. a. *FESEM image showing PANI suspension prepared by conventional acidic polymerization of aniline,* ***b.*** *FESEM image showing PANI hydrogel inside the CSA-GMP fiber matrix.*

Further investigation into the conformation of PANI nanofibers and their interfacial interaction with CSA-GMP scaffolds was conducted. The presence of PANI inside the PCGH hydrogel was confirmed by FTIR characteristic peaks of quinoid and benzenoid forms at 1588 cm^{-1} and 1467 cm^{-1}, respectively (**Figure 6.8 h**). Additionally, the C = O peak from the carboxylate group of CSA, along with broad

S=O and P=O stretching peaks, remained intact in all PCGH hydrogels. This indicates that the formation of PANI nano-fibers does not affect the CSA-GMP matrix scaffold.[26,60,61] The resonance Raman spectrum of PCGH showed characteristic peaks of PANI networks, confirming the presence of PANI. The band at 1345-1354 cm^{-1} corresponds to the carrier vibration mode of $C - N^+$ in the polaronic structure, suggesting the formation of the emeraldine salt form of polyaniline inside the PCGH matrix (**Figure 6.8 i**). Bands at around 1250 cm^{-1} and 1170 cm^{-1} are assigned to C – N stretching and C – H vibrations of aromatic rings, respectively, further indicating polyaniline formation. Notably, the band at around 1375 cm^{-1}, which is associated with less conductive forms of PANI in conventionally synthesized precipitates, was absent in PCGH, suggesting that only the conductive form of the emeraldine salt is formed within the fibril matrix.*[62]* X-ray diffraction (XRD) patterns of lyophilized PCGH hydrogel and conventionally synthesized PANI precipitate showed that PCGH samples exhibit a series of peaks from $2\theta \approx 20\text{-}30°$, characteristic of PANI (**Figure 6.8 j**). The crystallinity of PCGH samples contributes to their conductive properties. Although aniline polymerization within the CG matrix occurs rapidly and randomly, the incorporation of PANI into the CG matrix enhanced crystallinity from 60.89% in CG to 65.16% in PCGH. This increase indicates that the unidirectional in situ polymerization process effectively improves molecular regularity in PCGH (**Figure 6.8 k**). The aligned growth of PANI nanofibers with CG chains into the crystalline region enhances crystallinity, which significantly benefits the mechanical properties.[26] Thermogravimetric analysis (TGA) of the dried PCGH hydrogel revealed a solid-state macrostructure (**Figure 6.8 l**). The TGA curve showed an 18.37% weight loss at approximately 200°C, likely due to the unfolding of hydrogen-bonded networks. At around 300°C, all non-covalent bonds collapse, resulting in a steep weight loss of 13.15%. Beyond 300°C, the sharp decrease in weight indicates the condensation of organic moieties within the matrix. The CD spectrum of the PCGH3 hydrogel (diluted 1,000-fold) was analyzed to assess the

influence of polyaniline formation on the chiral supramolecular CSA-GMP condensate both prior to and after polymerization. The results demonstrated that the chiral resonance bands of the CSA-GMP condensate remained unchanged before and after aniline polymerization within the fibrillar matrix, indicating that the structural integrity of the CSA-GMP fibrillar condensate was preserved (**Figure 6.8 m**).

The CSA-GMP hydrogel matrix was synthesized via a straightforward mixing process involving bio-derived molecules, resulting in a hydrogel with anticipated high biocompatibility, consistent with previously reported GMP-based hydrogels. Polyaniline (PANI), recognized as one of the most extensively studied conductive polymers, offers significant potential for bioelectronic applications due to its hydrophilic character, low toxicity, environmental stability, and nanostructured morphology. Consequently, the synthesized PCGH hydrogel is expected to demonstrate excellent biocompatibility, rendering it highly suitable for a broad spectrum of bioelectronic applications. Notably, limitations such as poor processability and degradability commonly associated with PANI can be effectively addressed by its integration with various biopolymers. A comprehensive biodegradability assessment confirmed the facile degradability of the PCGH hydrogel. Owing to its formation through acid-induced non-covalent interactions, immersion of the PCGH hydrogel in a 0.1 M NaOH solution resulted in complete dissolution into a homogeneous solution within four hours, indicating superior biodegradability (**Figure 6.10**). In addition to biocompatibility and biodegradability, the synthesis process is facile, spontaneous, and straightforward, requiring no external energy input. This enables high scalability for industrial applications. Furthermore, the procedure does not require specialized environmental or energy conditions, and utilizes low-cost, industrial-grade precursors. Thus, the use of PCGH hydrogels in bioelectronic applications is both cost-effective and industrially viable.

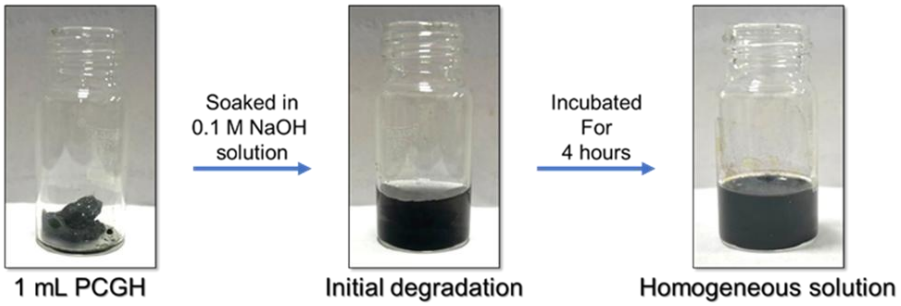


Figure 6.10. *Digital photographs showing the bio-degradation of the PCGH using 0.1 M NaOH solution.*

6.2.4. Mechanical properties of the PCGH hydrogel

To quantify the mechanical properties of the prepared hydrogels, rheological analyses were conducted on both the template CSA-GMP hydrogel and the PCGH hydrogels. The dynamic strain-sweep experiments, as shown in **Figure 6.11 a**, revealed a linear relationship between the storage modulus (G′) and loss modulus (G″) at low shear strain levels (≤ 20%) for all hydrogels, including CSA-GMP. However, as the strain increased, G′ decreased, indicating a gel-to-sol transition. Notably, the PCGH3 hydrogel demonstrated highest tolerance to higher strain among all samples. Dynamic frequency sweeps were performed on both CSA-GMP and PCGH hydrogels with a fixed strain of 1%. The results, presented in **Figure 6.11 b**, showed a wide linear viscoelastic region for both hydrogels, with the G′ consistently higher than the G″. This confirmed the viscoelastic nature of the hydrogels. Furthermore, the storage modulus for the PCGH hydrogels was approximately ~10^4 Pa, indicating that the mechanical strength of the PCGH hydrogels increased by about 1000 times compared to the template CSA-GMP hydrogel after aniline polymerization (**Figure 6.11 c**). This enhancement aligns with previous spectroscopic and microscopic analyses, which demonstrated the uniform polymerization of polyaniline nanofibers around CSA-GMP scaffolds. This polymerization not only induced electrochemical conductivity but also facilitated the self-association of dense phase fibrillar networks, resulting in more rigid and viscoelastic hydrogels.

To investigate the thixotropic loop behavior of the PCGH3 hydrogel, which exhibited a high viscoelastic nature and strain tolerance, step strain measurements were conducted. At a strain of 1%, the hydrogel displayed elastic properties with higher G′ values than G″ values. However, upon increasing the strain to 100%, the elastic behavior diminished, and G″ dominated over G′, indicating a gel-to-sol transition. Notably, the loop test revealed that the gel could be restored within a short period after releasing the high strain, and the reversible sol-gel transition could be achieved over multiple cycles. The recovery time was approximately 100 seconds per cycle (**Figure 6.11 d**). This rapid switching between sol and gel states by varying the strain enables the PCGH hydrogel to be injected through a needle or pen and quickly recover its mechanical strength at low strain, facilitating rapid shaping and direct 3D printing. For instance, the PCGH hydrogel can be used as an "ink" for printing or writing into any shape and structure (**Figure 6.11 f**). In addition to the thixotropic loop test, the physical self-healing ability of the PCGH hydrogel was evaluated. The hydrogel was subjected to a high strain of up to 1000%, which induced a gel-to-sol transition. When the strain was released to 1%, there was rapid reversal to a hydrogel state, demonstrating rapid self-recovery of its original strength within seconds (**Figure 6.11 e**). The self-healing ability of the hydrogel was further confirmed by cutting a cylindrical PCGH hydrogel into two pieces and rejoining them. Within 15 minutes, the pieces joined together suggesting excellent self-healing ability. After 4 hours of incubation, the hydrogel regained its original stiffness and mechanical integrity (**Figure 6.11 g**). These results highlight the rapid recovery and fluidity of PCGH, attributed to the non-covalent supramolecular interactions such as hydrogen bonding and π-π stacking. This demonstrates the high mechanical integrity of the biomolecular self-assembled PCGH hydrogel along with its exceptional self-recovery and self-healing capabilities, which are rare among self-assembled supramolecular networks with such high storage moduli.*[63,64]*

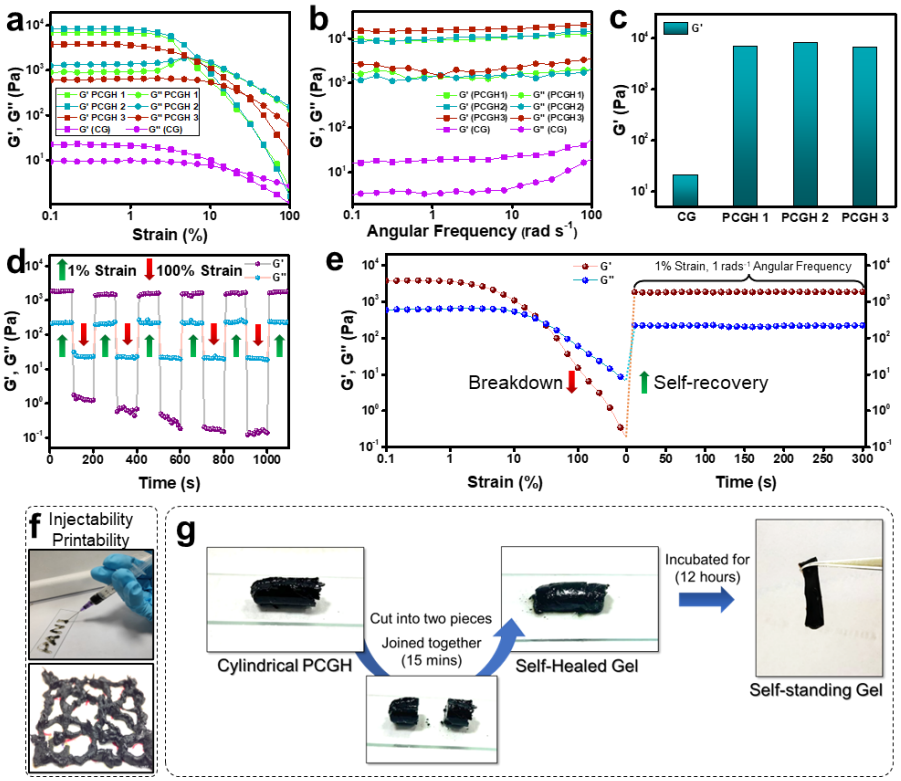


Figure 6.11. *Mechanical performance of the CSA-GMP (CG) and PCGH hydrogels. Rheological studies.* ***(a)*** *amplitude-sweep experiments at fixed frequency of 1 rads^{-1},* ***(b)*** *frequency sweeps at fixed strain of 1%,* ***(c)*** *comparative storage moduli (G') of PCGH with respect to CG hydrogel,* ***(d)*** *Thixotropic loop measurement for PCGH at a constant angular frequency of 10 rad s^{-1} with changing the strain from 1% to 100%,* ***(e)*** *Self-recovery of PCGH. strain sweep measurement (left) followed by immediate recovery from 1000% strain to 1% strain (right) of the PCGH at 298 K,* ***(f)*** *photographs showing injectability and printability and* ***(g)*** *digital photographs of the PCGH showing the physical self-healing ability.*

Hydrogels formed via non-covalent interactions exhibit temperature-dependent mechanical properties. Rheological analysis at 1% strain and 10 rad·s^{-1} revealed gel-sol transitions for CSA-GMP and PCGH hydrogels at precise transition temperatures of 52.7 °C and 66.5 °C, respectively (**Figure 6.12 a, b**). The higher transition temperature of PCGH likely results from enhanced network strength following aniline polymerization. Upon heating above the transition temperature, both hydrogels convert to sol, but revert to gel upon cooling to room temperature. This reversible process is repeatable over multiple thermal cycles (**Figure 6.12 c, d**), indicating dynamic non-covalent cross-linking within the supramolecular network. Both CSA-GMP and

PCGH hydrogels were successfully utilized to produce robust, homogeneous films and membranes that exhibit static mechanical properties comparable to their hydrogel counterparts, thereby broadening their application scope (**Figure 6.12 e-h**).

The strengthening and toughening mechanism of PCGH was further studied (**Figure 6.13 a**). The sacrificial nanofibril networks of PANI were entangled inside the H-bonded supramolecular network of self-assemble G-dimer. Thus, the PANI nanofibers were distributed homogeneously over the CSA-GMP fibril matrix (**Figure 6.13 b**). When an external strain (100%) is applied to PCGH, the homogeneously distributed PANI nanofibers were fractured from the matrix to form aggregates (**Figure 6.13 c**). Interestingly, upon increasing the external strain to 200%, the homogeneous fibril network was almost intact but the fibers were bundled together (**Figure 6.13 d**). Though the diameter of the fibers increased, no such disruption of the PANI networks over the CSA-GMP matrix was observed. To observe the effect of high external load, almost 500% strain was also applied to PCGH and from the SEM images, it was observed that the fibers got bundled up and bigger aggregates were formed inside the network (**Figure 6.13 e**). But the fibrillation did not break even after applying such high external load. These show the self-recovery of the non-covalently interacted fibril networks. Also, these results suggested the compressibility of the fibril network. Benefiting from all these mechanical performances, it can be inferred that a highly robust network interconnecting self-assembled GMP and PANI scaffolds was formed inside PCGH.

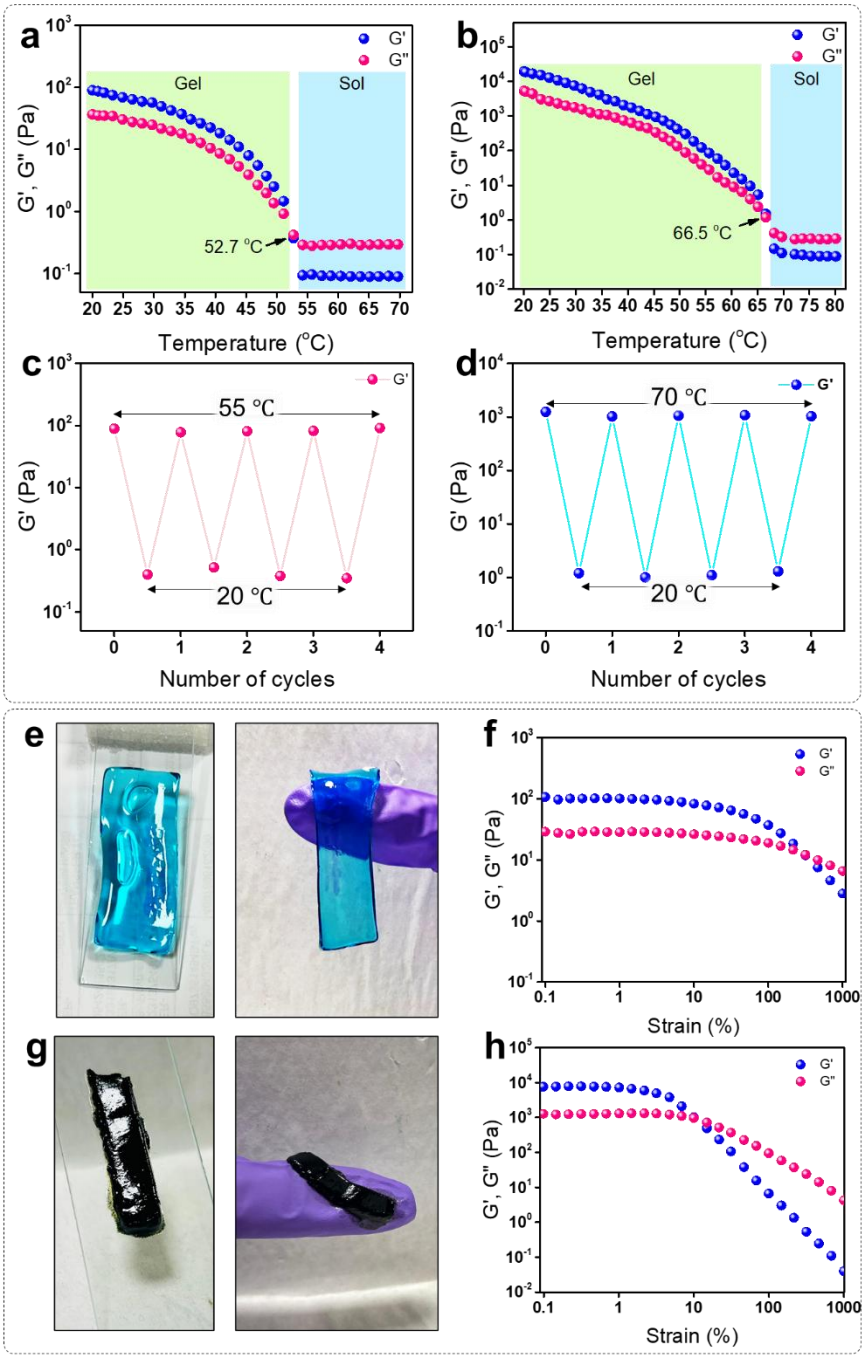


Figure 6.11. *Temperature dependent rheological analysis of* ***(a)*** *CSA-GMP hydrogel,* ***(b)*** *PCGH3 hydrogel, at constant strain of 1% and constant angular frequency of 10 rads^{-1} and Thermo-reversible storage modulus cycles for* ***(c)*** *CSA-GMP and* ***(d)*** *PCGH3 hydrogel. Digital photographs showing the films and membrane formation using* ***(e)*** *CSA-GMP hydrogel (dye stained) and* ***(g)*** *PCGH hydrogel and amplitude sweep rheological experiments of the* ***(f)*** *CSA-GMP and* ***(h)*** *PCGH films of width 1mm showing their structural integrity.*

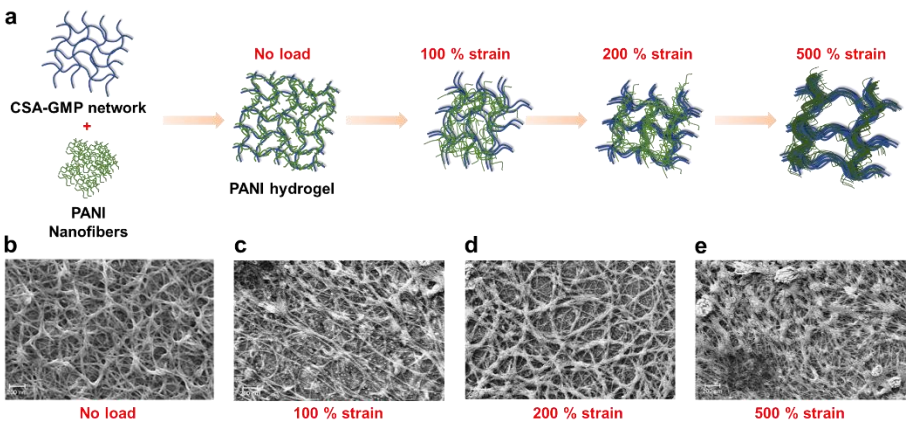


Figure 6.12. (a) *Schematic illustration of the compressibility test of PCGH at different external strain ranges and ex-situ FESEM images of* ***(b)*** *PCGH with no load,* ***(c)*** *100% strain,* ***(d)*** *200% strain and* ***(e)*** *500% strain. (Scale bars ~ 200 nm)*

6.2.5. Electrochemical performance of the biomolecular matrix embedded PCGH hydrogel

6.2.5.1. As an Electrochromic Supercapacitor Electrode

Most conductive polymer hydrogels are fabricated within prefabricated polymeric structures, which can compromise biocompatibility and biodegradability. Forming conductive polymers within biomolecule-based self-assembled hydrogels enhances biocompatibility, making them suitable for applications like biosensing, wearable devices, and soft robotics.*[13,14,65]* Herein, the prepared PCGH condensate hydrogels were employed for their evaluation as electrochromic as well as energy storage applications via electrode fabrication and an "all solid-state" hydrogel supercapacitor. The electrochemical properties for the PCGH were evaluated by cyclic voltammetry (CV) and galvanostatic charge/discharge (GCD) tests. To evaluate the electrochromic and capacitance performance, a simple bilayer device was fabricated as shown in **Figure 6.14 a**. The indium tin oxide (ITO) coated glass plates were used as the conductive surface, where the PCGH condensate hydrogel was evenly coated using their excellent temperature dependent gel-sol-gel properties.*[66,67]*

The surrounded areas of the CV curves of the PCGH electrodes at 10 mV s^{-1} demonstrated their capacitances following the order of PCGH3 < PCGH2 < PCGH1 (**Figure 6.14 b**), which was consistent with

the results based on the GCD tests (**Figure 6.14 c**). The Nyquist plots of the PCGH electrodes showed three frequency regions of high-, mid- and low frequency, that corresponds to the electro-transfer process, diffusion process and capitative behavior respectively. All the plots from the three electrodes of PCGH1, PCGH2 and PCGH3 were nearly vertical to the x-axis which suggested an ideal capacitive behavior (**Figure 6.14 d**). At the high-frequency region, the charge transfer of the electrolyte interface was expressed as a semicircle (**Figure 6.14 d,** inset), indicating pseudocapacitive behaviour of PCGH. This is a consequence of the overlapping of mid-frequency and high-frequency redox reactions owing to the presence of dense PANI scaffolds.*[26,60]* The phase angle started near 90° at low frequencies, indicating dominant capacitive behavior in the Bode plots (**Figure 6.14 e**) of the PCGH electrodes. As frequency increased, the phase angle decreased gradually and approached 0°, reflecting a transition to resistive behavior at high frequencies. This behavior suggested a combination of faradaic and non-faradaic processes in pseudo-capacitors, which contribute to both pseudo-capacitance and double-layer capacitance. The CV curves of the PCGH3 electrode at different scan rates from 10-100 mVs^{-1} exhibited redox peaks, thus indicating dominated pseudocapacitive characteristics (**Figure 6.14 f**). The GCD curves of the PCGH3 electrodes were collected at different current densities, which gave the areal capacitance of the PCGH electrodes (**Figure 6.14 g**). Notably, the PCGH electrodes showed a comparatively high areal capacitance of 136 $mFcm^{-2}$ at a current density of 1.25 $mAcm^{-2}$ (0.5 Ag^{-1}) (**Figure 6.14 h**).

The supercapacitance performance of the PCGH hydrogel device coated on ITO electrode was also accompanied by distinct electrochromic behavior. The redox reaction of the PANI nano-fibers inside PCGH was monitored using a three-electrode electrochemical system (**Figure 6.14 i**).*[68]* At a potential of +1 V (versus Ag/AgCl), the PCGH working electrode was at anion doping state (emeraldine salt) with dark emerald green color, where the oxidation state was dominating. On the other hand, when the applied external voltage was 0

V or -1 V (versus Ag/AgCl), a leucoemeraldine state with yellow-green color was observed indicating anion de-doping process. To further understand the color switchability and reversibility of the device in situ, bias (voltage) dependent absorbance spectra of the device were recorded (**Figure 6.14 i**) at 0 V, 1 V, and -1 V. The positive biased (1 V) device showed an absorption maximum at 660 nm and thus transmitting a dark blue color (a combination of green and blue). The overall absorbance of the device decreased under an unbiased (0 V) or at -1 V, showing light green color of the device, as can be understood from less absorbed red and black lines. This confirmed the reversibility of the bias-induced color switching. Reversible switching from a simple PCGH hydrogel-based two-layered device at a small voltage of 1 V is extremely significant to be developed as a color sensor for various smart device fabrications.

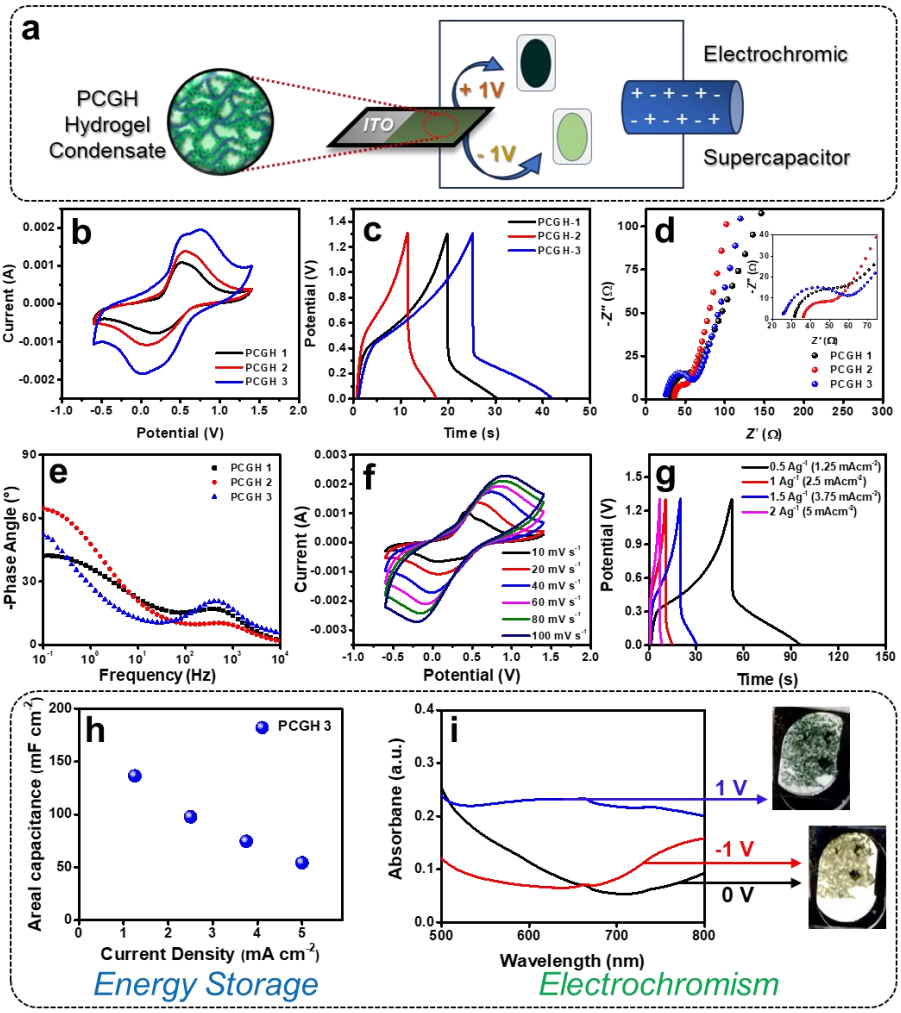


Figure 6.14. *PCGH as electrochromic supercapacitor electrode.* ***(a)*** *Schematic showing the formation and function of the PCGH electrode,* ***(b)*** *Cyclic voltammetry (CV) curves,* ***(c)*** *Galvanostatic charge/discharge (GCD) curves,* ***(d)*** *Nyquist plots (inset showing high-frequency region),* ***(e)*** *Bode plots of the PCGH-1, PCGH-2 and PCGH-3 electrodes,* ***(f)*** *CV curves of the PCGH-3 electrode at different scan rates,* ***(g)*** *GCD curves of the PCGH-3 electrodes at different current densities,* ***(h)*** *Areal capacitances of the PCGH-3 electrodes at different current densities and* ***(i)*** *electrochromic property of the PCGH-3 electrode corresponding in situ bias-dependent absorbance spectra.*

6.2.5.2. A "All Solid-State Hydrogel Supercapacitor" device

The PCGH hydrogel showed very high mechanical strength with excellent mechanical properties like self-recovery, stimuli responsiveness, shape tunability etc. Taking advantage of these properties, the PCGH hydrogels were employed to fabricate "all-solid-state" supercapacitor*[26]* using a Swagelok cell (**Figure 6.15 a**). Following the intercept of EIS with real axis in the high-frequency region, the equivalent series resistance of the electrode was estimated to be ~ 3.3 Ω for the PCGH3 hydrogel (**Figure 6.15 b**). The low resistance could be ascribed to the interconnected conductive PANI nanofibrils having electric conductivity of 0.05 S cm^{-1}, which can provide a 3D continuous pathway for electron transport through the ionic channels of G-dimers in the PCGH hydrogel. The CV curves of the PCGH3 hydrogel device exhibited redox peaks of PANI at different scan rates, inferring the pseudo-capacitance behavior of the device (**Figure 6.15 c**). The areal capacitance of the PCGH3 hydrogel at different current density was calculated using the GCD curves (**Figure 6.15 d**). The PCGH3 hydrogel showed a high areal capacitance of 343 $mFcm^{-2}$, at a current density of 1$mAcm^{-2}$. During the device fabrication, the thickness of the hydrogel was maintained at 5 mm, which implies that the continuous PANI phase of 3D interconnected nanofibrous scaffold endows a fast electron transport and ion diffusion in the PCGH3 matrix (**Figure 6.15 e**). The Ragone plots of the PCGH3 solid-state device showing a high energy density of 93.36 $Whcm^{-2}$ at a power density 0.7 $mWcm^{-2}$ (inset, **Figure 6.15 e**). Further, at high power density (5.5 Wcm^{-2}), the energy density

was maintained (14 $Whcm^{-2}$). These results are comparable to those of recently reported PANI-based flexible supercapacitors; however, the integration of a biomolecular framework exhibits slightly lower cycling stability due to its non-covalent nature (**Table 6.1)**.

A solid-state symmetric supercapacitor device was fabricated in a two-electrode configuration, utilizing a PCGH electrode as the supercapacitor layer, Whatman filter paper as the separator, and PEO/$LiClO_4$ as the gel electrolyte (**Figure 6.15 g**). To demonstrate its practical applicability, two identical supercapacitor devices were connected in series to expand the potential window. The device was initially charged for one minute at a constant voltage of 3.0 V. Subsequently, the charged device was connected to a clock via wires (**Figure 6.15 h**, OFF state). When switched to the ON state, the device successfully powered the clock, illustrating its real-world functionality (**Figure 6.15 i**). Furthermore, the device exhibited outstanding durability, maintaining 80% of its maximum capacitance even after 1000 cycles, with the cycle shapes remaining consistent throughout the initial, middle, and final cycles. Since the cyclic performance tests were conducted using the PCGH symmetric supercapacitor device, this high level of cyclic stability highlights the robust performance of PCGH electrodes under real-world environmental conditions (**Figure 6.15 f**). Due to presence of a bi-continuous electrically active PANI nano-fibrillar scaffold along with an ionic conductive G-dimeric fibrillar network, the solid-state PCGH device demonstrated good capacitance along with high energy density and cyclic stability. Thus, by using the enzymatically active GMP hydrogels, a biomolecular self-assembly can be easily and reproducibly fabricated into a highly active energy storage device, which has the potential of replacing synthetic polymeric frameworks for designing bio-electronic interfaces with better biocompatibility.*[4]*

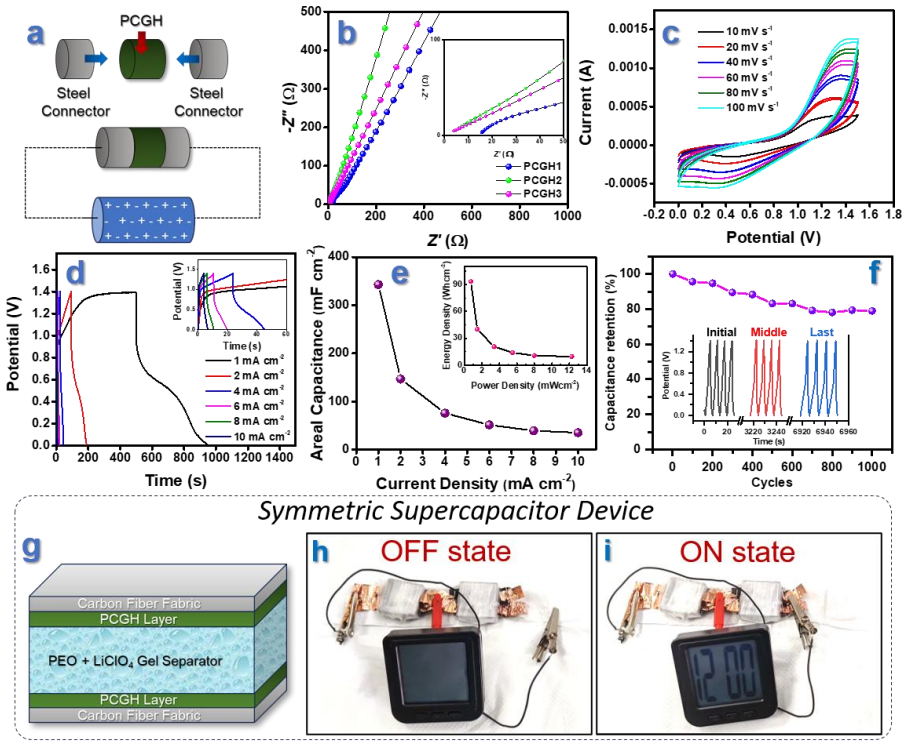


Figure 6.14. ***(a)*** *Fabrication strategy of device using PCGH hydrogel,* ***(b)*** *Cyclic voltammetry (CV) of all-solid-state device of PCGH-3 at different scan rates,* ***(c)*** *The galvanostatic charge/discharge plots of PCGH-3 at different current densities of 0.1 mA* cm^{-2} *to mA* cm^{-2}*,* ***(d)*** *Nyquist plots of the device and EIS plot showing the high frequency region (inset),* ***(e)*** *Areal capacitances of the PCGH electrodes at different current densities (inset showing the corresponding Ragone plots),* ***(f)*** *Cycling performance of the PCGH3 symmetric device for 1000 cycles (Inset showing GCD curves during the initial, middle and last four cycles),* ***(g)*** *Schematic illustration of the assembly of the device PCGH symmetric supercapacitor device on carbon fiber fabric substrate and PCGH3 condensate hydrogel symmetric device in* ***(h)*** *OFF state and* ***(i)*** *ON state while lighting a clock.*

Table 6.1. Comparison of electrochemical performances of PANI-based flexible supercapacitors.

Electrode Material	Specific Capacitance	Energy Density	Cycling Stability	Mechanical Properties	Ref.
PANI/CNT/PVA	15.8 mF cm^{-2} @0.044 $mAcm^{-2}$	0.9 µWh cm^{-2}	~85% @2500	Bendable	*[69]*
PANI/CNT/PMMA	44.13 mF cm^{-2} @0.2 mA cm^{-2}	4 µWh cm^{-2}	87% @20000	Stretchable	*[70]*

PANI/PAM/HA/Ag-lignin NP	364 mF cm^{-2} @0.3 mA cm^{-2}	16.4 µWh cm^{-2}	100% @6000	All flexible	*[71]*
PANI/PVA (Cryopolymerization)	260 Fg^{-1} @0.5 A g^{-1}	27.5Wh kg^{-1}	90% @2000	stretchable, compressible, bendable	*[72]*
PANI/V_2O_5 nanowire	76 F g^{-1} @0.58 A g^{-1}	-	83.3% @10,000	-	*[73]*
PANI/PVA/PHEA	98 $mFcm^{-2}$ @0.2 mA/cm^2	8.48 µwh/cm^2	99% @8000	High strength, toughness, fatigue resistance, self-healing	*[74]*
Schiff base crosslinked PANI hydrogel	912 Fg^{-1} @1 Ag^{-1}	54 µWhcm^{-2}	74% @1,000	-	*[75]*
PANI/PVA hydrogel	306 mF cm^{-2}	13.6 Wh kg^{-1}	100% @1000	-	*[76]*
PANI/GMP hydrogel (Enzyme-catalyzed polymerization)	343 $mFcm^{-2}$, @1$mAcm^{-2}$	93.36 Whcm^{-2}	81% @1000	High Strength, Self-healable, Thermo-reversible, Injectable, Bio-degradable	This Work

6.3. Conclusion

This study unveils a bioinspired pathway for fabricating multifunctional hydrogels through the organic acid-triggered self-assembly of guanosine monophosphate (GMP). The resulting dimeric nanofibers form mechanically robust hydrogels via a simple, metal-free supramolecular condensation process. Crucially, these nanostructures exhibit intrinsic peroxidase-mimetic activity, governed by Michaelis-Menten kinetics with low K_M values (0.5445 mM for TMB; 0.6017 mM for H_2O_2), rivaling natural enzymes. The enhanced catalytic efficiency arises from efficient substrate channeling within the aqueous nanofibrous architecture, establishing these metal-free nano assemblies as potent enzyme mimics. By leveraging the hydrogel as a dynamic template, we engineered a semiconducting polyaniline composite (PCGH) with exceptional injectability, printability, and stimuli-responsive behavior. These traits enable precise spatial patterning for

advanced devices, as demonstrated by high-performance electrochromic supercapacitor electrodes and solid-state energy-storage systems (high capacitance 343 $mFcm^{-2}$ and energy density 93.36 $Whcm^{-2}$). The PCGH's synergy of mechanical adaptability and electrical conductivity positions it as a transformative material for wearable bioelectronics and shape-morphing interfaces. This work establishes a universal blueprint for designing enzyme-mimetic hydrogels with hierarchical control, bridging molecular self-assembly and macroscopic functionality. The use of small biomolecules to form supramolecular polymerized products, which can be used as templates for the fabrication of conductive polymer hydrogels and soft material devices, will open new avenues for the development of bio-derivable and biocompatible functional materials.

6.4. Experimental Section

6.4.1. Preparation of CSA-GMP condensate and matrix hydrogel

CSA-GMP condensation was performed under physiological conditions by mixing equimolar (1 mM) aqueous solutions of CSA and GMP, followed by 1-hour incubation. Tyndall effect confirmed liquid-liquid phase separation. Spectroscopic and microscopic analysis were employed varying CSA/GMP ratios. For hydrogel preparation, 100 mM CSA and 150 mM GMP aqueous solutions were stirred at moderate temperature for 10-15 min, yielding a colorless transparent hydrogel validated by vial inversion. Post-formation characterization utilized diluted condensates or lyophilized hydrogel powder.

6.4.2. Characterization of Enzymatic Activity

Catalyzed reactions were conducted using 100 μL of CSA-GMP hydrogel within a 10 mM acetate buffer solution (pH ~4.4). Initial trials-maintained substrate concentrations at 1 mM TMB and 10 mM H_2O_2. UV-visible spectroscopy tracked absorbance at 652 nm to quantify TMB oxidation rates. Kinetic analyses involved systematically altering TMB concentrations with fixed H_2O_2 levels (and vice versa) under optimized

reaction conditions. The Lineweaver-Burk equation ($\frac{1}{V} = \frac{K_M}{V_{max} \times [S]} + \frac{1}{V_{max}}$) derived kinetic constants K_M (Michaelis constant) and V_{max} (maximum reaction rate) from initial reaction velocities (V_0). These velocities were calculated using absorbance changes within the first 600 seconds for: TMB: 0.01-2.5 mM and H_2O_2: 0.1-10 mM.

6.4.3. Preparation of Polyaniline Incorporated CSA-GMP Hydrogel (PCGH)

The PCGH hydrogel was synthesized via in-situ polymerization of aniline within the hydrogel matrix. Initially, the CSA-GMP hydrogel was dissolved and thoroughly mixed on a magnetic stirrer. Aniline (0.05 M) was then added, resulting in a color change from colorless to light-yellow. Subsequent addition of an equimolar amount of H_2O_2 led to a rapid transition to emerald green. After cooling at room temperature, a dark green opaque hydrogel formed. This procedure was replicated to create PANI hydrogels with varying aniline and H_2O_2 concentrations (0.1 M and 0.2 M). Following synthesis, the PANI hydrogels were characterized in either their native or lyophilized forms.

6.4.4. Methods

- **Calculation of crystallinity (χ_c):**

the χ_c is calculated from XRD patterns as follows:

The χ_{c1}, obtained from XRD patterns through an interactive peak-fit procedure, can be estimated by *Equation 1*:

$$\chi_{c1} = \frac{\Sigma A_{crys}}{\Sigma A_{crys} + \Sigma A_{amor}} \quad (1)$$

Where A_{crys} and A_{amor} are the fitted areas of crystals and amorphous phases.

- **Rheological Measurements:**

The dynamic strain sweep measurements were taken at a constant angular frequency (ω) of 10 $rads^{-1}$ and frequency sweep experiments of hydrogel were measured at a constant strain (γ) value of 1% at 25 °C.

The thixotropic step-strain measurements with respect to time intervals were carried out at variable strain values of 1% and 500% at a constant 10 $rads^{-1}$ of ω. Temperature dependent storage modulus values were collected using variable temperature extension on the parallel plate.

- **Electrochemical measurement:**

All the electrochemical tests were performed on Metrohm Autolab M204 potentiostat electrochemical workstation at room temperature. For all the in-situ bias-dependent UV-visible measurements, the PerkinElmer make lambda 365 spectrometer was used.

CV tests were performed in the potential range of -0.5 to 2 V under a scan rate of 10-100 mV s^{-1}. GCD tests were performed by scanning from 0 to 1.4 V at the current density from 0.5 to 2 A g^{-1} for the PCGH electrode and 1-10 $mAcm^{-2}$ for the solid-state PCGH device. EIS measurements were conducted with a frequency range of 10^4 Hz to 0.1 Hz with a 10 mV amplitude at open circuit potential for both electrode and device. Cycling stability of electrodes was carried out by repeating the GCD tests at 0.5 mA cm^{-2}, for the device.

The conductivity of APPH samples was determined by EIS measurements and calculated by *Equation 2*:

$$\sigma = t / (R \times A) \quad (2)$$

Where, t, A, and R are the height, area and bulk resistance of hydrogel samples inside the device respectively.

Areal capacitances of PCGH electrodes as well as the PCGH device were calculated from GCD curves according to *Equation 3*:

$$C_s = I \times t / (A \times V) \quad (3)$$

where I is the discharge current; t is the discharge time; A is the area of the PCGH electrodes on the ITO or the area of the PCGH hydrogel inside the device within two electrodes; and V is the voltage change upon discharging.

Energy density and power density of PCGH device were obtained based on *Equations 4 and 5*, respectively:

$$E = (1/2) \times C_s \times V^2 \quad (4)$$

$$P = E / t \quad (5)$$

where E, Cs, V, P, and t are the energy density, areal capacitance of PCGH, voltage change upon discharging, power density and discharge time, respectively.

6.5. References

1. Zhang, Y.S., Khademhosseini et al. (2017), Advances in engineering hydrogels, Science, 356, eaaf3627 (DOI: 10.1126/science.aaf3627.)
2. Hoffman, A.S. (2012), Hydrogels for biomedical applications, Adv. Drug Delivery Rev., 64, 18–23 (DOI: 10.1016/j.addr.2012.09.010.)
3. Yuk, H., Wu et al. (2022), Hydrogel interfaces for merging humans and machines, Nat Rev Mater, 7, 935–952 (DOI: 10.1038/s41578-022-00483-4.)
4. Zhong, R., Tang et al. (2018), Self-Assembly of Enzyme-Like Nanofibrous G-Molecular Hydrogel for Printed Flexible Electrochemical Sensors, Adv. Mater., 30, 1706887 (DOI: 10.1002/adma.201706887.)
5. Tian, B., Liu et al. (2012), Macroporous nanowire nanoelectronic scaffolds for synthetic tissues, Nat. Mater, 11, 986–994 (DOI: 10.1038/nmat3404.)
6. Wu, H., Yang et al. (2021), Materials, Devices, and Systems of On-Skin Electrodes for Electrophysiological Monitoring and Human–Machine Interfaces, Adv. Science, 8, 2001938 (DOI: 10.1002/advs.202001938.)
7. Park, J., Lee et al. (2024), Soft Sensors and Actuators for Wearable Human–Machine Interfaces, Chem. Rev., 124, 1464–1534 (DOI: 10.1021/acs.chemrev.3c00356.)

8. Fang, K., Wan et al. (2023), Hydrogel-Based Sensors for Human–Machine Interaction, Langmuir, 39, 16975–16985 (DOI: 10.1021/acs.langmuir.3c02444.)
9. Wang, Y., Zhu et al. (2023), Recent Advances in Hydrogel-Based Self-Powered Artificial Skins for Human–Machine Interfaces, Adv. Intel. Sys., 5, 2300162 (DOI: 10.1002/aisy.202300162.)
10. Chakraborty, P., Guterman et al. (2019), A Self-Healing, All-Organic, Conducting, Composite Peptide Hydrogel as Pressure Sensor and Electrogenic Cell Soft Substrate, ACS Nano, 13, 163–175 (DOI: 10.1021/acsnano.8b05067.)
11. Nezakati, T., Seifalian et al. (2018), Conductive Polymers: Opportunities and Challenges in Biomedical Applications, Chem. Rev., 118, 6766–6843 (DOI: 10.1021/acs.chemrev.6b00275.)
12. Tajik, S., Beitollahi et al. (2020), Recent developments in conducting polymers: applications for electrochemistry, RSC Adv., 10, 37834–37856 (DOI: 10.1039/D0RA06160C.)
13. Stejskal, J. (2017), Conducting polymer hydrogels, Chem. Pap., 71, 269–291 (DOI: 10.1007/s11696-016-0072-9.)
14. Tomczykowa, M., Plonska-Brzezinska et al. (2019), Conducting Polymers, Hydrogels and Their Composites: Preparation, Properties and Bioapplications, Polymers, 11, 350 (DOI: 10.3390/polym11020350.)
15. Jia, M., Rolandi et al. (2020), Soft and Ion-Conducting Materials in Bioelectronics: From Conducting Polymers to Hydrogels, Adv. Healthc. Mater., 9, 1901372 (DOI: 10.1002/adhm.201901372.)
16. Du, X., Zhou et al. (2015), Supramolecular Hydrogelators and Hydrogels: From Soft Matter to Molecular Biomaterials, Chem. Rev., 115, 13165–13307 (DOI: 10.1021/acs.chemrev.5b00299.)
17. Bhavsar, A., Pati et al. (2025), Supramolecular Conductive Hydrogels for Tissue Engineering Applications, ChemBioChem, 26, e202400733 (DOI: 10.1002/cbic.202400733.)

18. Buwalda, S.J., Vermonden et al. (2017), Hydrogels for Therapeutic Delivery: Current Developments and Future Directions, Biomacromolecules, 18, 316–330 (DOI: 10.1021/acs.biomac.6b01604.)
19. El Hamoui, O., Saydé et al. (2022), Nucleoside-Derived Low-Molecular-Weight Gelators as a Synthetic Microenvironment for 3D Cell Culture, ACS Biomater. Sci. Eng., 8, 3387–3398 (DOI: 10.1021/acsbiomaterials.2c00308.)
20. Zhao, L., Zhou et al. (2023), Natural Polymer-Based Hydrogels: From Polymer to Biomedical Applications, Pharmaceutics, 15, 2514 (DOI: 10.3390/pharmaceutics15102514.)
21. Johnson, E.K., Adams et al. (2011), Peptide based low molecular weight gelators, J. Mater. Chem., 21, 2024–2027 (DOI: 10.1039/C0JM03099F.)
22. Peters, G.M., Davis et al. (2016), Supramolecular gels made from nucleobase, nucleoside and nucleotide analogs, Chem. Soc. Rev., 45, 3188–3206 (DOI: 10.1039/C6CS00183A.)
23. Pu, F., Ren et al. (2018), Nucleobases, nucleosides, and nucleotides: versatile biomolecules for generating functional nanomaterials, Chem. Soc. Rev., 47, 1285–1306 (DOI: 10.1039/C7CS00673J.)
24. Ilhami, F.B., Birhan et al. (2024), Hydrogen-Bonding Interactions from Nucleobase-Decorated Supramolecular Polymer: Synthesis, Self-Assembly and Biomedical Applications, ACS Biomater. Sci. Eng., 10, 234–254 (DOI: 10.1021/acsbiomaterials.3c01097.)
25. Zhu, F., Lin et al. (2018), Tough and Conductive Hybrid Hydrogels Enabling Facile Patterning, ACS Appl. Mater. Interfaces, 10, 13685–13692 (DOI: 10.1021/acsami.8b01873.)
26. Li, L., Zhang et al. (2020), Cryopolymerization enables anisotropic polyaniline hybrid hydrogels with superelasticity and highly deformation-tolerant electrochemical energy storage, Nat Commun, 11, 62 (DOI: 10.1038/s41467-019-13959-9.)

27. Ikura, R., Park et al. (2022), Design of self-healing and self-restoring materials utilizing reversible and movable crosslinks, NPG Asia Mater, 14, 1–17 (DOI: 10.1038/s41427-021-00349-1.)
28. E, Y., Ju et al. (2022), Tunable and Self-Healing Properties of Polysaccharide-Based Hydrogels through Polymer Architecture Modulation, ACS Sustainable Chem. Eng., 10, 14053–14063 (DOI: 10.1021/acssuschemeng.2c05125.)
29. Gellert, M., Lipsett et al. (1962), Helix formation by guanylic acid, Proc. Natl. Acad. Sci. U. S. A., 48, 2013–2018 (DOI: 10.1073/pnas.48.12.2013.)
30. Walmsley, J.A., Sagan et al. (1986), The effect of monovalent cations on the association behavior of guanosine 5′-monophosphate, cytidine 5′-monophosphate, and their equimolar mixture in aqueous solution, Biopolymers, 25, 2149–2172 (DOI: 10.1002/bip.360251109.)
31. Sarma, S., Thakur et al. (2024), Chromatin inspired bio-condensation between biomass DNA and guanosine monophosphate produces all-nucleic hydrogel as a hydrotropic drug carrier, Commun Chem, 7, 1–13 (DOI: 10.1038/s42004-024-01353-6.)
32. Wong, A., Ida et al. (2005), Disodium Guanosine 5‘-Monophosphate Self-Associates into Nanoscale Cylinders at pH 8: A Combined Diffusion NMR Spectroscopy and Dynamic Light Scattering Study, J. Am. Chem. Soc., 127, 6990–6998 (DOI: 10.1021/ja042794d.)
33. Gao, M., Harish et al. (2017), Temperature and pressure limits of guanosine monophosphate self-assemblies, Sci Rep, 7, 9864 (DOI: 10.1038/s41598-017-10689-0.)
34. Otero, R., Schöck et al. (2005), Guanine Quartet Networks Stabilized by Cooperative Hydrogen Bonds, Angew. Chem. Int. Ed., 44, 2270–2275 (DOI: 10.1002/anie.200461586.)

35. Rosenzweig, B.A., Hamilton et al. (2009), Self-Assembly of a Four-Helix Bundle on a DNA Quadruplex, Angew. Chem. Int. Ed., 48, 2749–2751 (DOI: 10.1002/anie.200804849.)
36. Thakur, N., Chaudhary et al. (2021), Ion Conductive Phytic Acid-G Quadruplex Hydrogel as Electrolyte for Flexible Electrochromic Device, ChemNanoMat, 7, 613–619 (DOI: 10.1002/cnma.202100072.)
37. Tao, Y.H., Schulke et al. (2024), Hydration water drives the self-assembly of guanosine monophosphate, Biophy. J., 123, 931–939 (DOI: 10.1016/j.bpj.2024.03.005.)
38. Chakraborty, A., Dash et al. (2024), Polyoxometalate-Guanosine Monophosphate Hydrogels with Haloperoxidase-like Activity for Antibacterial Performance, Biomacromolecules, 25, 104–118 (DOI: 10.1021/acs.biomac.3c00845.)
39. Chakraborty, A., Rani et al. (2025), Guanosine Monophosphate Induced Solubilization of Folic Acid Leading to Hydrogel Formation for Targeted Delivery of Hydrophilic and Hydrophobic Drugs, ACS Appl. Mater. Interfaces, 17, 11848–11860 (DOI: 10.1021/acsami.4c21306.)
40. Sousa, V., Amaral et al. (2023), Self-Supporting Hyaluronic Acid-Functionalized G-Quadruplex-Based Perfusable Multicomponent Hydrogels Embedded in Photo-Cross-Linkable Matrices for Bioapplications, Biomacromolecules, 24, 3380–3396 (DOI: 10.1021/acs.biomac.3c00433.)
41. Renaud de la Faverie, A., Guédin et al. (2014), Thioflavin T as a fluorescence light-up probe for G4 formation, Nucleic Acids Res., 42, e65 (DOI: 10.1093/nar/gku111.)
42. Mohanty, J., Barooah et al. (2013), Thioflavin T as an Efficient Inducer and Selective Fluorescent Sensor for the Human Telomeric G-Quadruplex DNA, J. Am. Chem. Soc., 135, 367–376 (DOI: 10.1021/ja309588h.)

43. Panda, M., Walmsley et al. (2011), Circular Dichroism Study of Supramolecular Assemblies of Guanosine 5′-Monophosphate, J. Phys. Chem. B, 115, 6377–6383 (DOI: 10.1021/jp201630g.)
44. Umesh, C. Chandran et al. (2024), A hydrogel based on Fe(II)-GMP demonstrates tunable emission, self-healing mechanical strength and Fenton chemistry-mediated notable antibacterial properties, Nanoscale, 16, 13050-13060 (DOI: 10.1039/D4NR01011F.)
45. Wu, G., Kwan et al. (2009), Helical Structure of Disodium 5′-Guanosine Monophosphate Self-Assembly in Neutral Solution, J. Am. Chem. Soc., 131, 3180–3182 (DOI: 10.1021/ja809258y.)
46. Biancalana, M., Koide et al. (2010), Molecular mechanism of Thioflavin-T binding to amyloid fibrils, Biochimica et Biophysica Acta (BBA) - Proteins and Proteomics, 1804, 1405–1412 (DOI: 10.1016/j.bbapap.2010.04.001.)
47. Ghosh, A., Parasar et al. (2016), Chiral carbon dots derived from guanosine 5′-monophosphate form supramolecular hydrogels, Chem. Commun., 52, 11159–11162 (DOI: 10.1039/C6CC05947C.)
48. Detellier, C., Laszlo et al. (1980), Role of alkali metal and ammonium cations in the self-assembly of the 5’-guanosine monophosphate dianion, J. Am. Chem. Soc., 102, 1135–1141 (DOI: 10.1021/ja00523a033.)
49. Vázquez-González, M., Wang et al. (2020), Biocatalytic cascades operating on macromolecular scaffolds and in confined environments, Nat Catal, 3, 256–273 (DOI: 10.1038/s41929-020-0433-1.)
50. Altenburg, W.J., Yewdall et al. (2020), Programmed spatial organization of biomacromolecules into discrete, coacervate-based protocells, Nat Commun, 11, 6282 (DOI: 10.1038/s41467-020-20124-0.)

51. Koga, S., Williams et al. (2011), Peptide–nucleotide microdroplets as a step towards a membrane-free protocell model, Nature Chem, 3, 720–724 (DOI: 10.1038/nchem.1110.)
52. Abbas, M., Lipiński et al. (2021), Peptide-based coacervates as biomimetic protocells, Chem. Soc. Rev., 50, 3690–3705 (DOI: 10.1039/D0CS00307G.)
53. Harraz, D.M., Davis et al. (2018), A self-assembled peroxidase from 5′-GMP and heme, Chem. Commun., 54, 1587–1590 (DOI: 10.1039/C7CC09900B.)
54. Bhuyan, S.K., Wang et al. (2023), Directed Evolution of a G-Quadruplex Peroxidase DNAzyme and Application in Proteomic DNAzyme–Aptamer Proximity Labeling, J. Am. Chem. Soc., 145, 12726–12736 (DOI: 10.1021/jacs.3c02625.)
55. Zhang, P., Sun et al. (2019), Modified carbon nitride nanozyme as bifunctional glucose oxidase-peroxidase for metal-free bioinspired cascade photocatalysis, Nat Commun, 10, 940 (DOI: 10.1038/s41467-019-08731-y.)
56. Jain, S., Panigrahi et al. (2019), Counter Anion-Directed Growth of Iron Oxide Nanorods in a Polyol Medium with Efficient Peroxidase-Mimicking Activity for Degradation of Dyes in Contaminated Water, ACS Omega, 4, 13153–13164 (DOI: 10.1021/acsomega.9b01201.)
57. Tan, X., Yang et al. (2022), PdIr Aerogels with Boosted Peroxidase-like Activity for a Sensitive Total Antioxidant Capacity Colorimetric Bioassay, ACS Appl. Mater. Interfaces, 14, 10047–10054 (DOI: 10.1021/acsami.1c22625.)
58. Cai, S., Fu et al. (2020), Zero-Dimensional/Two-Dimensional AuxPd100–x Nanocomposites with Enhanced Nanozyme Catalysis for Sensitive Glucose Detection, ACS Appl. Mater. Interfaces, 12, 11616–11624 (DOI: 10.1021/acsami.9b21621.)
59. Huang, J., Kaner et al. (2004), A General Chemical Route to Polyaniline Nanofibers, J. Am. Chem. Soc., 126, 851–855 (DOI: 10.1021/ja0371754.)

60. Zhou, K., He et al. (2018), A Hydrogel of Ultrathin Pure Polyaniline Nanofibers: Oxidant-Templating Preparation and Supercapacitor Application, ACS Nano, 12, 5888–5894 (DOI: 10.1021/acsnano.8b02055.)
61. Butoi, B., Groza et al. (2017), Morphological and Structural Analysis of Polyaniline and Poly(o-anisidine) Layers Generated in a DC Glow Discharge Plasma by Using an Oblique Angle Electrode Deposition Configuration, Polymers, 9, 732 (DOI: 10.3390/polym9120732.)
62. Rohom, A.B., Londhe et al. (2014), Electropolymerization of polyaniline thin films, High Performance Polymers, 26, 641–646 (DOI: 10.1177/0954008314538081.)
63. Kabir, M.M., Sabur et al. (2025), Hydrogels in next-generation energy solutions, Desalination, 603, 118639 (DOI: 10.1016/j.desal.2025.118639.)
64. Tadesse, M.G., Lübben et al. (2023), Review on Hydrogel-Based Flexible Supercapacitors for Wearable Applications, Gels, 9, 106 (DOI: 10.3390/gels9020106.)
65. Seliktar, D. (2012), Designing Cell-Compatible Hydrogels for Biomedical Applications, Science, 336, 1124–1128 (DOI: 10.1126/science.1214804.)
66. Bansal, L., Ahlawat et al. (2024), Nano-Nest Type Porous $NiCo_2S_4$@polyindole Core–Shell Array: Efficient Energy Storage Supercapacitor Device, ACS Materials Lett., 6, 3736–3744 (DOI: 10.1021/acsmaterialslett.4c00866.)
67. Bansal, L., Ghosh et al. (2023), Exploiting Charge Storage Capabilities of $NiTiO_3/TiO_2$ for Achieving the Most Efficient Hybrid Electrochromic Device, ACS Appl. Eng. Mater., 1, 577–583 (DOI: 10.1021/acsaenm.2c00140.)
68. Chakraborty, A., Ghosh et al. (2024), A multi-stimuli responsive polyoxometalate-guanosine monophosphate hybrid chromogenic smart hydrogel, J. Mater. Chem. C, 12, 13447–13456 (DOI: 10.1039/D4TC01973C.)

69. Guo Y., Zheng K., Wan P. (2018), A Flexible Stretchable Hydrogel Electrolyte for Healable All-in-One Configured Supercapacitors, Small, 14, 1704497 (DOI: 10.1002/smll.201704497)
70. Li L., Lou Z., Han W. et al. (2017), Highly Stretchable Micro-Supercapacitor Arrays with Hybrid MWCNT/PANI Electrodes, Adv Mater Technol, 2, 1600282 (DOI: 10.1002/admt.201600282)
71. Wang D., Yang F., Wang C. et al. (2023), In-situ polymerization of PANI on hydrogel electrolyte enabling all-in-one supercapacitors mechanically stable at low temperatures, Chem Eng J, 455, 140949 (DOI: 10.1016/j.cej.2022.140949)
72. Li L., Zhang Y., Lu H. et al. (2020), Cryopolymerization Enables Anisotropic Polyaniline Hybrid Hydrogels with Superelasticity and Highly Deformation-Tolerant Electrochemical Energy Storage, Nat Commun, 11, 62 (DOI: 10.1038/s41467-019-13959-9)
73. Zhou K., He Y., Xu Q. et al. (2018), A Hydrogel of Ultrathin Pure Polyaniline Nanofibers: Oxidant-Templating Preparation and Supercapacitor Application, ACS Nano, 12, 5888–5894 (DOI: 10.1021/acsnano.8b02055)
74. Yang J., Yu X., Sun X. et al. (2020), Polyaniline-Decorated Supramolecular Hydrogel with Tough, Fatigue-Resistant, and Self-Healable Performances for All-In-One Flexible Supercapacitors, ACS Appl Mater Interfaces, 12, 9736–9745 (DOI: 10.1021/acsami.9b20573)
75. Ghosh S., Majhi J., Sharma S. et al. (2025), Synthesis of Schiff base crosslinked polyaniline hydrogels with enhanced electrochemical performance for supercapacitor applications, Mater Chem Front, 9, 1340–1354 (DOI: 10.1039/D4QM01135J)
76. Li W., Gao F., Wang X. et al. (2016), Strong and Robust Polyaniline-Based Supramolecular Hydrogels for Flexible

Supercapacitors, Angew Chem, 128, 9342–9347 (DOI: 10.1002/ange.201603417)

Chapter 7

7. Conclusion and Future Prospects

7.1. Summary

This thesis demonstrates that the remarkable self-assembly of biomolecules can be harnessed to transform them into sophisticated functional materials through rational supramolecular design. By establishing 5′-guanosine monophosphate (5′-GMP) as a versatile molecular building block for engineering multifunctional hydrogels, this work shows how simple, low-molecular-weight biomolecules assembled exclusively through reversible non-covalent interactions can generate dynamic soft materials with structural precision and diverse functions. Collectively, the studies presented in this thesis expand the fundamental understanding of nucleotide self-assembly while providing a unified platform for biomedical, catalytic, and bioelectronic applications.

At the molecular level, all the developed systems rely on the intrinsic self-assembly capability of 5′-GMP through cooperative Hoogsteen hydrogen bonding, π–π stacking and electrostatic interactions. These interactions drive the formation of G-quadruplexes, and G-dimers, which subsequently organize into one-dimensional fibrillar networks and finally macroscopic hydrogels. More importantly, this work demonstrates that the self-assembly pathway is highly programmable. By introducing complementary biomolecules such as biomass-derived DNA, adenosine phosphates (ADP and ATP), amino acid-metal complexes, solvent engineering, or ionic crosslinking, the molecular packing and supramolecular architecture can be precisely regulated without disrupting the fundamental nucleotide assembly mechanism. This molecular-level tunability provides direct control over network morphology, mechanical properties, molecular transport, catalytic microenvironments, and electronic behaviour, illustrating how

subtle intermolecular interactions can dictate macroscopic material function.

The biomedical potential of this platform was first demonstrated through the development of "all-nucleic" DNA-GMP hydrogels capable of acting as universal hydrotropic drug carriers. By exploiting the intrinsic biocompatibility of biomass DNA and the programmable assembly of GMP, sustained encapsulation and controlled release of chemically diverse anticancer drugs were achieved. Furthermore, minimalist modulation through glycerol incorporation and calcium-ion crosslinking enabled precise switching between different drug release mechanisms, highlighting how physical interactions alone can regulate the kinetics of therapeutic delivery without requiring complex chemical modification.

Beyond drug delivery, the thesis establishes nucleotide hydrogels as functional catalytic materials. The ADP/ATP-GMP supramolecular hydrogel exhibited intrinsic peroxidase-like activity while simultaneously serving as a compatible scaffold for native enzymes, enabling efficient enzyme cascade reactions. This dual functionality demonstrates that supramolecular nucleotide assemblies can mimic both catalytic activity and cellular compartmentalization, providing simplified biomimetic systems for artificial metabolic networks.

The work further advances the field of artificial metalloenzymes by demonstrating that native enzyme active centers can be stabilized within a completely non-proteinaceous supramolecular scaffold. The copper-histidine-GMP hydrogel successfully reproduced the structural and functional characteristics of catechol oxidase, illustrating how rational confinement of metal coordination complexes inside dynamic nucleotide fibrillar networks generates biomimetic catalytic environments. This strategy bridges supramolecular chemistry and metalloenzyme engineering, providing a general pathway for constructing artificial enzymes from minimal biological components.

Finally, the versatility of the nucleotide scaffold was extended beyond biology through its transformation into electrically active functional materials. The supramolecular hydrogel served as a template for in situ polymerization of conductive polymers, producing electrochromic supercapacitor materials that integrate ionic transport with electronic conductivity. This demonstrates that biomolecular self-assembly can provide sustainable pathways toward multifunctional bioelectronic materials.

Collectively, this thesis establishes a comprehensive molecular design framework in which a single nucleotide building block can be programmed into multiple functional materials spanning drug delivery, biomimetic catalysis, enzyme engineering, and bioelectronics. The work highlights that hierarchical self-assembly, rather than synthetic complexity, is the key determinant of function. This minimalist design philosophy not only deepens the understanding of supramolecular nucleotide assembly but also provides a versatile and sustainable platform for the next generation of adaptive biomaterials, artificial enzymes, and multifunctional soft matter.

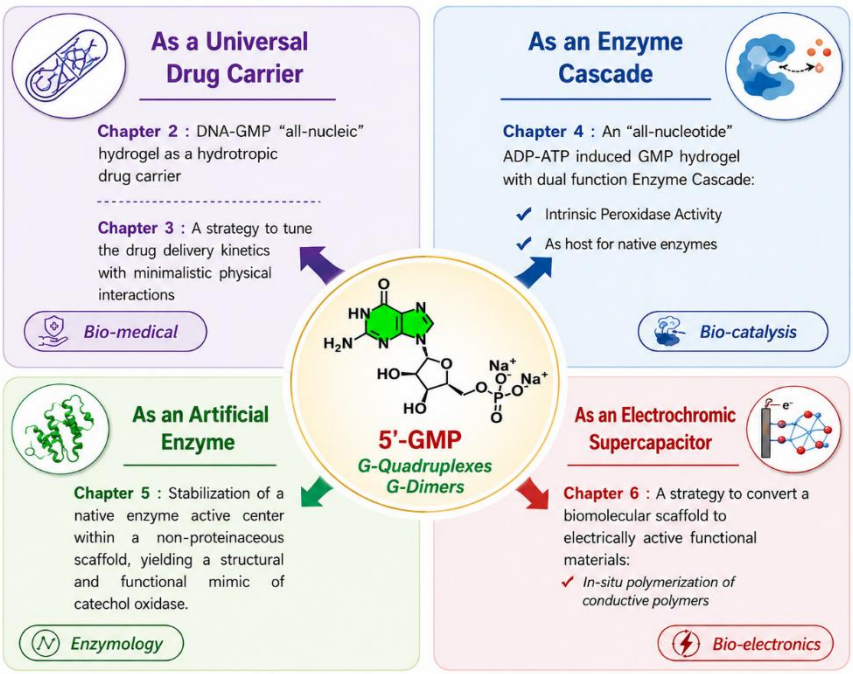


Figure 7.1. *Schematic overview of the thesis highlighting the versatile functional landscape of 5'-GMP-based supramolecular self-assembly.*

7.2. Future Scopes

The findings presented in this thesis provide a strong foundation for the continued development of multifunctional supramolecular nucleotide hydrogels. A key future direction is the *in vivo* evaluation of the developed drug-delivery systems to comprehensively investigate their pharmacokinetics, biodistribution, therapeutic efficacy, biodegradation, long-term biocompatibility, and translational potential. Such studies will be essential for validating their clinical relevance and advancing these materials toward preclinical development. Compared with conventional drug carriers, the pristine nucleotide-based hydrogels developed in this work offer a unique biomolecular platform with intrinsically programmable drug encapsulation and tunable release kinetics through simple physical modulation, eliminating the need for complex chemical modifications. While lipid nanoparticles have revolutionized drug delivery and have demonstrated remarkable clinical success, their large-scale manufacturing, formulation complexity, and associated production costs remain important considerations. In contrast, the minimalist design of the nucleotide hydrogels, composed entirely of naturally occurring biomolecules, presents a simple, biocompatible, and potentially cost-effective alternative for sustained drug delivery. With comprehensive *in vivo* validation and optimization, these hydrotropic nucleotide-based hydrogels hold significant promise as a versatile platform for the next generation of programmable therapeutic delivery systems.

Further understanding of the developed artificial enzymes can be achieved through molecular dynamics simulations and complementary computational studies to elucidate their structural flexibility, catalytic pathways, and structure-activity relationships. These investigations will provide molecular-level insights into the feasibility of 5′-GMP-based supramolecular assemblies as functional surrogates for natural protein scaffolds and guide the rational design of next-generation biomimetic catalysts.

The conductive hydrogels developed in this work also offer significant opportunities for bioelectronic and biomedical applications, including wearable health-monitoring systems, flexible biosensors, implantable electronics, soft robotics, and electrochemical energy-storage devices. Future efforts may focus on improving their conductivity, mechanical robustness, and long-term operational stability under physiological conditions.

Overall, this work is expected to inspire further research into functional, adaptive, and sustainable supramolecular hydrogel systems, accelerating the development of next-generation biomimetic materials that seamlessly integrate molecular self-assembly with advanced biomedical, catalytic, and bioelectronic technologies.



D.O.B. 5th May, 1997

Email: suryakamal1234@gmail.com

Phone: +917896060234

Mr. Suryakamal Sarma, from Guwahati, Assam, India has completed his Bachelor of Science in Chemistry (Honors) from B. Borooah College, affiliated with Gauhati University, in 2018, followed by a Master of Science in Chemistry from Gauhati University, Assam, in 2020. In August 2021, he joined the Indian Institute of Technology Indore to pursue his doctoral studies under the supervision of Dr. Tridib Kumar Sarma. His doctoral research focused on "*Bio-Inspired Engineering of Supramolecular Hydrogels Using Guanosine 5'-Monophosphate as a Primordial Biomolecular Scaffold: From Design Strategies to Emerging Applications*." This thesis embodies his humble efforts to contribute to the continually evolving landscape of scientific research during the past five years.